PH.D. DISSERTATION / TESIS DOCTORAL

# LIDAR DEPOLARIZATION TECHNIQUE: ASSESSMENT OF THE HARDWARE POLARIZING SENSITIVITY AND APPLICATIONS

**Author:**

JUAN ANTONIO BRAVO ARANDA

Universidad de Granada

Instituto Interuniversitario de
Investigación del Sistema Tierra
en Andalucía

Grupo Física de la Atmósfera

# UNIVERSIDAD DE GRANADA

## DEPARTAMENTO DE FÍSICA APLICADA
## GRUPO DE FÍSICA DE LA ATMÓSFERA

TESIS DOCTORAL

## LIDAR DEPOLARIZATION TECHNIQUE: ASSESSMENT OF THE

## HARDWARE POLARIZING SENSITIVITY AND APPLICATIONS

Tesis presentada por Juan Antonio Bravo Aranda para optar al grado de Doctor.

Directores de la Tesis:

Dr. Francisco José Olmo Reyes
Catedrático de la UGR
Dep. Física Aplicada
Univ. de Granada

Dr. Lucas Alados Arboledas
Catedrático de la UGR
Dep. Física Aplicada
Univ. de Granada

Dr. Juan Luis Guerrero Rascado
Investigador de la UGR
Dep. Física Aplicada
Univ. de Granada

Granada, abril de 2014

El trabajo de investigación que se expone en la presente memoria, titulado: «LIDAR DEPOLARIZATION TECHNIQUE: ASSESSMENT OF THE HARDWARE POLARIZING SENSITIVITY AND APPLICATIONS», para aspirar al grado de Doctor en Física que presenta Juan Antonio Bravo Aranda, ha sido realizado en la Universidad de Granada gracias a la beca concedida por el Ministerio de Educación «Formación de Profesorado Universitario (convocatoria 2009)», bajo la dirección de:

VºBº los directores:

Dr. FRANCISCO JOSÉ OLMO REYES

Dr. LUCAS ALADOS ARBOLEDAS          Dr. JUAN LUIS GUERRERO RASCADO

Aspirante a grado de Doctor:

Ldo. JUAN ANTONIO BRAVO ARANDA

El doctorando Juan Antonio Bravo Aranda y los directores de la tesis Francisco José Olmo Reyes, Lucas Alados Arboledas y Juan Luis Guerrero Rascado garantizamos, al firmar esta tesis doctoral, que el trabajo ha sido realizado por el doctorando bajo la dirección de los directores de la tesis y hasta donde nuestro conocimiento alcanza, en la realización del trabajo, se han respetado los derechos de otros autores a ser citados, cuando se han utilizado sus resultados o publicaciones.

Granada, abril de 2014

Directores de la Tesis:

Fdo.: Dr. Francisco José Olmo Reyes

Fdo.: Dr. Lucas Alados Arboledas          Fdo.: Dr. Juan Luis Guerrero Rascado

Doctorando:

Juan Antonio Bravo Aranda

A mis padres, Juan y María,

por darme la *vida*,

y a mi esposa, María del Pilar,

por hacer que merezca la pena vivirla.

Teniendo en cuenta la crisis económica, que me ha acompañado a lo largo del doctorado como un desagradable *leitmotiv*, vendría más a colación usar «estoy en "deuda"» que «estoy agradecido». Sin embargo, de tanto deber…, terminaría obligado a declararme en concurso de acreedores y viéndome en la tesitura de recurrir, como si de un banco de crédito se tratara, al conocido «que Dios te lo pague…». Supongo que este será el motivo de que la gente en mi situación sea más partidaria de dar las gracias… —nótese, a su vez, que *gracias* procede del latín *gratia* cuya forma de ablativo plural es *gratiis* que mucho tiene que ver con el siempre bienvenido *gratis*—. Así pues, entiéndanse mis agradecimientos como una fórmula por la que me declaro insolvente ante el incondicional apoyo y la abrumadora ayuda que he recibido a lo largo de toda mi vida.

Atónitos me miraron mis padres cuando les pedí un microscopio para mi cumpleaños. Supongo que esperaban algo más acorde con mis ¿12-13 años?, pero, a pesar del precio —más que considerable— y de la rareza de la petición, me lo compraron sin dudarlo. Aquel microscopio se convirtió en el tótem por el cual supe a ciencia cierta que mis padres me apoyarían siempre. «Gracias, papá y mamá, por darme la vida; no solo sois la causa de que me lata el corazón sino la fuerza que me ayuda a cumplir mis sueños».

«Belén, como hermana mayor, he aprendido a ver el mundo con tus ojos llenos de optimismo y a disfrutar de cada momento por banal que pareciese, gracias a ti soy feliz en casi cualquier circunstancia. Gracias por haber estado activamente a mi lado y gracias por seguir estándolo a pesar de la distancia».

Según una teoría de mi amigo Enrique, la suerte se gasta. Pues bien, fundamentándome en esta teoría y en que la familia no se escoge, sino que «te toca», puedo asegurar que yo gasté toda la suerte de mi vida en la familia que tengo. «Gracias por hacer que todo parezca más fácil a vuestro lado».

El camino hacia la lectura de mi tesis doctoral comenzó en la escuela rural La Gavia, donde mi primera maestra fue mi tía Elvira. Ella me abrió los ojos al mundo y convirtió mi curiosidad en pasión por el conocimiento. Ella me enseñó que esforzarse nunca es en vano y me dio el primer empujón que me ha traído hasta aquí. A ella, a mis maestros y profesores y a todo el que ha contribuido a mi educación les agradezco su tiempo y dedicación. Ojalá esta tesis les valga como recompensa.

Mi pasión general por el conocimiento colapsó en un entusiasmo desbordante por la Física. Por ella, me vine a Granada, donde descubrí auténticas joyas. «Adolfo, Anto, Domingo, José Antonio, Noe y Yassir. Os admiro profundamente. Muchas gracias por vuestra amistad y la incuestionable contribución a mi trabajo. No solo he aprendido de vosotros, sino que me exijo cada día más para poder corresponderos». «Anto y Noe, quiero agradeceros, especialmente, vuestra ayuda tanto técnica como artística para poder hacer realidad la cubierta de la tesis».

Siguiendo con un poco de historia… Fue un día a caballo entre la primavera y lo que viene siendo el infierno estival granadino, en el que Lucas me preguntó:

—¿Estás interesado en hacer el doctorado?

*«¡¿Que si estoy interesado?!* —pensé—. *¡Llevo desde los 10 años queriendo ser científico!»*.

Aquel día comenzó mi particular sueño hecho realidad. «Lucas, por tu confianza, dedicación y amistad, te estaré eternamente agradecido».

Ahora bien, debo reconocer que el inicio de ese sueño fue más bien una pesadilla. Tuve que madurar a salto de mata entre errores de la talla de «"Conserjería" de Medio Ambiente» y pasos en falso como mi primera introducción «científica» que más parecía un circunloquio rococó venido a

menos. Si no hubiera sido por la infinita paciencia de mi querido Hassan, nunca hubiera seguido adelante. Se valió de mis errores para darme lecciones magistrales y nunca me juzgó por mis equivocaciones sino por mi esfuerzo. Él convirtió mi miedo al fracaso en valentía. « Muchas gracias Hassan por todo lo que me has dado sin pedir nada a cambio».

Tras dos años de incertidumbre, conseguí una beca FPU con la que se allanó considerablemente el camino para la culminación de la tesis. Mis directores, Lucas, Paco Pepe y Juanlu, no solo me han dirigido el trabajo, sino que, acompañándome más allá de lo profesional, se han convertido en grandes amigos. «Siempre os agradeceré vuestra compañía, paciencia, ayuda y amistad».

Mi tesis doctoral va de lidar —como ya habrá observado mi avispado lector—, un instrumento un tanto complejo que requiere mayor cuidado y mimo que un agaporni bajo de ánimos. El caso es que detrás de cada figura, dato, test o comentario «lidariano» no sólo hay ciencia sino un grupo de amigos apostando por un futuro común. En pocas palabras… un trabajo en equipo con espíritu s*olidar*io. «Fran, Juanlu, y María José, muchas gracias por vuestra ayuda y apoyo trabajando codo con codo. Gracias por preocuparos por mí tanto dentro como fuera del trabajo y sobrellevar mis defectos. Si la tesis tuviera alma, tendría un pedacito de cada uno de vosotros».

Grata sorpresa me llevé cuando la programación se convirtió en afición de la noche a la mañana, lo cual no hubiera sido posible sin Jaime. Si MATLAB fuera la *Fuerza*, Jaime sería mi maestro *Jedi*. Con él aprendí a respirar en *Matrix* y a mantenerme lejos del lado oscuro ante una pantalla llena de errores de código. INDRA y LPSS nunca hubieran visto la luz sin el favor desinteresado de Jaime. «Mucha gracias, Jaime, por ser mi maestro y por las horas pasadas ante la ventana de quién sabe cuántas funciones…; de ti aprendí,

además, que ser autodidacta significa esfuerzo extra pero también una gran satisfacción personal». No puedo hablar de *Matrix* sin acordarme de Juan Alfredo, compañero de ocio y mi salvación en lo que a la informática se refiere. Siempre he tenido la sospecha de que detrás de la informática hay algo de «magia negra», de tal forma que para formatear decentemente un ordenador era necesario sacrificar una gallina blanca en luna menguante recitando hacia atrás la autobiografía de Bill Gates o, en caso contrario, un pantallazo azul de Windows convocaría un «demonio menor» borrando selectivamente los archivos por su urgencia, importancia y dificultad de reposición y en ese orden para más inri. Sin embargo, Juan Alfredo me enseñó que es más una cuestión de paciencia y de entender que el ordenador no hace lo que se desea, sino lo que se le ordena… «Muchas gracias Juan Alfredo, por socorrerme sin descanso. Hablar el mismo "idioma" ha sido una de las razones de mi gran calidad de vida en el CEAMA».

Cuando llegué al Centro Andaluz de Medio Ambiente para trabajar en mi tesis doctoral, no pude evitar verlo como una comunidad surgida de la mismísima Tierra Media… Catedráticos y profesores titulares —los más sabios de todos los seres—, post-doctorales —barrenando datos y tallando teorías en búsqueda de la próxima joya publicable en primer cuartil— y becarios precarios —trabajadores infatigables con ánimo impertérrito ante la inabordable tarea encomendada—. «Muchas gracias, Inma Foyo, por tu cercanía, esforzándote para que el GFAT sea siempre un grupo especial de grandes amigos»; «muchas gracias, Inma Alados, por estar siempre ojo avizor y salvaguardarme de las avispas asesinas»; «muchas gracias, Andy, por tu punto de vista claro y nítido: pura ciencia sin colorantes ni conservantes»; «muchas gracias, Alberto, por ayudarme a resolver cualquier encrucijada que me planteara y mediar con mi *arapahoe* a base de inglés poceño»; «muchas gracias, Óscar, por todo lo que me

xiv

has aportado en los cientos de conversaciones que hemos tenido»; «muchas gracias, Enrique, por tus ánimos, tu confianza… y tu genial sentido del humor»; «Manuel Antón y Mar, muchas gracias por vuestra grata compañía, sois *gfaties* de pleno derecho»; «muchas gracias, Dani, por tu compañía y los buenos momentos post-seminario». «Antonio, siempre has estado a mi lado —y no me refiero solo a lo juntos que están nuestros escritorios— así que te agradezco la compañía y tu mejor enseñanza: a mayor reto, mayor templanza y paso firme».

Continuando con la Tierra Media… Penélope y Gloria; Arwin y Eowin. Sabias compañeras de viaje luchando por romper la maldición del científico sin final feliz. Ante los momentos de desesperación: palabras esperanzadoras; ante la plomiza rutina: fotópica novedad; ante la flaqueza: eterna motivación. «Penélope y Gloria, muchas gracias por ayudarme a no perder el norte; ojalá os tenga siempre cerca».

Si cuando llegué al CEAMA se me antojó una Tierra Media, el tiempo ha dejado claro que este lugar siempre ha sido el caldo de cultivo perfecto para desarrollar mi labor. «Gracias, Marian, por ser mi guía en los oscuros vericuetos de la burocracia» y «Gracias, Luis, por alegrarme las mañanas con chistes cada vez más malos y cortos —exactamente los que me gustan—». «Muchas gracias a los dos por hacer real el complejo trato con la administración».

I switch the language to acknowledge the help I received from abroad. I would like to thank Dr. Jana Preißler for her help with the improvement of this thesis and for the strong friendship we have. Also, I want to thank Dr. Volker Freudenthaler all his help and dedication during my research stay in Munich and through tens of mails. He was always willing to teach me everything and thus, I learnt a lot about science… but not only. I cannot forget to thank Ina her friendship since the *earlinet* years and the special welcome that I and my wife received during the weekend in her home. I would like to acknowledge Dr.

Doina Nicolae for trusting me and for giving me the opportunity to visit RADO, where I felt at home.

Las personas se pueden agrupar entre las que se dejan el mejor bocado del plato para el final y las que no. Pues bien, aquí viene lo último… y lo mejor… Pili, mi esposa, parte de mí desde los 12 años de edad. Si mi vida fuera una tonalidad, Pili sería su tónica. Me gusta pensar que la felicidad es un acorde mayor en el que Pili es la fundamental, mi vida laboral su quinta justa y la gente que me rodea su tercera mayor sin la que la vida sonaría un tanto hueca… Pili ha sido la nota pedal que me ha ayudado a seguir adelante, independientemente de las modulaciones que sufrieran nuestras vidas, y la razón de cuanto esfuerzo he realizado. «Muchas gracias, Pili, por tu eterna comprensión y cuanto has sacrificado por mí. Ojalá la vida me dé la oportunidad de hacerte tan feliz como tú me has hecho».

Firmo esta tesis como único autor, aunque al término de estos agradecimientos bien se entendería firmada como *Bravo-Aranda et «all»*.

«La verdadera ciencia enseña, por encima de todo,
a dudar y a ser ignorante».
*'True science teaches, above all,*
*to doubt and be ignorant'.*

Miguel Unamuno (1864-1936)
Filósofo y escritor español
*Spanish philosopher and writer*

# Abstract

This PhD dissertation tries to reduce the lack of knowledge about the polarizing response of lidar systems which is particularly crucial for the lidar depolarization technique. Furthermore, the potential of the lidar depolarization technique is presented through its applications in atmospheric aerosol research.

First, this thesis includes a summary presentation of key concepts of aerosol theory and the active optical remote sensing used. Then, the experimental site and the multiwavelength Raman lidar (MULHACEN) and the scanning Raman lidar (VELETA) are presented. The experimental site is the Andalusian Institute for Earth System Research (IISTA-CEAMA) located in the Southern part of the city of Granada in South-eastern Spain (37.16°N, 3.61°W, 680 m above sea level). MULHACEN and VELETA systems are described in detail providing information about their configuration and the quality assurance methods used. Both MULHACEN and VELETA, operated by the Atmospheric Physics Group, are part of the European Aerosol Research Lidar Network (EARLINET). Besides, basic information on other instruments used in the development of this thesis, such as the sun-photometer and microwave radiometer, is included.

Concerning methodological aspects, this thesis mainly includes: a detailed description of the pre-processing steps to be applied to raw lidar signals and an explanation of the elastic, inelastic and depolarization algorithms.

The following paragraphs briefly present the main issues discussed in this thesis.

The assessment of the lidar polarizing sensitivity was performed using the Stokes-Müller formulism to model the polarizing response of lidar systems. To this aim, different parts of lidar systems were grouped following its functionality and thus, five functional blocks were analysed: laser, laser emitting optics, receiving optics, detection unit (polarizing beam splitter and

photomultipliers) and calibrator. The quantification of the polarizing influence of each functional block was performed by means of a simulator, the so-called *Lidar Polarizing Sensitivity Software (LPSS)*, developed to this aim in the framework of this study. General results were obtained modelling a synthetic lidar based on lidar properties and its uncertainties, derived from different technical specifications of commercial optical devices. The use of this tool demonstrates that the lidar polarization sensitivity can affect the depolarization measurements, causing relative errors even larger than 100% in the depolarization products (volume and particle linear depolarization ratios). The most critical properties are the purity parameter of the laser and the effective diattenuation of the receiving optics. Particularly, LPSS was used to retrieve the total uncertainty of the volume linear depolarization ratio derived from lidar measurements obtained by the MULHACEN and VELETA lidar systems.

Improving the knowledge on lidar polarizing sensitivity leads to a better understand of the depolarization calibration and the development of new experimental procedures to characterize the lidar systems. Firstly, the Δ90°-calibration method, with a rotator in front of the polarizing beam splitter and with a linear polarizing filter in front of the receiving optics, was experimentally and theoretically studied. The Δ90°-calibration method with a rotator in front of the polarizing beam splitter allows the correction of the detection unit influence (polarizing beam splitter and photomultipliers), whereas the Δ90°-calibration method with a polarizer in front of the receiving optics allows the same correction also including the correction of the influence of the effective diattenuation of the receiving optics. This discovery allowed the combination of both modes of the Δ90°-calibration method to experimentally determine the effective diattenuation of the receiving optics. This combination was implemented and used in MULHACEN, estimating an effective

2

diattenuation of the receiving optics of 0.35±0.03. Furthermore, the MULHACEN characterization was improved by means of a new experimental procedure to determine the misalignment angle of the laser polarizing plane with respect to the incident plane of the polarizing beam splitter. This misalignment angle was experimentally determined at 7°±1°.

Once the lidar polarizing sensitivity and the improvement of the depolarization calibration were performed, lidar depolarization technique was applied in different ways using MULHACEN measurements: the detection of the planetary boundary layer height ($z_{PBL}$) and the study of mixing processes between free tropospheric aerosol layers and the planetary boundary layer (PBL).

The first application of the lidar depolarization technique is related to the automatic determination of the planetary boundary layer height. Previous studies have shown that the automatic determination of $z_{PBL}$ presents difficulties when the aerosol layering in the PBL is complex or when advected aerosol layers in the free troposphere are coupled to the PBL. In order to improve the detection of the $z_{PBL}$, a new method has been developed. The new method, called POLARIS (PBL height estimatiOn based on Lidar depolARISation), is based on three candidates for $z_{PBL}$ extracted from the wavelet covariance transform applied to the range corrected signal and the uncalibrated depolarization ratio. Then the attribution of the $z_{PBL}$ is performed by means of an algorithm developed to this aim.

The optimization of the POLARIS method was performed using the 36-hour continuous lidar measurement performed in the framework of the ChArMEx (Chemistry-Aerosol Mediterranean Experiment) campaign 2013 (http://charmex.lsce.ipsl.fr). The optimization process was based on the

comparison with the $z_{PBL}$ determined independently and the verification of the coherence of the results with the temporal evolution of the range corrected signal and the uncalibrated depolarization ratio. With the optimized POLARIS method, it was applied in an unsupervised way to the 72-hour continuous lidar measurement performed in the framework of ChArMEx campaign 2012 under Saharan dust scenarios. Results indicate that POLARIS provides correct $z_{PBL}$ even with dust aerosol layer coupled to the PBL. However, in the period from sunrise to midday, the mixing and the residual layers coexist until the convective processes are strong enough and the mixing exceeds the residual layer height. This is a handicap for the derivative methods as both mixing and residual layer heights can be interchangeably detected. This fact is the responsible for the artificial abrupt increase of $z_{PBL}$, detected each morning during the campaign. Ultimately, this work demonstrates that lidar depolarization technique can be a useful tool to determine the $z_{PBL}$ especially in those regions frequently influenced by dust events.

The lidar depolarization technique was also applied to a study of mixing processes between coupled layers and the PBL. This case study was performed taking the advantage of co-located and simultaneous measurements with in-situ, passive and active remote sensing instrumentation in combination with airborne in-situ measurements under Saharan mineral dust conditions. This study allowed the characterization of the interaction mechanisms between a Saharan-dust lofted layer and the PBL, and the influence of mineral dust on the aerosol properties at the surface. Results showed that the convective processes enhance the PBL which 'catches' the dust layer accelerating the downward dust entrainment. The entrainment of dust layer into the PBL caused significant variations on the aerosol optical properties changing the typical hourly

evolution observed on working days. In this sense, the gas-to-particle conversion may be less effective due to the gas deposition on particle surfaces under the presence of mineral dust at surface level.

# Resumen

Esta tesis intenta reducir la falta de conocimiento sobre la respuesta polarizadora de los sistemas lídar cuyo efecto tiene especial relevancia en la técnica de despolarización lídar. Además, se incluye el uso de la técnica de despolarización lídar en el campo de investigación del aerosol atmosférico.

En primer lugar, se presentan los conceptos claves usados en el campo de investigación del aerosol atmosférico y en la teledetección óptica activa. Seguidamente, se describe el sitio experimental y los dos lídares caracterizados en la tesis: el lídar Raman multiespectral (MULHACEN) y el lídar Raman de escaneo (VELETA). Las medidas con MULHACEN y VELETA se realizan en el Instituto Interuniversitario de Investigación del Sistema Tierra en Andalucía (IISTA-CEAMA), al sur de la ciudad de Granada (37.16° N, 3.61° O, 680 m sobre el nivel del mar). Ambos lídares son caracterizados detalladamente en los primeros capítulos donde se muestra información sobre su configuración y el control de calidad de las medidas. El Grupo de Investigación de Física de la Atmósfera realiza medidas de forma regular con ambos lídares como miembro de la red de lídares europea de investigación del aerosol (EARLINET, European Aerosol Reaserch Lidar Network). Por otra parte, también se incluye información sobre otros instrumentos, como son el fotómetro solar y el radiómetro de microondas, usados en los estudios llevados a cabo en esta tesis doctoral.

En lo referente a aspectos metodológicos, se incluye principalmente una descripción detallada sobre el pre-procesado de las señales lídar y los algoritmos de inversión elástica, inelástica y de despolarización.

La evaluación de la sensibilidad despolarizadora de los equipos lídar se realizó usando el formulismo de Stokes-Müller para modelar ambos sistemas. Con este propósito, se agruparon las diferentes partes de un equipo lídar basándose en su funcionalidad. Se han analizado cinco bloques funcionales:

láser, óptica emisora láser, óptica receptora, unidad de detección (divisor de haz polarizante y fotomultiplicadores) y calibrador. La cuantificación de la influencia polarizadora de cada bloque funcional se realizó a partir de un simulador, llamado *Lidar Polarizing Sensitivity Software (LPSS)*. Con el objetivo de obtener resultados generales, se consideró un sistema lídar sintético basado en propiedades e incertidumbres de los distintos componentes derivadas de especificaciones técnicas comerciales. El uso de esta herramienta demostró que la sensibilidad polarizadora de los lídares puede afectar a las medidas de despolarización causando errores relativos incluso mayores del 100 % en los productos derivados (razón de despolarización lineal volúmica y de partículas). Las propiedades más importantes son el parámetro de pureza del láser y la diatenuación efectiva de la óptica receptora. Además, el programa LPSS se usó para calcular la incertidumbre total de la razón de despolarización volúmica medida con MULHACEN y VELETA.

Mejorar el conocimiento de la respuesta polarizadora de los lídares nos permitió comprender los métodos de calibración de la despolarización y desarrollar nuevos procedimientos experimentales para caracterizar los sistemas lídar. En primer lugar, se estudió, experimental y teóricamente, el método de calibración de Δ90°, basado en rotaciones del divisor de haz polarizante o en rotaciones de un polarizador lineal antes de la óptica receptora. El primer método de calibración de Δ90° permite la corrección de la influencia del divisor de haz polarizante y los fotomultiplicadores, mientras que el segundo permite realizar la misma corrección además de incluir la corrección de la diatenuación efectiva de la óptica receptora. Este descubrimiento permitió combinar ambos modos de calibración para determinar experimentalmente el valor de la diatenuación efectiva de la óptica receptora. Esta combinación se implementó en MULHACEN obteniéndose una diatenuación efectiva de la óptica receptora

10

de 0.35±0.03. Además, la caracterización de MULHACEN se mejoró gracias a un nuevo procedimiento experimental para determinar el ángulo de desalineamiento entre el plano de polarización del láser y el plano de incidencia del divisor de haz polarizante. Este ángulo de desalineamiento es de 7°±1°.

Tras los análisis de la sensibilidad despolarizadora y la mejora de los sistemas de calibración, la técnica de despolarización lídar se aplicó a medidas de despolarización de MULHACEN para la detección de la altura de la capa límite planetaria ($z_{PBL}$) y el estudio de procesos de mezcla entre capas de aerosol acopladas a la capa límite planetaria (PBL).

La primera aplicación de la técnica de despolarización lídar está relacionada con la detección automática de $z_{PBL}$. Estudios anteriores muestras que este proceso presenta dificultades cuando el aerosol presenta una estratificación compleja en la PBL, bajo la presencia de capas de aerosol en la troposfera libre y ante el acoplamiento entre capas de aerosol y la PBL. Con el fin de mejorar la detección automática de la $z_{PBL}$, se ha desarrollado un nuevo método llamado *POLARIS* (*PBL height estimatiOn based on Lidar depolARISation*). Este nuevo método se basa en la generación de tres candidatos a $z_{PBL}$ extraídos de la transformada *wavelet*, aplicada a la señal corregida de rango y a la razón de despolarización sin calibrar. Una vez se han generado los tres candidatos, POLARIS elige la $z_{PBL}$ entre ellos. La optimización de POLARIS se hizo con la medida lídar de 36 horas realizada en el marco de la campaña experimental ChArMEx 2013 (http://charmex.lsce.ipsl.fr). El proceso de optimización se basó en la comparación de la $z_{PBL}$ determinada con POLARIS con la $z_{PBL}$ determinada con otra instrumentación, comprobando la coherencia de los resultados con la evolución temporal de la señal corregida de rango y la razón de despolarización.

Una vez optimado, POLARIS se aplicó automáticamente a la medida lídar de 72 horas consecutivas realizada en el marco de la campaña experimental ChArMEx 2012 durante un evento de intrusión de masas de aire de origen sahariano. Los resultados indican que POLARIS proporciona correctas $z_{PBL}$ incluso cuando hay capas de aerosol acopladas a la PBL. Sin embargo, desde el amanecer al mediodía, las capas de mezcla y residual coexisten hasta que los procesos convectivos son suficientemente intensos para que la capa de mezcla exceda la altura de la capa residual. Este hecho se presenta como una contrapartida para los métodos derivativos, ya que las alturas de la capa de mezcla y la capa residual pueden ser detectadas indistintamente durante este periodo. Esto está relacionado con el falso aumento brusco de la $z_{PBL}$ detectado cada mañana durante la campaña. En definitiva, este trabajo demuestra que la técnica de despolarización lídar puede ser una herramienta útil para determinar la $z_{PBL}$ especialmente en aquellas regiones frecuentemente influenciadas por eventos de intrusión desértica.

La técnica de despolarización lídar también se usó para estudiar los procesos de mezcla entre capas de aerosol acopladas y la PBL. Este caso de estudio se realizó aprovechando una especial situación experimental bajo una intrusión sahariana en la que se midió simultáneamente con instrumentación activa, pasiva e in situ en combinación con instrumentación in situ a bordo de un avión. Este estudio permitió la caracterización de los mecanismos de interacción entre una capa de aerosol elevada procedente del desierto del Sáhara y la PBL, así como la influencia de las partículas minerales sobre las propiedades del aerosol en superficie. Los resultados de este estudio ponen de manifiesto que los procesos convectivos que se desarrollan en la PBL «atrapan» la capa de polvo mineral arrastrando el polvo hacia abajo. El arrastre del polvo

mineral dentro de la PBL produce cambios significativos en las propiedades ópticas del aerosol en superficie modificando, por ejemplo, la típica evolución horaria observada en días laborales. En este sentido, la presencia de polvo mineral a nivel superficial provoca una disminución de la conversión gas-partícula debido a la mayor deposición de las moléculas gaseosas en la superficie de las partículas.

# 1 Introduction

Since the 90s, climate change has been directly linked to the emission of greenhouse gases *Houghton et al.* [1990]. However, as research on climate change progressed, the lack of knowledge on the role of atmospheric aerosol[1] on global climate has motivated its research. As summarized in the *Chapter 7 Cloud and aerosol* of the IPCC fifth assessment report [*Boucher et al.*, 2013], atmospheric aerosol has two main roles in the Earth-atmosphere energy budget due to its interaction with the solar and terrestrial radiation and its interaction with clouds (Figure 1-1). Furthermore, one can distinguish between the traditional concept of radiative forcing[2] and the relatively new concept of effective radiative forcing (ERF) that also includes rapid adjustments which indirectly modify the radiative budget through fast atmospheric and surface changes. For aerosols one can further distinguish forcing processes arising from aerosol-radiation interactions (ari) and aerosol-cloud interactions (aci).

The radiative effect due to aerosol-radiation interactions (REari), formerly known as direct radiative effect, is the change in radiative flux caused by the combined scattering and absorption of radiation by anthropogenic and natural aerosols. Figure 1-2 schematizes the aerosol-radiation interactions. The REari results are close to be an observable quantity. However, our knowledge on aerosol and environmental characteristics needed to quantify the REari at a

---

[1] Liquid or solid particles suspended in the atmosphere.
[2] The change in net (down minus up) irradiance ($W \cdot m^{-2}$) at the tropopause after allowing stratospheric temperatures to readjust to radiative equilibrium, but with surface and tropospheric temperatures and state held fixed at the unperturbed values [Forster, P., et al. (2007), *Changes in Atmospheric Constituents and in Radiative Forcing. In: Climate Change 2007: The Physical Science Basis. Contribution of Working Group I to the Fourth Assessment Report of the Intergovernmental Panel on Climate Change [Solomon, S., D. Qin, M. Manning, Z. Chen, M. Marquis, K.B. Averyt, M.Tignor and H.L. Miller (eds.)]*, Cambridge University Press, Cambridge, United Kingdom and New York, NY, USA.]
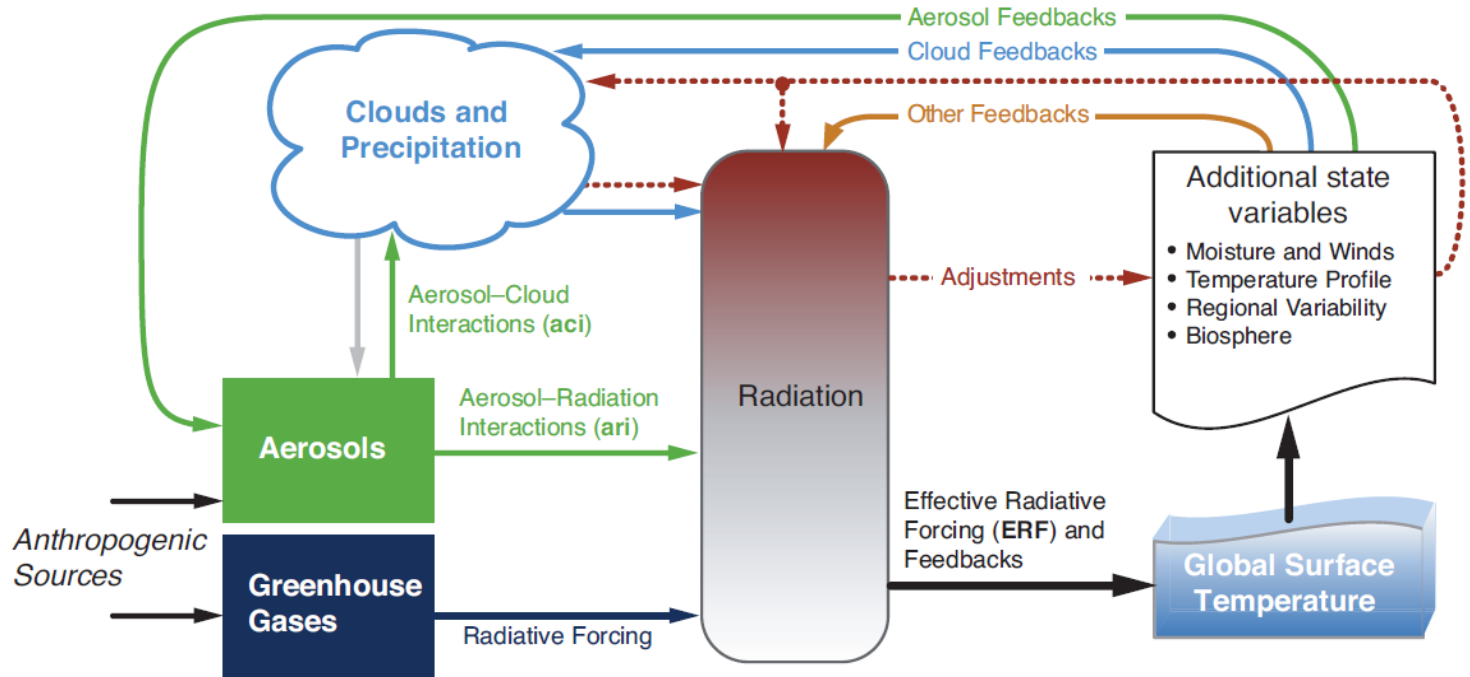
**Figure 1-1: Overview of forcing and feedback pathways involving greenhouse gases, aerosols and clouds. Forcing agents are in the green and dark blue boxes, with forcing mechanisms indicated by the straight green and dark blue arrows. The forcing is modified by rapid adjustments of which pathways are independent of changes in the globally averaged surface temperature and are denoted by brown dashed arrows. Feedback loops, which are ultimately rooted in changes ensuing from changes in the surface temperature, are represented by curving arrows (blue denotes cloud feedbacks; green denotes aerosol feedbacks; and orange denotes other feedback loops such as those involving the lapse rate, water vapour and surface albedo). The final temperature response depends on the effective radiative forcing (ERF) that is felt by the system, that is, after accounting for rapid adjustments, and the feedbacks. From *Boucher et al.* [2013].**

global scale remains incomplete [*Anderson et al.*, 2005; *Satheesh et al.*, 2008; *Jaegle et al.*, 2011].

The cloud-aerosol interaction is based on the capability of the aerosol to act as water droplet nuclei and ice forming nuclei (see Figure 1-2). *Denman and Brasseur* [2007] catalogued several possible pathways via which the aerosol might affect clouds. Given the number of possible aerosol-cloud interactions and the difficulty of isolating them individually, there is little value in attempting to assess each effect in isolation, especially since modelling studies suggest that the effects may interact and compensate [*Stevens and Brenguier*, 2009; *Morrison and Grabowski*, 2011]. Instead, all radiative consequences of aerosol-cloud interactions are grouped into an "effective radiative forcing due to aerosol-cloud interactions" (ERFaci). ERFaci accounts for aerosol-related microphysical modifications to the cloud albedo [*Twomey*, 1977], as well as any secondary effects that result from clouds adjusting rapidly to changes in their environment [*Pincus and Baker*, 1994].

According to the *Chapter 7* of the fifth assessment of the IPCC [*Boucher*
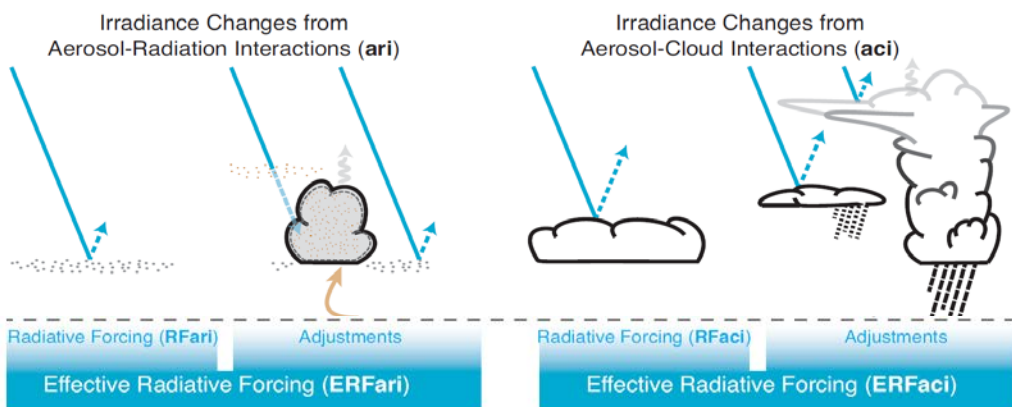


**Figure 1-2: Schematic of the aerosol-radiation and aerosol-cloud interactions. The blue arrows depict solar radiation, the grey arrows terrestrial radiation and the brown arrow symbolizes the importance of couplings between the surface and the cloud layer for rapid adjustments. Adapted from *Boucher et al.* [2013].**

*et al.*, 2013], the uncertainties in the estimation of the radiation-aerosol and cloud-aerosol interactions together with the poor knowledge of the spatial and temporal distribution of the atmospheric aerosol cause a large uncertainty in the estimation of the radiative forcing due to atmospheric aerosol. In order to determine the aerosol influence on the Earth energy budget, and thus on global climate, the use of climate models and measurements within the framework of observational networks and intensive campaigns is necessary. In the field of measurements of the vertical structure of the aerosol, lidar (portmanteau of "light" and "radar" according to Oxford English Dictionary[3]) has become a very important instrument in atmospheric science.

Lidar and radar agree in the modus operandi. Both instruments emit an electromagnetic signal and record the backscattered signal. The time between the emission and the reception determines the distance between the emitter and the scatterer. The main difference between lidar and radar is the wavelength which ranges between the infrared and ultraviolet in lidar and microwaves in radar. Due to the aerosol particle size, radar is not a suitable instrument for its study.

Having its own radiation source, lidars can be operated during night and daytime excepting with rainfall and fog. Lidars provide vertical profiles of different optical and physical properties with a very high spatial and temporal resolution allowing us to analyse the influence of the aerosol height distribution. Therefore, at present, these advantages of lidar compared to other instruments make the lidar one of the instruments with huge potential in atmosphere research.

---

[3]Lidar is also understood as an acronym, "LIght Detecting And Ranging".

The relevance of lidar can also be highlighted in atmospheric science due to its range of applications. It allows the study of the planetary boundary layer [e.g., *Baars et al.*, 2008; *Granados-Muñoz et al.*, 2012], the long-range aerosol transport [e.g., *Ansmann et al.*, 2003; *Guerrero-Rascado et al.*, 2009], the atmospheric aerosol originated in volcanic eruptions [e.g., *Ferrare et al.*, 1992; *Navas-Guzmán et al.*, 2013], the optical and physical properties of the cirrus clouds [e.g., *Ansmann et al.*, 1992; *Reichardt et al.*, 2003], the hygroscopic aerosol growth [*Ferrare et al.*, 1998a; *Ferrare et al.*, 1998b; *Stelitano et al.*, 2013], the air quality [*Philbrick*, 2002] and the water vapour content profile [e.g., *Whiteman et al.*, 1992; *Guerrero-Rascado et al.*, 2008b]. Some of these applications are based on the lidar depolarization technique.

The lidar depolarization technique is based on the change of the polarization state between the emitted and received signal as spherical scatterers depolarize less than non-spherical ones. As lidar systems used to be operated with almost-perfect polarized light, this change (called depolarization) can be measured. Initially, the lidar depolarization technique was used in the 1970s to distinguish the thermodynamic phase of clouds. Since then, several hydrometeors have been studied using the lidar depolarization technique as tropospheric clouds [e.g., *Schotland et al.*, 1971; *Pal and Carswell*, 1973; *Sassen*, 1991; *Sassen et al.*, 2000] and stratospheric clouds [e.g., *Adriani et al.*, 2004; *Scarchilli et al.*, 2005; *Córdoba-Jabonero et al.*, 2013]. Moreover, the lidar depolarization technique is becoming more relevant due to its role in the atmospheric aerosol research. On the one hand, the analysis of different degrees of depolarization in combination with other optical properties allow the characterization of different aerosol types such as biomass burning aerosol and Saharan dust [e.g., *Winker and Osborn*, 1992; *Murayama et al.*, 2004; *Tafuro et al.*, 2006; *Tesche et al.*, 2009b; *Gross et al.*, 2011b; *Gross et al.*, 2011a; *Bravo-*

*Aranda et al.*, 2013]. On the other hand, the use of aerosol depolarization information is a very relevant improvement for the aerosol microphysical properties research. Particle shape information provided by lidar depolarization measurements in combination with the aerosol optical properties derived by lidar can be used in those inversion methods which include features of non-spherical particles [e.g., *Olmo et al.*, 2006; *Olmo et al.*, 2008].

Besides aerosol typing, lidar measurements can be used in the determination of the planetary boundary layer height ($z_{PBL}$), which is a key variable in climate modelling and has an enormous influence on air pollution [*Stull*, 1988]. The $z_{PBL}$ determines the available volume for pollutants dispersion and indicates the volume where the pollution remains in the atmosphere during night-time [*Stull*, 2000]. Generally, lidar measurements can be used to detect the boundary layer as a sharp decrease of the aerosol load which height usually coincides with the $z_{PBL}$. Among other methods, the use of the wavelet covariance transform seems to be a promising tool as it is highlighted by *Baars et al.* [2008] and *Granados-Muñoz et al.* [2012]. However, the determination of the $z_{PBL}$ using the vertical distribution of the aerosol load is somewhat difficult when the aerosol layering in the planetary boundary layer (PBL) is complex or when advected aerosol layers in the free troposphere are coupled to the PBL.

The reliability of the lidar depolarization technique is limited due to the complexity of the depolarization calibration: first, relative depolarization calibration introduces a high uncertainty due to the low signal-to-noise ratio (SNR) and thus, an absolute calibration is required; second, absolute calibration methods used until now correct part of the lidar polarizing response, but not others like the polarizing-dependent receiving transmission as it was indicated

by *Mattis et al.* [2009]. Therefore, improvements on the depolarization calibration is still necessary and it is a very active research field [e.g., *Álvarez et al.*, 2006; *Freudenthaler et al.*, 2009; *Hayman and Thayer*, 2012; *Bravo-Aranda et al.*, 2013; *Freudenthaler*, 2014].

## 1.1   Objectives and structure

The aim of this thesis is the improvement of the lidar depolarization technique and its application on atmospheric aerosol research. The improvement of the lidar depolarization technique will be performed by means of:

a) The study of the polarizing response of lidar systems using the Stokes-Müller formulism.

b) The determination of the total uncertainty of the volume depolarization ratio due to the lidar polarizing sensitivity of MULHACEN and VELETA.

c) The correction of the depolarization measurements of VELETA and MULHACEN by means the depolarization calibrations and available procedures developed to this aim.

Regarding the application of the lidar depolarization technique, MULHACEN depolarization measurements will be used for two topics:

a) The improvements of the detection of the planetary boundary layer height.

b) The study of the interaction mechanisms between a Saharan dust layer and the planetary boundary layer and its influence on the aerosol properties at the surface.

The thesis is organized as follow:

Chapter 2 presents key concepts to understand the results presented in this thesis. First, the atmosphere is briefly described in terms of its structure and components. Later, atmospheric aerosol is described in detail focusing on its

types, properties and its effects on the Earth's climate. Also, the lidar principle is included in this chapter, paying special attention to lidar depolarization concepts.

Chapter 3 describes the experimental site where the instrumentation was operated. Moreover, the main characteristics of the used instrumentation are presented.

Chapter 4 is dedicated to the methodological aspects. Different sections introduce the pre-processing and lidar technique as well as information of procedures related to other instruments as the sun-photometer or the microwave radiometer.

Chapter 5 details the depolarization calibration implemented in the two lidar systems used in this thesis.

Chapter 6 presents in detail the uncertainty of the lidar depolarization technique. Firstly, the lidar depolarization uncertainties are assessed for a synthetic lidar setup including the possible ways to reduce the uncertainties for each functional block of the lidar system. Then, lidar depolarization uncertainties of the lidar systems used in this thesis are presented.

Chapter 7 includes a new method, called POLARIS, proposed to determine the planetary boundary layer height. This new approach is based on the application of the wavelet covariance transform to the different lidar products.

Chapter 8 exposes a case study of the interaction mechanism between the Saharan dust and the planetary boundary layer, and the influence of mineral dust on the aerosol properties at the surface.

Chapter 9 summarizes the main achievements and conclusions of this thesis and gives an outlook of future research activities.

# 2 Fundamentals

This chapter introduces the basis of the research field in order to facilitate the understanding of the results presented in this thesis. First, the atmosphere is briefly described in terms of its structure and components. Later, atmospheric aerosol is described in detail focusing on its types, properties and its effects on the Earth's climate. Also, the lidar principles are included in this chapter.

## 2.1 Atmosphere: structure and properties

The atmosphere is the gaseous layer that surrounds the Earth and is composed by gases, suspended particles and clouds. The atmosphere presents an almost uniform gas composition in the first 80 km. Most of the atmospheric mass is located in the first kilometres. In fact, 50% of the atmospheric mass is located within the first five kilometres while above the 60 km only about one thousandth of this mass is present. The atmosphere can be divided into a number of rather well-marked horizontal layers, mainly on the basis of
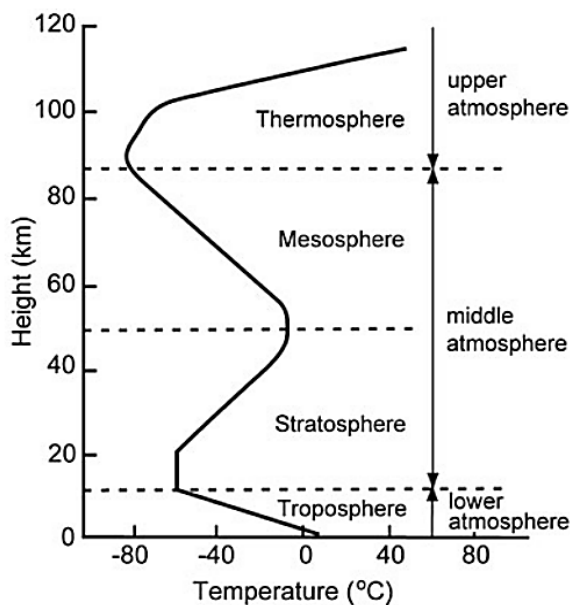


**Figure 2-1: Atmosphere structure and temperature profile.**
**Source: www.azimuthproject.org adapted from [*Moran et al.*, 1997].**

temperature (see Figure 2-1). From the point of view of the atmospheric aerosol, the troposphere and the stratosphere are the most important layers and thus, explained below.

Troposphere: this is the lowest layer of the atmosphere; located from the Earth's surface up to 10-15 km altitude depending on latitude and time of year. The upper limit is called tropopause separating troposphere and stratosphere. This layer is characterized by decreasing temperature with height (mean rate of about 6.5 °C/km) and efficient vertical mixing. Almost all meteorological phenomena and atmospheric turbulence occur in this layer, and it contains 75% of the total molecular or gaseous mass of the atmosphere and virtually all the water vapour and suspended particles [*Seinfeld and Pandis*, 1998].

Stratosphere: this region covers from the tropopause up to about 50 km. It is characterized by increasing temperature with height, leading to a layer in which vertical mixing is reduced. The presence of atmospheric aerosol is constrained to the lower stratosphere and usually related to volcanic injection where the aerosol time residence depends on the injected amount varying between several months to few years [*Alados-Arboledas and Olmo*, 1997; *Seinfeld and Pandis*, 1998].

The gases which compose the Earth's atmosphere can be separated in two groups: those with a nearly permanent concentration that is almost constant up to 80 km altitude and those with variable concentration (Table 2-1). The amount of the last gas group is small with less than ~0.04%, but some of these gases play an important role in the energy budget as water vapour and ozone.

As atmospheric aerosol particles are the object of this dissertation, it is worthy to dedicate a section to the definition and classification of atmospheric aerosol.

**Table 2-1: Average composition of the dry atmosphere below 25 km**
**[*Barry and Chorley*, 1987].**

| Permanent | | Variable | |
|---|---|---|---|
| **Element** | **Volume (%)** | **Element** | **Volume (%)** |
| Nitrogen | 78.08 | $H_2O$ | 0-4 |
| Oxygen | 20.98 | $O_3$ | $0-12\times10^{-4}$ |
| Argon | 0.93 | $NO_2$ | $0.001\times10^{-4}$ |
| Carbon dioxide | 0.035 | $SO_2$ | $0.001\times10^{-4}$ |
| Neon | $18\times10^{-4}$ | $NH_3$ | $0.004\times10^{-4}$ |
| Helium | $5\times10^{-4}$ | $NO_3$ | $0.0005\times10^{-4}$ |
| Hydrogen | $0.6\times10^{-4}$ | $H_2S$ | $0.00005\times10^{-4}$ |
| Krypton | $11\times10^{-4}$ | | |
| Xenon | $0.9\times10^{-4}$ | | |
| Methane | $0.19\times10^{-4}$ | | |

## 2.2 Atmospheric aerosol

In general, aerosol is defined as a system composed by a gas and solid and/or liquid particles suspended in it at least several minutes excluding the water droplets and ice crystals. Therefore, the system formed by atmospheric gas and particles is called atmospheric aerosol [*Harrison and Grieken*, 1998]. However, common usage refers to the aerosol as only the particulate component only. Additionally, in those cases where the particulate matter consists mainly of a particle type (e.g., dust), the atmospheric aerosol is denoted as an aerosol type (e.g., dust aerosol).

The atmospheric aerosol is very variable on global scale and includes such types as mineral, anthropogenic and volcanic aerosols and aerosol generated by biomass burning, among others, with a size range between a few nanometers and tens of micrometers.

## 2.2.1 Aerosol characterization

Most atmospheric aerosol classifications are based on its size, origin source and origin process. According to size, fine and coarse modes are constituted by particles with radii smaller and greater than 1 µm, respectively. Also, fine mode contains two other modes known as Aitken and accumulation modes. The Aitken mode is constituted by particles which radii are less than 0.1 µm whereas accumulation mode particles have radii between 0.1 and 1 µm. An idealized scheme of the distribution of the particle surface area is shown in Figure 2-2 where principal modes, sources and particle formation/removal mechanisms are indicated. More details were given by *Seinfeld and Pandis* [1998] and *Liou* [2002]. Another possible classification is based on the mechanism that produces aerosols. In this sense the atmospheric aerosols are divided in primary and secondary aerosol depending on whether they have been emitted directly to the atmosphere or have been formed in the atmosphere by gas-to-particle conversion process [*Schryer*, 1982]. According to the origin, the atmospheric aerosol can arise from natural sources, such as windborne dust, sea spray and volcanoes and from anthropogenic activities, such as man-made tropical fires and fuels combustion. Among different aerosol types, some of them are described in detail due to its relevance in this thesis.

Mineral dust: this is the term to describe the mineral aerosol lifted by wind. Solid particles are produced by mechanical disintegration of material such as crushing, grinding and blasting. Main dust sources are deserts including the Sahara as one of the most active sources for the injection of mineral dust to the atmosphere on global scale [*Tegen and Miller*, 2004; *Kondratyev et al.*, 2006]. Other dust sources are local such as the wind erosion of cropland and the roadway dust from paved and unpaved roads. Typically, mineral dust particle diameter is larger than 1 µm so it would be included mainly in the coarse mode.
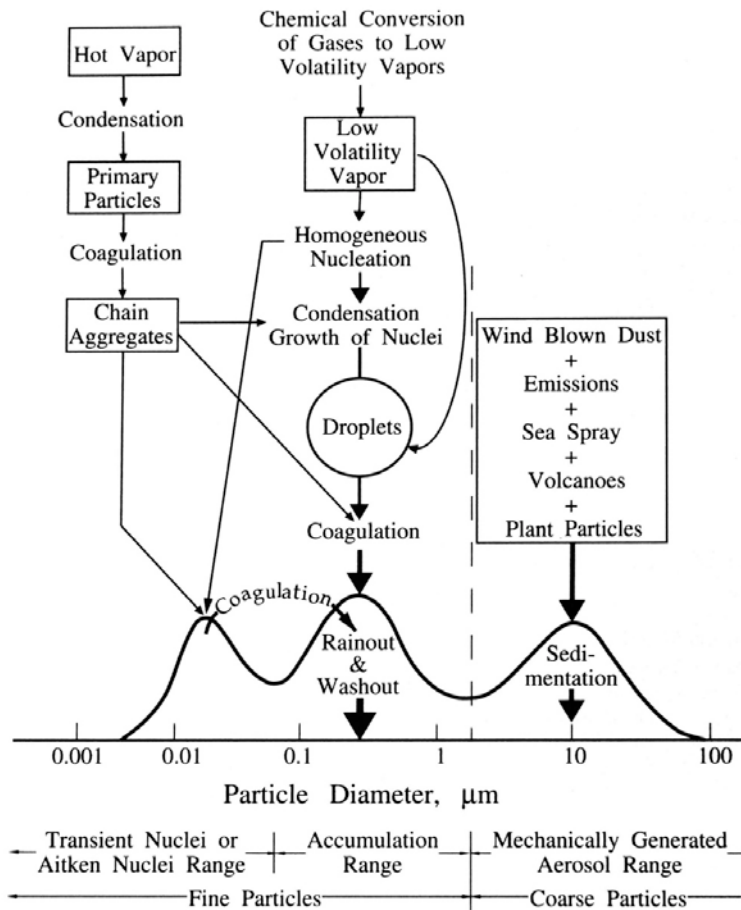
**Figure 2-2: Idealized scheme of the distribution of particle surface area of an atmospheric aerosol [*Whitby et al.*, 1976]. Principal modes, sources and particle formation and removal mechanisms are also indicated (adapted from *Seinfeld and Pandis* [1998]).**

Smoke/biomass burning aerosol: it is the atmospheric aerosol with a large amount of particles from biomass burning. The intentional burning of land results in a major release of combustion products into the atmosphere. Smoke includes a huge quantity of gases and elemental and organic particulate matter. The quantity and type of smoke depend not only on the type of vegetation, but on its ambient temperature, humidity, local wind speed and ageing process.

31

Anthropogenic aerosol: it is used by the scientific community to name the atmospheric aerosol originating from human activities. The more relevant components are the soot/black carbon and the sulphates. The soot/black carbon is formed in the incomplete combustion of carbonaceous material and the atmospheric sulphate aerosol which may be considered as sulphuric acid particles that are partly or totally neutralized by ammonia. Sulphates can be present as liquid droplets or partly crystallized.

Once the atmospheric aerosol has been introduced, we focus our attention on its influence on the Earth's climate.

### 2.2.2 Radiative properties

As introduced in Chapter 1, atmospheric aerosol is important for the Earth's climate due to the aerosol-radiation interaction. In this sense, the Beer-Bouguer-Lambert law establishes a logarithmic dependence between the transmitted light through an medium, i.e. atmosphere, and the distance the light travels through the material [*Liou*, 2002]. Applying this law to the atmosphere, we obtain that the fraction that gets lost due to crossing a certain path is given by:

$$T(z,\lambda) = e^{-\int_0^z \alpha_{aer}(\xi,\lambda)d\xi}$$ 

Eq. 2-1

where $T(z,\lambda)$ is the so-called transmittance and $\alpha_{aer}$ is the extinction coefficient (in [m$^{-1}$]) due to particles and molecules present in the atmospheric volume crossed. The extinction coefficient considers the total effect of two types of aerosol-radiation interaction: absorption and scattering processes. This two processes are also quantified by means of the aerosol absorption ($\sigma_a^{aer}$) and scattering ($\sigma_s^{aer}$) coefficients (both in [m$^{-1}$]). These coefficients depend on size, shape and complex refractive index of the scatterer and the wavelength of the

incident radiation. In addition, scattering is a mechanism which changes the polarizing state of the incident light [*Bohren and Huffman*, 1983].

Particularly, as the lidar principle is based on backward scattered radiation, it is worthy to define the aerosol backscatter coefficient ($\beta_{aer}$). Let $N_j$ be the concentration of scatterers (molecules and particles) of kind $j$ in the volume illuminated by the laser pulse, and $d\sigma_{j,sca}(\pi,\lambda)/d\Omega$ the differential scattering cross section of scatterers for the backward direction at wavelength $\lambda$. $\beta_{aer}$ can then be written as:

$$\beta_{aer} = \sum_{j} N_j \frac{d\sigma_{j,sca}(\pi,\lambda)}{d\Omega}$$

Eq. 2-2

Since the number concentration is given in units of $[m^{-3}]$ and the differential scattering cross section in $[m^2 sr^{-1}]$, $\beta_{aer}$ has the units: $[m^{-1} sr^{-1}]$.

Aerosol extinction, scattering and backscattering coefficients include the contribution of molecules and particles which can be treated separately and thus, particle extinction and scattering coefficients can be written as:

$$\sigma_s = \sigma_s^{aer} - \sigma_s^{mol}$$

Eq. 2-3

$$\alpha = \alpha_{aer} - \alpha_{mol}$$

Eq. 2-4

$$\beta = \beta_{aer} - \beta_{mol}$$

Eq. 2-5

By means of the physical law of radiation scattering proposed by Lord Rayleigh (John William Strutt), called Rayleigh scattering [*Rayleigh*, 1871], $\alpha_{mol}$, $\sigma_s^{mol}$ and $\beta_{mol}$ can be theoretically determined. The Rayleigh scattering assumes spherical shape of the scatterers and interactions where the wavelength of the incident radiation is much greater than the scatterer size. In terms of the size parameter defined by $x = 2\pi r/\lambda$ from the particle radius, $r$, and the wavelength of the incident light, $\lambda$, Rayleigh scattering can be used when

$x \ll 1$. The molecular scattering is given by the product of the total Rayleigh cross section per molecule and the molecular number density. The total Rayleigh cross section for atmospheric gases is known and thus, the molecular scattering can be retrieved from the molecular number density at a given pressure and temperature.

Particle scattering and absorption coefficients can be theoretically determined by means of the Mie solution to Maxwell's equations which uses different assumptions. The Mie theory describes the scattering of radiation by a sphere for wavelengths much greater than the scatter size up to wavelengths with the same order of magnitude than the scatterer size [*D'Almeida et al.*, 1991]. Mie scattering provides good results for the range $0.6 < x \leq 5$ [*Iqbal*, 1983]. However, Mie scattering presents discrepancies with experimental measurements, specifically related to the quantification of the particle backscatter coefficient and to the changes on the polarization state of the scattered radiation. Therefore, another solution to Maxwell's equation has been investigated avoiding the spherical-shape assumption. These solutions use the T-matrix approach [*Waterman*, 1971] where the Müller matrix elements of scatterers are obtained by matching boundary conditions for solutions of Maxwell equations. These new approximation obtains good agreements with experimental measurements [*Mishchenko et al.*, 1997; *Olmo et al.*, 2006; *Olmo et al.*, 2008; *Quirantes et al.*, 2012; *Valenzuela et al.*, 2012]. Therefore, the particle shape is a critical issue to be solved in the field of the radiative properties of the atmospheric aerosol.

Finally, the variable introduced in this section is the aerosol optical depth ($AOD$). $AOD$ is defined as the integral of the particle extinction coefficient ($\alpha$) over the distance between the surface and the top of the atmosphere (TOA):

$$AOD = \int_{0}^{TOA} \alpha(z)dz \qquad \text{Eq. 2-6}$$

This variable is very useful in atmospheric research to easily characterize the aerosol load in the atmosphere.

### 2.2.3 Physical properties

Physical properties are those properties describing the state of a physical system. Therefore, atmospheric aerosol physical properties are particulate matter size, size, total content and shape in the atmosphere. Particle size and total content are jointly characterized by means of the atmospheric aerosol number size distribution which is defined as the number of particles present according to size. The number size distribution is denoted as:

$$n(r) = \frac{dN}{dr} \qquad \text{Eq. 2-7}$$

where $r$ is the particle radius, $N$ is the total number of particles and $n$ is the number of particles in the range [$r$, $r+dr$]. Number particle distributions can be related to the mass, surface and volume of particles. Due to its large range, the volume size distribution is expressed on logarithmic scale for particle size:

$$v(r) = \frac{dV}{d\ln r} \qquad \text{Eq. 2-8}$$

where, assuming spherical particles, it can be related to the number size distribution as follow:

$$v(r) = \frac{4\pi}{3} r^3 \frac{dN}{d\ln r} \qquad \text{Eq. 2-9}$$

Similarly, the mass size distribution is derived considering a constant density for particles, $\rho$:

$$m(r) = \frac{dM}{d\ln r} = \frac{4\pi}{3} \rho r^3 \frac{dN}{d\ln r} \qquad \text{Eq. 2-10}$$

A number of analytic expressions have been developed to represent the particle size distributions. These include the Junge power law, the gamma distribution, the log-normal distribution and their modifications [*D'Almeida et al.*, 1991; *Liou*, 2002].

As indicated above, it is crucial to have a way to determine the particle shape. Unfortunately, the only way to determine the shape of particles is through microscopy which can become a vast task. Therefore, it is very useful to find a way that allows the evaluation of the effective aerosol particle shape. In this sense, the lidar technique allows the determination of an effective particle shape through the depolarization process.

## 2.3 Lidar: Principle and equation

Lidar[4] systems are active remote sensing instruments which operation is very similar to the radar obtaining information from the backscattered light (ultraviolet, visible or near-infrared wavelengths). Lidar systems are schematically composed by a laser emitting short and intense light pulses, a telescope collecting the light backscattered by the atmospheric components, a set of optical devices leading the light signal up to the optical detectors, converting the light signal into electrical one and, finally, a set of hardware (transient recorder + computer) which allows the data acquisition (Figure 2-3).

Considering elastic scattering[5], the mathematical expression of the lidar detection process is:

---

[4] Portmanteau of "light" and "radar" according to Oxford English Dictionary although it is also understood as an acronym, "LIght Detecting And Ranging".
[5] The same wavelength for both, incident and scattered light
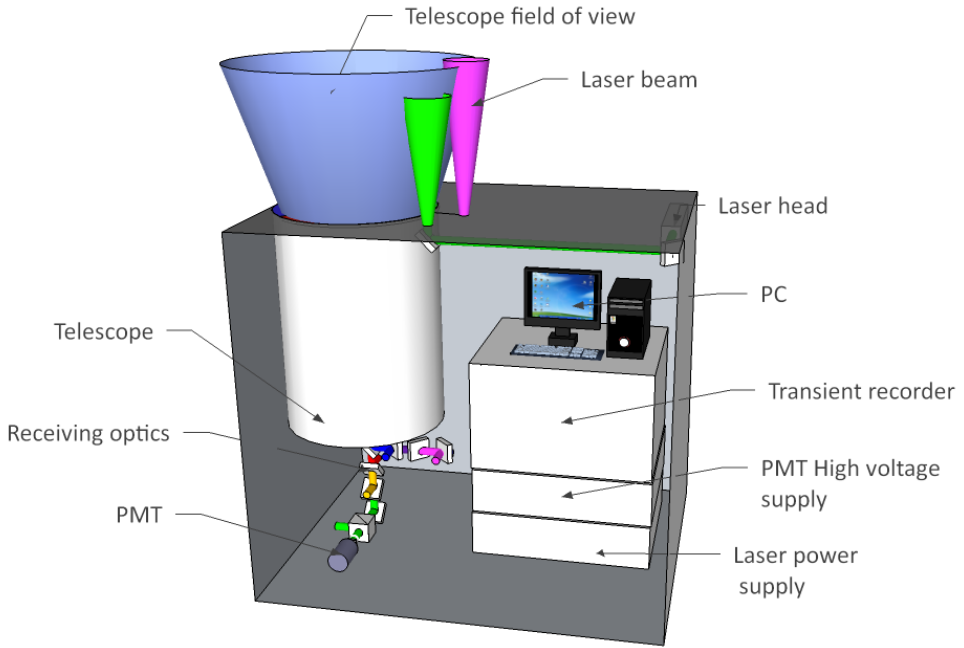
**Figure 2-3: Schematic representation of the main parts of a lidar system.**

$$P(z,\lambda) = P_0 \frac{c\tau\epsilon}{2} \frac{A}{z^2} O(z)\, \beta_{aer}(z,\lambda)\, T^2(z,\lambda) \qquad \text{Eq. 2-11}$$

$P(z,\lambda)$ is the power $P$ received from a distance $z$ at wavelength $\lambda$. $\epsilon$ is the system efficiency including the transmittance of the optical devices and the detectors' gain. $P_0$ is the power of the emitted laser pulse. $c\tau/2$ is the slice of the atmosphere from which backscattered light is received at a given instant, where $c$ is the light speed and $\tau$ is the temporal resolution of a lidar system. Strictly, $\tau$ must consider the interaction time, $\tau_i$, the pulse duration, $\tau_L$, and the detection time, $\tau_D$, resulting in $\tau = \tau_i + \tau_L + \tau_D$. However, $\tau_D$ is usually larger than $\tau_i$ and $\tau_L$ and thus, in practice, $\tau \cong \tau_D$. $A/z^2$ is the solid angle of the telescope. The overlap function $O(z)$ determines the part of the backscattered light of laser pulses which cannot reach the telescope due to the incomplete overlap between the laser beam and the field of view of the telescope. Finally,

37

the both terms $\beta_{aer}(z, \lambda)$ and $T(z, \lambda)$ are related to the optical properties of the atmospheric scatterers (molecular and particle contribution): firstly, aerosol backscatter coefficient at wavelength $\lambda$ determines the amount of backscattered light due to particles and molecules in the slice of the atmosphere at altitude $z$ which dimension is defined by $c\tau_D/2$ and a cross section that depends on the distance z and the beam divergence. Secondly, $T(z, \lambda)$ (see Eq. 2-1) considers the fraction of light lost on the way to the position $z$ due to extinction caused by the atmosphere. The transmittance is squared (Eq. 2-11) due to travel back and forth.

After the lidar equation has been presented, it is worth to define the range corrected signal, $RCS(z, \lambda)$, as the received power multiplied by the squared distance as it is proportional to the so-called aerosol attenuated backscatter $\beta_{aer}^{att}(z, \lambda)$:

$$RCS(z, \lambda) = P(z, \lambda)z^2 \propto \beta_{att}(z, \lambda) \qquad \text{Eq. 2-12}$$

$$\beta_{aer}^{att}(z, \lambda) = \beta_{aer}(z, \lambda) \, T^2(z, \lambda) \qquad \text{Eq. 2-13}$$

In the lidar equation previously presented, it has been considered that the same emitted and received wavelength. However, there is a type of scattering, called Raman or inelastic scattering, where the wavelength of the scattered light is shifted respect to the wavelength of the incident light. This scattering phenomenon is completely molecular (nitrogen, water vapour) and it has been used in remote sensing since late sixties. In this sense, Raman lidars are designed to measure both elastic and inelastic signals. The lidar equation of Raman signal can be expressed as follows:

$$P(z, \lambda_L, \lambda_R) = \frac{c\tau\epsilon}{2} \frac{A}{z^2} O(z) \, \beta_{Raman}(z, \lambda_R, \lambda_L) \, T(z, \lambda_R) \, T(z, \lambda_L) \qquad \text{Eq. 2-14}$$

where $\lambda_R$ and $\lambda_L$ are respectively the Raman received and emitted wavelengths and $\beta_{Raman}(z, \lambda_R, \lambda_L)$ is the molecular backscatter at $\lambda_R$. The inversion methods to derive $\beta(z)$ and $\alpha(z)$ at wavelength $\lambda_L$ using the Raman signal are presented in Chapter 4.

## 2.4 Depolarization lidar

It is well known that particles change the polarization state of a fraction of the incident light [*Bohren and Huffman*, 1983]. This change depends on the particle size with respect to the wavelength of the incident light (size parameter) and the shape of the particle. Taking into account the size parameter ($x$), it is possible to distinguish two types of depolarization sources. For $x \geq$ 50-100, the change of the polarization state is due to the rotation of the incident **E-**vector[6] according to the optics laws through those series of internal refractions and reflections. This depolarization origin usually occurs in clouds. More information about lidar depolarization applied to cloud research can be found in the publications by [*Sassen*, 1991], *Sassen and Cho* [1992] and *Hu et al.* [2009].

In addition, the depolarization can be caused by the nature of the scattering process. Assuming the Rayleigh scattering conditions, the scattering process can be understood as a particle under an electric field **E**. This electric field induces movements of the electrons of the particle in order to go against the external electric field. Then, the particle changes its electric configuration to a dipole. The electric field generates oscillations of the electric dipole in a fixed direction (scattering direction). The oscillating dipole, in turn, produces a plane**-**polarized electromagnetic wave (scattered wave). Other theories continue

---

[6] Bold symbols represent vector or matrices.

to be developed as the discrete dipole approximation [*Kahnert*, 2003], the T-matrix approach [*Macke et al.*, 1995; *Mishchenko et al.*, 1996] and the finite difference time domain method [*Baran et al.*, 2001]. These approximate theories are believed to yield reliable results for $x \leq 15$, $x \leq 100$ and $x \leq [15 - 20]$, respectively. It is worthy to note that in terms of Mie theory [*Mie*, 1908], the $x$ domain between ~5 and 40 is referred to as the resonance region because of the large variations in scattering parameters found with changing sphere size [*Weitkamp*, 2005].

**Table 2-2: Mathematical expressions of depolarization parameters.**

| Parameter | | Formula | |
|---|---|---|---|
| Volume linear depolarization ratio | $\delta'$ | $\delta' = \dfrac{\beta^\perp + \beta_{mol}^\perp}{\beta^\parallel + \beta_{mol}^\parallel}$ | Eq. 2-15 |
| Total volume linear depolarization ratio | $\delta^T$ | $\delta^T = \dfrac{\beta^\perp + \beta_{mol}^\perp}{\beta^\parallel + \beta_{mol}^\parallel + \beta^\perp + \beta_{mol}^\perp}$ | Eq. 2-16 |
| Particle linear depolarization ratio | $\delta^p$ | $\delta^p = \dfrac{\beta^\perp}{\beta^\parallel}$ | Eq. 2-17 |
| Total particle linear depolarization ratio | $\delta^{TA}$ | $\delta^{TA} = \dfrac{\beta^\perp}{\beta^\parallel + \beta_{par}^\perp}$ | Eq. 2-18 |
| Perpendicular linear backscatter ratio | $R^\perp$ | $R^\perp = \dfrac{\beta^\perp + \beta_{mol}^\perp}{\beta_{mol}^\perp}$ | Eq. 2-19 |

In order to quantify the depolarization capability of the atmospheric aerosol, different variables has been defined in scientific literature and unfortunately several of them have been ambiguously used over the years [*Cairo et al.*, 1999]. Therefore, it is worthy to list them and clarify the nomenclature. In Table 2-2, the most used variables are shown. Among them, the most used is the volume linear depolarization ratio *($\delta'$)*, defined as the ratio between the perpendicular ($\perp$) and parallel ($\parallel$) aerosol backscatter coefficient produced by a linear-polarized incident radiation. In order to avoid misunderstanding, it is worthy to note that the perpendicular-component of the backscattered light is not really 'perpendicular' but unpolarized as it was

indicated by *Gimmestad* [2008]. Low $\delta'$ values are related to spherical scatterers whereas high $\delta'$ values are related to non-spherical ones. Thus, values of $\delta'$ measured in the atmosphere range between the depolarization caused by molecules (e.g., $\delta'$=0.003656 at 532 nm using an interference filter with 0.5 nm of FWHM) and the depolarization caused by ice crystals of cirrus clouds with $\delta'$(532 nm) up to 0.5 [*Noel et al.*, 2002; *Noel et al.*, 2006].

Despite $\delta'$ is defined through the polarizing components of $\beta$ and $\beta_{mol}$, the direct $\beta^\perp$ retrieval cannot be performed due to the low SNR of the perpendicular signal. However, it can be easily retrieved from lidar equations. Solving for $\beta^{\|,\perp}(z,\lambda)$ in Eq. 2-14 and using Eq. 2-15, we obtain

$$\delta' = \frac{P^\perp(z,\lambda)}{P^\|(z,\lambda)} \frac{\epsilon^\perp}{\epsilon^\|} \left( \frac{T^\|(z,\lambda)}{T^\perp(z,\lambda)} \right)^2 \qquad \text{Eq. 2-20}$$

where $P^{\|,\perp}$, $\epsilon^{\|,\perp}$ and $T^{\|,\perp}$ are the signals, the system efficiencies and the transmittances for each polarizing component, respectively. This equation can be simplified because atmospheric extinction is most often independent on the polarization and thus:

$$\delta' = \eta \frac{P^\perp(z,\lambda)}{P^\|(z,\lambda)} \qquad \text{Eq. 2-21}$$

where $\eta$ is a calibration factor of the photodetectors ($\epsilon^\perp/\epsilon^\|$) that are also influenced by the crosstalk due to non-ideal behaviour of the polarizing beam splitter. This calibration method is only a first approximation to calibrate $\delta'$ as, except the influence of the PBS, the polarizing sensitivity of other parts of the lidar is omitted. In Chapter 5, the calibration of the depolarization will be analysed in detail. It is worthy to note that this expression must be replaced by Eq. 2-20 to study ice crystals as their stable orientation may cause significant
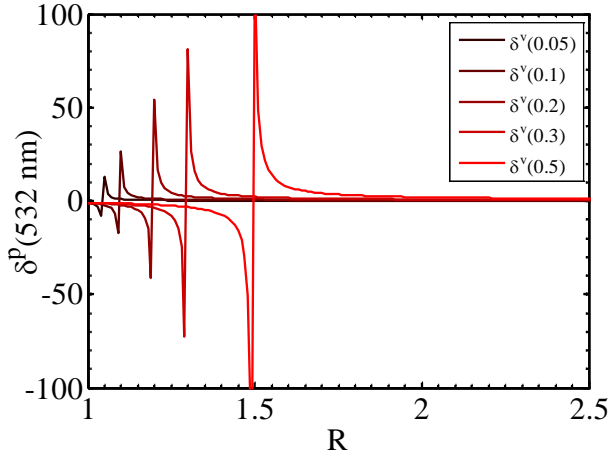
**Figure 2-4:** $\delta^p$ **as function of the backscattering ratio (R) parameterized by** $\delta'$. $\delta^p$ **becomes instable for low R and high** $\delta'$.

differences between the perpendicular and parallel extinction [*Schotland et al.*, 1971].

In order to separate the molecular and particle contribution, $\delta^p$ is defined by Eq. 2-17. However, as mentioned above, the direct $\beta^\perp$ retrieval cannot be performed and thus, $\delta^p$ is retrieved as function of $\delta'$, $\delta_m$ and the backscattering ratio ($R$) as follows:

$$\delta^p = \frac{R\delta'(\delta_m + 1) - \delta_m(\delta' + 1)}{R(\delta_m + 1) - (\delta' + 1)} \qquad \text{Eq. 2-22}$$

Unfortunately, this equations is unstable under low aerosol-load conditions ($R \sim 1$ and $\delta' \sim \delta_m$) (see Figure 2-4). In this sense, *Cairo et al.* [1999] recommends do not provide $\delta^p$ for $R < 1.1$. In this thesis, $\delta^p$ values are conversely considered for $R > 1.3$ for 532 nm, respectively.

By now, all depolarization variables have been defined taking into account linear-polarized incident radiation. However, although rarely used in lidar field, additional depolarization quantities exploited in radar research include the use of circular polarization. In these cases, the variation of the

electric field from right to left circular polarization determines the depolarization variables. Thus, the equivalent of the volume linear depolarization ratio, the volume circular depolarization ratio, $\delta'_C$, is expressed as

$$\delta'_C = \frac{\beta_a^{\circlearrowright} + \beta_m^{\circlearrowright}}{\beta_a^{\circlearrowleft} + \beta_m^{\circlearrowleft}}$$

<div align="right">Eq. 2-23</div>

By this way, different circular depolarization ratios can be defined following the scheme of Table 2-2. However, despite there are several manuscripts about the circular-depolarization theory in the science literature, to our knowledge, only preliminary experimental results of circular depolarization has been reported [*Woodward et al.*, 1998; *Roy et al.*, 2011].

As previously indicated, the volume and particle linear depolarization ratio has been commonly used by the lidar community at least during the last decade and thus this thesis is focused on these depolarization products.

## 2.5   Stokes-Müller formulism

In order to better understand the polarization state of the light and use a better tool to handle the lidar depolarization, it is very useful to introduce the Stokes-Müller formulism. In this section a brief summary of this formulism is presented.

The wave model of light describes light waves vibrating at right angles to the direction of propagation with all vibration planes being equally probable. This is referred to as "common" or "non-polarized" light. In polarized light there are only one or two vibration planes. The polarized light with one vibration plane is called linear polarized light. If the polarized light is composed of two plane waves of equal amplitude differing in phase by 90°, then the light is circularly polarized. Besides, when two plane waves of differing amplitude

are related in phase by 90°, or if the relative phase is other than 90° then the light is said to be elliptically polarized. Additionally, different combinations of polarization states are possible. Furthermore, the light can be partially polarized (combination of non-polarized and polarized light). The Stokes-Müller formulism describes and analyses the polarization state of light and the different polarization processes [*Hayman and Thayer*, 2009; 2012].

The Stokes formulism uses a 4x1 column matrix, called Stokes vector, which describes the polarization state of light. The Stokes vector contains the four Stokes parameters defined as follows:

$$\boldsymbol{S} = \begin{pmatrix} I \\ Q \\ U \\ V \end{pmatrix}$$

Eq. 2-24[7]

These Stokes parameters can be written in terms of the time averages of the parallel and perpendicular components of the electric field:

$$I = \langle E_\parallel E_\parallel{}^* + E_\perp E_\perp{}^* \rangle$$

Eq. 2-25

$$Q = \langle E_\parallel E_\parallel{}^* - E_\perp E_\perp{}^* \rangle$$

Eq. 2-26

$$U = \langle E_\parallel E_\perp{}^* + E_\perp E_\parallel{}^* \rangle$$

Eq. 2-27

$$V = \langle E_\parallel E_\perp{}^* - E_\perp E_\parallel{}^* \rangle$$

Eq. 2-28

where E represents the amplitude of the electric field in the planes parallel ($\parallel$) and perpendicular ($\perp$) to the reference plane, the asterisk represents the complex conjugate and brackets identifies a time average. Each component has units of irradiance (W/m$^2$). The first element, $I$, describes the total (polarized and unpolarized) irradiance. The second one, $Q$, is the irradiance linearly polarized in the direction parallel or perpendicular to the reference plane. The

---

[7] Bold symbols represent vectors and matrices.

third one, $U$, is the irradiance linearly polarized in the directions $45°$ to the reference plane, and the fourth one, $V$, is the irradiance circularly polarized.

The Stokes representation is very useful as all elements present the same units and are real and measurable quantities related by:

$$I^2 \geq Q^2 + U^2 + V^2 \qquad \text{Eq. 2-29}$$

where the identity occurs for polarized light, the expression $Q^2 + U^2 + V^2 = 0$ indicates unpolarized light and $I^2 > (Q^2 + U^2 + V^2) \neq 0$ means partially polarized light.

Müller formulism is the tool that allows the description of the polarizing properties of an optical system (optical element or medium). To this end, Müller formulism uses a 4x4 real matrix as it is shown:

$$M = \begin{pmatrix} m_{11} & m_{12} & m_{13} & m_{14} \\ m_{21} & m_{22} & m_{23} & m_{24} \\ m_{31} & m_{32} & m_{33} & m_{34} \\ m_{41} & m_{42} & m_{43} & m_{44} \end{pmatrix} \qquad \text{Eq. 2-30}$$

The Müller matrix of an optical system determines how the polarization state of an incident light (input Stokes vector) is changed into a new polarization state corresponding to the outgoing light (output Stokes vector):

$$S_{output} = MS_{input} \qquad \text{Eq. 2-31}$$

A way to intuitively understand how a Müller matrix works, each $m_{ij}$ element of the Eq. 2-30 can be seen as the amount of intensity that changes from the polarization state $i$ to the polarization state $j$, where $i$ and $j$ can be the $I$, $Q$, $U$ and $V$ as shown as follows:

$$M = \begin{pmatrix} m_{II} & m_{IQ} & m_{IU} & m_{IV} \\ m_{QI} & m_{QQ} & m_{QU} & m_{QV} \\ m_{UI} & m_{UQ} & m_{UU} & m_{UV} \\ m_{VI} & m_{VQ} & m_{VU} & m_{VV} \end{pmatrix} \qquad \text{Eq. 2-32}$$

As indicated by *Freudenthaler* [2014], all other optical elements in the lidar can be described as combinations of diattenuators and retarders and thus, it is worthy to describe the general Müller matrix of the retarding diattenuators:

$$\boldsymbol{M} = T \begin{pmatrix} 1 & D & 0 & 0 \\ D & 1 & 0 & 0 \\ 0 & 0 & Zcos(\Delta) & Zsin(\Delta) \\ 0 & 0 & -Zsin(\Delta) & Zcos(\Delta) \end{pmatrix}$$

Eq. 2-33

with

$$T = \frac{T_\parallel + T_\perp}{2}$$

Eq. 2-34

$$D = \frac{T_\parallel - T_\perp}{T_\parallel + T_\perp}$$

Eq. 2-35

$$Z = \sqrt{1 - D^2}$$

Eq. 2-36

$$\Delta = (\Delta_\parallel - \Delta_\perp)$$

Eq. 2-37

where $T_\parallel$ and $T_\perp$ are the parallel and perpendicular transmittance respect to the polarizing plane of the incident light, T is the total transmittance, D is the diattenuation and $\Delta$ is the phase shift between the parallel and perpendicular phase. A particular case of a retarding diattenuator is the polarizing beam splitter (PBS). This optical device is used to separate the input light beam into two where each output beam has the opposite linear state of polarization, noted as parallel (p) and perpendicular (s) to the plane of PBS. The Müller matrix is:

$$\boldsymbol{M_S} = T_S \begin{pmatrix} 1 & D_S & 0 & 0 \\ D_S & 1 & 0 & 0 \\ 0 & 0 & Zcos(\Delta_S) & Zsin(\Delta_S) \\ 0 & 0 & -Zsin(\Delta_S) & Zcos(\Delta_S) \end{pmatrix}$$

Eq. 2-38

where the subscript S makes reference to the transmitting (T) and reflecting (R) part of the polarizing beam splitter: $\boldsymbol{M_S} \in \{\boldsymbol{M_T}, \boldsymbol{M_R}\}, T_S \in \{T_T, T_R\}$, $Z_S \in \{Z_T, -Z_R\}$ and $\Delta_S \in \{\Delta_T, \Delta_R\}$. The PBS is used in lidar systems to separate

the state of polarization of the receiving signal into the parallel and perpendicular respect to the polarizing plane of the emitted laser beam.

The Stokes-Müller formulism is used in the Chapters 5 and 6 where the calibration is treated in detail and the influence of the lidar system on the depolarization measurements is analysed.

# 3 Experimental site and instrumentation

## 3.1 Experimental site

The measurements used in this thesis were performed at Granada in the Andalusian Institute for Earth System Research (IISTA-CEAMA). This centre is located in the Southern part of Granada, in South-western Spain (Granada, 37.16°N, 3.61°W, 680 m asl[8]) (Figure 3-1). Granada is a non-industrialized and medium-size city surrounded by mountains with altitudes up to 3479 m asl (Mulhacén peak). The total population is around 350 000 inhabitants (source: www.ine.es) considering the metropolitan area (240 000) and the main villages surround the city (110 000).

**Table 3-1: Climatic values of the meteorological station 'Armilla airbase' (37.13°N, 3.63°W) from the period 1971-2000.T: temperature; RH: relative humidity; RD: mean number of days with rainfall greater than 1 mm; SD: mean number of sunny days; SH: mean number of hours of sunshine (source: www.aemet.es).**

| Months | T (°C) | Rainfall (mm) | RH (%) | RD (days) | SD (days) | SH (hours) |
|---|---|---|---|---|---|---|
| January | 6.8 | 44 | 74 | 6 | 9 | 161 |
| February | 8.4 | 36 | 69 | 6 | 7 | 161 |
| March | 10.7 | 37 | 62 | 6 | 7 | 207 |
| April | 12.6 | 40 | 59 | 7 | 5 | 215 |
| May | 16.5 | 30 | 55 | 5 | 5 | 268 |
| June | 21.3 | 16 | 48 | 2 | 11 | 314 |
| July | 25.3 | 3 | 41 | 0 | 22 | 348 |
| August | 25.1 | 3 | 42 | 1 | 18 | 320 |
| September | 21.2 | 17 | 52 | 2 | 10 | 243 |
| October | 15.7 | 40 | 64 | 5 | 7 | 203 |
| November | 10.6 | 46 | 73 | 6 | 8 | 164 |
| December | 7.9 | 49 | 76 | 7 | 7 | 147 |
| Year | 15.2 | 361 | 60 | 54 | 115 | 2751 |

[8] Above sea level
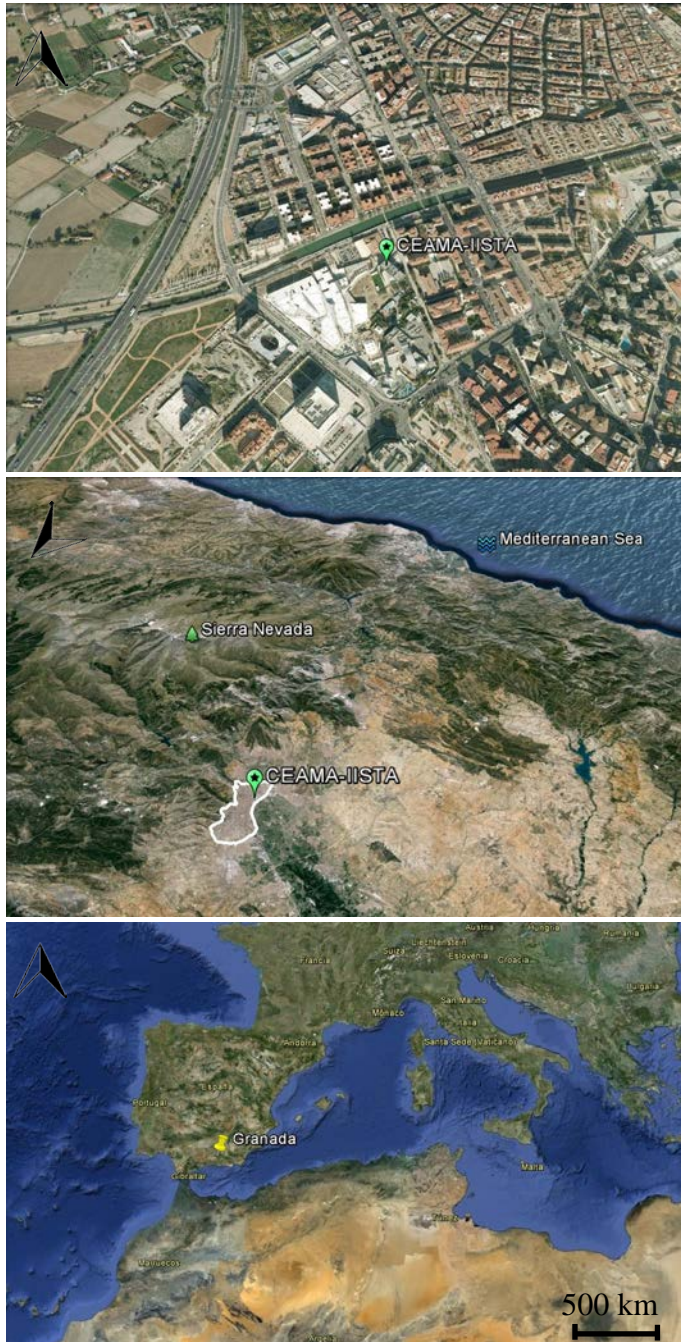
**Figure 3-1: Experimental site location: (top) neighbourhood of CEAMA-IISTA, (centre) Granada city location including Sierra Nevada and the Mediterranean Sea, and (bottom) South and Central Mediterranean Sea (source: Google Earth). Black arrow points towards the North Pole.**

Most relevant climatic values are shown in Table 3-1. The near-continental conditions prevailing at this site are responsible for large seasonal temperature differences, providing cool winters and hot summers. The rainy period corresponds to late autumn, winter and early spring while the rest of the year the rain is scarce.

The main local source of aerosol particles is the road traffic. Seasonally, there are also two important sources as the soil re-suspension during warm-dry season and the domestic heating based on fuel oil combustion during winter [*Titos et al.*, 2012]. The study area is about 50 km away from the Mediterranean coast and, due to its proximity to the African continent, is frequently affected by outbreaks of Saharan air masses. Due its location, Granada is an exceptional place to characterize the Saharan dust coming from Africa. Additionally, the Mediterranean basin represents an additional source of aerosol particles [*Lyamani et al.*, 2010].

## 3.2  Lidar systems

Lidar measurements were performed by two Raman lidar systems operated at CEAMA-IISTA: the multiwavelength Raman Lidar MULHACEN (Raymetrics Inc, model LR331-D400) and the scanning Raman Lidar VELETA (Raymetrics Inc, model LR111-D200). MULHACEN and VELETA systems mainly present the same lidar scheme: laser emitter, optical system and detection unit. Most important characteristics of the lidar systems are summarized in Table 3-2. Both MULHACEN and VELETA were incorporated into the European Aerosol Research Lidar Network (EARLINET, www.earlinet.org) in April 2005 and May 2011, respectively. EARLINET is the first aerosol lidar network, established in 2000, with the main goal to provide a comprehensive,

quantitative, and statistically significant database for the aerosol distribution on a continental scale. At present, EARLINET consists of 28 lidar stations.

### 3.2.1 MULHACEN

MULHACEN is a ground-based, six wavelength lidar system with a pulsed Nd:YAG laser, frequency doubled and tripled by Potassium Dideuterium Phosphate crystals. The emitted wavelengths are 355, 532 and 1064 nm with output energies per pulse of 60, 65 and 110 mJ, respectively. It has elastic backscatter channels at 355, 532 and 1064 nm and Raman-shifted channels at 387 (from $N_2$), 408 (from $H_2O$) and 607 (from $N_2$) nm. The laser beam is led toward the atmosphere by means of two steering mirrors. The laser beam also passes through two beam expanders and a high-transmittance window placed on the outer cover box of the lidar system. The beam expander reduces the divergence and increases the surface of the laser beam by a factor ×5 and ×4.5 for 355 nm and 532/1064 nm, respectively. The beam expanders are used in order to increase the illuminated portion of the atmosphere with respect to the field of view of the telescope, which increases the signal-to-noise ratio (SNR). Additionally, the beam expanders decrease the divergence of the laser beams. The alignment between the telescope and the laser beam is performed through an optical mount that allows the tilt of the laser beam with an accuracy of several microradians. The full overlap is reached around 1220 m agl [*Navas Guzmán et al.*, 2011] although the overlap is complete at 90% between 520 and 820 m asl [*Navas Guzmán et al.*, 2011; *Rogelj et al.*, 2014].
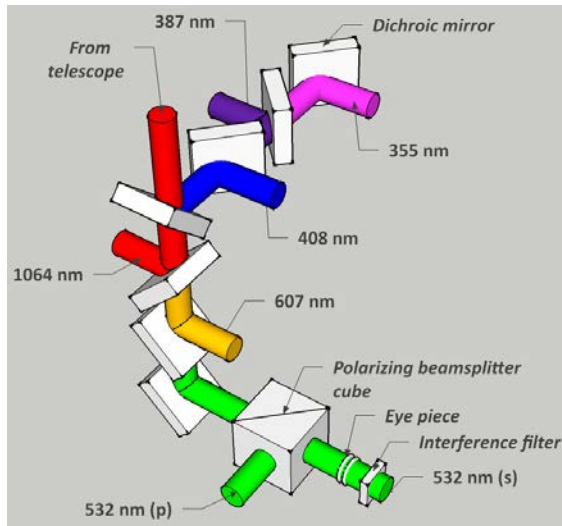
**Figure 3-2: Receiving optics except the telescope. Optical paths of 355, 387, 408, 532 (parallel, p, and perpendicular, s), 607 and 1064 nm are drawn. Rectangular plates are dichroic mirrors. The set consisting of eye piece and interference filter is used at each wavelength but only shown for 532 nm (s) channel for simplicity.**

The receiving optical system is the module that receives and collimates the backscattered light (telescope, diaphragm), separates it into different wavelengths (dichroic mirrors and interference filters) and into different polarizing components (polarizing beam-splitter cube) and finally focuses it (eye piece) on the surface of the detectors. The Cassegrain telescope has a primary mirror of 0.4m-diameter and a 7mm-diameter diaphragm located in the focal plane of the telescope avoiding spurious light. The wavelength separation is schematically shown in Figure 3-2. Optical devices are positioned with a high accuracy of 0.1° at 45° respect to the incident light direction. Interference filters are used in order to separate the wavelengths with a FWHM[9] between 0.5 and 2.7 nm, and neutral density filters adjust the signal intensity reaching the

---

[9] Full Width at Half Maximum

**Table 3-2: Technical characteristics of MULHACEN (LR331-D400) and VELETA (LR111-ESS-D200) (Raymetrics, S.A.)**

| Lidar units | MULHACEN | VELETA |
|---|---|---|
| Emitter | | |
| Pulse laser source | Nd:YAG (Quantel CFR Series) | Nd:YAG (Quantel Ultra Series) |
| Wavelength, nm (Pulse energy, mJ) | 355 (60), 532 (65) and 1064 (110) | 355 (33) |
| Pulse duration, ns | 8 | 5.04 |
| Repetition rate, Hz | 10 | 20 |
| Beam diameter, mm | 6 | 3.37 |
| Beam divergence, mrad | 0.1 | 0.063 |
| Optical system | | |
| Telescope Cassegrain (Primary/secondary mirror, mm) | 400/90 | 200/50 |
| Focal length (mm) | 3998 | 800 |
| Telescope-laser axes distance (mm) | 320 (532 and 1064 nm) and 350 (355 nm) | 167 |
| Wavelength (nm) split by polarizing components (parallel and perpendicular) | 532 | 355 |
| Wavelengths (nm) (FWHM) | 355 (1.0), 387 (2.7), 408 (1.0), 532 (0.5), 607 (2.7) and 1064 (1.0) | 355 (1.0) and 387 (1.0) |
| Detection Units | | |
| Detectors | APD (at 1064 nm), PMT (others) | PMT |
| Transient Recorder (range resolution in nm) | LICEL: TR20-160 and PR20-160P (7.5) | LICEL: TR20-160 and PR20-160P (7.5) |
| Pointing | Zenith | Elevation range = [0°, 90°] Azimuth range = [−90°, 270°] |

photodetectors. Finally, the polarizing beam splitter reflects the parallel and transmits the perpendicular components at 532 nm with a reflectance and transmittance of 0.995 and 0.99, respectively. Reflectance of commercial polarizing beam splitters is usually larger than transmittance. This configuration is used to minimize the cross-talk effect as it is explained in Section 4.1.5.

The optical signal is converted into an electrical one by means of 6 photomultipliers (PMT) and an Avalanche Photodiode Detector (APD) used for 1064 nm. The PMTs (Hamamatsu, R7400U) perform measurements in photon-counting mode with a gain factor around $8 \times 10^6$ depending on the applied voltage (linear range: 750-840 V), which is optimized depending on the intensity of the received signal. Finally, the APD works in analog mode with an applied voltage in the range 265-285 V.

Lidar signal is recorded by a LICEL transient recorder (Germany) especially designed for remote sensing applications. Signal measured by PMTs is simultaneously recorded in two different modes: analog by means of an analog-to-digital converter (A/D) and photon-counting. The combination of the signals of both detection modes is briefly explained in Section 4.1.1.5.

For further details, MULHACEN has been characterized by *Guerrero Rascado* [2008] and *Navas Guzmán* [2011].

### 3.2.2   VELETA

VELETA is a ground-based lidar system with a pulsed Nd:YAG with an emitted wavelength of 355 nm (33 mJ per pulse). It has channels at 355 (parallel and perpendicular) and 387 nm ($N_2$ Raman-shifted). VELETA presents a novel configuration by which the laser head, the telescope and the optical system are mounted on a sun-tracker (Kipp&Zonen sun-tracker) that allows the measurement pointing to any direction in the sky dome. The overlap
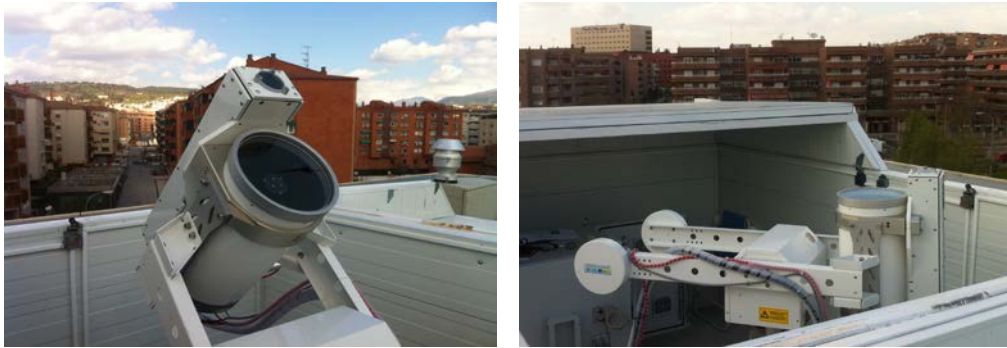
**Figure 3-3: VELETA pointing in two different positions.**

range of the system is between 200 and 400 m. Technical specifications can be found in Table 3-2.

The optical system consists of a Cassegrain telescope (0.2 m diameter primary mirror) with a 1.5 mm diaphragm. The wavelength separation is schematically shown in Figure 3-4. Optical devices are positioned with a high accuracy of 0.1° at 45° with respect to the incident light direction. Wavelengths are selected and adjusted by interference filters and neutral density filters. The polarizing beam-splitter cube is characterized by $R_s = 0.99$ and $T_p = 0.95$.
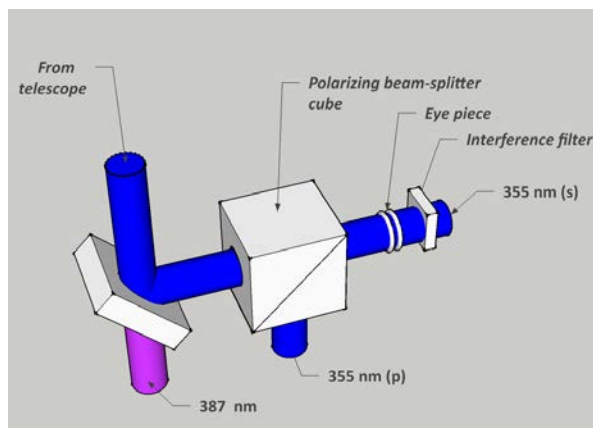


**Figure 3-4: Receiving optics except the telescope. Optical paths of 355 (parallel, p, and perpendicular, s) and 387 nm. The set consisting of eye piece and interference filter is used at each wavelength, but it is only shown for 355 nm (s) channel for simplicity.**

## 3.3 Quality assurance

The complexity of the lidar system requires appropriate quality control of the measurements. To do this, both MULHACEN and VELETA are under strict quality assurance based on several tests that assess the lidar response. This quality control is performed periodically under the supervision by the EARLINET quality control working group. Results of all the stations are included in the deliverables of the WP2 of ACTRIS[10] (Aerosol Cloud and Trace Gases Research Infrastructure Network). Particularly, MULHACEN's and VELETA's quality assurance was presented in the *Report on second internal quality checks for hardware* (deliverable D2.6). Additionally, the MULHACE's quality assurance was published in previous works [*Guerrero Rascado*, 2008; *Guerrero-Rascado et al.*, 2011; *Navas Guzmán*, 2011]. Thus, only the more relevant results (i.e., telecover, Rayleigh fit and trigger delay) for VELETA's quality assurance and the new test for the depolarization measurement for both MULHACEN and VELETA are presented in this thesis.

### 3.3.1 Telecover test

The telecover test is a self-check of the optical part of a lidar system. This test allows the determination of range-dependent transmission which results in a signal distortion. It can be also used to determine the correct alignment between the laser beam and telescope axes. It is based on the comparison of signals measured using different quadrants of the telescope. Quadrants are named

---

[10] ACTRIS is a European Project aiming at integrating European ground-based stations equipped with advanced atmospheric probing instrumentation for aerosols, clouds, and short-lived gas-phase species. ACTRIS has the essential role to support building of new knowledge as well as policy issues on climate change, air quality, and long-range transport of pollutants.

north, east, west and south, where north is the quadrant nearest to the laser beam axis and the others named following the clockwise sense (see Figure 3-5). To this end, four measurements are performed covering three quadrants at a time. Additionally, one extra north measurement is performed at the end of the telecover test in order to check the atmospheric stability. Then, three behaviours of the quadrant measurements are checked due to the design of the lidar: first, the height of perfect overlap of the different quadrants has to increase from north to south, passing through that east and west. Second, east and west signals should be equal due to the lidar symmetry. Third, signals should converge with height to become equal.

Figure 3-6 shows an example of a telecover test of the raw signal at 355p nm of VELETA. In this case, both north measurements are almost equal which indicates a good atmospheric stability. Thus, atmospheric conditions allow the assessment of the telecover test. As can be seen in Figure 3-6, the order of the signal maxima are north, located at 127.5 m agl (above ground level), then east and west at 165.5 and 172.5 m agl, respectively, and finally, south at 187.0 m agl. Therefore, the behaviour of the signals presents a correct trend according to the lidar design. Both east and west signals are also very similar between them
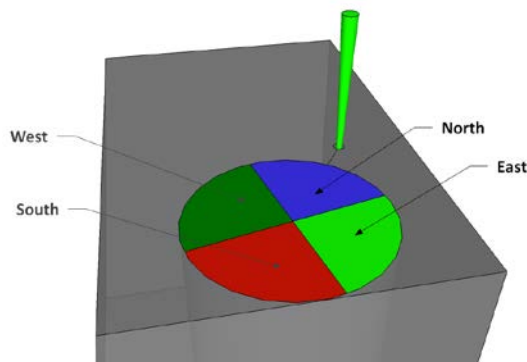


**Figure 3-5: Telecover scheme using MULHACEN design. Quadrants are north (blue), east (light green), west (dark green) and south (red).**
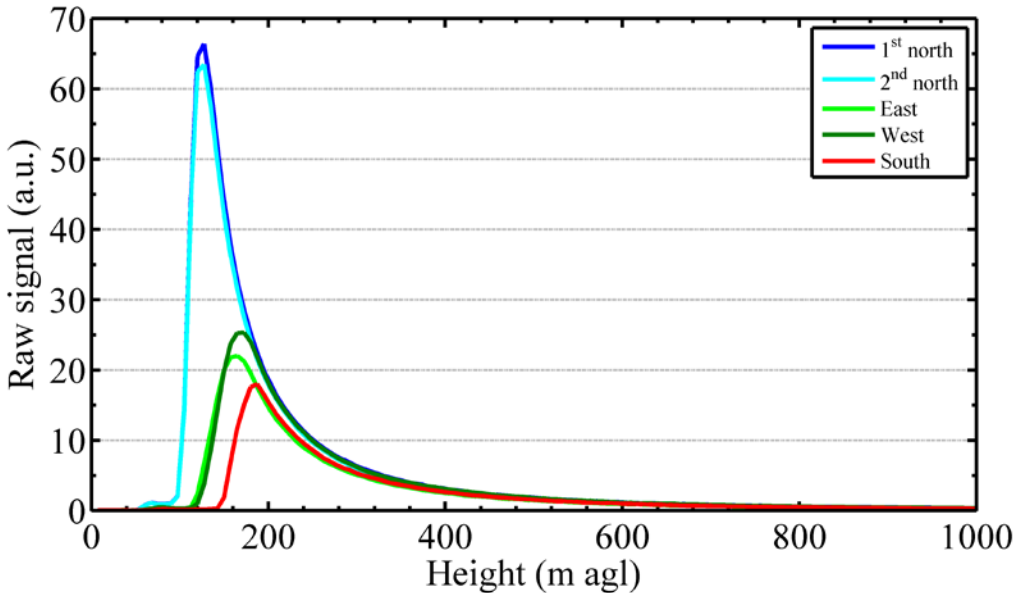
**Figure 3-6: 355p nm signals of the telecover test. North, east, west and south are the quadrant of the telescope. Signals are colored according to Figure 3-5.**

which spatial difference of the maxima of 1 bin (7.5 m). Finally, the four signals are equal approximately above at 500 m agl. The assessment of these results indicates a good alignment of the lidar as well as it highlights there are not artefacts in the signal.

### 3.3.2 Rayleigh fit

The Rayleigh fit is a tool for determining the good alignment of lidar systems in the far range. As it was indicated in Section 2.3 (Eq. 2-12), RCS is proportional to $\beta_{att}$. Therefore, the RCS normalized to an aerosol-free height and the molecular $\beta_{att}$ normalized to the same height should be equal in the aerosol-free region. This test is very important because it indicates the maximum range of the optical property profiles and shows the available calibration height range for the Klett-Fernald and Raman retrievals (see Section 4.1.2 and 4.1.3). The 355p nm Rayleigh fit is shown in Figure 3-7 where both
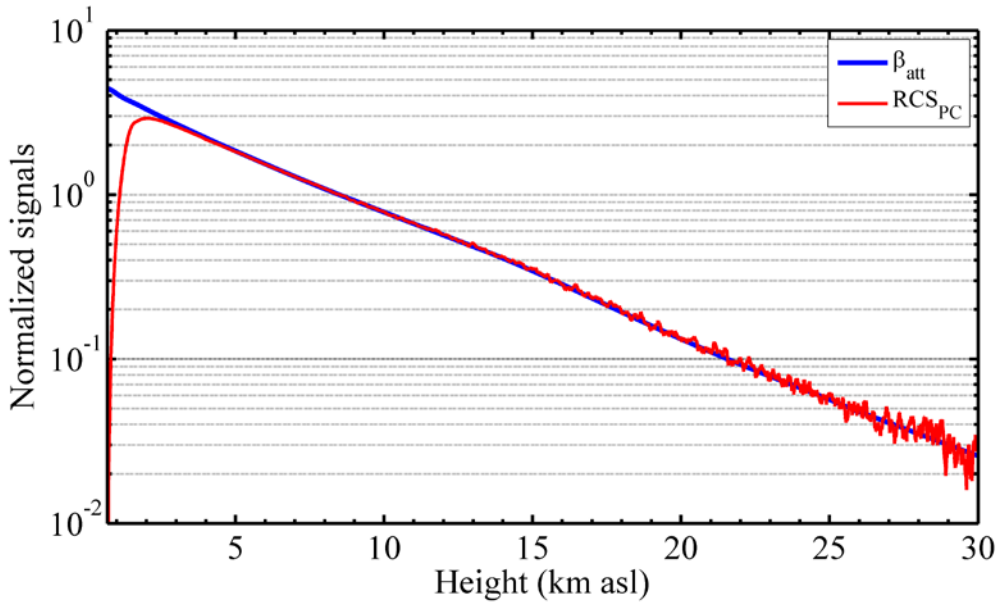
**Figure 3-7: Rayleigh fit of 355p nm channel. Both molecular attenuated backscatter and RCS are normalized in the range 8-9 km asl.**

molecular $\beta_{att}$ and $RCS$ are normalized in the range 8-9 km agl. In this test, only the photon-counting (PC) signal is used as the far range is studied. Results highlighted the good agreement between the normalized molecular $\beta_{att}$ and $RCS$ with a very similar trend from 5 to 30 km asl. In fact, relative deviation between both signals is less than 2% in the range 5-10 km asl. This range is the most important because the reference height required for the retrieval of optical properties is usually chosen between 6 and 10 km asl.

### 3.3.3 Δ90°-calibration method

In spite of the fact that Δ90°-calibration method of the depolarization measurements is not strictly a quality assurance test, it can be used to this aim. In fact, it was used with this purpose by the EARLINET stations of Munich, Limassol and Granada in the deliverable D2.6, *Report on second internal quality checks for hardware,* of the WP2 (ACTRIS) in February 2013. Due to

the novelty of this calibration and its relevance in this thesis, it will be explained in detail in Chapter 5.

## 3.4   Additional instruments

### 3.4.1   Sun-photometer

Measurements of total columnar aerosol properties at daytime were obtained using a CIMEL CE-318 sun-photometer. This instrument is included in the AERONET network [*Holben et al.*, 1998] (http://aeronet.gsfc.nasa.gov), which imposes standardization of instruments, calibration, processing and data



**Figure 3-8: Sun-photometer pointing at the sun.**

distribution. The sun-photometer provides solar extinction measurements at seven channels ranging from 340 to 1020 nm and sky radiances measured at 440, 675, 870 and 1020 nm. Solar extinction measurements are used to compute the aerosol optical depth (AOD) at 340, 380, 440, 675, 870 and 1020 nm. The AOD uncertainty ranges from ±0.01 in the infrared-visible to ±0.02 in the ultraviolet channels [*Eck et al.*, 1999]. The sky radiance measurements in conjunction with AOD data at four wavelengths are used to retrieve aerosol microphysical properties like columnar aerosol size distribution, refractive index and single scattering albedo, $\omega(\lambda)$, using the algorithm by *Dubovik and King* [2000] with improvements by *Dubovik et al.* [2006]. In addition, the inversion code provides other parameters such as the volume concentration, modal radius and standard deviation for fine and coarse modes of the retrieved aerosol size distribution. The uncertainty of the AERONET inversion products

is described by *Dubovik and King* [2000] and *Dubovik et al.* [2006]. The authors showed that the uncertainty in the retrieval of $\omega(\lambda)$ is ±0.03 for high aerosol load (AOD (440 nm) > 0.4) and solar zenith angle > 50°. For measurements with low aerosol load (AOD(440 nm) < 0.2), the retrieval accuracy of $\omega(\lambda)$ drops down to 0.02-0.07. For high aerosol load (AOD(440 nm) > 0.4) and solar zenith angle > 50°, uncertainties are about 30-50% for the imaginary part of the refractive index. The reported uncertainties for aerosol are around 10-35%, for the size distribution retrievals in the 0.1 µm < r < 7 µm size range, while for sizes retrieval outside of this range, uncertainties rise up to 80-100%. Finally, the fine fraction (η), defined as the fine AOD respect to the total AOD, provided by AERONET was used [*O'Neill et al.*, 2001a; *O'Neill et al.*, 2001b].

### 3.4.2 Microwave radiometer HATPRO

In addition, continuous monitoring of tropospheric temperature profiles during the studied period was performed using a ground-based passive microwave radiometer (RPG-HATPRO, Radiometer Physics GmbH). The passive microwave radiometer performs measurements of the sky brightness temperature with a



**Figure 3-9: Microwave radiometer.**

radiometric resolution between 0.3 and 0.4 K root mean square error at 1 s integration time. The radiometer uses direct detection receivers within two bands: 22-31 and 51-58 GHz. The radiation from the first band provides information about the tropospheric water-vapour profile, while the second band is related to the temperature profile. In addition, surface meteorological data

were also available from both the microwave radiometer itself and a co-located meteorological station. Temperature profiles are retrieved from brightness temperature and surface meteorological data using an inversion algorithm developed by *Rose et al.* [2005]. Temperature is provided with an accuracy of 0.8 K within the first 2 km and 1.2 K at higher altitudes. Tropospheric profiles are obtained from the surface up to 10 km using 39 heights with vertical resolution ranging from 10 m near the surface to 1 km for altitudes higher than 7 km agl. For heights below 3 km agl, where the PBL is usually located over Granada [*Granados-Muñoz et al.*, 2012], data at 25 independent points with resolution between 10 and 200 m are provided. Temperature profiles have been used to determine the PBL height using the parcel method [*Holzworth*, 1964]. Estimates of the PBL height using microwave radiometer temperature profiles have already been validated with independent measurements [*Granados-Muñoz et al.*, 2012].

# 4 Methodology

This chapter mainly describes the methodology applied to lidar measurements as the data pre-processing and the elastic, inelastic and depolarization retrievals. Additionally different tools used in the thesis are explained.

## 4.1 Lidar technique

### 4.1.1 Pre-processing

Database recorded by lidar systems cannot be directly used to retrieve optical properties and thus, different pre-processing steps are required. The basis of these pre-processing steps and the applied methodology are explained in the following subsections.

#### 4.1.1.1 Dead time correction

The lidar signal in photon-counting (PC) mode requires the so-called dead time correction. PC mode is based on the count of impact of photons, one by one, on the surface of the photodetector. This procedure requires a certain amount of time to discriminate and process each event. If a second event occurs during this time, it will not be counted. The minimum amount of time that allows the discrimination between two events such that both are counted is referred to as dead time. Because of the random nature of the arrival times of photons, there is always some time with some events that will not be counted. In lidar applications, the number of uncounted photons is significant in the near range decreasing in the far range. Assuming that the events occur randomly according to a Poisson process, if $N_m$ is the system measured count rate and $\tau$ is the known dead time, the actual number of events (N) may be estimated by,

$$N = \frac{N_m}{1 - N_m \tau}$$
Eq. 4-1

In the case of the PMT tubes (R7400U, Hammatsu) used in our Raman lidar systems, the value of the dead time is 4 ns. Therefore, photo-counting channels are corrected by Eq. 4-2.

### 4.1.1.2   Background subtraction: dark current and sky radiation

The background subtraction is necessary in order to remove from the measured signal the portion that is not related to the molecular or particle backscattering. This contamination has two sources: the dark current and the sky radiation.

The dark current is an artefact produced by the analog-to-digital converter of the elastic-backscatter photomultipliers due to small currents flowing through the detectors even when their sensor surfaces are not illuminated. This artefact is height-dependent so it modifies the signal and prevents a correct Rayleigh fit. The correction requires a dark-current measurement while the telescope or the diaphragm is completely covered. Then, the dark current measurement is subtracted from the actual measured profile. A 10-min dark current measurement is usually performed for each measurement session.

The sky radiation contribution to the background signal is mainly due to the sun-light scattered by atmospheric gases and particles. It depends on the time of the day, but is range independent. To remove its contribution, an average is performed in the height range 75-105 km where the laser signal can be neglected and then the mean value is subtracted from the whole profile.

### 4.1.1.3   Trigger delay

A trigger is a device that activates a firing mechanism on a system. In terms of laser, trigger is used to produce pulses with a certain frequency. Particularly, for the MULHACEN and VELETA systems, the laser trigger is also used to activate the data acquisition by means of the LICEL transient recorder. However, there is a delay between the laser beam emission and the start of the

data acquisition. In order to determine the trigger delay of MULHACEN and VELETA, three different tests have been performed. In order to illustrate these tests, MULHACEN data are used.

Near target test: The near target test consists of detecting a peak of the lidar signal backscattered by a near target (e.g., an A4-cardboard). Because this signal is backscattered by a very near target (less than 7.5 m, i.e. the nominal vertical resolution) the peak should be detected in the bin 0 (initial bin). If the peak is detected in a different bin, the trigger delay can be determined by a simple computation.

**Table 4-1: Trigger delay for MULHACEN elastic channels determined using the near target test.**

| Channel | AN trigger delay (bins) |
|---|---|
| 0 (532p nm) | **7** |
| 1 (532s nm) | 6 |
| 2 (355 nm) | 6 |
| 3 (1064 nm) | 6 |

This test was performed to obtain the trigger delay of analog (AN) and photon-counting (PC) signals of the elastic channels. However, no-signal peaks were detected on PC channels whereas the AN channels presented clear peaks at bins shown in Table 4-1. The AN trigger delay is around 45-52.5 m (1 bin corresponds to 7.5 m). As the PC trigger delay was not determined by this test, the optical fiber test was performed.

Optical fiber test: In this test, a 15-m optical fiber is used to capture and introduce a part of the emitted laser beam directly through the telescope to the photodetectors. As the light path is known (~15 m) and the spatial resolution of the LICEL is 7.5 m, the peak of light should be detected at the second bin. If the

input light is detected in another bin, the trigger delay can be determined through the difference of the bin locations. Results of this test are shown in Table 4-2. AN trigger delay presents similar values to the previous test so it seems that both tests are equivalent. Additionally, PC trigger delay is determined. Using the trigger delay of both AN and PC signal, the bin shift between both signals can be derived as it is also shown in Table 4-2.

Table 4-2: Trigger delay determined by means of optical fiber test.

| Channel | Trigger delay | | Bin shift |
|---|---|---|---|
| | AN | PC | |
| 0 (532p nm) | 7 | 2 | 5 |
| 1 (532s nm) | 7 | 1 | 6 |
| 2 (355 nm) | 7 | −1 | 8 |
| 3 (1064 nm) | 5 | 0 | - |
| 4 (387 nm) | - | −1 | - |
| 5 (532s nm) | - | 2 | - |
| 6 (387 nm) | - | 1 | - |

Once the trigger delay is corrected for all channels, the Rayleigh fit can be used to check if the results of the optical fiber test are correct. In Figure 4-1, a Rayleigh fit of the 532p nm signal corrected using the trigger delay in Table 4-2 is shown. As can be seen, the delay between both signals is obvious so this test
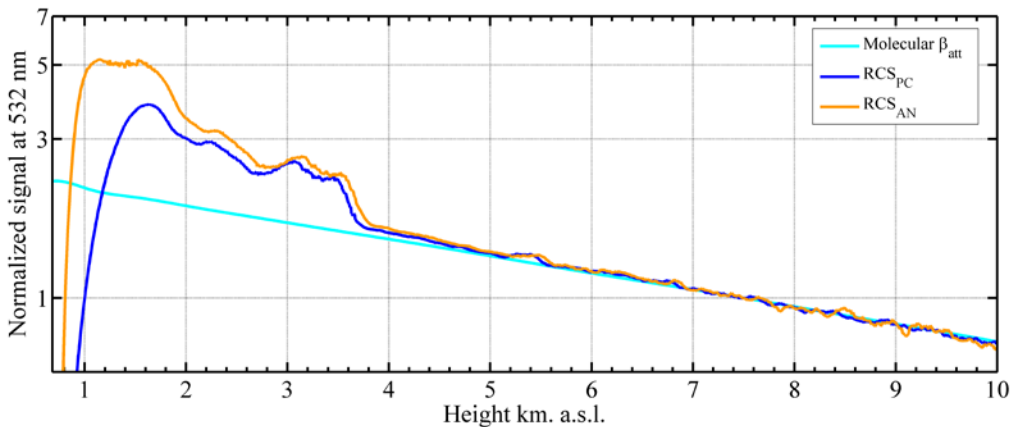


Figure 4-1: Analog and photon-counting signals displayed following the trigger delays determined by means of optical fiber test. Normalization range: 7-8 km asl.

does not provide good results for AN or PC channels. As AN trigger delay was the same (7-6 bins, approx.) for target and optical fiber tests, it was assumed that the determination of the PC trigger delay presented some problem. Then, another test was used in order to determine the correct PC trigger delay.

Slope test: For this test at least one well-corrected channel is required. In our case, the AN trigger delay is successfully determined by means of two tests. Then, the PC trigger delay is obtained using the slope test. To this end, the slopes of AN and PC signals are compared as both must detect the different structures of the atmosphere at the same height (e. g., an aerosol layer must be detected at the same height by AN and PC modes). In other words, AN and PC signals must be correlated. Hence, this test determines the bin shift by means of the best linear fit between AN and PC signals fixing the AN signal, once corrected of trigger delay, and displacing the PC signal from -20 to +20 bins.
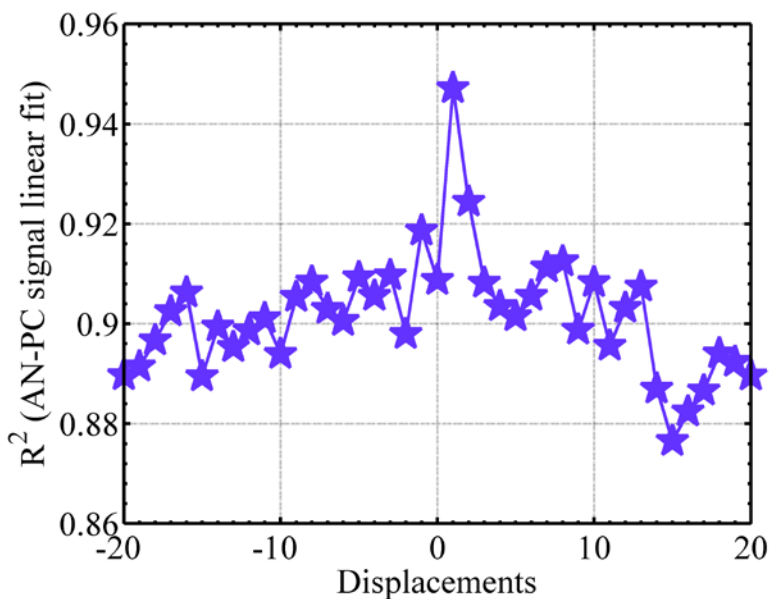


**Figure 4-2: $R^2$ computed for linear fitting between AN signal and different PC signals of channel 0 (532p nm). The PC signals were displaced between −20 and +20 bins. The best correlation is found with a displacement of two bins.**
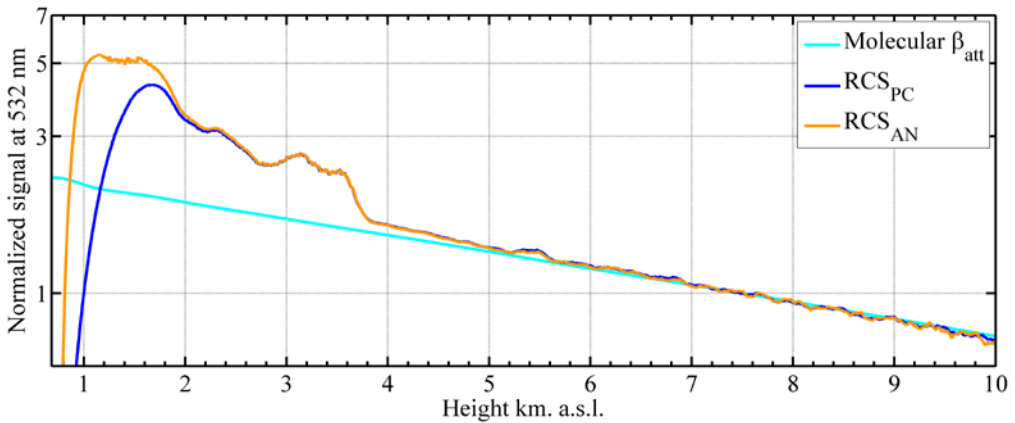
**Figure 4-3: Analog and photon-counting signals of channel 0 (532p) displayed after correcting for the trigger delays determined by means of slope test. Normalization range: 7-8 km asl.**

Then, the highest linear fit $R^2$ shows the bin shift.

As can be seen in Figure 4-2, a displacement of 2 bins of the PC signal respect to the corrected AN signal produces the best correlation. Then, the trigger delay of PC signal is 9 bins.

Figure 4-3 shows the Rayleigh fit of the 532p nm signal (MULHACEN) using the values obtained with the slope test. The comparison of Figure 4-3 (slope test) and Figure 4-1 (fiber test) proofs that results that the slope test provides better PC trigger delay than the fiber test. The trigger delay for Raman channels cannot be determined by means of near target or optical fiber methods as both methods gave wrong PC trigger delays and they cannot be determined using the slope test. Therefore, PC trigger delay of Raman channels was assumed equal to the PC trigger delay of the elastic channels as its value is almost constant (8-9 bins). In Table 4-3, the final trigger delays are presented.

**Table 4-3: MULHACEN trigger delays determined by means of the combination of near target and slope tests. Values in brackets are assumed.**

| Channel | Bin-zero | | Bin shift |
|---|---|---|---|
| | AN | PC | |
| 0 (532p nm) | 7 | 9 | 2 |
| 1 (532s nm) | 7 | 9 | 2 |
| 2 (355 nm) | 7 | 8 | 1 |
| 3 (1064 nm) | 5 | - | - |
| 4 (387 nm) | - | [8] | - |
| 5 (408 nm) | - | [8] | - |
| 6 (607 nm) | - | [8] | - |

Following the same procedure, AN and PC trigger delays were determined for VELETA (Table 4-4).

**Table 4-4: VELETA Trigger delays determined by means of the combination of near target and slope tests.**

| Channel | Bin-zero | | Bin shift |
|---|---|---|---|
| | AN | PC | |
| 0 (355p nm) | 6 | −2 | 8 |
| 1 (355s nm) | 6 | −3 | 9 |
| 2 (387 nm) | - | [−2] | - |

### 4.1.1.4 Overlap correction

As it was introduced in Section 2.3, the lidar signal is affected by the overlap function, $O(z)$, which is characterising the overlap of the laser beam and the telescope field of view. This overlap behaviour prevents obtaining information in a range close to the lidar. However, this effect can be partially corrected. Firstly, $O(z)$ needs to be determined experimentally and then, the retrieved $O(z)$ is applied to the lidar raw data in the pre-processing step. A detailed description of this correction was presented by *Wandinger and Ansmann* [2002] and applied in the IISTA-CEAMA by *Navas Guzmán* [2011].

### *4.1.1.5 Gluing signal*

The analog (AN) and photon-counting (PC) detection are two mode of recording the received signal due to its high dynamic range (around five orders of magnitude). In this sense, AN signal provides better signal and SNR in the near range whereas PC provides it in the far range. The combination of both AN and PC profiles would optimize the quality of the signal and SNR in the whole range. To this end, *Navas Guzmán* [2011] optimized the gluing process taking into account the better fitting range of the AN and PC signals.

### 4.1.2 Elastic backscatter retrieval

The elastic retrieval is a well-known solution of the lidar equation, named Klett-Fernald algorithm as it was proposed and improved by Frederick G. Fernald and James D. Klett between 1972 and 1985 [*Fernald et al.*, 1972; *Klett*, 1981; *Fernald*, 1984; *Klett*, 1985]. The procedure is based on: first, the assumption of a height-constant extinction-to-backscatter ratio, called particle lidar ratio (*LR*) and a known value of $\beta$ at a height reference $z_0$, $\beta(z_0)$; second, the determination of the molecular backscatter and extinction coefficients by means of Rayleigh's theory and the molecule number density calculated using the thermodynamic state of the atmosphere (temperature and pressure profiles). Under these assumptions, the lidar equation [11] can be handled to get the Bernoulli equation that is solved by means of boundary conditions. The solution is:

$$\beta(z) = -\beta_{mol}(z) + \frac{RCS(z)T^2(z,z_0)}{\frac{RCS(z_0)}{\beta(z_0) + \beta_{mol}(z_0)} - 2\int_{z_0}^{z_{ref}} LR(\xi)RCS(\xi)T(\xi,z_0)\,d\xi} \qquad \text{Eq. 4-2}$$

---

[11] See Section 2.3, Eq. 2-11.

where the wavelength dependence is omitted for simplicity, $\xi$ is a distance variable of integration, and $T(z, z_0)$ and $T(\xi, z_0)$ is the transmittance (Eq. 2-1) between the ranges $z - z_0$ and $\xi - z_0$, respectively. The aforementioned $\beta(z_0)$ is assumed to be zero in the reference height or derived using a backscatter-related Angström exponent, previously determined, as it is explained by *Navas-Guzman et al.* [2011]. The reference height is determined by means of the Rayleigh fit explained in Section 3.3.

As it was previously indicated, *LR* has to be assumed. *LR* is generally assumed height-constant and estimated by means of ancillary information (e.g., information derived from sun-photometer as it is explained by *Landulfo et al.* [2003] and *Córdoba-Jabonero et al.* [2011]).

### 4.1.3   Inelastic retrieval

The following approach for the retrieval of the particle extinction coefficient was first presented by *Ansmann et al.* [1990]. With the application of the so-called Raman method, no assumption of the lidar ratio is necessary for the calculation of the particle extinction and backscatter coefficients. It is based on the independent measurements at the laser wavelength, $\lambda_L$, as well as at the wavelength of the inelastically scattered light, $\lambda_R$, as it was introduced in Section 2.3 (Eq. 2-14). If the Raman scattering is produced by a gas with known atmospheric density (e.g., nitrogen or oxygen), the particle backscatter coefficient in the Raman lidar equation is known, and only the aerosol extinction and its wavelength dependence remain as unknowns.

Assuming a wavelength dependence of the extinction coefficient, $\alpha \propto \lambda^{-k}$, the Raman lidar equation is solved for particle extinction coefficient at $\lambda_L$ as follows [*Ansmann et al.*, 1990]:

$$\alpha(z) = \frac{\frac{d}{dz} \ln\left(\frac{N_R(z)}{RCS(z, \lambda_R)}\right) - \alpha_{mol}(z, \lambda_L) - \alpha_{mol}(z, \lambda_R)}{1 + \left(\lambda_L / \lambda_R\right)^k}$$

Eq. 4-3

where $N_R$ is the atmospheric number density of Raman scatterer and $\alpha_{mol}$ can be calculated from Rayleigh scattering coefficients and atmospheric number density profiles. Atmospheric number density profiles are derived from temperature and pressure profiles obtained from models or radiosonde measurements. Therefore, independent particle extinction coefficient can be determined from the detection of Raman scattered light.

Once $\alpha$ is retrieved, $\beta$ can be independently determined following the approach for the retrieval proposed by *Cooney et al.* [1969] and *Melfi* [1972].

$$\beta(z, \lambda_L) = \beta_{mol}(z, \lambda_L) \left(\frac{\beta(z_0, \lambda_R)}{\beta(z_0, \lambda_L)} \frac{P(z, \lambda_L)}{P(z, \lambda_R)} \frac{T(z, \lambda_R)}{T(z, \lambda_L)} - 1\right)$$

Eq. 4-4

where $\beta(z_0, \lambda_R)/\beta(z_0, \lambda_L)$ is the calibration constant determined at reference height. A detailed description was given by [*Ansmann et al.*, 1992]. As particle extinction and backscatter coefficients are independently determined, the lidar ratio ($LR$) profile can be calculated. The information obtained through the extinction- and backscatter-related Angström exponent, $LR$ and depolarization profiles allow the atmospheric aerosol typing.

### 4.1.4 Elastic and inelastic retrieval uncertainties

The causes of uncertainties of lidar measurements are summarized below:

a) Lidar system: each component in the optical path contributes to errors in the detected signal.

b) Signal-to-noise ratio: it decreases with height so the uncertainty increases with distance from the instrument.

c) Pre-processing: background and dark current subtraction, dead time, overlap and trigger delay corrections and averaged profiles (see Section 4.1.1).

Despite of the pre-processing required for the retrieval of lidar measurements, this step introduces uncertainties to the retrieved optical properties. For example, overestimation of the background signal can lead to negative values of the lidar signal which are physically unrealistic.

d) Retrieval: in both elastic and Raman inversion cases a reference value is required. Molecular extinction (calculated by means of temperature and pressure profiles) and molecular lidar ratio are also required in the case of elastic retrieval and spectral dependence has to be assumed in the case of Raman retrieval. All of these assumed or estimated values introduces uncertainties in $\alpha$ and $\beta$.

More information were given by *Preissler* [2012]. Using a common error propagation (linear or non-linear) considering all the sources of uncertainties listed above can lead to unrealistically high uncertainties of $\beta$, $\alpha$ and $LR$. Thus, the Monte Carlo technique was used for more realistic error estimation. This procedure is based on the random extraction of new lidar signals, each bin of which is considered a sample element of a given probability distribution with the experimentally observed mean value and standard deviation. Monte Carlo technique uses normal and Poisson distributions for AN and PC lidar measurements, respectively. The extracted lidar signals are then processed with the same algorithm to produce a set of solutions from which the standard deviation is calculated as a function of height. This standard deviation profile is the error profile of the derived optical property [*Ansmann et al.*, 1992; *Pappalardo et al.*, 2004; *Guerrero-Rascado et al.*, 2008a]. Typically, relative errors of $\beta$ derived with Raman and Klett-Fernald method are less than 15%, 20%, respectively, and relative errors of $\alpha$ derived with Raman is 25%.

### 4.1.5 Lidar measurements expressed in terms of Stokes-Müller formulism

As introduced in Section 2.5, Stokes-Müller formulism is a very useful tool to describe and analyse the polarization state of light and the different polarization processes. Thus, the study of the depolarization calibration and the polarizing sensitivity of lidar systems are performed by means of this formulism. This way of studying the polarization for lidar applications started in recent years [*Flynn et al.*, 2007; *Freudenthaler et al.*, 2009; *Hayman and Thayer*, 2009; 2012].

Lidar systems can be subdivided in functional blocks: laser, laser emitting optics (beam expander, steering mirrors), receiving optics (telescope, collimator, dichroic mirrors…), and polarizing splitter including the detectors as it is schematized in Figure 4-4. Multiplying the laser beam Stokes vector ($I_L$) by each functional block Müller matrix:

$$I_S = \eta_S M_S R_y M_o F M_E I_L \qquad \text{Eq. 4-5}$$

where the reflected (R) and transmitted (T) signals, noted by $I_S$, $S = \{R, T\}$, is obtained. $M_E$, $F$, $M_o$ and $M_S$ are the Müller matrices of the laser emitting optics, atmosphere, receiving optics and polarizing beam splitter, respectively, summarized in Appendix B: Müller matrices. Also, $\eta_S$ is the gain factor of the photomultipliers and $R_y$ refers to the axial rotation which allows the measurements with the polarizing beam splitter (PBS) in two configurations: 0° (y=1) and 90° (y=-1). If measurements are performed at an axial rotation angle of 0°, the transmitted and reflected signal corresponds to the parallel and perpendicular signals respect to the polarized plane of the laser, respectively, and oppositely with an axial rotation angle of 90°. Considering the cross-talk effect, the axial rotation angle of 90° is the best option as: first, commercial PBS usually presents better reflectance (~0.995) than transmittance (~0.95);

second, the parallel signal is stronger than the perpendicular one. Thus, the contamination of the perpendicular signal is lower if the parallel signal is split using the reflectance. Thus, the nominal axial rotation angle used for VELETA and MULHACEN is 90°.

Finally, the depolarization calibrator can also be considered as function block, **C**, and hence, a similar expression can be found for the calibration measurements:

$$I_S = \eta_S M_S R_y C M_o F M_E I_L \qquad \text{Eq. 4-6}$$

where the Müller matrix of **C** depends on its type (e.g., rotator or linear polarizing filter). The calibration method is analysed in detail in Chapter 5.

Particularly, laser light emitted by lidar systems is an almost-perfect linear polarized light. Therefore, the Stokes vector of the laser beam, $I_L$, is:

$$I_L = I_L \begin{pmatrix} 1 \\ a_L \\ 0 \\ 0 \end{pmatrix} \qquad \text{Eq. 4-7}$$

where $I_L$ is the laser intensity and $a_L$ is the depolarization parameter of the laser. In case of an almost-perfect linear polarized light, $a_L \sim 1$.

For the atmosphere, which can be modelled as a volume of randomly oriented, non-spherical particles with rotation and reflection symmetry, the Müller matrix **F** can be written as:
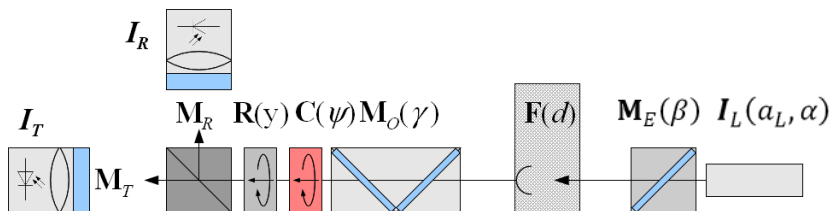


**Figure 4-4: Lidar scheme based on functional blocks (from [*Freudenthaler*, 2014]).**

$$F = \begin{pmatrix} F_{11} & 0 & 0 & 0 \\ 0 & F_{22} & 0 & 0 \\ 0 & 0 & -F_{33} & 0 \\ 0 & 0 & 0 & -F_{44} \end{pmatrix} = F_{11} \begin{pmatrix} 1 & 0 & 0 & 0 \\ 0 & a & 0 & 0 \\ 0 & 0 & -a & 0 \\ 0 & 0 & 0 & (2a-1) \end{pmatrix} \qquad \text{Eq. 4-8}$$

with $F_{33} = F_{22}$ and $a$ is the polarization parameter defined by:

$$a = \frac{F_{22}}{F_{11}} \qquad \text{Eq. 4-9}$$

and

$$F_{44} = F_{11} - 2F_{22} = F_{11}(1 - 2a) \qquad \text{Eq. 4-10}$$

Assuming an ideal behaviour of laser emitting optics (i.e., $M_E$ = identity matrix), an example of Stokes-Müller formulism can be the interaction of pure linear polarized light and the atmosphere resulting a partially polarized light, $I_{out}$, as follows:

$$I_{out} = FI_L = F_{11} \begin{pmatrix} 1 & 0 & 0 & 0 \\ 0 & a & 0 & 0 \\ 0 & 0 & -a & 0 \\ 0 & 0 & 0 & (2a-1) \end{pmatrix} I_L \begin{pmatrix} 1 \\ 1 \\ 0 \\ 0 \end{pmatrix} = F_{11}I_L \begin{pmatrix} 1 \\ a \\ 0 \\ 0 \end{pmatrix} \qquad \text{Eq. 4-11}$$

where the aerosol backscatter coefficient is related to the $F_{11}$ element and the volume linear polarization ratio $\delta'$ is related to $a$ through the elements $F_{11}$ and $F_{22}$:

$$\delta' = \frac{F_{11} - F_{22}}{F_{11} + F_{22}} \qquad \text{Eq. 4-12}$$

$$a = \frac{F_{22}}{F_{11}} \qquad \text{Eq. 4-13}$$

$$\delta' = \frac{1 - a}{1 + a} \qquad \text{Eq. 4-14}$$

The Stokes-Müller formulism introduced in this section will be very useful in Chapters 5 and 6 to study the depolarization calibration and the polarizing sensitivity of the lidar systems.

### 4.1.6   Depolarization retrieval

In Section 2.4, the main depolarization concepts were introduced and, among them, the definition of the volume linear depolarization ratio ($\delta'$) (Eq. 2-22). However, *Freudenthaler* [2014] presents a general equation to retrieve the volume linear depolarization ratio, $\delta'$, which in addition to correcting the influence of the gain of the photomultipliers, also includes the correction of the polarizing effects of the hardware through the parameters $G_T$, $G_R$, $H_T$ and $H_R$:

$$\delta' = \frac{\delta^*(G_T + H_T) - (G_R + H_R)}{(G_R - H_R) - \delta^*(G_T - H_T)}$$

Eq. 4-15

with

$$\delta^*(y) = \frac{1}{\eta}\frac{I_R(y)}{I_T(y)}$$

Eq. 4-16

where $\eta$ is the depolarization calibration factor and $y$ indicates the two axial possible rotations: 0° or 90°. Particularly, both MULHACEN and VELETA use 90°. Assuming a suitable behaviour of $\boldsymbol{M}_E$ (i.e., identity matrix), no cross-talk in the PBS, and no rotational misalignment of the receiving optics, $G_T$, $G_R$, $H_T$ and $H_R$ can be written as:

$$G_T = 1 - D_o$$

Eq. 4-17

$$G_R = 1 + D_o$$

Eq. 4-18

$$H_R = (D_o + 1)c_{2\alpha}$$

Eq. 4-19

$$H_T = (D_o - 1)c_{2\alpha}$$

Eq. 4-20

These parameters only depend on the effective diattenuation of the receiving optics ($D_o$) and the rotational misalignment of the polarizing plane of the laser with respect to the incident plane of the PBS ($\alpha$). Then, substituting expressions from Eq. 4-16 to Eq. 4-20 in Eq. 4-15 results in the new equation to retrieve $\delta'$:

$$\delta' = \frac{\eta \frac{I_R}{I_T}(y)\left(\frac{1-D_o}{1+D_o}\right)tan^2\alpha - 1}{tan^2\alpha + \eta \frac{I_R}{I_T}(y)\left(\frac{1-D_o}{1+D_o}\right)}$$

Eq. 4-21

The experimental determination of $\delta'$ depends on the depolarization calibration method and thus will be presented in Chapter 5. Finally, once $\delta'$ is retrieved, the particle linear depolarization ratio, $\delta^p$, can be retrieved using Eq. 2-22.

### 4.1.7 INDRA (Interface for Depolarization and Raman Analysis)

As it has been detailed in previous sections, the lidar technique requires a complex processing of the signal which can be grouped in pre-processing (Section 4.1.1) and elastic, inelastic and depolarization retrievals (Sections 4.1.2, 4.1.3 and 4.1.6). The complexity and number of the operations would be unapproachable by hand, and hence, the software implementation of the pre-processing and the retrieval algorithms was initialized by *Guerrero Rascado* [2008] and improved by *Navas Guzmán* [2011]. After more than 5 years of development and implementation of these algorithms, a graphical user interface has been developed including the new deliverables produced since then. This interface is called INDRA: *Interface for Depolarization and Raman Analysis*. In Figure 4-5, a screenshot of INDRA with the analysis of a real case is shown. The last version of this software, INDRA 4.1.8 includes the elastic, inelastic and depolarization retrieval as well as the error bars calculus. Another tool saves the retrieved optical profiles following the EARLINET protocol. These procedures are available for MULHACEN and VELETA data. A detailed tutorial of INDRA is included in Appendix A: Software.
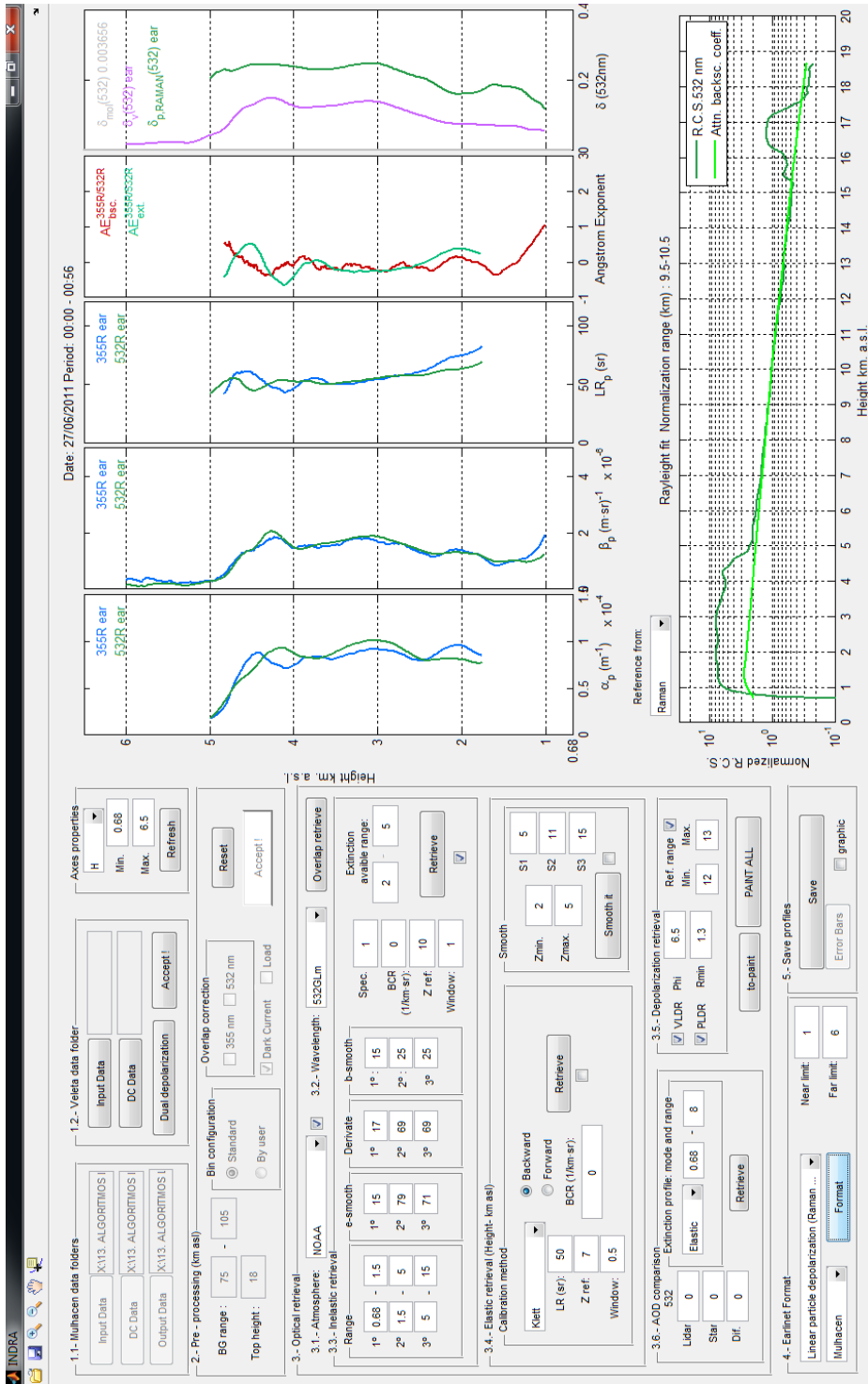
**Figure 4-5: Screenshot of INDRA with an example of inelastic and depolarization retrieval.**

## 4.2 Polarizing Lidar Photometer Networking (POLIPHON)

The Polarizing Lidar Photometer Networking (POLIPHON) is a technique which allows the retrieval of the mass concentration of each component of an external mixture of two aerosol types [*Shimizu et al.*, 2004; *Tesche et al.*, 2009a]. First, the method makes use of lidar observations of $\beta$ and $\delta^p$ (532 nm) and requires an opposite depolarizing capability for each aerosol type (strong and weak $\delta^p$ (532 nm), $\delta_s^p$ and $\delta_w^p$, respectively). Then, POLIPHON separates the particle backscatter contributions: $\beta$ of the weak and strong depolarizing aerosol ($\beta_w$ and $\beta_s$) as follows:

$$\beta_s = \beta \cdot \frac{\left(\delta^p - \delta_s^p\right)}{\left(\delta_s^p - \delta_w^p\right)} \frac{\left(1 - \delta_w^p\right)}{\left(1 - \delta^p\right)} \qquad \text{Eq. 4-22}$$

$$\beta_w = \beta - \beta_s \qquad \text{Eq. 4-23}$$

This separation method is outlined in detail by *Tesche et al.* [2009a]. Once the separation is performed, the weak and strong depolarizing capability is linked to the fine and coarse mode of the volume size distribution and thus, the mass concentration of the strong depolarizing aerosol [µg/m$^3$] is given by:

$$m_s = \rho_s \frac{C_s}{AOD_s} \beta_s LR_s \qquad \text{Eq. 4-24}$$

where $\rho_s$ and $LR_s$ are the particle mass density [µg/m$^3$] and the lidar ratio [sr] of the strong depolarizing capability aerosol. The ratio $C_s/AOD_s$, also called mean extinction-to-mass conversion factor [µg$^3$/µg$^2$], represents the ratio of volume concentration to AOD for the coarse mode. Following a similar procedure, the mass concentration of the weak depolarizing capability aerosol can be retrieved.

This technique is applied in Chapter 8 to retrieve the mineral dust mass concentration in a mixture of dust and anthropogenic aerosol.

## 4.3 Aerosol intensive properties

From the aerosol properties derived with the aforementioned instrumentation, some other optical and physical properties can be calculated as summarized in Table 4-5. The AOD-related Angström exponent in the wavelength range from $\lambda_1$ to $\lambda_2$, $\mathring{a}_{AOD}(\lambda_1 - \lambda_2)$, allows the analysis of the spectral dependence of AOD. The AOD-related Angström exponent increases with decreasing particle size and takes values around 2 when the scattering process is dominated by fine particles, while it is close to 0 when the scattering process is dominated by coarse particles [*Seinfeld and Pandis*, 1998; *Dubovik et al.*, 2002; *Schuster et al.*, 2006]. Similarly, different Angström exponents $\mathring{a}(\lambda_1 - \lambda_2)$ are defined related to β, α, and $\sigma_{sca}$ with different combinations of $\lambda_1$ and $\lambda_2$.

**Table 4-5: Aerosol optical and physical properties derived from optical properties. Properties are dimensionless except lidar ratio of which units are [sr]. Wavelength units are [nm].**

| Property | Symbol/Equation | |
|---|---|---|
| AOD-related Angström exponent | $\mathring{a}_{AOD}(440 - 675) = -\dfrac{ln(AOD(440)/AOD(675))}{ln(440/675)}$ | Eq. 4-25 |
| $\sigma_{sca}$-related Angström exponent | $\mathring{a}_{sca}(450 - 700) = -\dfrac{ln(\sigma_{sca}(450)/\sigma_{sca}(700))}{ln(450/700)}$ | Eq. 4-26 |
| α, β-related Angström exponent | $\mathring{a}_{\alpha,\beta}(355 - 532) = -\dfrac{ln(\alpha,\beta(355)/\alpha,\beta(532))}{ln(355/532)}$ | Eq. 4-27 |
| Simple scattering albedo | $\omega(\lambda) = \dfrac{\sigma_s(\lambda)}{\sigma_s(\lambda) + \sigma_a(\lambda)}$ | Eq. 4-28 |
| Particle lidar ratio | $LR(\lambda) = \dfrac{\alpha(\lambda)}{\beta(\lambda)}$ | Eq. 4-29 |
| Particle linear depolarization ratio | $\delta^p = -\dfrac{\delta'(1 + \delta^m)R - \delta^m(1 + \delta')}{(1 + \delta^m)R - (1 + \delta')}$ | Eq. 4-30 |

The particle lidar ratio, *LR*, is independently retrieved using night-time lidar measurements. This property depends on the size distribution, refractive index and particle shape [*Mishchenko et al.*, 1997; *Ackermann*, 1998]. Large LR values are associated with highly light-absorbing particles while low LR values

are indicative of non-light-absorbing particles [*Franke and Collins*, 2003; *Müller et al.*, 2003; *Navas-Guzmán et al.*, 2013].

Finally, the particle linear depolarization ratio ($\delta^p$), which was introduced in Section 2.4 (Eq. 2-17 and Eq. 2-22), provides information about the particle shape. Large $\delta^p$ values are related to non-spherical particles (e.g., mineral dust, ash) and vice versa (e.g., sulphates and nitrates).

## 4.4  Parcel method: determination of the mixing layer height

The parcel method[12] [*Holzworth*, 1964] determines the mixing layer height where the potential temperature profiles coincides with the potential temperature at surface. This is based on a hypothetical parcel of air, lifted from the surface, would be in equilibrium with its environment at this height (see Figure 4-6). The parcel method can be used only under convective scenarios.
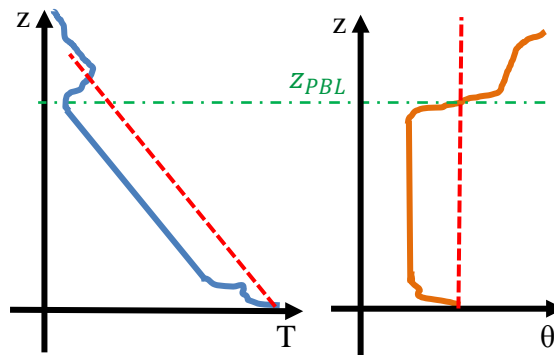


**Figure 4-6: Scheme of the parcel method using the temperature, T, and the potential temperature, θ, profiles. The blue line is a given temperature profile, the orange lines is its potential temperature and the red dashed line represents the dry adiabatic temperature at surface. The height at which the potential temperature profile takes the value of the potential temperature at surface (green dash-dot line) is the $z_{PBL}$.**

---

[12] It is also known as *Holzworth method* in honor of its discoverer: Holzworth, G. C. (1964), Estimate of mean maximum mixing depths in the contiguous United States, *Mon Weather Rev*, *92*(5), 235-242.

The resulting PBL height ($z_{PBL}$) is commonly used in air pollution and dispersion studies to estimate the dilution of a pollutant released within the boundary layer.

This method depends strongly on the surface temperature [*Seibert et al.*, 2000] and a high uncertainty may occur in situations without a clear inversion at the convective boundary layer top.

The uncertainty of the mixing layer height depends on the vertical resolution of the temperature profile, and the stability of the surface temperature. Additionally, the temperature profile might be in the lower part of a thermal or in the downward phase of a convective loop. Considering these uncertainty sources, a boundary layer height uncertainty of ±100 m is estimated.

# 5 Calibration and determination of lidar depolarization ratios

It is well known that the laser light is polarized and that its interaction with gases, aerosol particles and clouds induces some depolarization which depends on the shape and size of the scatterers. The depolarization lidar technique makes use of this phenomenon by different approaches [*Cairo et al.*, 1999]. Different depolarization definitions are issued by the lidar community, where the linear volume depolarization ratio ($\delta'$, Eq. 2-15) is one of the most frequently used.

Various phenomena have been studied by polarization lidar, such as hydrometeors, clouds and polar stratospheric clouds [e.g., *Schotland et al.*, 1971; *Cho et al.*, 2008; *Ansmann et al.*, 2009; *Córdoba-Jabonero et al.*, 2013]. On the other hand, the different degrees of depolarization in combination with other optical properties allow the characterization of atmospheric aerosol such as biomass burning aerosol and Saharan dust [*Murayama et al.*, 2004; *Gross et al.*, 2011a].

At present, the scientific community considers the use of polarization lidar as a key for climate-related cloud and aerosol studies. However, the linear volume depolarization ratio takes into account the induced depolarization both by molecules and particles (Eq. 2-15). Thus, the study of the atmospheric aerosol particles requires a different variable that depends exclusively on the particle shape and size, i.e. the particle volume depolarization ratio ($\delta^p$). This variable is derived from the combination of the $\delta'$, $\beta$ and $\beta_{mol}$ as shown in Eq. 2-17. $\beta$ can be estimated through the Klett-Fernald algorithm [*Fernald et al.*, 1972; *Klett*, 1981; *Fernald*, 1984; *Klett*, 1985] or the Raman method [*Ansmann et al.*, 1992].

As shown in Eq. 2-17, $\delta'$ requires a calibration factor of the instrument ($\eta$). Different calibration methods have been proposed. Some of them use the theoretical value of molecular depolarization [*Cairo et al.*, 1999]. Others are

designed to determine the instrumental gain factor between the perpendicular and parallel polarization photodetectors in order to calculate directly the relative amplification factor. Some of these methods are based on the use of optical components like half-wave plates or polarization filters [*Álvarez et al.*, 2006; *Snels et al.*, 2009] or the Δ90°-calibration method with a rotator which does not need any additional optical device [*Freudenthaler et al.*, 2009]. In both MULHACEN and VELETA lidar systems operated at the Granada station, the Δ90°-calibration method with a rotator in front of the polarizing beam splitter (PBS) was implemented. Subsequently, a new mode of the Δ90°-calibration method was set up in MULHACEN. This new mode uses a linear polarizing filter (hereafter, polarizer) in front of the receiving optics.

In this chapter, the Δ90°-calibration method using a rotator in front of the PBS (Section 5.1) and using a polarizer in front of the receiving optics (Section 5.2) are described. Finally, we present two methods to determine the value of the effective diattenuation of the receiving optics and the misalignment angle of the laser polarizing plane with respect to the incident plane of the polarizing beam splitter.

## 5.1 Δ90°-calibration method: rotator in front of the polarizing beam splitter

This method was initially developed by *Freudenthaler et al.* [2009] as the ±45°-calibration method and then improved to the Δ90°-calibration by *Freudenthaler* [2014]. The aim of this calibration is to correct the influence of the instrument on the depolarization measurements through the determination of the depolarization calibration factor ($\eta$) introduced in Section 2.4. This factor is directly related to the relative amplification factor of the

photomultipliers that measures the reflected and transmitted signal, R-PMT and T-PMT. Hereafter, the subscripts R and T make reference to the reflected and transmitted signal. As the PMTs are located behind the PBS (see Figure 5-1), R-PMT and T-PMT gains are influenced by the cross-talk caused by the transmission parameters of the PBS, and thus:

$$\eta = \frac{\eta_R T_R}{\eta_T T_T} \qquad \qquad \text{Eq. 5-1}$$

where $T_R$ and $T_T$ are reflecting and transmitting transmittance of the PBS. In order to determine $\eta$, the Δ90°-calibration method uses two measurements in which the calibrator is rotated at the position $\Psi_1$ and $\Psi_2$ around the nominal axial rotation with $|\Psi_2 - \Psi_1| = 90°$. Specifically in the case of VELETA and MULHACEN, the calibration measurements are performed rotating the PBS around the axial rotation by +45° and -45°. As the nominal axial rotation angle is 90° (y=-1 in the Stokes-Müller formulism), the calibration measurements are performed at 135° and 45°. The angle uncertainty is around 0.1° due to the fixing system with pins. In order to simplify the notation, $\Psi$ is written as $x45° + \varepsilon$ where $x = \pm1$ and $\varepsilon$ is linked to the 0.1° of rotational misalignment uncertainty. In Figure 5-2, the calibration positions are indicated. Once the calibration measurements are obtained:

$$\boldsymbol{I}_S(y, \varepsilon) = \eta_S \boldsymbol{M}_S \boldsymbol{R}_y \mathbf{R}(x45° + \varepsilon) \boldsymbol{M}_o \boldsymbol{F} \boldsymbol{M}_E \boldsymbol{I}_L \qquad \qquad \text{Eq. 5-2}$$

the measured calibration factor, $\eta^*$, can be calculated by:
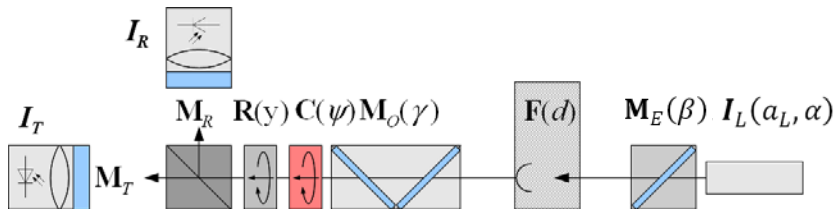


**Figure 5-1: Lidar scheme based on functional blocks (from *Freudenthaler* [2014]).**
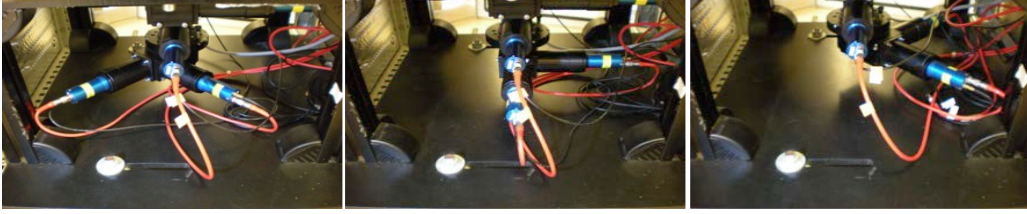
**Figure 5-2: Pictures illustrating the calibration procedure: normal position at 90° (center) and calibration positions at 45° (left) and 135° (right).**

$$\eta^*(x, y, \varepsilon) = \frac{I_R(y, x45° + \varepsilon)}{I_T(y, x45° + \varepsilon)} \qquad \text{Eq. 5-3}$$

However, the dependence of $\eta^*$ on $\varepsilon$ is very large as presented by *Freudenthaler et al.* [2009]. In order to decrease the influence of $\varepsilon$ on $\eta^*$, the geometric mean of the measurements performed at $(+45° + \varepsilon)$ and $(-45° + \varepsilon)$ is used:

$$\eta^*_{\sqrt{\pm}}(y, \varepsilon) = \sqrt{\eta^*(y, +45° + \varepsilon)\eta^*(y, -45° + \varepsilon)} \qquad \text{Eq. 5-4}$$

In fact, assuming a suitable behaviour of $\boldsymbol{M}_E$ (i.e., identity matrix) and a cleaned PBS ($\boldsymbol{M}_S^{\#}$, see Appendix C), it can be obtained that:

$$\eta^*_{\sqrt{\pm}}(y, \varepsilon) = \eta^{\#} \qquad \text{Eq. 5-5}$$

where the superscript # only indicates that a cleaned PBS was assumed. This procedure was discussed in detail by *Freudenthaler* [2014].

Besides $\eta$ is a single number, $\eta^*_{\sqrt{\pm}}$ is a constant profile equal to $\eta$. Furthermore, $\eta^*_{\sqrt{\pm}}$ must be independent of the aerosol load and the depolarization capability of the aerosol as it can be derived from Eq. 5-5. Therefore, in order to check the reliability of the calibration, the height independence of $\eta^*_{\sqrt{\pm}}$ and the effect of the aerosol load or the depolarization capability on $\eta^*_{\sqrt{\pm}}$ are analysed. As indicated in Section 3.2, measurements are obtained in analog (AN) and photo-counting (PC) mode which can be glued

(GL) as indicated in Section 4.1.1.5. Thus, the analysis is performed taking into account both modes and the glued signal.

An example of $\eta^*_{\sqrt{\mp}}$ profiles of MULHACEN and VELETA measured on 9 January 2014 and 19 March 2012, respectively, are shown in Figure 5-3. As can be seen, AN and PC $\eta^*_{\sqrt{\mp}}$ profiles are height-independent in the near and far range, respectively, as expected. In this sense, the PC $\eta^*_{\sqrt{\mp}}$ profile is not height-independent below 1.5 km asl because the strong detected signal causes non-linear response in the PC detection mode. Besides, the AN $\eta^*_{\sqrt{\mp}}$ profile is
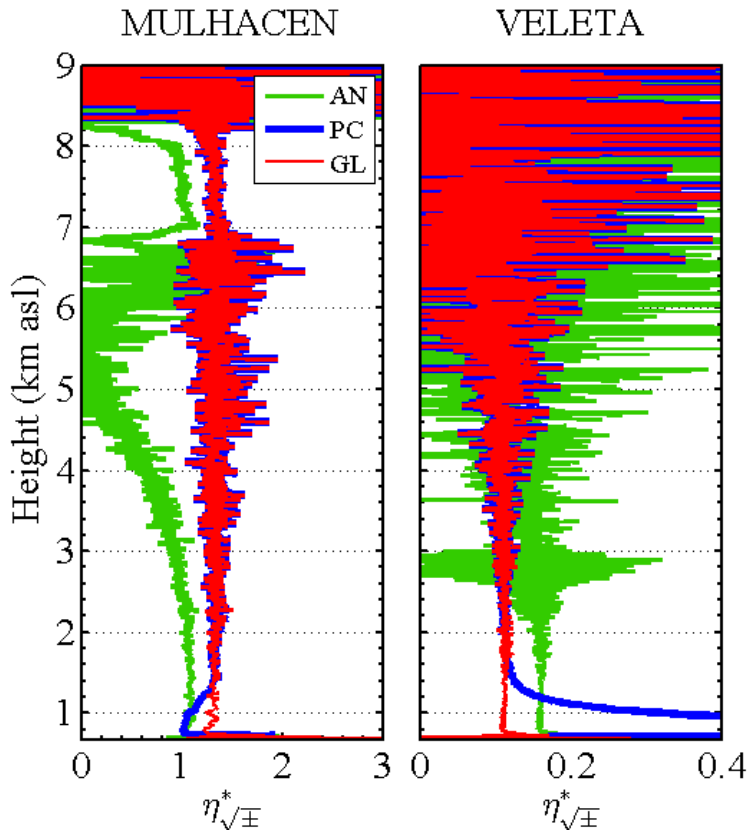


**Figure 5-3: Examples of the measured calibration factor profiles retrieved by means of the Δ90°-calibration method with a rotator in front of the polarizing beam splitter for MULHACEN (left) and VELETA (right). Profiles corresponds to different signals: analog (green), photon-counting (blue) and glued (red).**

not height-independent in altitudes higher than 2 km asl. This is because the AN mode requires strong received signal (e.g., aerosol layers or clouds). Supporting this explanation, both AN and PC $\eta_{\sqrt{\pm}}^*$ present a height-independent behaviour in the cloud detected in the range 7.2-8.0 km asl due to the good signal-to-noise ratio in presence of a cirrus cloud (Figure 5-3 right). In order to avoid the height-dependent profile due to the mode of detection (AN or PC), the glued signal (GL) is used. In both cases shown in Figure 5-3, the height-independent range of the GL $\eta_{\sqrt{\pm}}^*$ profiles cover almost the whole range between surface and 9 km asl. Thus, it can be concluded that $\eta_{\sqrt{\pm}}^*$ is height-independent. In order to provide a single value from the $\eta_{\sqrt{\pm}}^*$ profile, a height range is selected to compute a $\eta_{\sqrt{\pm}}^*$ mean, noted by $\langle \eta_{\sqrt{\pm}}^* \rangle_M$, where M can be AN, PC and GL detection mode.

The following analyses in this section were performed for both MULHACEN and VELETA. As similar results were obtained, only the MULHACEN analysis will be shown.

As $\langle \eta_{\sqrt{\pm}}^* \rangle_{AN}$ and $\langle \eta_{\sqrt{\pm}}^* \rangle_{PC}$ must be independent of the aerosol load and particle type, both $\langle \eta_{\sqrt{\pm}}^* \rangle_{AN}$ and $\langle \eta_{\sqrt{\pm}}^* \rangle_{PC}$ are retrieved in two regions: the aerosol layer near to the surface (1.2-2.2 km asl for AN and 1.8-3 km asl for PC) and the cloud at 7.1-7.9 km. $\langle \eta_{\sqrt{\pm}}^* \rangle_{AN}$ ($\pm$ standard deviation) is 1.07±0.02 in the range near the surface and 1.00±0.05 in the cloud and $\langle \eta_{\sqrt{\pm}}^* \rangle_{PC}$ ($\pm$ standard deviation) is 1.34±0.05 in both ranges. As can be seen, the differences of $\langle \eta_{\sqrt{\pm}}^* \rangle_{AN}$ and $\langle \eta_{\sqrt{\pm}}^* \rangle_{PC}$ between the aerosol layer near to the surface and the cloud are negligible for both modes. Therefore, $\eta_{\sqrt{\pm}}^*$ remains constant when the aerosol load and/or particle type changes. This test can be used as an indicator of quality of the lidar measurements. In fact, this calibration method was

implemented for the first time in the quality assurance of EARLINET as it was aforementioned in Section 3.3.3.

The height independence of $\eta^*_{\sqrt{\mp}}$ with the aerosol load and the aerosol depolarization capability has been demonstrated but, as it was previously indicated, AN $\eta^*_{\sqrt{\mp}}$ is constant with height only in a height range where the SNR is large enough. Thus, $\langle\eta^*_{\sqrt{\mp}}\rangle_{AN}$ depends on the minimum height and the height range to calculate the mean. For analysing this influence, different $\langle\eta^*_{\sqrt{\mp}}\rangle_{AN}$ are calculated using a constant minimum height and varying the average range. For this purpose, we use calibration data measured on 26 August 2011. As can be seen in Figure 5-4, when the height range increases, $\langle\eta^*_{\sqrt{\mp}}\rangle_{AN}$ shows a small decreasing trend. In fact, $\langle\eta^*_{\sqrt{\mp}}\rangle_{AN}$ values calculated from the range 1.75-3 km are 3% smaller than $\langle\eta^*_{\sqrt{\mp}}\rangle_{AN}$ calculated in the range 1.75-8 km. Therefore, the lower height range is better suitable to avoid the aerosol-free region, where
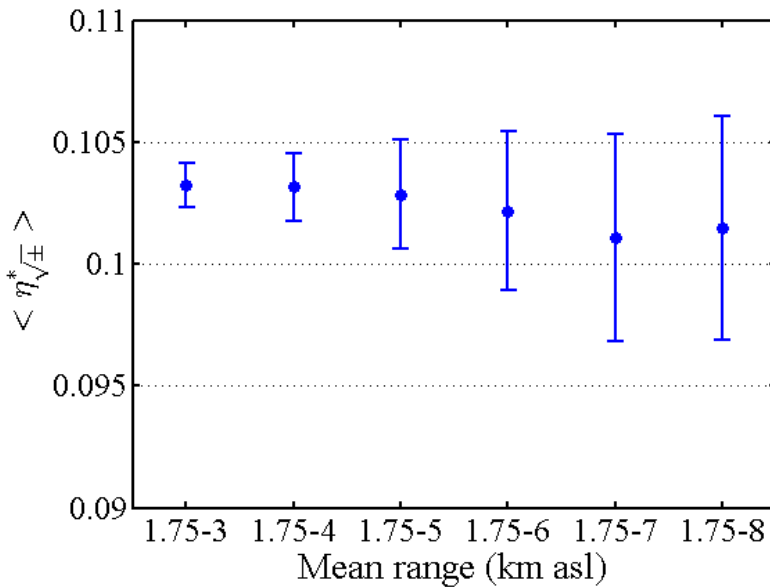


**Figure 5-4: Mean and standard deviation of $\eta^*_{\sqrt{\mp}}$ (dimensionless) averaged in different ranges for a MULHACEN calibration performed on 26 August 2011.**

SNR decreases. However, in order to decrease the noise influence on $\langle \eta^*_{\sqrt{\pm}} \rangle_{AN}$, the selected range should be large enough. Thus, we propose that the mean value of $\eta^*_{\sqrt{\pm}}$ should be computed using a 1-km range below 4 km asl. In this way we can guarantee a low standard deviation of $\langle \eta^*_{\sqrt{\pm}} \rangle_{AN}$.

The calibration measurements at ±45° are performed periodically to follow changes associated to the required modifications in the setup of the instrument. As the atmospheric variations between these calibration measurements would affect the results, the calibration is performed during stable atmospheric conditions and the time of each measurement has to be as short as possible. In this sense, the optimal time interval needs to be analysed as well. For this purpose, $\eta^*_{\sqrt{\pm}}$ has been measured with time intervals of 3, 4 and 6 minutes in the same calibration procedure. Then, $\langle \eta^*_{\sqrt{\pm}} \rangle$ and the standard deviation was calculated resulting in the same values, 0.231±0.003, for all the intervals. This result indicates that $\langle \eta^*_{\sqrt{\pm}} \rangle$ is not influenced by the temporal changes of the aerosol load during calibration procedures using short periods. Thus, the 3-min interval has been selected to determine $\langle \eta^*_{\sqrt{\pm}} \rangle$. In addition, it is necessary to reduce the background signal and thus, the night-time measurements are recommended. In fact, during night-time the standard deviation of $\langle \eta^*_{\sqrt{\pm}} \rangle_{PC}$ is around 50% lower than during daytime.

As photomultiplier gain changes with the applied voltage, it is expected that the depolarization calibration also changes. This fact is clearly visible in Figure 5-5, where AN $\eta^*_{\sqrt{\pm}}$ profiles vary for different voltage combinations. The relationship between AN $\eta^*_{\sqrt{\pm}}$ and the applied voltages can be determined using the potential dependence between the PMT gain ($\eta_S$) and the applied voltage ($V_S$),

$$\eta_S = \zeta_S V_S^{k_S} \qquad\qquad \text{Eq. 5-6}$$

where $\zeta_S$ and $k_S$ are the parameters that define the potential dependence. Assuming that $k_R = k_T$ and solving $\eta_S$ in Eq. 5-5, AN $\eta^*_{\sqrt{\mp}}$ can be written as:

$$\eta^*_{\sqrt{\mp}} = \frac{T_R}{T_T} \frac{\zeta_R}{\zeta_T} \left(\frac{V_R}{V_T}\right)^k \qquad\qquad \text{Eq. 5-7}$$

Applying the logarithm to the previous equation, we obtain a linear dependence between $log\left(\eta^*_{\sqrt{\mp}}\right)$ and $log\left(\frac{V_R}{V_T}\right)$:

$$log\left(\eta^*_{\sqrt{\mp}}\right) = log\left(\frac{T_R}{T_T} \frac{\zeta_R}{\zeta_T}\right) + k \cdot log\left(\frac{V_R}{V_T}\right) \qquad\qquad \text{Eq. 5-8}$$
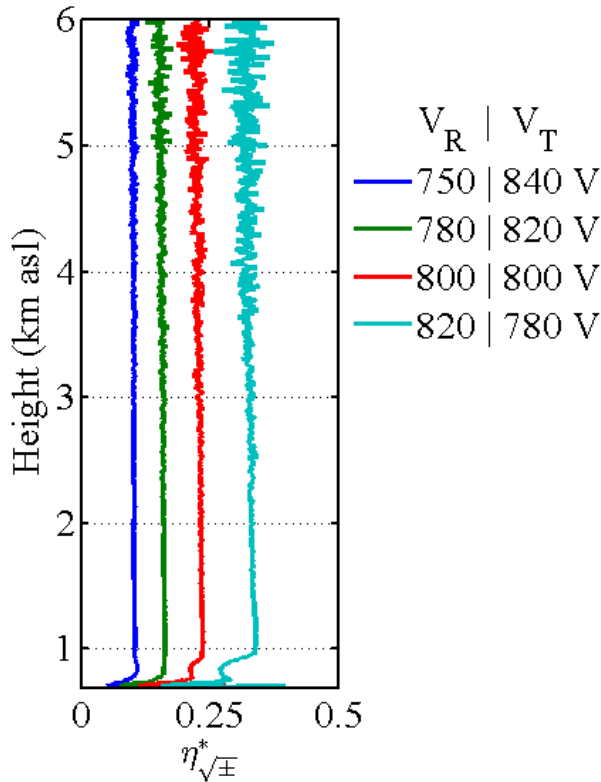


**Figure 5-5: AN $\eta^*_{\sqrt{\mp}}$ profiles measured with different voltage combinations for $V_R$ (voltage for the reflected signal) and $V_T$ (voltage of the transmitted signal).**

In order to perform a linear fit, $log(\langle\eta^*_{\sqrt{\mp}}\rangle_{AN})$ was calculated for the four different calibrations presented in Figure 5-5. The result is shown in Figure 5-6. As can be seen, there is a clear linear dependence between the AN $\eta^*_{\sqrt{\mp}}$ and the ratio of applied voltages. This fitting allows the determination of $\langle\eta^*_{\sqrt{\mp}}\rangle_{AN}$ for any voltage combination. Unfortunately, non-linear behaviour was found for $\langle\eta^*_{\sqrt{\mp}}\rangle_{PC}$.

In order to estimate the reproducibility of the power dependence, $\langle\eta^*_{\sqrt{\mp}}\rangle_{AN}$ values retrieved following the calibration procedure at different dates during 6 months and those computed using Eq. 5-8 were compared. As can be seen in Figure 5-7, the points are scattered along the 1:1 line (slope = 0.994±0.004 with $R^2 = 0.999$). In most cases, the differences between the estimated and measured $\langle\eta^*_{\sqrt{\mp}}\rangle_{AN}$ are less than 10% and clearly below the standard deviation. Therefore, the reproducibility of the depolarization calibration is considerably high. However, due to the possible degradation of the coating of optical devices and the gain of the PMTs, it is recommended to perform the depolarization
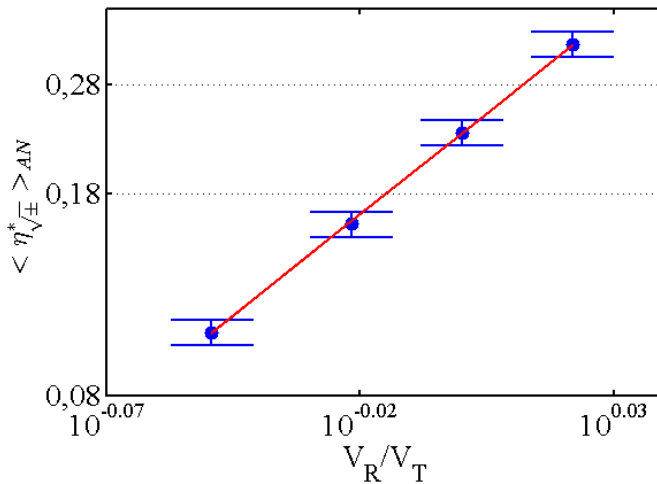


**Figure 5-6: Linear fit ($R^2$=0.9987) using Eq. 5-8 with different combination of voltages. Error bars have been neglected for $V_R/V_T$.**
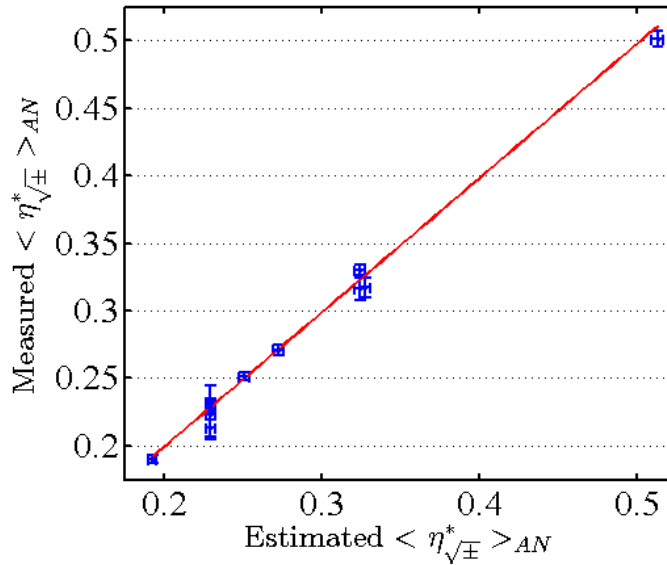
**Figure 5-7: Comparison between the measured and estimated $\langle \eta^*_{\sqrt{\pm}} \rangle_{AN}$. Red line depicts the linear fit along the 1:1 line ($R^2$=0.9987).**

calibration every three months.

## 5.2 Δ90°-calibration method: polarizer in front of the receiving optics

After the Δ90°-calibration using a rotator in front of the PBS was explained and analysed, in this section the Δ90°-calibration using a polarizer in front of the receiving optics is presented. This mode of the Δ90°-calibration was installed in MULHACEN after the calibration in order to determine the influence of the receiving optics.

In this case, the procedure to retrieve the relationship between $\eta^*_{\sqrt{\pm}}$ and $\eta^*$ is similar to the previous one excluding the calibration measurements, $\boldsymbol{I_S}$, using the following equation in Stokes-Müller formulism

$$\boldsymbol{I_S}(y,\varepsilon) = \eta_S \boldsymbol{M_S R_y M_o M_P}(x45° + \varepsilon)\boldsymbol{F M_E I_L} \qquad \text{Eq. 5-9}$$
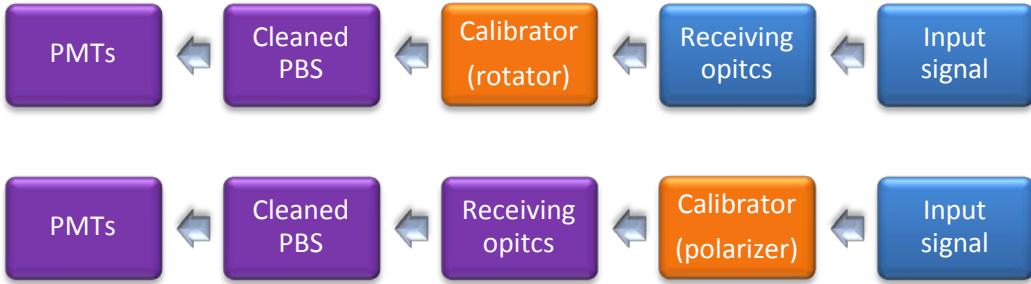
**Figure 5-8: Calibration lidar setup. Blue boxes are related to the non-calibrated functional blocks, orange boxes are the calibrators and purple boxes are the functional blocks calibrated by the Δ90°-calibration modes. Arrows indicates the lidar signal direction.**

where $\boldsymbol{M}_P$ is the Müller matrix of a linear polarizing filter (polarizer, see Appendix B: Müller matrices). Following the same steps as in the previous section and assuming that there is not rotational misalignment of the receiving optics, the expression $\eta^*_{\sqrt{\pm}}$ is:

$$\eta^*_{\sqrt{\pm}}(y, \varepsilon) = \eta^\# \frac{1 - yD_o}{1 + yD_o} \qquad \text{Eq. 5-10}$$

with the dependence of $\eta^*_{\sqrt{\pm}}$ of the effective diattenuation of the receiving optics, $D_o$. The Δ90°-calibration method with the rotator in front of the PBS corrects the influence of the photomultiplier gains and the cross-talk of the PBSs, whereas in the case of using a polarizer in front of the receiving optics, the influence of the diattenuation of the receiving optics is additionally corrected. Therefore, these results indicate that the Δ90°-calibration method allows the correction of the polarizing influence of the functional blocks after the calibrator as it is illustrated in Figure 5-8. In those cases where $D_o$ can be neglected, both calibration modes are equivalent.

## 5.3 Determination of the effective diattenuation of the receiving optics

The diattenuation of dichroic mirrors used in the receiving optics is not usually provided in the technical specification. Additionally, it is not a parameter optimized by manufacturers to keep it close to zero. Therefore, $D_o$ should not be generally assumed as zero and hence, it has to be determined. To this aim, a new method has been developed by means of both calibration modes of the $\Delta 90°$-calibration method. From Eq. 5-4 and Eq. 5-9, $\langle \eta^*_{\sqrt{\pm}} \rangle$ can be determined with the rotator, $\langle \eta^*_{\sqrt{\pm}} \rangle^{rot}$, and the polarizer, $\langle \eta^*_{\sqrt{\pm}} \rangle^{pol}$, as follows:

$$\langle \eta^*_{\sqrt{\pm}} \rangle^{pol} = \langle \eta^*_{\sqrt{\pm}} \rangle^{rot} \frac{1 - yD_o}{1 + yD_o} \qquad \text{Eq. 5-11}$$

where $y = -1$ as MULHACEN's nominal axial rotation is 90°. Then, solving the equation for $D_o$:

$$D_o = \frac{\langle \eta^*_{\sqrt{\pm}} \rangle^{pol} \Big/ \langle \eta^*_{\sqrt{\pm}} \rangle^{rot} - 1}{\langle \eta^*_{\sqrt{\pm}} \rangle^{pol} \Big/ \langle \eta^*_{\sqrt{\pm}} \rangle^{rot} + 1} \qquad \text{Eq. 5-12}$$

the effective diattenuation of the receiving optics is experimentally determined. This method is advantageous for two reasons: firstly, it doesn't require dismounting of the optical system of the lidar which could cause a misalignment, and secondly, it allows the correction of the previous calibrations which were performed only with the rotator in front of the PBS. In this sense, the old calibration $\langle \eta^*_{\sqrt{\pm}} \rangle_{old}^{rot}$ can be corrected by:

$$\langle \eta^*_{\sqrt{\pm}} \rangle_{new}^{rot} = \langle \eta^*_{\sqrt{\pm}} \rangle_{old}^{rot} \frac{1 + D_o^{exp}}{1 - D_o^{exp}} \qquad \text{Eq. 5-13}$$

where *new* and *old* subscripts indicates respectively the recalculated and old calibration value, and $D_o^{exp}$ is the experimental value determined for $D_o$. Following the procedures above, we can guarantee the correct depolarization calibration of MULHACEN since April 2010, when the $\Delta90°$-calibration method was implanted. For VELETA the $\Delta90°$-calibration method was set up during the manufacturing process and thus the depolarization is correctly calibrated since its initial deployment in March 2011.

## 5.4 Determination of misalignment angle of the laser polarizing plane with respect to the incident plane of the polarizing beam splitter

As introduced in Eq. 5-3, the measured calibration factor, $\eta^*(x, y, \varepsilon)$, depends on the rotational misalignment, $\varepsilon$, the calibration locations ($\pm45°$; x=$\pm1$) and the axial rotation angle ($0°$ and $90°$) noted by $y = \pm1$. For the particular case of MULHACEN (rotator in front of the PBS, axial rotation angle at $90°$, no rotated receiving optics and cleaned PBS), $\eta^*$ can be expressed as follows:

$$\eta^*(x, \varepsilon) = \eta \frac{1 + d'D_o c_{2\alpha} - x\left(D_o s_{2\varepsilon} + d'\left(s_{2(\varepsilon-\alpha)} + W_o s_{2\alpha} c_{2\varepsilon}\right)\right)}{1 + d'D_o c_{2\alpha} + x\left(D_o s_{2\varepsilon} + d'\left(s_{2(\varepsilon-\alpha)} + W_o s_{2\alpha} c_{2\varepsilon}\right)\right)} \qquad \text{Eq. 5-14}$$

where the following notation has been used:

$$sin(2\alpha) \equiv s_{2\alpha}$$

$$cos(2\alpha) \equiv c_{2\alpha}$$

and α is the misalignment angle of the laser polarizing plane with respect to the incident plane of the PBS. As can be seen, $\varepsilon$ and $\alpha$ are related in this equation, indicating that a misalignment angle of the calibration angle can compensate the misalignment angle of the laser. This relationship can be used to determine $\alpha$

through known values of $\varepsilon$. To this goal, it is worthy to rewrite the Eq. 5-14 substituting the term $(1 + d'D_o c_{2\alpha})$ with $A$:

$$\eta^*(x, \varepsilon) = \eta \frac{A - x\left(D_o s_{2\varepsilon} + d'\left(s_{2(\varepsilon-\alpha)} + W_o s_{2\alpha} c_{2\varepsilon}\right)\right)}{A + x\left(D_o s_{2\varepsilon} + d'\left(s_{2(\varepsilon-\alpha)} + W_o s_{2\alpha} c_{2\varepsilon}\right)\right)} \qquad \text{Eq. 5-15}$$

In the special case of $\varepsilon = \alpha$,

$$\eta^*(x, \varepsilon = \alpha) = \eta \frac{A - x\left(D_o + \frac{1}{2} d' W_o\right) s_{2\alpha}}{A + x\left(D_o + \frac{1}{2} d' W_o\right) s_{2\alpha}} \qquad \text{Eq. 5-16}$$

Therefore $\eta^*(+45°, \varepsilon = \alpha)$ and $\eta^*(-45°, \varepsilon = \alpha)$ are different only due to the term $\left(D_o + \frac{1}{2} d' W_o\right) s_{2\alpha}$. However, considering that $A \geq 1$ and that low values of $\alpha$ means $\left(D_o + \frac{1}{2} d' W_o\right) s_{2\alpha} \ll 1$, it can be assumed that,

$$\eta^*(x, \varepsilon = \alpha) = \eta \frac{A - x\left(D_o + \frac{1}{2} d' W_o\right) s_{2\alpha}}{A + x\left(D_o + \frac{1}{2} d' W_o\right) s_{2\alpha}} \sim \eta \frac{A}{A} = \eta \qquad \text{Eq. 5-17}$$

and thus:

$$\eta^*(+45°, \varepsilon = \alpha) = \eta^*(-45°, \varepsilon = \alpha) \qquad \text{Eq. 5-18}$$

Therefore, the experiment consists in performing calibration measurements at ±45° with different $\varepsilon$ angles until obtain the same $\eta^*$ profile at $\left(+45°, \varepsilon_{exp}\right)$ and $\left(-45°, \varepsilon_{exp}\right)$ and thus, $\alpha = \varepsilon_{exp}$. The procedure to determine
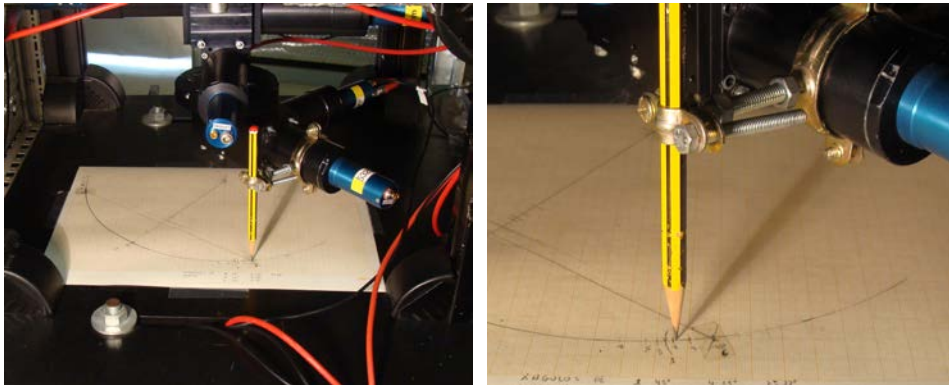


**Figure 5-9: New procedure developed to measure the ε angle.**

107
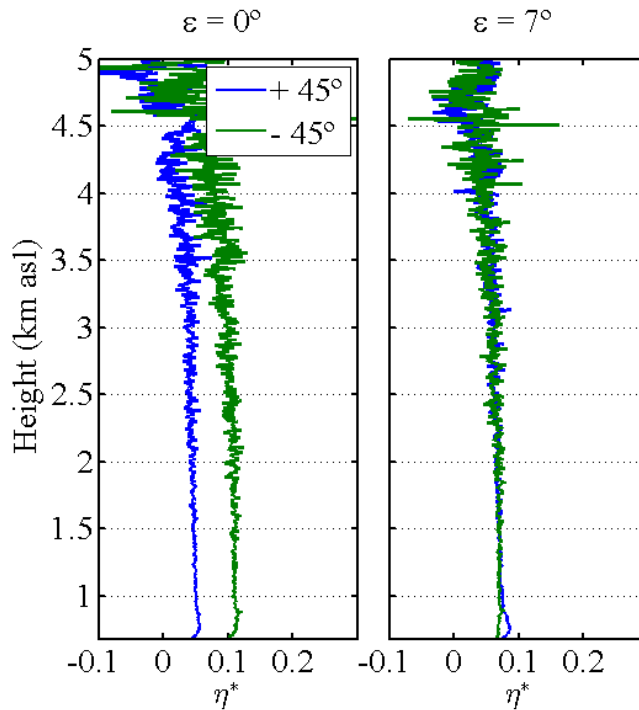
**Figure 5-10:** $\eta^*(+45°)$ **(blue) and** $\eta^*(-45°)$ **(green) profiles at** $\varepsilon = 0°$ **(left) and** $\varepsilon = 7°$ **(right). According to Eq. 5-18,** $\eta^*(+45°)$ **and** $\eta^*(-45°)$ **coincides for** $\varepsilon = \alpha$ **(right).**

the values of ε is shown in Figure 5-9. Unfortunately, this procedure was possible in MULHACEN. VELETA design does not allow the measurement of ε angles and thus, α was only determined for MULHACEN.

In Figure 5-10, $\eta^*(\pm 45°, \varepsilon = 0°)$ and $\eta^*(\pm 45°, \varepsilon = 7°)$ are shown. As can be seen, when $\varepsilon = 7°$ both $\eta^*(+45°)$ and $\eta^*(+45°)$ are equal. Therefore, the misalignment angle of the laser polarizing plane with respect to the incident plane of the PBS, α, was experimentally determined at $7°\pm1°$.

## 5.5 Determination of the volume linear depolarization ratio

In this chapter, two modes of the Δ90°-calibration method has been presented as well as the experimental determination of the effective diattenuation of the receiving optics, $D_o$, and the misalignment angle of the

laser polarizing plane with respect to the incident plane of the PBS, $\alpha$. In Section 4.1.6, the equation of $\delta'$ was introduced (Eq. 4-15). However, this equation must be rewritten depending on the depolarization calibration method.

In the case of the $\Delta 90°$-calibration method with a rotator in front of the PBS, it is necessary to substitute $\eta$ by $\langle \eta_{\sqrt{\pm}}^* \rangle^{rot}$:

$$\delta'(y) = \frac{\langle \eta_{\sqrt{\pm}}^* \rangle^{rot} \frac{I_R}{I_T}(y) \left( \frac{1 - D_o}{1 + D_o} \right) tan^2 \alpha - 1}{tan^2 \alpha + \langle \eta_{\sqrt{\pm}}^* \rangle^{rot} \frac{I_R}{I_T}(y) \left( \frac{1 - D_o}{1 + D_o} \right)} \qquad \text{Eq. 5-19}$$

Therefore, it is necessary to experimentally derive $D_o$ and $\alpha$ or assume their values. In the case of the $\Delta 90°$-calibration method with a polarizer in front of the receiving optics, it is necessary to use the Eq. 4-22 to obtain:

$$\delta'(y) = \frac{\langle \eta_{\sqrt{\pm}}^* \rangle^{pol} \frac{I_R}{I_T}(y) tan^2 \alpha - 1}{tan^2 \alpha + \langle \eta_{\sqrt{\pm}}^* \rangle^{pol} \frac{I_R}{I_T}(y)} \qquad \text{Eq. 5-20}$$

where it is only necessary to determine $\alpha$ by means of the calibration procedure presented in Section 5.4. In the case of MULHACEN, $D_o = 0.35 \pm 0.02$ and $\alpha = 7° \pm 1°$ have to be used depending on the measured calibration factor available whereas for VELETA, $D_o = 0$ and $\alpha = 0°$ values are assumed.

## 5.6   Concluding remarks

In summary, the $\Delta 90°$-calibration method with a rotator in front of the PBS was presented in this chapter as the new depolarization calibration procedure for both MULHACEN and VELETA. The methodology includes in detail the steps to obtain the measured depolarization calibration factor. The $\Delta 90°$-calibration method was analysed and some indications to successfully perform the calibration were provided.

By means of the combination of two modes of the $\Delta90°$-calibration method (rotator in front of the PBS and polarizer in front of the receiving optics), the influence of the effective diattenuation of the receiving optics was determined and calculated. In addition, a new procedure to determine the misalignment angle of the laser polarizing plane with respect to the incident plane of the PBS was presented. Both methods were applied only to MULHACEN because VELETA's design does not allow the measurement of $\varepsilon$ angles and the calibration in front of the receiving optics. During the process, certain functional blocks or properties has been assumed as suitable. In the next Chapter 6, the influence of these assumptions is analysed, quantified and included in the $\delta'$ uncertainty assessment.

# 6 Depolarization uncertainties

As introduced in Chapter 1, lidar depolarization measurements are becoming a very important tool for typing the atmospheric aerosol [*Gross et al.*, 2011a] and improving the retrieval of microphysical properties [*Granados-Muñoz et al.*, 2014]. The most relevant properties derived from the lidar depolarization measurements are the volume ($\delta'$) and particle ($\delta^p$) linear depolarization ratios. In terms of uncertainties, both properties are different as the volume linear depolarization ratio is retrieved directly from the lidar measurements whereas the particle linear depolarization ratio is a secondary product as shown in Section 2.4.

According to the error model described by *Grabe* [2005], measurement uncertainties are caused by the normally[13] distributed random errors and the unknown systematic errors. In the case of $\delta'$, random errors are determined by means of the Monte Carlo technique (Section 4.1.4). Additionally, uncertainty range of $\delta'$ due to the unknown systematic errors ($U_\delta$) can be estimated by means of a simulation of the hardware polarizing sensitivity. In this sense, for the first time, $U_\delta$ is quantified in detail by means of the simulator *Lidar polarizing sensitivity simulator* (LPSS).

First, $U_\delta$ is assessed for a synthetic lidar setup including the possible ways to reduce the systematic errors for each functional block. Then, $U_\delta$ of MULHACEN and VELETA lidar systems are presented. Once $U_\delta$ is determined, the uncertainty of $\delta^p$ due to $U_\delta$ is derived following the general error theory.

---

[13] In lidar measurements, the distribution depends on the measurement mode: analog or photon-counting. See Section 4.1.4 for further details.

## 6.1 Description of the Lidar Polarizing Sensitivity Simulator (LPSS)

As introduced by *Freudenthaler* [2014], the setup of a lidar system can be subdivided in functional blocks: laser, laser emitting optics (beam expander, steering mirrors), receiving optics (telescope, collimator, dichroic mirrors…), and the polarizing beam splitter including the detectors. In addition, the depolarization calibrator must be considered as function block. In Figure 6-1, a scheme is depicted with the functional blocks of a lidar system.

The Lidar Polarizing Sensitivity Simulator (LPSS) has been developed based on the work by *Freudenthaler* [2014] in order to simulate the hardware polarizing sensitivity of the volume linear depolarization ratio, $\delta'$. As input data, LPSS uses a set of lidar properties and an uncertainty range for each property. In addition, $\delta'$ of the atmosphere is assumed to be height-independent and known, $\delta'_r$. The measurement is simulated following equations Eq. 4-5 and Eq. 4-6 shown in Section 4.1.5.

There are different types of calibrations depending on the element used (e.g., polarizer, rotator) and the calibration can be located at different places (e.g., rotator in front of the PBS or in front of the receiving optics). Thus, LPSS has been developed to simulate the most used depolarization calibration methods.
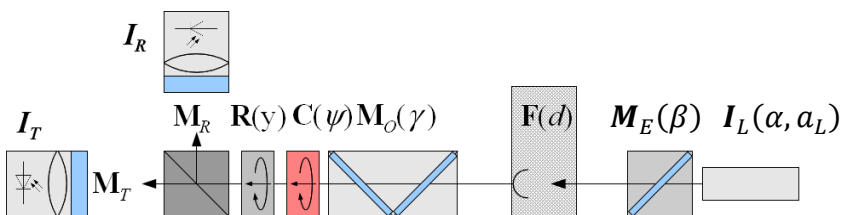


**Figure 6-1: Lidar scheme based on functional blocks (from *Freudenthaler* [2014]).**

LPSS retrieves the volume linear depolarization ratio, $\delta'_s$ (subscript indicates that it is the output value retrieved by simulator), varying the value of a certain property (e.g., effective diattenuation of the receiving optics) within its uncertainty range (e.g., [–0.1, 0.1]) keeping other parameters constant. The $\delta'$ systematic error due to this property uncertainty ($E_\delta$) is given by the absolute difference between $\delta'_s$, and $\delta'_r$ (subscript indicates that it is the input value sets as real by the simulator):

$$E_\delta = \delta'_s - \delta'_r \qquad \text{Eq. 6-1}$$

Accordingly, the $\delta'$ uncertainty range ($U_\delta$) is the minimum and maximum of $E_\delta$.

$$U_\delta = [min(E_\delta), max(E_\delta)] \qquad \text{Eq. 6-2}$$

Finally, the total $\delta'$ uncertainty of a lidar system is the sum in absolute terms of $U_\delta$ caused by each property uncertainty.

Some simplifications and assumptions are performed in the LPSS in order to simplify the simulation. As LPSS products use the perpendicular-to-parallel ratio, the intensity of the laser ($I_L$) and the gain of the photomultipliers ($\eta_S$) are set to 1. As can be derived from *Freudenthaler* [2014], a set of steering and dichroic mirrors can be modelled as a unique effective optical device with an effective diattenuation and a phase shift. In addition, the misalignment angles of the optical devices within a functional block are simplified by a misalignment angle of the whole functional block. The polarizing sensitivity of the Cassegrain telescope and lens used in lidar systems can be neglected according to ZEMAX simulations (Freudenthaler, personal communication).

## 6.2 Depolarization uncertainties according to functional blocks

In this Section, LPSS is used to simulate the $\delta'$ uncertainty of a synthetic lidar system due to the uncertainties in lidar properties that can influence the polarization state of the laser or the receiving signal. The uncertainties of these lidar properties have been derived or assumed from different technical specifications of commercial optical devices (Table 6-1). In some cases, the uncertainty ranges are very high (e.g., effective phase shift) as the knowledge about these properties uses to be poor. The $\Delta90°$-calibration method with a rotator in front of the PBS is used as calibrator.

**Table 6-1: Property values and uncertainties of the synthetic lidar system.**

| PROPERTY | | NAME | Value | Uncertainty |
|---|---|---|---|---|
| $I_L$ | $a_L$ | Parameter a of the laser | 0.90 | ±0.05 |
| | $\alpha$ | Misalignment angle of the polarizing plane of the laser[14] | 0° | ±1° |
| $M_E$ | $D_E$ | Effective diattenuation | 0 | ±0.1 |
| | $\Delta_E$ | Effective phase shift | 0° | ±180° |
| | $\beta$ | Effective misalignment angle[14] | 0° | ±1° |
| $M_o$ | $D_o$ | Effective diattenuation | 0 | ±0.1 |
| | $\Delta_o$ | Effective phase shift | 0° | ±180° |
| | $\gamma$ | Effective misalignment angle[14] | 0° | ±0.5° |
| C | $\varepsilon_r$ | Misalignment angle[14] | 0.1° | ±0.1° |
| $M_S$ | $T_p/R_p$ | Transmittance and reflectance for parallel[14] polarised light | 0.97/0.03 | ±0.01 |
| | $T_s/R_s$ | Transmittance and reflectance for perpendicular[14] polarised light | 0.001/0.999 | ±0.001 |

### 6.2.1 Functional block: Laser

Laser used in lidar systems generally produce linear polarized light. However, the purity of the polarization state of the laser light is usually unknown and

---

[14] With respect to the incident plane of the polarizing beam splitter.

thus, it is common to assume that the laser purity parameter $a$, $a_L$, is 1. From the point of view of the detection of aerosol and cloud vertical distribution, this uncertainty can be omitted. However, the parameter $a$ is crucial to provide quality depolarization results. In addition, the misalignment angle of the polarizing plane of the laser with respect to the incident plane of the PBS ($\alpha$) introduces an error in the depolarization measurements. This fact is because the parallel signal (with respect to the polarizing plane of the laser) will be split into two other polarizing components (parallel and perpendicular with respect to the
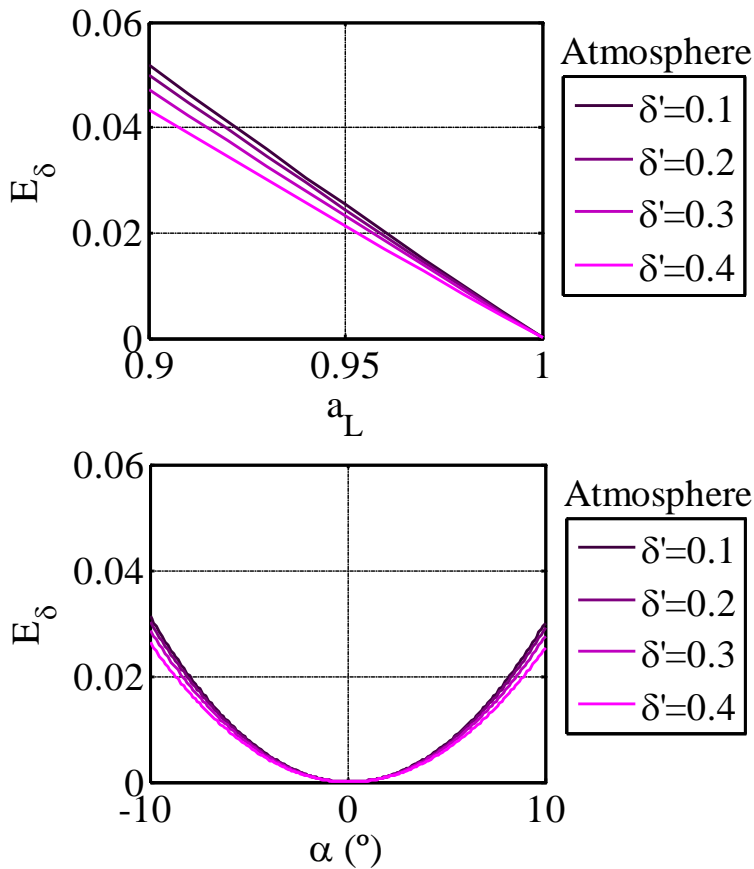


**Figure 6-2:** $E_\delta$ **depending on the parameter** $a$ **of the laser** ($a_L$) **(top) and the misalignment angle between the polarizing plane of the laser respect to the PBS incident plane** ($\alpha$) **(bottom).**

incident plane of the PBS).

As can be seen in Figure 6-2 (top), an uncertainty of 10% in $a_L$ (that is $a_L \in [0.9, 1]$), causes $U_\delta = [0, 0.05]$. This means that the relative error of $\delta'$ would be around 17% for mineral dust ($\delta'$=0.30) or 100% for biomass burning aerosol ($\delta'$=0.05). The misalignment angle between the polarizing plane of the laser with respect to the plane of the PBS, $\alpha$, affects the determination of $\delta'$ (Figure 6-2, bottom) although its influence ($U_\delta = [0, 0.03]$) is lower than $a_L$. $U_\delta$ due to $\alpha$ could be neglected if $\alpha$ is fixed in the range $0° \pm 3°$ or known with an uncertainty lower than 2%.

## 6.2.2 Laser emitting optics

The laser emitting optics, $\boldsymbol{M}_E$, is the first optical part of lidar systems. $\boldsymbol{M}_E$ usually leads the laser beam to the atmosphere and, optionally, includes beam expanders to decrease the laser beam divergence. Because the divergence depends on the wavelength, some multiwavelength lidar systems include dichroic mirrors in $\boldsymbol{M}_E$ to split the laser beam according to the wavelength and use different beam expanders for different wavelengths. Because the beam expanders are a set of lenses, it has been assumed that they do not cause any depolarizing influence as indicated in Section 6.1. Additionally, the set of steering and dichroic mirrors is considered as an effective optical device in order to simplify the analysis. The $\boldsymbol{M}_E$ properties are the effective diattenuation $D_E$ and phase shift, $\Delta_E$, and the angle $\beta$ which described the rotational misalignment of $\boldsymbol{M}_E$ with respect to the PBS incident plane.

The influence of $\beta$ is related to $D_E$ so that if the effective diattenuation is zero, $\beta$ does not produce any effect. In this sense, the analysis of $E_\delta$ according to $\beta$ is performed parameterizing $D_E$ in the range [–0.3, 0.3]. Following the Figure 6-3 (top), $E_\delta$ ranges between 0 and 0.001 (i. e., $U_\delta$=[0,0.001]) due to $\beta$
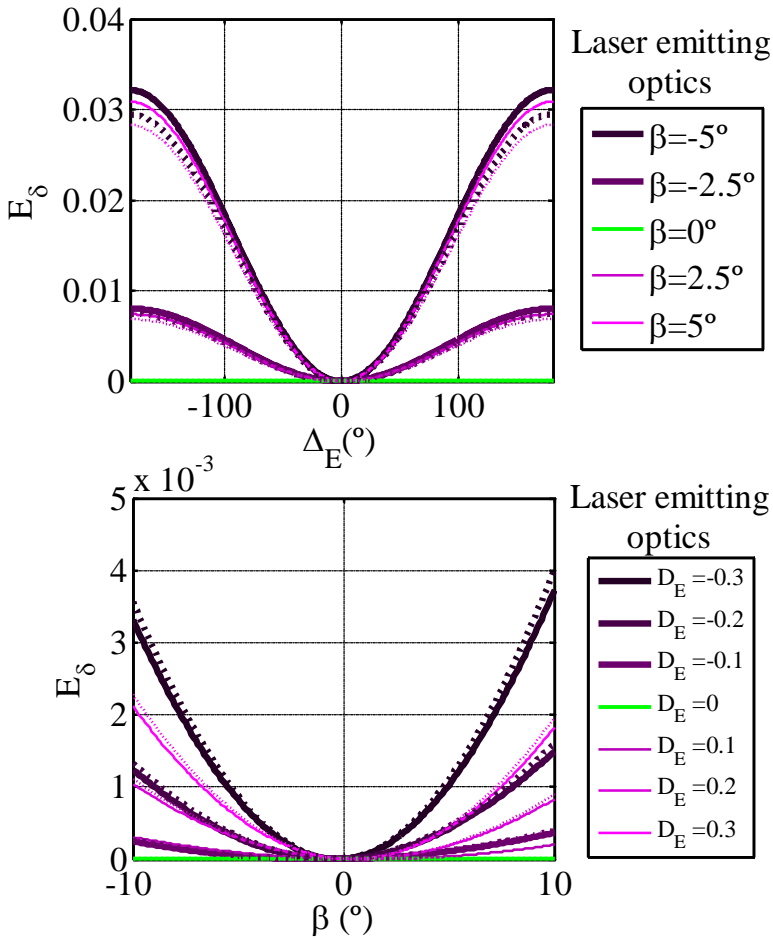
**Figure 6-3:** $E_\delta$ depending on $\Delta_E$ parameterized by $\beta$ (top) and $E_\delta$ depending on $\beta$ parameterized by $D_E$ (bottom). Solid and dot lines correspond to $\delta'$ values of 0.005 and 0.3, respectively.

and $D_E$ uncertainties, and considerably decreases with $D_E$. When $D_E = 0$, $E_\delta = 0$ independently of $\beta$ as it was indicated.

It is worthy to pay attention to the dependence of $E_\delta$ with $\Delta_E$ in order to analyse the relevance of $\beta$. The phase shift of steering and dichroic mirrors is generally unknown as the majority of the technical specifications do not provide this information and it is difficult to measure it. Hence, because the

119

knowledge on the phase shift is very low, $E_\delta$ is represented with respect to $\Delta_E$ for the range [-180°, 180°] and parameterized in terms of $\beta$ in Figure 6-3 (bottom). As can be seen, $E_\delta$ could be larger than 0.03 if $\beta$ is larger than 5° in absolute terms. Therefore, it is evident that the lack of information of $\Delta_E$ can lead to huge uncertainties.

Besides, Figure 6-3 shows $E_\delta$ depending on $\Delta_E$ and $\beta$, the influence of $\delta'$ on $E_\delta$ is also assessed. In this case, the simulations consider the $\delta'$ influence by means of two $\delta'$ values: 0.005 and 0.3 corresponding to the solid and dotted lines, respectively. From the results it can be concluded that the influence of $\delta'$ on $\boldsymbol{M}_E$ systematic errors can be neglected.

In summary, the total $U_\delta$ due to the uncertainty of $\boldsymbol{M}_E$ ($\beta$, $D_E$ and $\Delta_E$) is [0, 0.04]. In order to avoid this source, it is highly recommended to fix $\beta = 0°$ with a maximum $\beta$ uncertainty of $\pm 1.5°$ to keep $E_\delta$ below 0.001 independently of $\Delta_E$ and $D_E$.

### 6.2.3 Receiving optics

The properties of the receiving optics ($\boldsymbol{M_o}$) are the effective diattenuation $D_o$ and phase shift $\Delta_o$, and the misalignment angle between the receiving optics and the PBS incident plane, $\gamma$. As was explained in the previous section, $D_o, \Delta_o$ and $\gamma$ are related among them. However, the relationship between $\gamma$ and $D_o$ is very weak and thus, Figure 6-4 depicts $E_\delta$ versus $D_o$ and $E_\delta$ versus $\Delta_o$ parameterized by $\delta'$ and $\gamma$, respectively. Additionally, Figure 6-4 (right) presents the $\delta'$ influence by means of two $\delta'$ values: 0.005 and 0.3 corresponding to the solid and dotted lines, respectively.
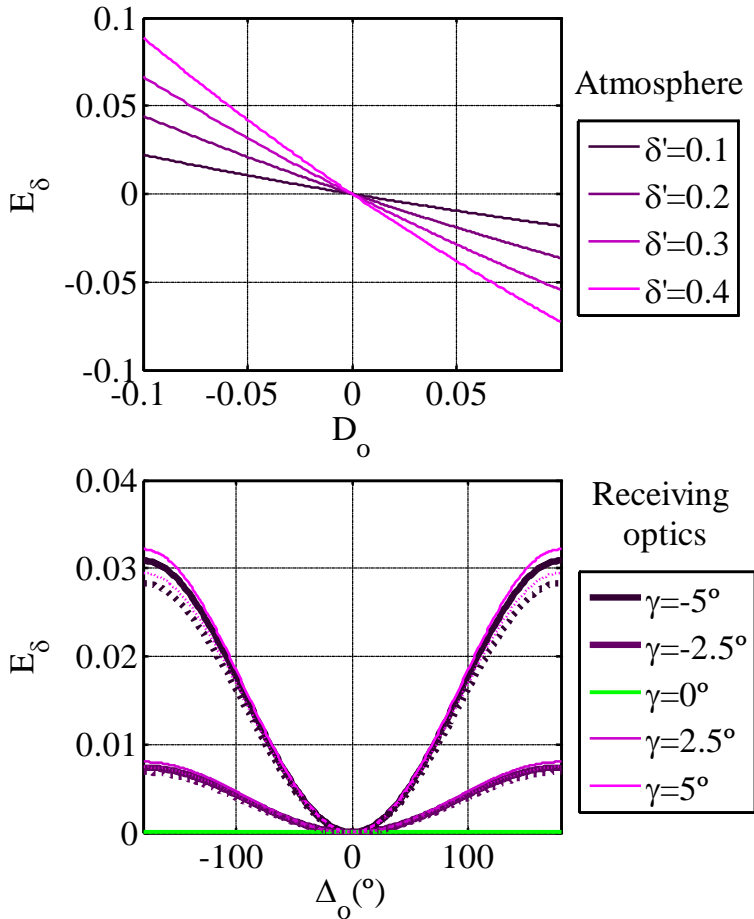
**Figure 6-4:** $E_\delta$ depending on $D_o$ (top) and $\Delta_o$ (bottom) parameterized by $\delta'$ and $\gamma$, respectively. Solid and dotted lines correspond to $\delta'$ values of 0.005 and 0.3, respectively.

According to Figure 6-4, $E_\delta$ considerably increases with $D_o$ reaching values around 0.09 for $D_o \sim 0.1$. Therefore, the effective diattenuation of the receiving optics has a large impact on the depolarization measurements. Additional simulations (not shown) revealed that $E_\delta$ is extremely high for $D_o$ larger than 0.15 in absolute terms. Additionally, it is worthy to note that negative values of $D_o$ causes larger $E_\delta$ than positive ones (e.g., $D_o = -0.05$ caused $E_\delta = 0.042$ whereas $D_o = +0.05$ leads to $E_\delta = -0.038$, both

considering $\delta'=0.3$). This is because the parallel signal is stronger than the perpendicular one. In the case of $D_o$, its uncertainty should be lower than $\pm 0.0017$ to keep $E_\delta$ lower than 0.001, which shows the demand for an extremely high precision. As shown in Chapter 5, there are calibrations correcting the influence of $D_o$ so this precision would not be necessary. Moreover, it is worthy to highlight that $E_\delta$ due to $D_o$ increases with $\delta'$. Thus, the influence of $D_o$ is especially relevant for atmospheric aerosol with high depolarization capability (e.g., mineral dust or volcanic ash).

As can be seen in Figure 6-3 (bottom) and Figure 6-4 (bottom), the dependence of $E_\delta$ due to the uncertainties in $\Delta_o$ and $\Delta_L$ presents a similar behaviour. Therefore, it can be concluded that it is highly recommended to fix $\gamma = 0°$ with a maximum uncertainty of $\pm 1°$ to keep $E_\delta$ below 0.001 independently of the value of $\Delta_o$. Summarising, $U_\delta$ due to the uncertainty of $\boldsymbol{M}_o$ properties ($\gamma$, $D_o$ and $\Delta_o$) would be [–0.07, 0.12]. Hence, this is the most critical functional block and thus, it is very important to carefully determine the properties $\gamma$ and $D_o$ of the receiving optics.

### 6.2.4  Influence of polarizing beam splitter

Polarizing beam splitter (PBS) split light into two orthogonally polarized beams at 90° to each other, the transmitted beam is ideally polarized parallel to the plane of incidence ($T_p = 1$), and the reflected beam is ideally polarized perpendicular to the plane of incidence ($R_s = 1$); therefore, $T_s = R_p = 0$. However, commercial PBS does not present a perfect behaviour and, consequently, part of the polarized perpendicular is transmitted and part of the polarized parallel is reflected. This phenomenon is called cross-talk and it has been previously studied [e.g., *Álvarez et al.*, 2006; *Freudenthaler et al.*, 2009; *Snels et al.*, 2009]. The $E_\delta$ due to the PBS transmission parameters depends on
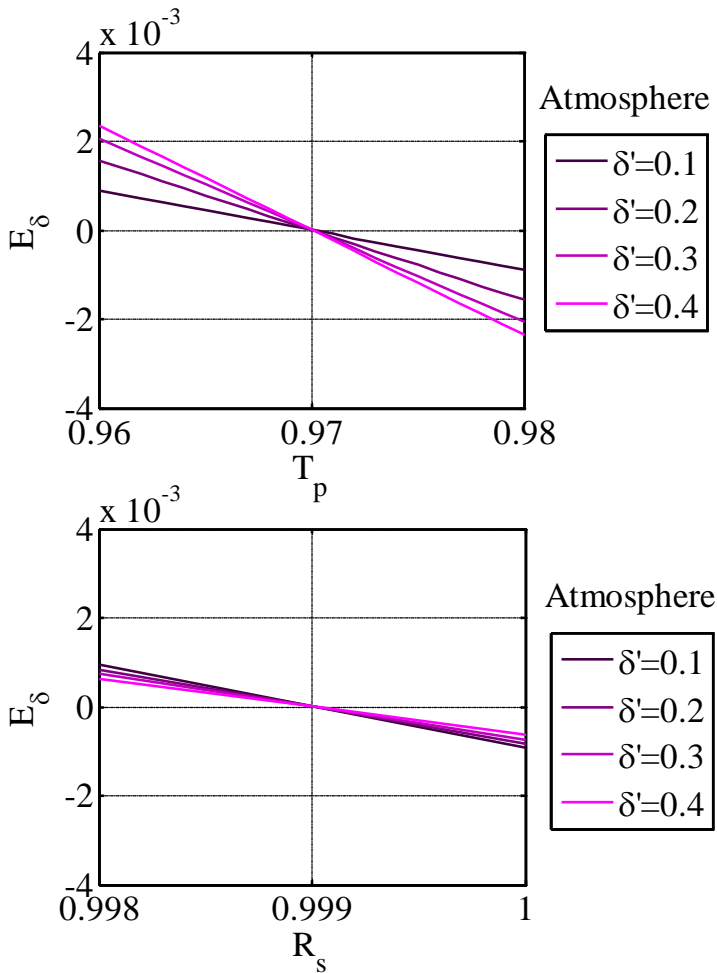
**Figure 6-5: $E_\delta$ depending on $T_p$ (top) and $R_s$ (bottom).**

the axial rotation angle of the measurements $[0°, 90°]$ as the PBS reflectance is usually larger than the PBS transmittance. Because of this, an axial rotation angle of $90°$ minimizes the contamination of the perpendicular signal due to the cross-talk and, thus, the axial rotation angle of the measurements was established at $90°$ for the synthetic lidar. As $T_p + R_p = 1$ and $T_s + R_s = 1$, uncertainties of transmittance and reflectance of each polarizing component are linked. Therefore, $E_\delta$ due to the uncertainties of $T_p$ and $R_p$ is the same. In

123

Figure 6-5, $E_\delta$ due to the uncertainties of $T_p(\pm 0.01)$ and $R_s(\pm 0.001)$ are shown. As can be seen, $U_\delta$ is larger due to the $T_p$ uncertainty than due to the $R_s$ uncertainty. However, $E_\delta$ presents the same order of magnitude despite of the relative uncertainty of $R_s$ (0.1%) is ten times lower than the relative uncertainty of $T_p$ (1%). Thus, the influence of $R_s$ is considerable larger than $T_p$. This is because the parallel signal intensity is larger than the perpendicular one and thus, the contamination of the perpendicular signal with a part of parallel signal intensity (e.g., 1%) is larger than contamination of the parallel signal with the same part of perpendicular signal. In order to avoid the cross-talk effect and the $U_\delta$ due to the PBS, *Freudenthaler* [2014] advices to include additional polarising elements behind the transmitting and reflecting sides of the PBS. This configuration allows the assumption of a perfect PBS and therefore it avoids this uncertainty source.

### 6.2.5   Influence of the Δ90°-calibration method

The Δ90°-calibration method is explained in detail in Chapter 5. In this case, the assessment is performed with a rotator as calibrator located in front of the PBS (see Figure 6-1). As can be seen in Figure 6-6, the misalignment angle of the rotator $\varepsilon_r$ in the range $\varepsilon_r \in [-5°, 5°]$ causes a $U_\delta$ of [0, 0.0002] and thus, it can be neglected. It is worthy to note that the uncertainty of $\varepsilon_r$ affects to the calibration measurements as well as the normal measurements. Therefore, the use of other elements for the calibration (e.g., polarizing filter, see Section 5.2) only affecting the calibration measurements would decrease the influence of $\varepsilon_r$. Despite the influence of the uncertainty of $\varepsilon$ is negligible, the Δ90°-calibration performed in front of the PBS presents problems when the diattenuation of the receiving optics, $D_o$, is unknown as it was indicated in the Chapter 5. Thus, the location of the calibrator must be taken into account when $U_\delta$ is studied.
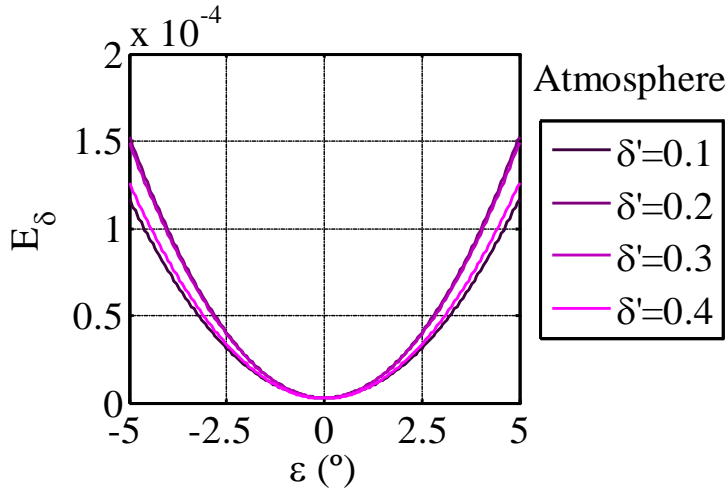
**Figure 6-6: $E_\delta$ depending on $\varepsilon_r$.**

### 6.2.6 Total uncertainty

In previous sections, the $\delta'$ systematic error $(E_\delta)$ due to property uncertainties of each functional block has been determined. Then, the total $U_\delta$ due to the lidar polarization sensitivity can be determined as the sum of the $U_\delta$ caused by each property uncertainty as it is presented in Table 6-2. As can be seen, the total $U_\delta$ is [–0.082, 0.243]. As typical $\delta'$ values are in the range 0.05-0.10 [e.g., *Murayama et al.*, 2004; *Gross et al.*, 2011a] for biomass burning aerosol and in the range 0.15-0.30 for mineral dust [e.g., *Gross et al.*, 2011a; *Bravo-Aranda et al.*, 2013], it can be concluded that the hardware polarization sensitivity can affect the depolarization results causing relative errors even larger than 100%.

The most critical properties are the purity parameter of the laser $(a_L)$ and the effective diattenuation of the receiving optics $(D_o)$ with a contribution to the total $U_\delta$ larger than 0.05. Next, $\Delta_E$, $\Delta_o$ and $\alpha$ are relevant lidar properties as well, contributing with 0.03 to the total $U_\delta$. It is worthy to note that the

125

uncertainty range is asymmetric being greater the positive deviation, and thus, it can be concluded that the lidar polarizing sensitivity usually overestimates $\delta'$.

Table 6-2: $U_\delta$ and lidar properties (value and uncertainty) of the synthetic lidar system.

| | Property | Reference | Uncertainty | $U_\delta$ |
|---|---|---|---|---|
| $I_L$ | $a_L$ | 0.90 | ±0.05 | 0, 0.05 |
| | $\alpha$ | 0° | ±1° | 0, 0.03 |
| $M_E$ | $D_E$ | 0 | ±0.1 | - |
| | $\Delta_E$ | 0° | ±180° | 0, 0.03 |
| | $\beta$ | 0° | ±1° | 0, 0.001 |
| $M_o$ | $D_o$ | 0 | ±0.1 | −0.07, 0.09 |
| | $\Delta_o$ | 0° | ±180° | 0, 0.03 |
| | $\gamma$ | 0° | ±0.5° | - |
| C | $\varepsilon_r$ | 0.1° | ±0.1° | 0, 0.001 |
| $M_S$ | $T_p/R_p$ | 0.97/0.03 | ±0.01 | ±0.002 |
| | $T_s/R_s$ | 0.001/0.999 | ±0.001 | ±0.009 |
| | | | TOTAL | −0.08, 0.24 |

$U_\delta$ can be reduced improving the accuracy of the lidar properties or improving the response of each functional block. In this sense, the laser beam ($I_L$) could be assumed as suitable if a high-energy polarizing filter is located between the emission and the laser emitting optics.

To decrease the $U_\delta$ due to $M_E$ and $M_o$ it is necessary to align the optical devices as well as possible being that the $M_E$ influence could be neglected and $M_o$ only would affect due to the $D_o$ uncertainty. In fact, the accuracy required for $D_o$ (±0.0017 for obtaining $E_\delta<0.001$) is very difficult to reach and thus lidar systems must be modified, for example, locating the calibration system in front of the receiving optics. The influence of the PBS due to the cross-talk can be removed using additional polarising elements behind the transmitting and reflecting sides of the PBS.

## 6.3 Depolarization uncertainties for MULHACEN and VELETA

Following the steps of the previous sections, $U_\delta$ has been determined for the MULHACEN and VELETA lidar systems. In Table 6-3 and Table 6-4, the values and uncertainties of the properties of each functional block, $U_\delta$ caused by each property and the total $U_\delta$ are presented for both lidar systems. As can be seen, the negative uncertainty is lower than the positive one. This fact, aforementioned in Section 6.2.6, is due to there are more properties contributing to overestimate $\delta'$. $U_\delta$ is lower for MULHACEN than for VELETA mainly due to the values of $D_o$ and $\alpha$ and their low uncertainties due to the new procedures developed to MULHACEN. The uncertainty ranges, presented in Table 6-3, should be considered as the maximum $U_\delta$ in which the real unknown systematic error is present.

Once $\delta'$ uncertainty has been retrieved, the uncertainty of the particle linear depolarization ratio, $\delta^p$, is retrieved through the general theory of error propagation applied to Eq. 2-22:

$$\Delta\delta^p = \left|\frac{\partial\delta^p}{\partial\delta'}\right|\Delta\delta' + \left|\frac{\partial\delta^p}{\partial R}\right|\Delta R + \left|\frac{\partial\delta^p}{\partial\delta^m}\right|\Delta\delta^m \qquad\text{Eq. 6-3}$$

The partial derivatives of this equation can be written as

$$\frac{\partial\delta^p}{\partial R} = \frac{\delta' - \delta^p}{(R-1) - (\delta' - \delta_m)} \qquad\text{Eq. 6-4}$$

$$\frac{\partial\delta^p}{\partial\delta'} = \frac{R + \delta^p}{(R-1) - (\delta' - \delta_m)} \qquad\text{Eq. 6-5}$$

$$\frac{\partial\delta^p}{\partial\delta_m} = \frac{\delta^p - 1}{(R-1) - (\delta' - \delta_m)} \qquad\text{Eq. 6-6}$$

**Table 6-3: Values and uncertainties of MULHACEN and $U_\delta$**

| Property | | MULHACEN | | |
|---|---|---|---|---|
| | | Reference | Uncertainty | $U_\delta$ |
| $I_L$ | $a_L$ | 0.9 | ±0.06 | −0.03, 0.03 |
| | $\alpha$ | 7° | ±1° | 0, 0.005 |
| $M_E$ | $D_E$ | 0 | ±0.1 | - |
| | $\Delta_E$ | 0° | ±180° | 0, 0.001 |
| | $\beta$ | 0° | ±1° | 0, $1\times10^{-6}$ |
| $M_o$ | $D_o$ | 0.35 | ±0.02 | $(-6, 15)\times10^{-7}$ |
| | $\Delta_o$ | 0° | ±180° | 0, 0.0001 |
| | $\gamma$ | 0° | ±0.5° | - |
| C | $\varepsilon_p$ | 0° | ±0.1° | $(-6.8, -5.5)\times10^{-7}$ |
| $M_S$ | $T_p/R_p$ | 0.97/0.03 | ±0.01 | ±0.002 |
| | $T_s/R_s$ | 0.001/0.999 | ±0.001 | ±0.009 |
| | | | TOTAL | −0.03, 0.05 |

**Table 6-4: Values and uncertainties of VELETA and $U_\delta$**

| Property | | VELETA | | |
|---|---|---|---|---|
| | | Reference | Uncertainty | $U_\delta$ |
| $I_L$ | $a_L$ | 1 | −0.1, 0 | 0, 0.05 |
| | $\alpha$ | 0° | ±10° | 0, 0.03 |
| $M_E$ | $D_E$ | 0 | ±0.1 | - |
| | $\Delta_E$ | 0° | ±180° | 0, 0.001 |
| | $\beta$ | 0° | ±1° | 0, $1\times10^{-6}$ |
| $M_o$ | $D_o$ | 0 | ±0.1 | −0.07, 0.09 |
| | $\Delta_o$ | 0° | ±180° | 0, $3\times10^{-6}$ |
| | $\gamma$ | 0° | ±0.2° | - |
| C | $\varepsilon_r$ | 0° | ±0.1° | 0, $30\times10^{-7}$ |
| $M_S$ | $T_p/R_p$ | 0.95/0.05 | ±0.01 | ±0.002 |
| | $T_s/R_s$ | 0.01/0.99 | ±0.01 | ±0.01 |
| | | | TOTAL | −0.08, 0.18 |

and thus,

$$\Delta\delta^p = \frac{|\delta' - \delta^p|\Delta R + |R + \delta^p|\Delta\delta' + |\delta^p - 1|\Delta\delta_m}{(R-1) - (\delta' - \delta_m)}$$

Eq. 6-7

where $\Delta\delta'$ and $\Delta R$ are the random errors of $\delta'$ and the backscattering ratio (R) computed by means of the Monte Carlo technique, and $\Delta\delta_m$ is assumed negligible. Besides, the influence of the $\delta'$ uncertainty due to the systematic error has been estimated to be in the range from 0.04 to 0.1 for low and high depolarization capability of the atmospheric aerosol (e.g., anthropogenic aerosols (~0.05) and mineral dust (~0.3), respectively). As $\Delta\delta^p$ due to systematic error is considered height- and time-constant perturbation is not depicted in graphics and thus, following the EARLINET protocol, only statistical errors are shown in Chapter 8.

## 6.4   Concluding remarks

In this chapter, the Stokes-Müller formulism was used to model the lidar polarizing response by means of the simulator LPSS. The applications of this software are: first, the detection of the main systematic error sources (e.g., the purity polarizing parameter and the effective diattenuation of the receiving optics); second, the determination of the $\delta'$ total uncertainty of lidar systems due to the systematic error due to the uncertainty of the different lidar properties. Particularly, the LPSS software was used to determine the $\delta'$ total uncertainty of MULHACEN and VELETA.

# 7 Planetary boundary layer detection by means of depolarization measurements

The planetary boundary layer (PBL) is defined as the part of the troposphere directly influenced by the Earth's surface, which responds to surface forcing with a time scale of about one hour or less [*Stull*, 1988]. The PBL is structured into different layers depending on the time of day. During daytime there is a mixing layer which height can be defined as the height up to which vertical dispersion by turbulent mixing takes place [*Seibert et al.*, 2000]. During night-time two layers are defined: the stable boundary layer, in direct contact with the surface, and the residual layer which contains the pollutants and moisture from the previous day's mixing layer [*Stull*, 1988]. Moreover, the absence of convective processes during night-time allows the dry deposition of the aerosol particles due to gravitational sedimentation and diffusion motion, among others [*Seinfeld and Pandis*, 1998].

The mixing and residual layer heights are key variables in climate modelling and have an enormous influence on air pollution. The mixing layer height determines the available volume for pollutant dispersion and the residual layer height indicates the volume where the pollution remains in the atmosphere. In recent years, estimation of the PBL height, $z_{PBL}$, based on lidar data has been widely used applying different methods [e.g., *Morille et al.*, 2007; *Granados-Muñoz et al.*, 2012; *Wang et al.*, 2012]. Among them, the wavelet covariance transform method applied to the lidar range corrected signal (RCS, Eq. 2-12) has already proved to be an interesting tool for an automatic and unsupervised $z_{PBL}$ detection [*Morille et al.*, 2007; *Baars et al.*, 2008; *Pal et al.*, 2010; *Granados-Muñoz et al.*, 2012; *Wang et al.*, 2012]. This procedure is equivalent to the gradient method applied to a RCS profile smoothed by a low-pass spatial filtering [*Comerón et al.*, 2013] These methods are based on the detection of a sharp decrease of the aerosol load with height which is usually

coincident with the top of the PBL. However, this method presents difficulties when the aerosol layering in the PBL is complex, with different structures within the PBL or when advected aerosol layers in the free troposphere are coupled to the PBL [*Granados-Muñoz et al.*, 2012; *Summa et al.*, 2013]. In these cases, the top of the PBL can be under- or overestimated.

In this chapter, a new method, called POLARIS (PBL height estimatiOn based on Lidar depolARISation) is presented as an improved version of the method described by *Granados‑Muñoz et al.* [2012]. POLARIS uses the combination of the wavelet covariance transform applied to the RCS and the perpendicular-to-parallel signal ratio ($\delta$) profiles. By means of these profiles, different candidates for the $z_{PBL}$ are chosen and the attribution is performed through an algorithm. Because lidar depolarization ratio profiles provide information about the particle shape and allows the differentiation of aerosol types, POLARIS is especially useful when advected aerosol layers are coupled to the PBL. Furthermore, as $\delta$ cancelled the incomplete overlap effect, POLARIS can detect $z_{PBL}$ at lower heights than those determined using methods based only on RCS (affected by incomplete overlap). Hereafter to simplify the nomenclature, we will refer only to the $z_{PBL}$ understanding mixing and residual layer height according to time of day (day- or night-time, respectively) except when needed.

The fitting and application of POLARIS method is performed using lidar data measured in the framework of the ChArMEx, Chemistry-Aerosol Mediterranean Experiment (www.charmex.lsce.ipsl.fr). The main objective of ChArMEx was the scientific assessment of the present and future state of the atmospheric environment in the Mediterranean Basin, and its impacts on regional climate, air quality, and marine biogeochemistry. Two ChArMEx

campaigns have been performed including several stations around the Mediterranean basin during the summers of 2012 and 2013.

The POLARIS method's results are assessed using $z_{PBL}$ determined by means of microwave radiometer and radiosondes measurements.

## 7.1 Experimental site and instruments

The study described in this chapter was performed at Granada station with the Multiwavelength Raman lidar MULHACEN, the microwave radiometer (RPG-HATPRO) and radiosonde measurements. MULHACEN and the microwave radiometer RPG-HATPRO are explained in detail in Chapter 3 while the main features of the radiosonde are explained in this section.

The radiosounding data are obtained using a GRAW radiosonde DFM-06, which is a lightweight weather radiosonde that provides temperature (resolution 0.01 °C, accuracy 0.2 °C), pressure (resolution 0.1 hPa, accuracy 0.5 hPa), relative humidity (resolution 1%, accuracy 2%) and wind (accuracy 0.2 m/s) data with a vertical resolution around 5 m depending on the balloon weight. The radiosonde is connected to a Ground station GS-E (GRAW Radiosondes).

The temperature profile derived with the microwave radiometer (MWR) is used to locate the $z_{PBL}$ using the parcel method explained in Section 4.4 [*Holzworth*, 1964]. Further details were given by *Granados-Muñoz et al.* [2012]. The $z_{PBL}$ determined by the MWR, $z_{PBL}^{MWR}$, is retrieved between 06:00 UTC and 18:00 UTC as convective conditions are needed and are fuelled by solar irradiance absorption at the surface and the associated heating. Because of the low vertical resolution of the temperature profile measured by the microwave radiometer (100-500 m above 2 km), the uncertainty is estimated to be 200 below 2 km, and 400 m otherwise.

The radiosounding data used in this work are obtained from three radiosondes launched at 20:00 UTC from 9 to 11 July 2012. As radiosondes are launched early in the night, convective conditions cannot be expected and thus, the residual layer is determined. To this end, according to *Stull* [2000], the residual layer height was located at the height where the first abrupt increase of the potential temperature is detected, the so-called $z_{PBL}^{RS}$.

## 7.2 The POLARIS method

### 7.2.1 Wavelet Covariance Transform

The wavelet covariance transform applied to a generic function of height, $W_F(a, b)$, is defined as follows:

$$W_F(a, b) = \frac{1}{a} \int_{z_b}^{z_t} F(z) h\left(\frac{(z - b)}{a}\right) dz \qquad \text{Eq. 7-1}$$

where z is the height, $F(z)$ is a generic function (e.g., RCS), $z_b$ and $z_t$ are the integral limits and $h((z - b)/a)$ is the Haar's function defined by the dilation ($a$) and the translation ($b$) as it is illustrated in Figure 7-1. The wavelet covariance transform can be understood as a convolution between the RCS or δ and the Haar's function.
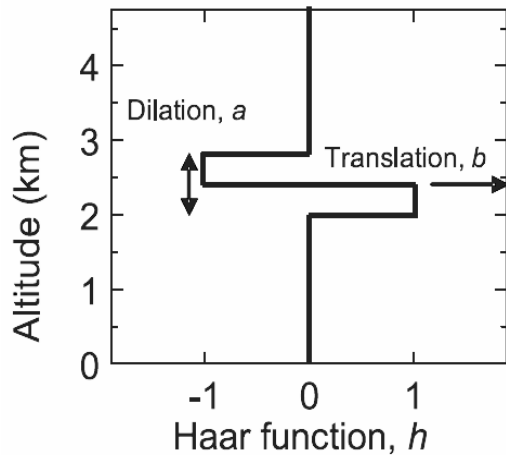


**Figure 7-1: Haar's function defined by the dilation ($a$) and the translation ($b$).**

Figure 7-2 shows an example of the wavelet covariance transform applied to the RCS ($W_{RCS}$). As can be seen, $W_{RCS}$ presents a maximum in coincidence with the sharpest decrease of the RCS. Therefore, the maximum of the $W_{RCS}$ can be associated to $z_{PBL}$ as sharp decrease of the aerosol load with height is usually coincident with the PBL height. However, this attribution cannot be generalized. Hence, *Baars et al.* [2008] proposed using the first maximum in the $W_{RCS}$ profile from surface larger than a threshold value for the wavelet profile. An improvement of this methods was provided by *Granados-Muñoz et al.* [2012] introducing an iterative procedure by which the threshold starts at 0.05 and it is reduced in steps of 0.005. However, there are complex scenarios in which aerosol load presents stratification within the PBL or aerosol layers are
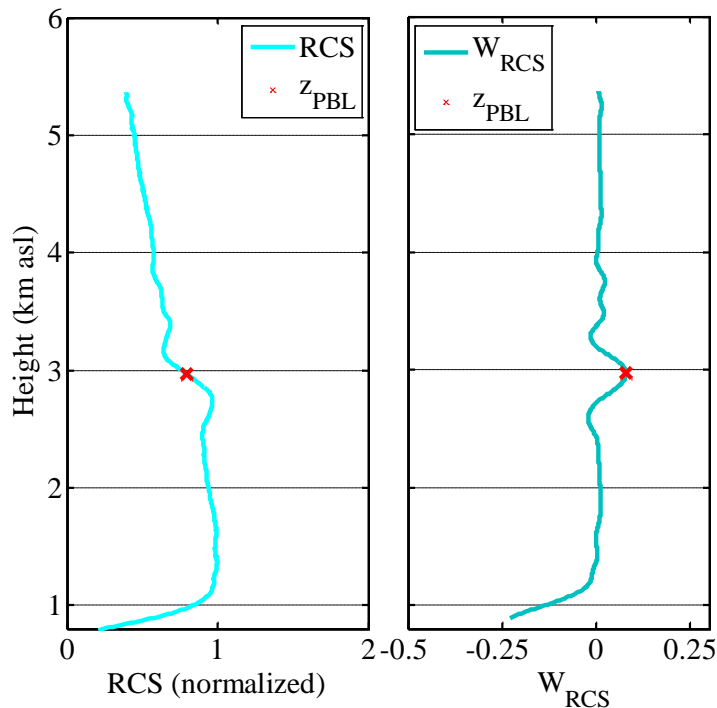


**Figure 7-2: Example of a normalized RCS and its wavelet covariance transform. Red cross indicates the possible location of the PBL height.**

coupled to the PBL. In these cases, the automatic detection of the $z_{PBL}$ with the wavelet method applied to the RCS provides inappropriate attributions. Further details related to the wavelet method were given by *Baars et al.* [2008] and *Granados-Muñoz et al.* [2012].

### 7.2.2 Description of POLARIS

The POLARIS method uses 10-min averaged range corrected signal (RCS) and the 10-min averaged perpendicular-to-parallel signal ratio (δ). It is worthy to note that δ is the un-calibrated volume linear depolarization ratio [*Cairo et al.*, 1999] so low δ values are related to spherical particle shapes. Both δ and the calibrated volume linear depolarization ratio ($\delta'$) were tested to determine the PBL height. As both variables provided similar results, δ is finally used as the depolarization calibration is not necessary. Therefore, POLARIS can be applied to data from instruments that have not been fully characterized. This fact facilitates the calculus and increases the applicability of the POLARIS method.

POLARIS performs the following steps:

1) The wavelet covariance transform is applied to the RCS ($W_{RCS}$) and to δ ($W_\delta$). Then, both $W_{RCS}$ and $W_\delta$ signals are normalized respectively to the maximum value of RCS and δ in the first kilometre above the surface.

2) The second step consists of determining three candidates according to a maximum of $W_{RCS}$ and the maximum and minimum of $W_\delta$. In this sense, the first candidate, the so-called $C_{RCS}$, is determined following the procedure established by *Granados-Muñoz et al.* [2012]. Thus, $C_{RCS}$ is determined as the height of the maximum of $W_{RCS}$ closest to the surface exceeding a certain threshold $\eta_{RCS}$. This threshold is decreased iteratively, starting in 0.05, until $C_{RCS}$ is found. The dilation ($a_{RCS}$) was also established as 300 m according to

138
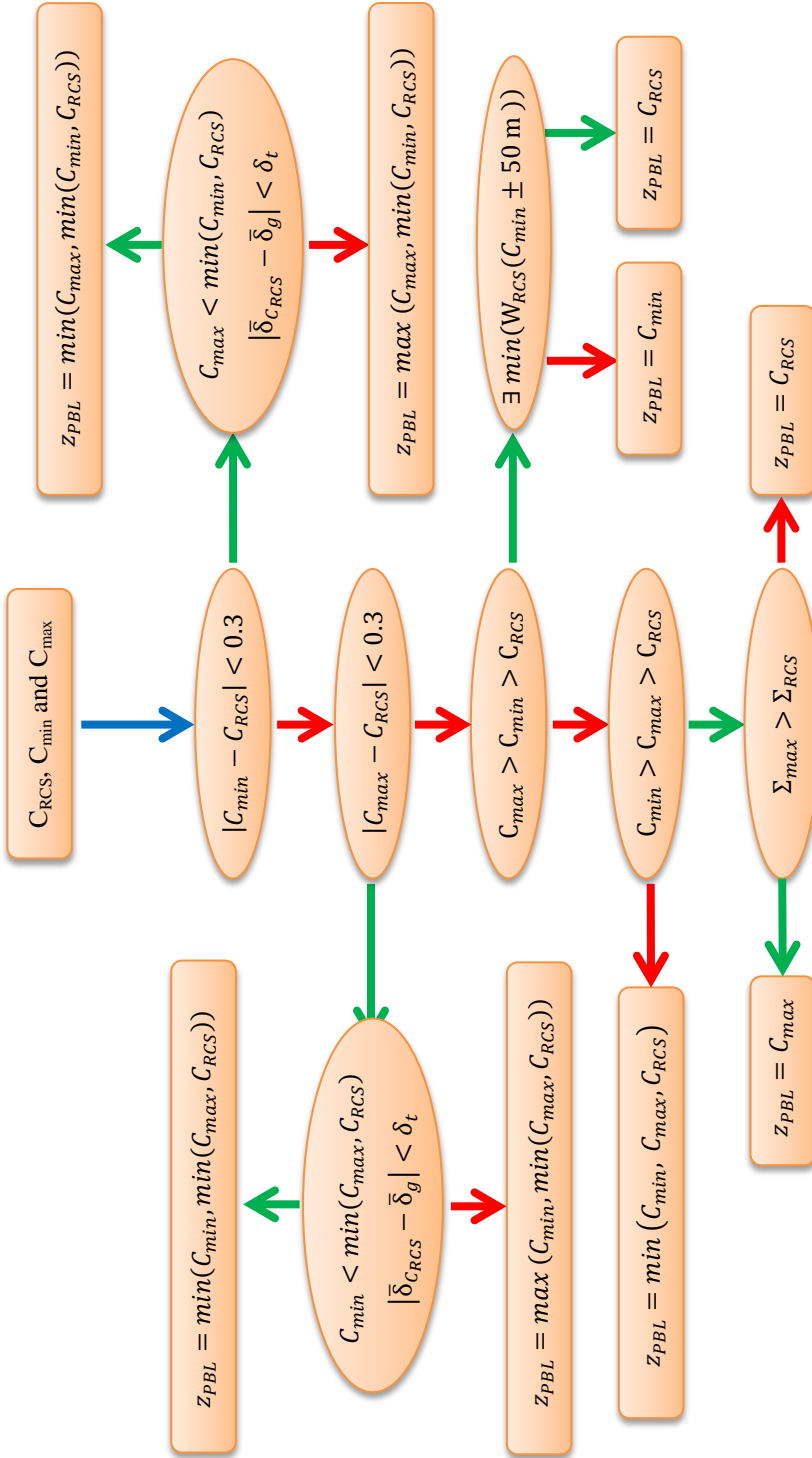
**Figure 7-3: Flux diagram of the algorithm used by POLARIS to determine the $z_{PBL}$. $C_{min}$, $C_{max}$ and $C_{RCS}$ are the candidates. The blue arrow indicates the start. Conditions are marked in ellipses and the final attribution of the $z_{PBL}$ in rectangles. The green and red arrows indicate the compliance and noncompliance of the conditions, respectively. The rest of the symbols are explained in the text.**

*Granados-Muñoz et al.* [2012]. Similarly, $C_{max}$ and $C_{min}$ are determined as the height of the maximum and minimum of $W_\delta$ closest to the surfaceexceeding the thresholds $\eta_{max}$ or $\eta_{min}$. Values of these thresholds will be determined during the optimization process explained latter. Hence, $C_{min}$ and $C_{max}$ indicate the heights where strong increases or decreases of $\delta$ are detected, respectively.

3) The $z_{PBL}$ attribution is performed assessing the relative location of the candidates. We have experimentally found that the relative location of the candidates is linked to different aerosol layering (e.g., dust layer coupled to the PBL is usually linked to a height distribution of the candidates as: $C_{RCS}=C_{max}>C_{min}$). This algorithm is schematized in the flow chart shown in Figure 7-3 and explained below.

The algorithm for $z_{PBL}$ attribution among the candidates includes the following steps:

a. If one of the candidates is not found, the minimum of the other two candidates is chosen as $z_{PBL}$.

b. If the three candidates are successfully determined, the attribution of the $z_{PBL}$ has two well-differentiated ways:

b.1. Coincidence between two candidates: if the distance between either $C_{min}$ or $C_{max}$ and $C_{RCS}$ is less than 300 m, this is interpreted as coincidence. Then, the highest (in altitude) of the coincident candidates is discarded, leaving only two candidates. In these cases, the average of $\delta$ in two different height ranges is necessary. These averages are performed in the ranges: 100 m below $C_{RCS}$ and 100 m above 1 km asl, being noted as $\bar{\delta}_{C_{RCS}}$ and $\bar{\delta}_g$, respectively. If $\left|\bar{\delta}_{C_{RCS}} - \bar{\delta}_g\right|$ is lower than

a threshold, $\delta_t$, the $z_{PBL}$ is taken as the minimum of the two candidates, and otherwise the maximum.

b.2. No coincidence among the candidates: $z_{PBL}$ is always taken as the minimum of the candidates except in two cases: $C_{max} > C_{min} > C_{RCS}$ and $C_{min} > C_{max} > C_{RCS}$. These cases require additional information. First, the situation $C_{max} > C_{min} > C_{RCS}$ was experimentally linked to an aerosol layer coupled to the PBL or the presence of a lofted aerosol layer within the free troposphere. Then, in order to distinguish between both situations, the minimum of the $W_{RCS}$ in the range $C_{min} \pm 50\ m$, $min\big(W_{RCS}(C_{min} \pm 50\ m)\big)$ higher than $\eta_{RCS}^{min}$ is required. If $min\big(W_{RCS}(C_{min} \pm 50\ m)\big)$ exists, we assume that $C_{min}$ indicates the bottom of a decoupled layer and thus, the $z_{PBL}$ corresponds to $C_{RCS}$. Otherwise, $C_{min}$ detects the beginning of a layer coupled to the PBL and thus, $z_{PBL}$ corresponds to $C_{min}$. Second, the situation $C_{min} > C_{max} > C_{RCS}$ indicates that $\delta$ and RCS decrease strongly but at different altitudes ($C_{max} > C_{RCS}$) and, at higher altitude, the depolarization increases again ($C_{min}$). This situation is linked to a multi-layered PBL. In this case, the attribution of the $z_{PBL}$ is performed attending to the candidate, $C_{max}$ or $C_{RCS}$, where both RCS and $\delta$ show a sharp decrease. To this aim, $\Sigma_{max}$ and $\Sigma_{RCS}$ are defined by:

$$\Sigma_{max} = W_\delta(C_{max}) + max\big(W_{RCS}(C_{max} \pm 50\ m)\big) \qquad \text{Eq. 7-2}$$

$$\Sigma_{RCS} = W_{RCS}(C_{RCS}) + max\big(W_\delta(C_{RCS} \pm 50\ m)\big) \qquad \text{Eq. 7-3}$$

where $max\big(W_{RCS}(C_{max} \pm 50\ m)\big)$ is the maximum of $W_{RCS}$ in the range $C_{max} \pm 50\ m$ and $max\big(W_\delta(C_{RCS} \pm 50\ m)\big)$ is the maximum of

$W_\delta$ in the range $C_{RCS} \pm 50 \; m$. The parameters $\Sigma_{max}$ and $\Sigma_{RCS}$ show the candidate where the combination of RCS and $\delta$ profiles show the sharper decrease. Then, if $\Sigma_{max} > \Sigma_{RCS}$, the $z_{PBL}$ corresponds to $C_{max}$, otherwise to $C_{RCS}$.

Finally, the temporal coherence of the $z_{PBL}$ is checked using the procedure proposed by *Angelini et al.* [2009] and *Wang et al.* [2012]. Once the $z_{PBL}$ has been determined for a certain period, each $z_{PBL}$ is compared with its previous and subsequent value. Using $z_{PBL}^{MWR}$ as reference, it has been estimated that $z_{PBL}$ variations with the previous and subsequent values larger than 300 m are unrealistic. In these cases, the $z_{PBL}$ considered unrealistic is replaced by the average value of its three or six previous and latter values subject to availability. In this way we guarantee the smoothness of the temporal series of the $z_{PBL}$. Further, occasional aerosol stratification, occurring within the mixing layer, could cause an inappropriate attribution of the $z_{PBL}$. As stratification presents short temporal duration compared to the mixing-layer temporal evolution [*Angelini et al.*, 2009], a 7-bin moving median filter is used to reject the possible attributions related to aerosol stratification.

An example of $z_{PBL}$ determination is illustrated in Figure 7-4. The normalized RCS and $\delta$ at 532 nm, $W_{RCS}$, $W_\delta$, the candidates ($C_{RCS}$, $C_{max}$ and $C_{min}$) and the $z_{PBL}$ determined by the POLARIS ($z_{PBL}^{POL}$) are shown. As can be seen, $C_{RCS}$ and $C_{max}$ were located at 5.2 km asl whereas $C_{min}$ is located around 1.3 km asl. At 20:30 UTC, the $z_{PBL}$ is not expected to be located around 5 km asl at the experimental site, and thus, $C_{RCS}$ and $C_{max}$ are probably detecting the top of an aerosol layer coupled to the PBL. However, $C_{min}$ indicates an abrupt increase of $\delta$ caused by the transition between the lowermost layer (considered anthropogenic aerosol layer) and the coupled layer (considered mineral dust
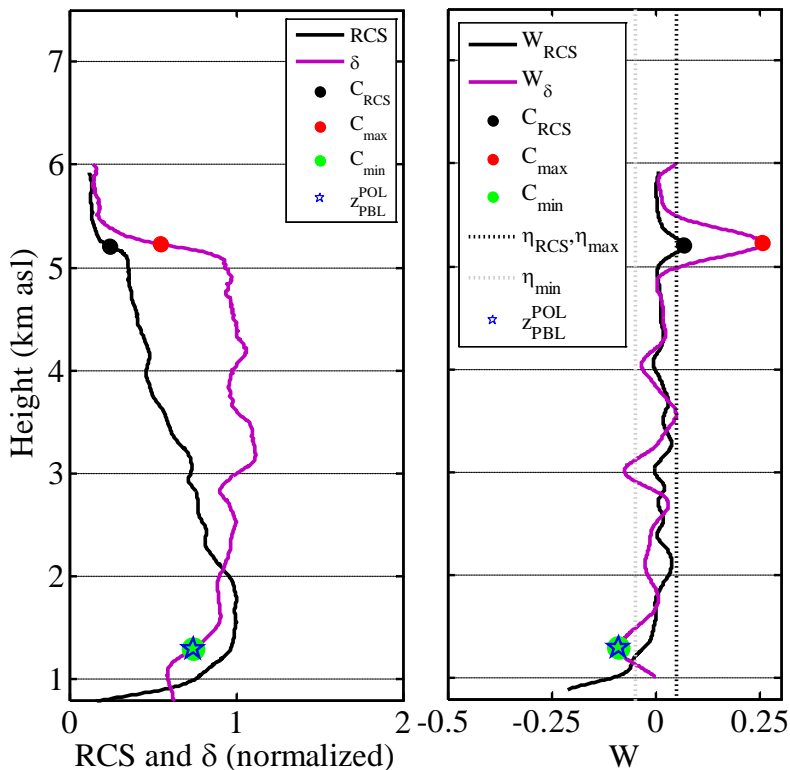
**Figure 7-4: Normalized RCS and δ profiles (left). WCT of the RCS, δ and thresholds $\eta_{min}$ (–0.05) and $\eta_{RCS}$, $\eta_{max}$ (0.05) (right) at 20:30 UTC 16 June (ChArMex 2013). $C_{RCS}$, $C_{min}$ and $C_{max}$ candidates and $z_{PBL}^{POL}$ are shown in both axes.**

layer). As the depolarization capability of the anthropogenic aerosol, mainly presented within the PBL, is lower than depolarization capability of the mineral dust layer coupled to the PBL, the abrupt increase of δ can be related to the $z_{PBL}$ and for that the algorithm chooses $C_{min}$ as the $z_{PBL}$ instead of $C_{max}$ or $C_{RCS}$.

## 7.3   Optimization and validation of POLARIS

First, the fitting of POLARIS is performed applying the method to a 36-hour continuous lidar measurement (10:00 UTC 16 June – 19:30 UTC 17 of June, during ChArMEx 2013) and comparing the results to the $z_{PBL}$ derived from a microwave radiometer using the parcel method ($z_{PBL}^{MWR}$). This comparison is

based on the good agreement between the $z_{PBL}^{MWR}$ and the $z_{PBL}$ determined using the method proposed by *Granados-Muñoz et al.* [2012]. That comparison was performed using measurements at noon when the mixing layer is expected to be well developed. As the whole daytime period is used this study, it is possible to find differences between both methods due to the different daily cycles of the aerosol-load and temperature profiles. Therefore, the optimization process is based on the comparison between the $z_{PBL}$ determined by the POLARIS method ($z_{PBL}^{POL}$) and the $z_{PBL}^{MWR}$ and the additional assessment of the vertical structure of the RCS and δ and their temporal evolution shown in Figure 7-5 and Figure 7-6. This additional assessment is very important due to the dependence of the parcel method on the surface temperature and the low vertical resolution of the temperature derived with the MWR. Once POLARIS is adjusted, it is applied in an automatic and unsupervised way to 72-hours of lidar measurements (12:00 UTC 9 July – 06:00 UTC 12 July, CHArMEx 2012 campaign).

### 7.3.1   Optimization of POLARIS

The temporal evolution of the RCS and δ at 532 nm for the 36-hour lidar measurement (10:00 UTC 16 – 19:30 UTC 17 June) of CHArMEx 2013 campaign, the $C_{RCS}$, $C_{max}$ and $C_{min}$ candidates and the $z_{PBL}^{POL}$ and $z_{PBL}^{MWR}$ are shown in Figure 7-5. This measurement campaign was used to optimize the algorithm, the dilation used for $W_\delta$, $a_\delta$, and the different thresholds ($\eta_{min}$, $\eta_{RCS}$, $\eta_{RCS}^{min}$ and $\delta_t$). Optimal $a_\delta$ is established at 450 m which is larger than the $a_{RCS}$ (300 m) determined by [*Granados-Muñoz et al.*, 2012]. This difference is
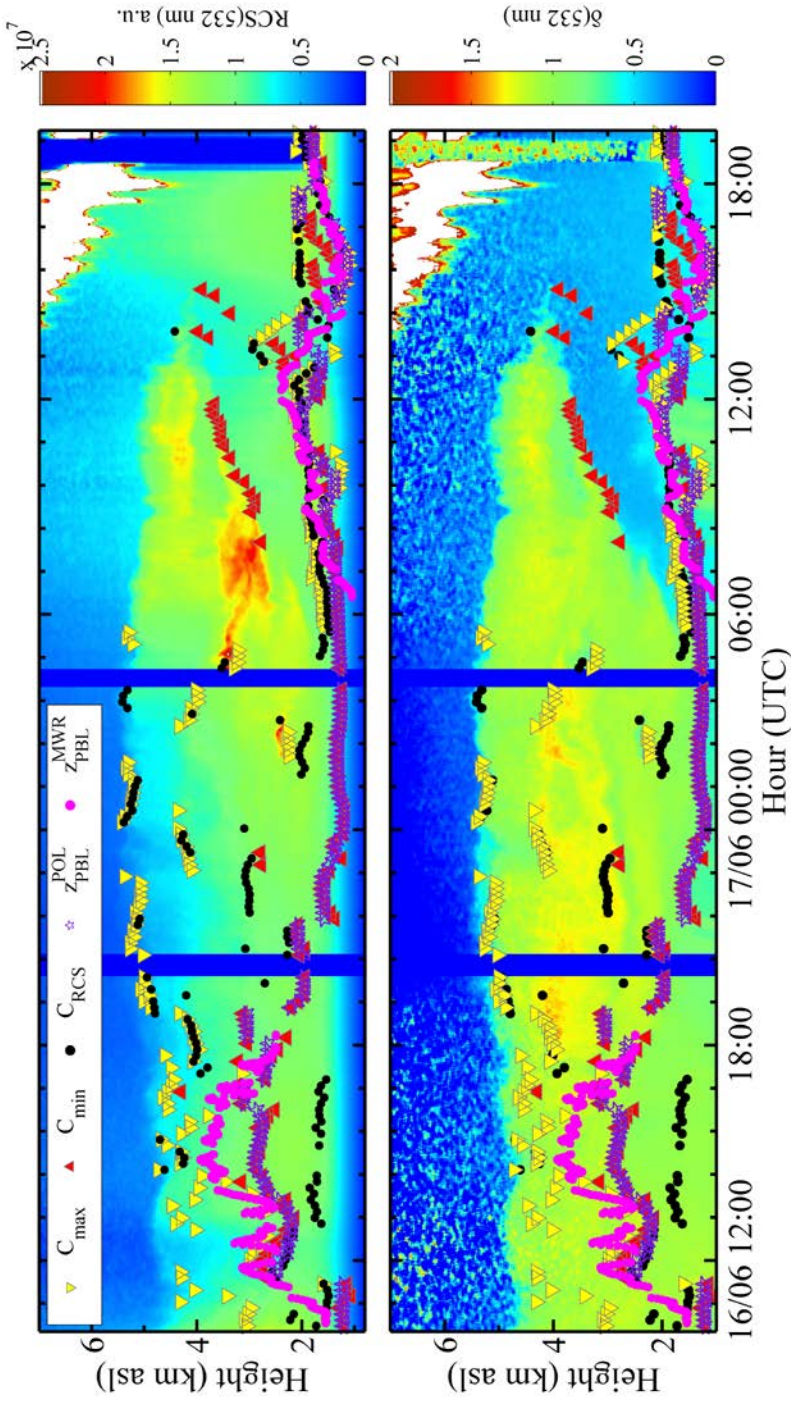
Figure 7-5: Temporal evolution of the Range Corrected Signal (RCS) and the perpendicular-to-parallel signal ratio (δ) in the period 09:00 16 June - 20:00 17 June 2013 (colour maps). The scatter plots represent the candidate for $z_{PBL}$ ($C_{RCS}$ (black dot), $C_{min}$ (red triangle) and $C_{max}$ (yellow inverted triangle)). The purple stars and the pink dots are the $z_{PBL}$ determined with POLARIS and the parcel method using MWR measurements, respectively. Measure gaps are dark-current measurements.

145

because $\delta$ profiles are noisier than RCS ones. The thresholds[15], $\eta_{min}$ and $\eta_{max}$ are equal to $\eta_{RCS}$ (0.05) in absolute value. In the case of $\eta_{RCS}^{min}$ threshold[16] used to distinguish decoupled layers, a value of 0.01 is chosen. Finally, the threshold[17] $\delta_t$ is established as 0.06 according to the results obtained in the optimization process.

During night-time, $C_{RCS}$ mainly detects interchangeable the top of the PBL and different stratification within the dust layer overlaying the PBL whereas POLARIS detects the transition between the residual aerosol layer and the dust layer. The mean and standard deviation of the $C_{RCS}$ and the $z_{PBL}^{POL}$ is 3.1±1.6 and 1.5±0.3 km asl, respectively, for the period from 20:30 UTC on 16 June to 04:00 UTC 17 June. Therefore, taking into account the lower values of $z_{PBL}$ determined by POLARIS and the lower standard deviation, POLARIS significantly improves the detection of the $z_{PBL}$ during night-time. During daytime, $z_{PBL}^{POL}$ and $z_{PBL}^{MWR}$ are compared. In order to obtain the most reliable results from the microwave radiometer, the period from 13:00 to 17:00 UTC is used when convection processes are expected. On 16 June, the mean and standard deviation of $z_{PBL}^{POL}$, $z_{PBL}^{MWR}$ and $C_{RCS}$ is 3.4±0.4, 2.7±0.3 and 2.2±1.1 km asl, respectively. $C_{RCS}$ is more than 1 km lower than $z_{PBL}^{MWR}$ probably because $C_{RCS}$ indicates structure in the PBL. In addition, the standard deviation of the $C_{RCS}$ is 1.1 km due to several detections at 4.5 km asl around 14:50 UTC (Figure 7-5). These results demonstrate the inconveniences of the situations with dust layer overlaying the PBL. On the contrary, the $z_{PBL}^{POL}$ shows better

---

[15] $\eta_{min}$ and $\eta_{max}$: thresholds used to find $C_{min}$ and $C_{max}$ by means of the minimum and maximum of $W_\delta$.
[16] $\eta_{RCS}^{min}$: threshold used to find a local maximum of $W_{RCS}$ in the height range $C_{min}$±50 m.
[17] $\delta_t$: depolarization threshold used in those cases with coincidence between two candidates.

agreement with the $z_{PBL}^{MWR}$, although the $z_{PBL}^{POL}$ has lower values than the $z_{PBL}^{MWR}$ probably due to the fundamentals of the methods: $z_{PBL}^{MWR}$ determines the $z_{PBL}$ using thermodynamic processes whereas $z_{PBL}^{POL}$ uses the aerosols as tracers. Besides this discrepancy, both $z_{PBL}^{POL}$ and $z_{PBL}^{MWR}$ show similar temporal evolution and the standard deviations are considerably lower indicating a good response of the method. Therefore, the results demonstrate the improvement in the $z_{PBL}$ detection using POLARIS also during daytime. POLARIS yields an incorrect detection on 16 June as $z_{PBL}^{POL}$ increases abruptly from 1200 to 2500 m asl between 11:20 and 11:30 UTC. This behaviour could be due to the strong stratification of the residual layer which abruptly disappears once the convection processes are strong enough. This explanation is supported by the sharp increase detected in $z_{PBL}^{MWR}$ from 1.48 km at 10:15 UTC up to 2.7 km at 11:30 UTC.

### 7.3.2   Validation of POLARIS

After optimizing POLARIS using the 36-hour continuous lidar measurement campaign, it is applied in an automatic and unsupervised way to the 72-hour continuous lidar measurement performed in the framework of ChArMEx 2012 campaign. The assessment of this method is performed by comparing $z_{PBL}^{POL}$, $z_{PBL}^{MWR}$ and $z_{PBL}^{RCS}$. Additionally, the temporal evolution of the range-corrected signal and $\delta$ is used to locate the aerosol layers through the intensity of the signal. The lidar measurement was performed between 9 and 12 July 2012. During these days, the Southern Iberian Peninsula was under the effects of a Saharan dust event. In fact, $\delta$ values in the lofted aerosol layers were larger than those encountered in layers close to the surface (see Figure 7-6), indicating a greater contribution of non-spherical particles in the lofted layers, as it is expected for dust aerosol plumes.

147
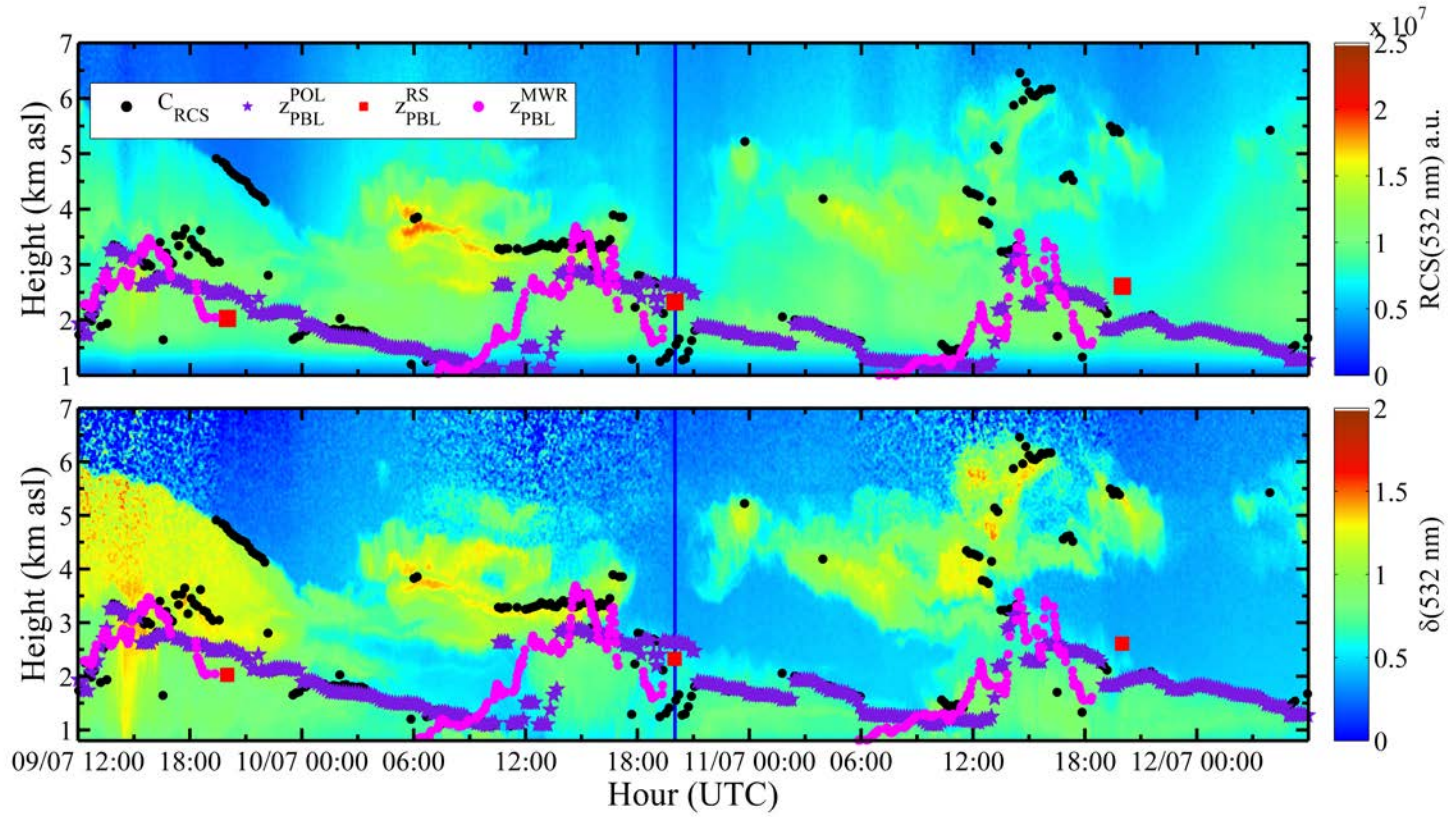
**Figure 7-6: RCS and δ temporal evolution in the period 12:00 9 July – 06:00 12 July 2012 (colour maps). Purple stars and pink dots represent $z_{PBL}^{POL}$ and $z_{PBL}^{MWR}$, respectively. Red squares are the $z_{PBL}$ determined using radiosondes.**

First of all, it is worthy to note that in those periods where the dust layer was located in the free troposphere, the method applied by*Granados‑Muñoz et al.* [2012] and POLARIS agreed with discrepancies lower than 250 m. (e.g., 00:00-08:00 UTC 10 July, 00:00-09:00 UTC 11 July and 18:00 11 July - 04:45 UTC 12 July). However, even in these periods, the temporal filter used by POLARIS helped to improve the detection of the $z_{PBL}$ as it was predicted by *Granados‑Muñoz et al.* [2012].

As we can see in Figure 7-6, $z_{PBL}^{POL}$ and $z_{PBL}^{MWR}$ are mainly in agreement when convection is well developed (13:00-16:00 UTC). However, differences between $z_{PBL}^{POL}$ and $z_{PBL}^{MWR}$ can reach close to 1 km (e.g., 14:46 UTC 10 July 2012 and 15:51 UTC 11 July 2012). According to the temporal evolution of the RCS, these differences seem to be not related to fails of POLARIS. Conversely, they could be associated to the high temporal fluctuation of the$z_{PBL}^{MWR}$ caused by the
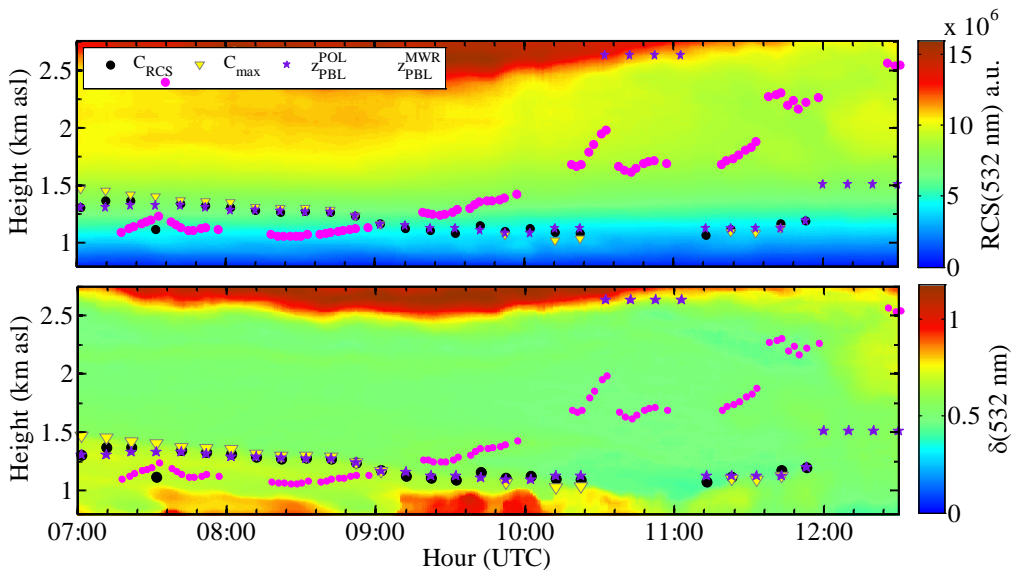


**Figure 7-7: Zoom of Figure 7-6 showing the RCS and δ temporal evolution during the period 07:00-13:00 UTC on 10 July 2012 (colour maps). C$_{RCS}$ (black dots), C$_{max}$ (yellow triangles), $z_{PBL}^{POL}$ (purple stars) and $z_{PBL}^{MWR}$ (pink dots) are included.**

sensitivity of the parcel method to the surface temperature. Furthermore, the comparison between $z_{PBL}^{POL}$ and $z_{PBL}^{MWR}$ revealed that the detection of the $z_{PBL}$ becomes particularly complex when the mixing is ongoing (07:00-13:00 GMT) and the residual and mixing layer coexist. In this sense, as can be seen in Figure 7-7, from 07:00 until 13:00 UTC on 10 July, $z_{PBL}^{MWR}$ showed an increasing trend whereas $z_{PBL}^{POL}$ decreased until 10:00-11:00 UTC. This is because POLARIS detected the residual layer height until 11:15 UTC and then, started to detect the mixing layer height. Moreover, the larger discrepancies between $z_{PBL}^{POL}$ and $z_{PBL}^{MWR}$ occurred after sunrise (06:00-09:00 UTC) and before sunset (17:00-19:00 UTC). This is explained according to the larger inertia of the aerosol (used as tracer by POLARIS) compared with inertia of the temperature profile (used as tracer by the parcel method).

During the ChArMEx campaign, three radiosondes were launched, one each day at 20:00 UTC, and thus the residual layer height was determined using the potential temperature profile ($z_{PBL}^{RS}$, see red squares in Figure 7-6). In Table 7-1, $z_{PBL}^{RS}$ obtained for each day is compared to $z_{PBL}^{POL}$ and $C_{RCS}$. At 20:00 UTC on 9 July, $C_{RCS}$ detected the top of the dust layer overestimating the residual layer height at 2.6 km. However, $z_{PBL}^{POL}$ improves the $z_{PBL}$ detection. The difference of 0.5 km between $z_{PBL}^{POL}$ and $z_{PBL}^{RS}$ could be related to the different tracers to determine $z_{PBL}^{POL}$ and $z_{PBL}^{RS}$. On 10 July, $z_{PBL}^{RS}$, $z_{PBL}^{POL}$ and $C_{RCS}$ were 2.3, 2.6 and 1.6 km asl.

Table 7-1: The $z_{PBL}$ determined with different methods at 20:00 UTC for different days.

| Day of June 2012 | $z_{PBL}^{RS}$ (±0.1 km asl) | $z_{PBL}^{POL}$ (±0.2 km asl) | $C_{RCS}$ (±0.15 km asl) |
|---|---|---|---|
| 9 | 2.0 | 2.5 | 4.60 |
| 10 | 2.3 | 2.6 | 1.60 |
| 11 | 2.6 | 1.9 | 1.90 |

Thus, good agreement was also detected between $z_{PBL}^{RS}$ and $z_{PBL}^{POL}$. However, $C_{RCS}$ was located at 1.6 km asl underestimating the residual layer height due to the multi-layering structure of the residual layer as it can be corroborated by the RCS (Figure 7-6). Therefore, POLARIS also improves the detection of the $z_{PBL}$ in those cases of multi-layering structure within the PBL.

On 11 July, both $z_{PBL}^{POL}$ and $C_{RCS}$ fail to attribute the residual layer height according to its comparison with $z_{PBL}^{RS}$ (see Figure 7-8). Both methods fail because they are based on strong variations with height of the aerosol load (RCS) and depolarization ratio ($\delta$) and, as can be seen in Figure 7-8, there are not sharp changes in these profiles at 2.6 km asl. Thus, it seems that there are not always correlation between the residual layer height determined by means
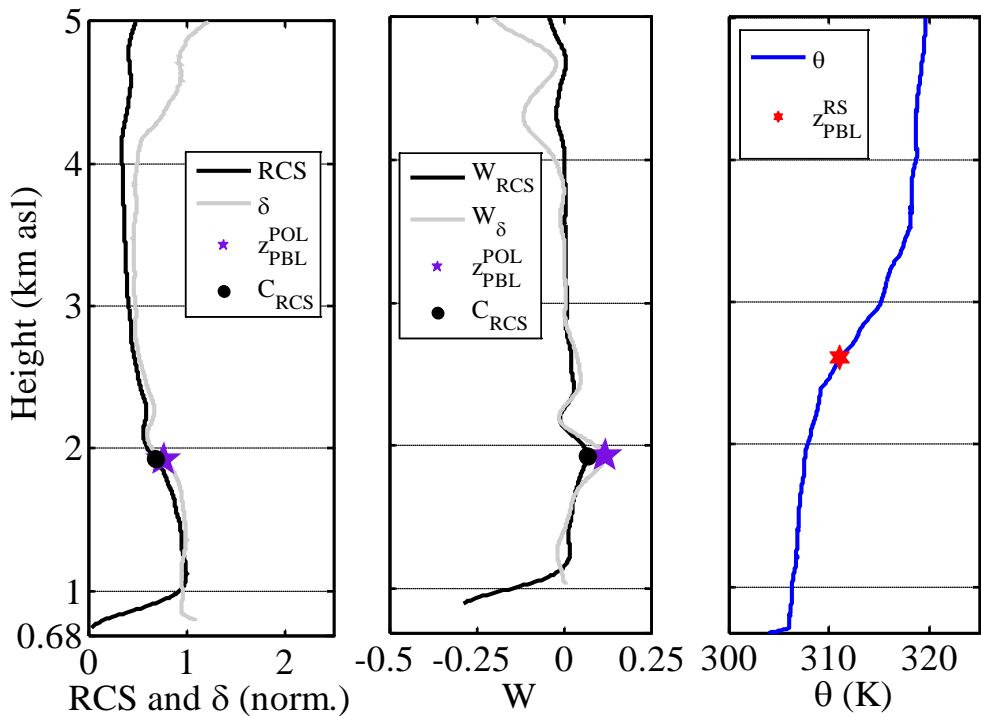


**Figure 7-8: Normalized RCS and δ, W$_{RCS}$, W$_{δ}$, and potential temperature (θ) profiles at 20:00 UTC on 11 July 2012 (radiosonde launch).**

151

of temperature profiles and aerosols as tracers.

## 7.4   Concluding remarks

According to the results presented in this chapter, it can be concluded that the lidar depolarization technique can be an useful tool for the automatic determination of the $z_{PBL}$. In this sense, the POLARIS method was developed based on the wavelet covariance transform applied to the range corrected signal and the uncalibrated depolarization ratio. Generally, POLARIS improves the automatic detection of the $z_{PBL}$ especially under scenarios in which mineral dust layers are coupled with the PBL. Besides, POLARIS provided good results during night- and daytime except during the morning due to the coexistence of the residual and mixing layers. This handicap seems to be a general problem for the derivative methods. Furthermore, a comparison between the $z_{PBL}$ determined using POLARIS, the parcel method and the potential temperature profile was performed. This comparison indicates that the discrepancies among POLARIS and the other methods are not only based on POLARIS's procedural error but on the differences between the aerosol and temperature profiles used as tracers. Particularly, it was detected a larger temporal inertia for the aerosol than for temperature.

# 8 Mixing of Saharan dust and boundary layer aerosols

According to the fifth assessment report of the IPCC (2013) [*Boucher et al.*, 2013], the uncertainties in the estimation of the radiation-aerosol and cloud-aerosol interactions together with the poor knowledge of the spatial and temporal aerosol distribution cause a large uncertainty in the estimation of the radiative forcing due to atmospheric aerosol. On a global scale, mineral dust is one of the main components of the atmospheric aerosol [*Formenti et al.*, 2011; *Shao et al.*, 2011]. Specifically Saharan dust represents the main source of mineral dust on the Earth [*Tegen and Fung*, 1995; *Miller et al.*, 2004]. In fact, estimated annual dust emission for North Africa is around 1150 Mt·yr$^{-1}$ [*Shao et al.*, 2011]. Therefore, an improved knowledge on microphysical and optical properties of mineral dust is one of the main objectives in atmospheric aerosol research. Furthermore, mineral dust has a potential impact on human health [e.g., *Kwon et al.*, 2002; *Pérez et al.*, 2008] and on regional air quality via the visibility impairment [*Prospero*, 1999]. However, the impact of anthropogenic aerosol on human health can be ever larger than that of mineral dust at ground level and thus, EU legislation about air quality (Directive 2008/50/EC) specifies the possibility to discount the particulate matter of natural sources (e.g., Saharan dust) when assessing compliance against limit values of, for example, PM$_{10}$ (e.g., particle matter with particles diameters of less than 10μm). Although mineral dust intrusions over European countries can affect at surface level, dust usually reach them as advected layers at high altitudes. Then, the entrainment of the mineral dust into the planetary boundary layer (PBL) occurs due its deposition or advection or due to strong convective processes within the PBL. Due to the relevance of the mineral dust, there are models (e.g., BSC-DREAM8b and NAAPS) which forecast its presence in the whole atmospheric column or on the surface. Regarding the forecast aerosol models,

they weakly consider interactions between aerosol layers in the free troposphere (FT) and the PBL due to convective processes.

Mineral dust has been previously investigated by means of study cases after its medium or long range transport [*Reid et al.*, 2003; *Tanre et al.*, 2003; *Redelsperger et al.*, 2006; *Haywood et al.*, 2008; *Chen et al.*, 2011] and field campaigns developed in different regions of the Earth as the Aerosol Characterization Experiments 2 (ACE-2) [*Raes et al.*, 2000], the Saharan Dust Experiment (SHADE) [*Tanre et al.*, 2003], the Aerosol Characterization Experiments Asia (ACE-Asia) [*Huebert et al.*, 2003], the Dust and Biomass-burning Experiment (DABEX) [*Osborne et al.*, 2008] and the Saharan Mineral Dust Experiment (SAMUM) [*Heintzenberg*, 2009]. Statistical analysis in different locations has been performed [e.g., *Mona et al.*, 2004; 2006; *Preissler et al.*, 2013]. Particularly, *Valenzuela et al.* [2012] performs a statistical analysis on column-integrated aerosol optical and microphysical properties during desert dust events over the South-eastern Iberian Peninsula during the period 2005-2010.

In this chapter, we take the advantage of measurements performed by co-located in-situ, passive and remote sensing instrumentation in combination with airborne in-situ measurements under Saharan mineral dust conditions on 27 June 2011.

The combination of these measurements allows the study of the interaction mechanisms between the Saharan dust and the PBL and the influence of mineral dust on the aerosol properties at the surface.

## 8.1   **Instrumentation** and experimental data

In Chapter 3, active and passive remote sensing instrumentation used in this thesis was explained in detail. Hence, only ground-based and airborne in-situ instrumentation is explained in this section.

### 8.1.1   Ground-based in-situ instrumentation

In-situ aerosol light-scattering and absorption measurements were obtained by means of an integrating nephelometer (TSI 3563) and a Multi-Angle Absorption Photometer (MAAP, Thermo ESM Andersen Instruments), respectively. The nephelometer was used to measure the aerosol scattering coefficient, $\sigma_{sca}$, at 450, 550 and 700 nm. This instrument is periodically calibrated using $CO_2$ and filtered air. Additionally, the raw $\sigma_{sca}$ data were corrected for truncation and non-Lambertian illumination errors using the method described by *Anderson and Ogren* [1998]. The uncertainty in $\sigma_{sca}$ is of 7% [*Heintzenberg et al.*, 2006]. The aerosol absorption coefficient at 637 nm, $\sigma_a(637 \text{ nm})$, was measured by means of a Multi-Angle Absorption Photometer (MAAP). The total method uncertainty for the aerosol light absorption coefficient inferred from MAAP measurement is around 12% [*Petzold and Schonlinner*, 2004; *Petzold et al.*, 2005]. More details on the instruments and the experimental setup were given by *Lyamani et al.* [2010]. In addition, levels of $PM_{10}$ and $PM_1$ were measured in real time using a DustTrak DRX (TSI 8533) which precision is 1% according to the technical specifications. This instrument was calibrated by comparison with simultaneous $PM_{10}$ and $PM_1$ gravimetric measurements with an $R^2$ of 0.83.

### 8.1.2 Airborne in-situ instrumentation

Airborne data provided by INTA aircraft were available over Granada on 27 June 2011. Airborne measurements were carried out by the INTA CASA C-212-200 atmospheric aircraft (Figure 8-1, top). Measurements of temperature, relative humidity, GPS position and aerosol size distribution were performed during the flight.

The airborne platform developed a vertical profile following a pseudo spiral centred at (37.19°N, 3.57°W) close to the experimental site (37.16°N, 3.61°W), with a diameter of about 4500 m. The aircraft overpass around the lidar systems was performed at several altitudes between 1200 and 5200 m asl. A gentle ascent and descent rate was used of about 2.5 m/s in order to increase vertical resolution and avoid problems with the inlets. Figure 8-2 shows the ascending track of the INTA-C212-200 aircraft during this flight, which took place around 10:30 UTC. The CASA C-212-200 atmospheric research aircraft was equipped with two optical particle counters designed by Droplet



**Figure 8-1: Picture of the INTA CASA C-210-200 aircraft for atmospheric research (from www.eufar.org) and the CAPS (left bottom) and PCASP-100X (right bottom), taken from www.dropletmeasurement.com.**
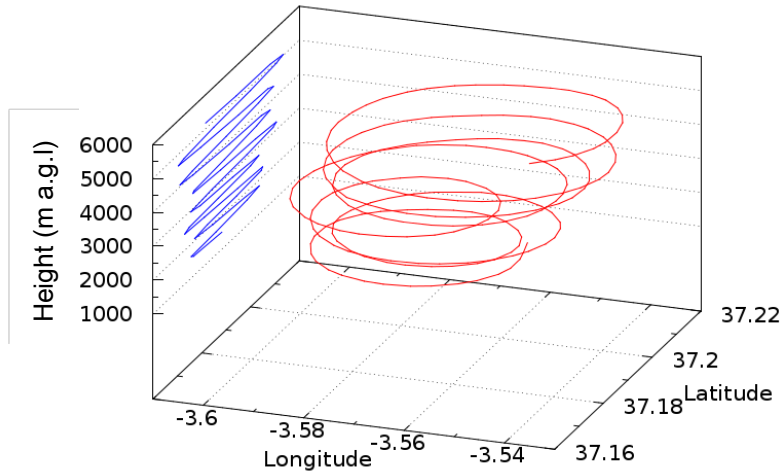
**Figure 8-2: Ascending track of the INTA C212-200 aircraft above CEAMA experimental site during the flight on 27 June 2011 around 10:30 UTC.**

Measurement Technologies (DMT) PCASP-100X and CAPS sonde. The instruments were fixed at two hard points located under the aircraft wings.

The CAPS (Cloud, Aerosol, and Precipitation Spectrometer) sonde located on board the C-212-200 combines five different instruments in one flight container, covering a sizing range with diameters from 0.51 to 1550 µm (Figure 8-1, bottom left). The five instruments included in the CAPS are the Cloud Imaging Probe (CIP), the Cloud and Aerosol Spectrometer (CAS), the Hotwire Liquid Water Content Sensor (Hotwire LWC), a GPS system and meteorological sensors. For the purposes of our analysis, data corresponding to the CAS optical counter were used. The CAS measures in the diameter range of 0.51-50 µm, in 30 different size bins. Its measuring principle is based on light-scattering, i.e. particles scatter light from an incident laser, and collecting optics guide the light scattered in the 4° to 12° range into a forward-sizing photodetector. This light is measured and used to infer particle size. Backscatter optics also measure light in the 168° to 176° range, which allows the determination of the real component of the refractive index for spherical

159

particles. The uncertainty of this sonde varies between 15 and 20% for the size distributions [*Feingold et al.*, 2006].

The PCASP-100X (Passive Cavity Aerosol Spectrometer Probe) provides size distributions of aerosol particles in the range 0.1-3 µm of diameter in 15 different bins (Figure 8-1, right bottom). The measuring principle is similar to the CAS sonde. A laser beam illuminates the particles and light is scattered in all directions. Some of the scattered light is collected by a mirror within a scattering angle from about $35^{o}$-$135^{o}$. This collected light is focussed onto a photodetector and then amplified, conditioned, digitized and classified into one of fifteen size channels. The size of the particle is determined by measuring the light scattering intensity and using Mie scattering theory to relate this intensity to the particle size for a fixed refractive index. Size distributions are provided with an uncertainty of 20% [*Baumgardner et al.*, 2005].

From the combination of the data from the CAS and PCASP-100X sondes, volume concentration profiles for the fine mode (radius between 0.05 and 0.5 µm) and coarse mode (radius from 0.5 to 25 µm) were obtained. In order to retrieve the volume concentration profiles from the on-board instrumentation, Mie theory was applied considering aerosol particles as spheres and a refractive index correction was performed, in a similar way to that explained by *Andrey et al.* [2014].

## 8.2  Methodology

From the aerosol properties derived with the in-situ and remote instrumentation, some other optical and physical properties can be calculated as summarized in Table 8-1. The derived aerosol optical and physical properties are described in

detail in Section 4.3 except $AOD_{PBL}$ and $AOD_{FT}$ which are the PBL and the free troposphere (FT) contributions to the AOD.

**Table 8-1: Aerosol optical and physical properties derived from optical properties.**

| Property | Symbol/Equation |
|---|---|
| AOD-related Angström exponent | $\text{å}_{AOD}(440-870nm) = -\dfrac{ln(AOD(440)/AOD(870))}{ln(440/870)}$ |
| $\sigma_{sca}$-related Angström exponent | $\text{å}_{sca}(450-700nm) = -\dfrac{ln(\sigma_{sca}(450)/\sigma_{sca}(700))}{ln(450/700)}$ |
| $\alpha, \beta$-related Angström exponent | $\text{å}_{\alpha,\beta}(355-532nm) = -\dfrac{ln(\alpha,\beta(355)/\alpha,\beta(532))}{ln(355/532)}$ |
| Simple scattering albedo | $\omega(\lambda) = \dfrac{\sigma_{sca}(\lambda)}{\sigma_{sca}(\lambda) + \sigma_{abs}(\lambda)}$ |
| Lidar ratio | $LR(\lambda) = \dfrac{\alpha(\lambda)}{\beta(\lambda)}$ |
| Particle linear depolarization ratio | $\delta^p = -\dfrac{\delta'(1+\delta^m)R - \delta^m(1+\delta')}{(1+\delta^m)R - (1+\delta')}$ |
| $AOD_{PBL}$ | $\displaystyle\int_0^{z_{PBL}} \alpha(z)\,dz \equiv \int_0^{z_{PBL}} \beta(z)LR\,dz$ |
| $AOD_{FT}$ | $\displaystyle\int_{z_{PBL}}^{z_{ref}} \alpha(z)\,dz \equiv \int_{z_{PBL}}^{z_{ref}} \beta(z)LR\,dz$ |

As the measurements were performed during daytime, elastic retrieval is used for determining the lidar ratio through the comparison of the lidar and sun-photometer AOD. Lidar AOD is determined integrating $\alpha$ from surface up to the reference height where the absence of aerosol is indicated by the Rayleigh fit (described in Section 3.3.2). In the incomplete overlap range (from surface to ~0.9 km agl [*Navas Guzmán et al.*, 2011]), the lowermost value of $\beta$ is assumed constant down to the surface. For the $AOD_{PBL}$ and $AOD_{FT}$, a similar procedure is followed changing the integral top by the PBL height and the integral bottom by the PBL height. The uncertainties of this procedure may be

very large due to the assumption of height-independent lidar ratio. However, the results were verified through the coherence between the sun-photometer $AOD$ (whole column) and $AOD_{PBL} + AOD_{FT}$ derived from lidar with discrepancies below 0.03 at 532 nm. The sun-photometer $AOD$ at 532 nm was derived interpolating the $AOD$ at 500 and 670 nm.

The planetary boundary layer height, $z_{PBL}$, was determined by means of the parcel method described in Section 4.4 using temperature profiles measured by the microwave radiometer. It is worthy to remark that convective processes are required to use this method and that the uncertainty of the $z_{PBL}$ is estimated to be 200 and 400 m above and below 2 km, respectively, due to the low vertical resolution of the temperature profile and the high sensibility of the parcel method to the surface temperature.

In order to distinguish between anthropogenic aerosol and mineral dust contribution to the particle backscatter coefficient, $\beta$ , the POLIPHON (Polarizing Lidar Photometer Networking) method, given by *Shimizu et al.* [2004] and *Tesche et al.* [2009a], was used. This method is described in detail in Section 4.1.6. In this case, POLIPHON is used to separate the mass concentration of dust and anthropogenic aerosols which present opposite depolarizing effects. We remark that the method was applied under the assumption of external mixing. As the analysed mixing process occurred in several hours, external mixing is assumed predominant. Then, the dust backscatter coefficient, $\beta_{dust}$, can be calculated as:

$$\beta_{dust} = \beta \cdot \frac{\left(\delta^p - \delta^p_{dust}\right)}{\left(\delta^p_{dust} - \delta^p_{ant}\right)} \frac{\left(1 - \delta^p_{ant}\right)}{\left(1 - \delta^p\right)} \qquad \text{Eq. 8-1}$$

where the height and spectral dependence was omitted for simplicity, $\delta^p$ is the measured particle linear depolarization ratio, and $\delta^p_{dust}$ and $\delta^p_{ant}$ represent $\delta^p$

values for pure dust and the anthropogenic aerosol, respectively. $\delta_{dust}^{p}$ value is reasonably well known 0.31±0.10 according to the SAMUM campaign performed in Ourzazate (Morocco) [*Gross et al.*, 2011a] whereas $\delta_{ant}^{p}$ value is typically 0.05±0.02 over the Granada station. Once $\beta_{dust}$ is determined, the mass concentrations of dust, $m_{dust}$, is given in terms of particle backscatter coefficient as:

$$m_{dust} = \rho_{dust} \frac{C_{dust}}{AOD_{dust}} \beta_{dust} LR_{dust} \qquad \text{Eq. 8-2}$$

where $\rho_{dust}$ and $LR_{dust}$ are the particle mass density and the dust lidar ratio. The ratio $C_{dust}/AOD_{dust}$, also called mean extinction-to-mass conversion factors, represents the ratio of volume concentration to AOD for the coarse (dust) mode. For pure dust particles, $\rho_{dust}$= 2.6 g·cm$^{-3}$ [*Pérez et al.*, 2006] and $LR_{dust}$ = 55±10 sr [*Tesche et al.*, 2009b]. $C_{dust}$ was calculated from AERONET-derived level 1.5 inversion products on 27 June 2011 at 11:19 UTC as there were not level 2.0 inversions available between 08:00 and 16:30 UTC.
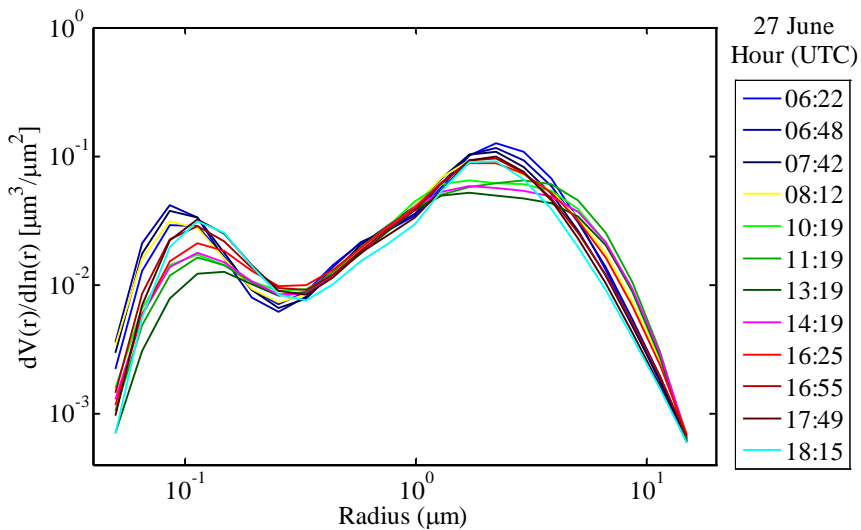


**Figure 8-3: Volume size distribution provided by AERONET (level 1.5) on 27 June. The extinction-to-mass conversion factor was retrieve using the distribution at 11:19 UTC.**

The size distributions are shown in Figure 8-3. $AOD_{dust}$ was derived using the total AOD at 532 nm and the fine fraction at 500 nm provided by AERONET [*O'Neill et al.*, 2001a; *O'Neill et al.*, 2001b]. Then, the ratio $C_{dust}/AOD_{dust}$ was $0.95 \cdot 10^{-6}$ m. By applying the law of error propagation to Eq. 8-2, the uncertainty in the mass concentration is estimated to be about 40-45%, considering the following individual uncertainties: 25% for the mass densities, 20% for the lidar ratios, and 15% for the mean extinction-to-mass conversion factors [*Tesche et al.*, 2009b; *Ansmann et al.*, 2011]. Concerning the particle backscatter coefficient, its uncertainty is retrieved of the order of 10-20% (see Chapter 4). As was discussed in Chapter 6, the uncertainty of the particle depolarization ratio is between 0.04 and 0.10.

The attribution of the air masses origin was performed by means of backward trajectories calculated with the HYSPLIT model [*Draxler and Rolph*, 2003]. The model version used in this work employed the GDAS database (Global Data Assimilation System) at six different levels (500, 1500, 2500, 3500, 4500 and 6000 m agl). This analysis enables the interpretation of the different source regions of air masses reaching the study area. To this end, 5-day back trajectories were calculated ending at 22:00 UTC on 26 June and at 13:00 UTC on 27 June 2011 at Granada. The trajectories can have large relative error (about 40%) under low wind conditions [*Stunder*, 1996].

## 8.3 Results and discussion

The range corrected signal at 532 nm, RCS(532 nm), the $z_{PBL}$, and the total AOD(532 nm), $AOD_{PBL}$ and $AOD_{FT}$ obtained on 27 June 2011 are shown in Figure 8-4. The RCS(532 nm) shows that the aerosol load was confined in the region from the surface up to 4.5 km both at night and daytime. The total
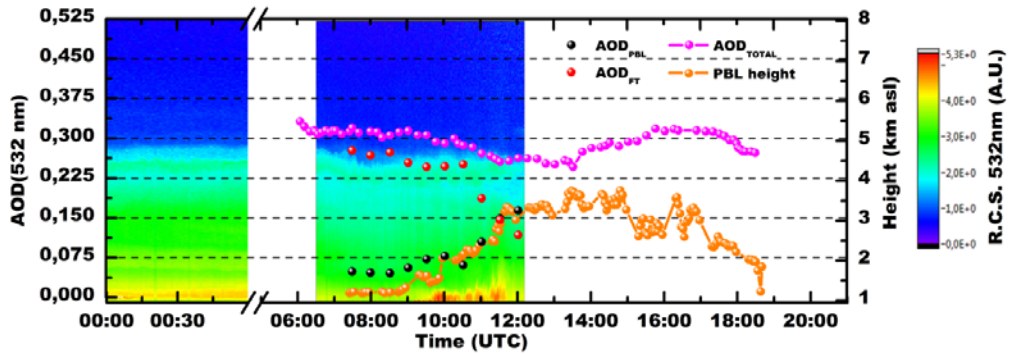
**Figure 8-4: Colour map represents the lidar range corrected signal at 532 nm on 27 June 2011 from 00:00-01:00 and 06:30-12:15 UTC. The PBL height is marked in orange and the total, PBL and FT AOD at 532 nm is marked in pink, black and red, respectively.**
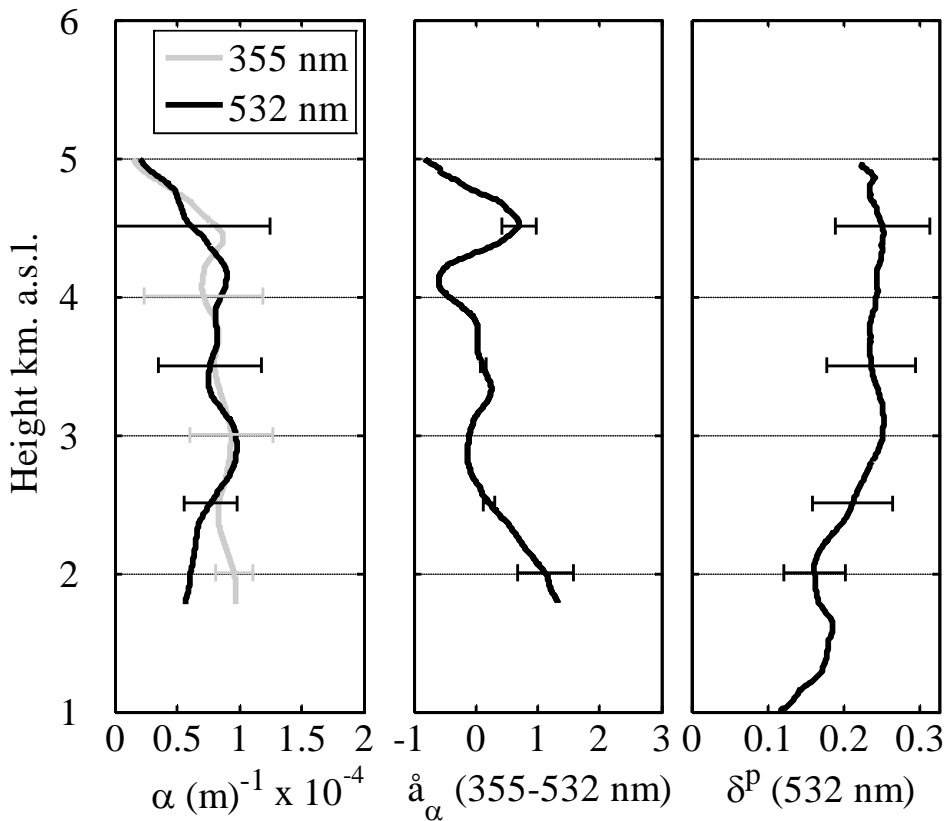


**Figure 8-5: Particle extinction coefficient ($\alpha$) at 355 and 532 nm, $\text{å}_\alpha$ (355-532 nm) and $\delta^p$(532 nm) at 00:00-01:00 UTC on 27 June 2011.**

AOD(532 nm) was around 0.28 along the day. In Figure 8-5, the particle extinction coefficient, $\alpha$, at 355 and 532 nm derived by inelastic retrieval, $\mathring{a}_\alpha$(355-532 nm) and $\delta^p$(532 nm) profiles at 00:00-01:00 UTC are shown. As can be seen, $\mathring{a}_\alpha$ and $\delta^p$ profiles show two well differentiated regions: the upper region, 3-5 km asl, with a mean and standard deviation of 0.1±0.1 and 0.26±0.05 for $\mathring{a}_\alpha$ and $\delta^p$, respectively, and the lower region, 1-3 km asl, characterized by an anticorrelation between $\mathring{a}_\alpha$ and $\delta^p$. In this inelastic retrieval, $\mathring{a}_\alpha$(355-532 nm) and $\delta^p$(532 nm) profiles at 00:00-01:00 UTC are shown. As can be seen, $\mathring{a}_\alpha$ and $\delta^p$ profiles show two well inelastic retrieval, $\mathring{a}_\alpha$(355-532 nm) and $\delta^p$(532 nm) profiles at 00:00-01:00 UTC are shown. As can be seen, $\mathring{a}_\alpha$ and $\delta^p$ profiles show two well differentiated regions: the upper region, 3-5 km asl, with a mean and standard deviation of 0.1±0.1 and 0.26±0.05 for $\mathring{a}_\alpha$ and $\delta^p$, respectively, and the lower region, 1-3 km asl, characterized by an anticorrelation between $\mathring{a}_\alpha$ and $\delta^p$. In this sense, $\mathring{a}_\alpha$ and $\delta^p$ values vary from 1.3 and 0.11, close to the surface, to –0.1 and 0.25, respectively, at 3 km asl.

The values of $\mathring{a}_\alpha$ and $\delta^p$ of the upper region indicate the predominance of coarse and non-spherical particles and agree with the values of $\mathring{a}_\alpha$(355-532 nm) (0.19±0.20) and $\delta^p$(532 nm) (0.31±0.10) measured for pure Saharan mineral dust by *Tesche et al.* [2011]. The LR(532 nm) mean value is 50±5 sr for this layer (not shown) which is also in the range 55±10 sr given by *Tesche et al.* [2009b] for Saharan mineral dust. Additionally, the obtained LR(532 nm) agrees with several studies of Saharan dust previously performed at this station [*Guerrero-Rascado et al.*, 2009; *Bravo-Aranda et al.*, 2013] and other stations during medium-transport dust events [*Müller et al.*, 2009; *Preissler et al.*, 2013]. Moreover, the backward trajectories at 00:00 and 11:00 UTC on 27 June (Figure 8-6) show that air masses came from the North of Africa at 3500, 4500
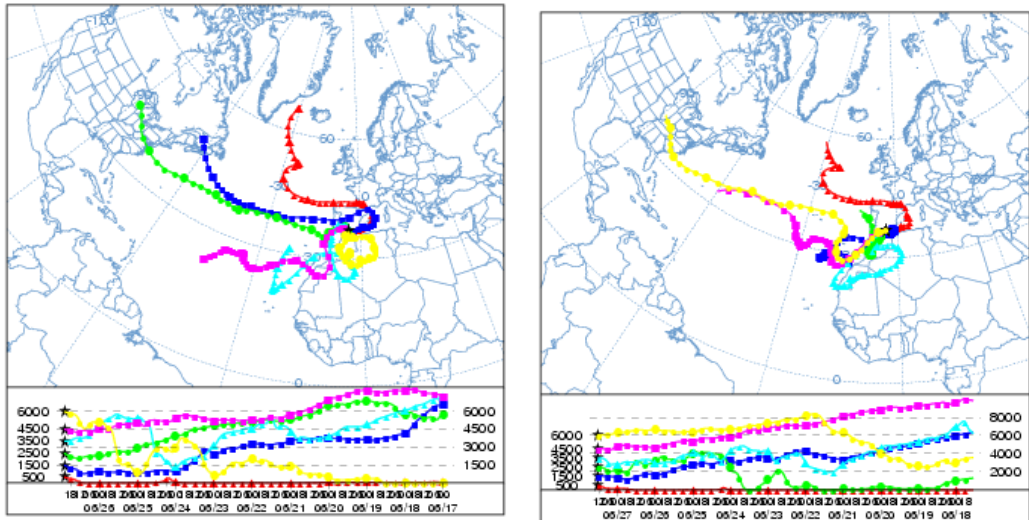
**Figure 8-6: HYSPLIT backward trajectories ending at 22:00 on 26 June (left) and at 13:00 UTC (right) on 27 June 2011 at 500, 1500, 2500, 3500, 4500 and 6000 m agl (Granada, 37.16°N, 3.61°W).**

and 6000 m agl. Therefore, the assessment of these results indicates the presence of Saharan dust over the Granada station on 27 June. Previous lidar measurements indicate that the dust outbreak affected the South of the Iberian Peninsula since 21-22 June 2011 (not shown). The dust outbreak was successfully predicted by both, NAAPS and BSC-DREAM8b forecast models on 27 June 2011 (Figure 8-7).

Regarding the lower region, $\delta^p$ values increase with height from 0.12 at 1 km asl to 0.26 at 3 km asl whereas $\mathring{a}_\alpha$ values decrease from 1.34 at 2 km asl to −0.13 at 3 km asl, indicating a gradual increase with height of the predominance of coarse and non-spherical particles in the region 1-3 km asl (Figure 8-5). This trend can be due to different degrees of external mixture of mineral dust and anthropogenic aerosol. Larger presence of mineral dust is expected at high altitudes as mineral dust (anthropogenic aerosol) is characterized by coarse (fine) mode predominance and non-spherical (spherical) particles. This shape of the $\delta^p$ profile is also observed during daytime as well as in $\mathring{a}_\beta$ profile. Indeed, as

167
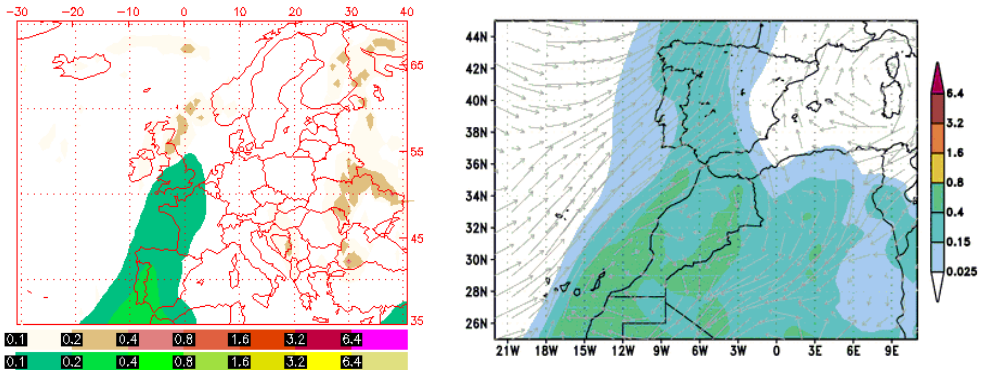
**Figure 8-7: Aerosol optical depth at 12:00 UTC on 27 June 2011 forecasted by NAAPS: colours indicate the aerosol type: sulphates (orange/red) and dust (green/yellow) (left). Dust optical depth at 550 nm (see colour bar) and wind direction at 3000 m forecasted by BSC-DREAM8b at 12:00 UTC on 27 June 2011 (right).**

can be seen in Figure 8-8, $å_\beta$ and $\delta^p$ profiles at 07:30 UTC are similar to the $å_\alpha$ and $\delta^p$ ones measured at 00:30 UTC. However, along the morning, $å_\beta$ progressively decreases whereas $\delta^p$ increases in the lowermost part of the profiles (<2 km asl). Particularly, $å_\beta$ and $\delta^p$ mean values of the 100-m layer nearest to the surface vary from 2 and 0.08 at 07:00 UTC to 0.8 and 0.19 at 11:30 UTC, respectively. This variation could be linked to the downward entrainment of the dust into the PBL due to the interaction mechanisms caused by the strong convective processes.

The mass concentration of dust, $m_{dust}$, at 10:30 and 11:30 UTC and the mass concentration retrieved with the volume concentration of the coarse mode provided by the airborne in-situ measurement, $m_c$, are shown in Figure 8-9. As can be seen, there is a very good agreement in the upper layer. Mean of $m_{dust}$ and $m_c$ in the range 3.3-4.5 km asl are 140 and 110 $\mu g \cdot m^{-3}$. Additionally, in the layer below 3 km asl, $m_{dust}$ and $m_c$ mean values are 100 and 60 $\mu g \cdot m^{-3}$, respectively, and hence, the assessment of the results shown a better agreement for the dust layer with larger values provided by POLIPHON in the whole profile. The differences found between both methods would be linked to the
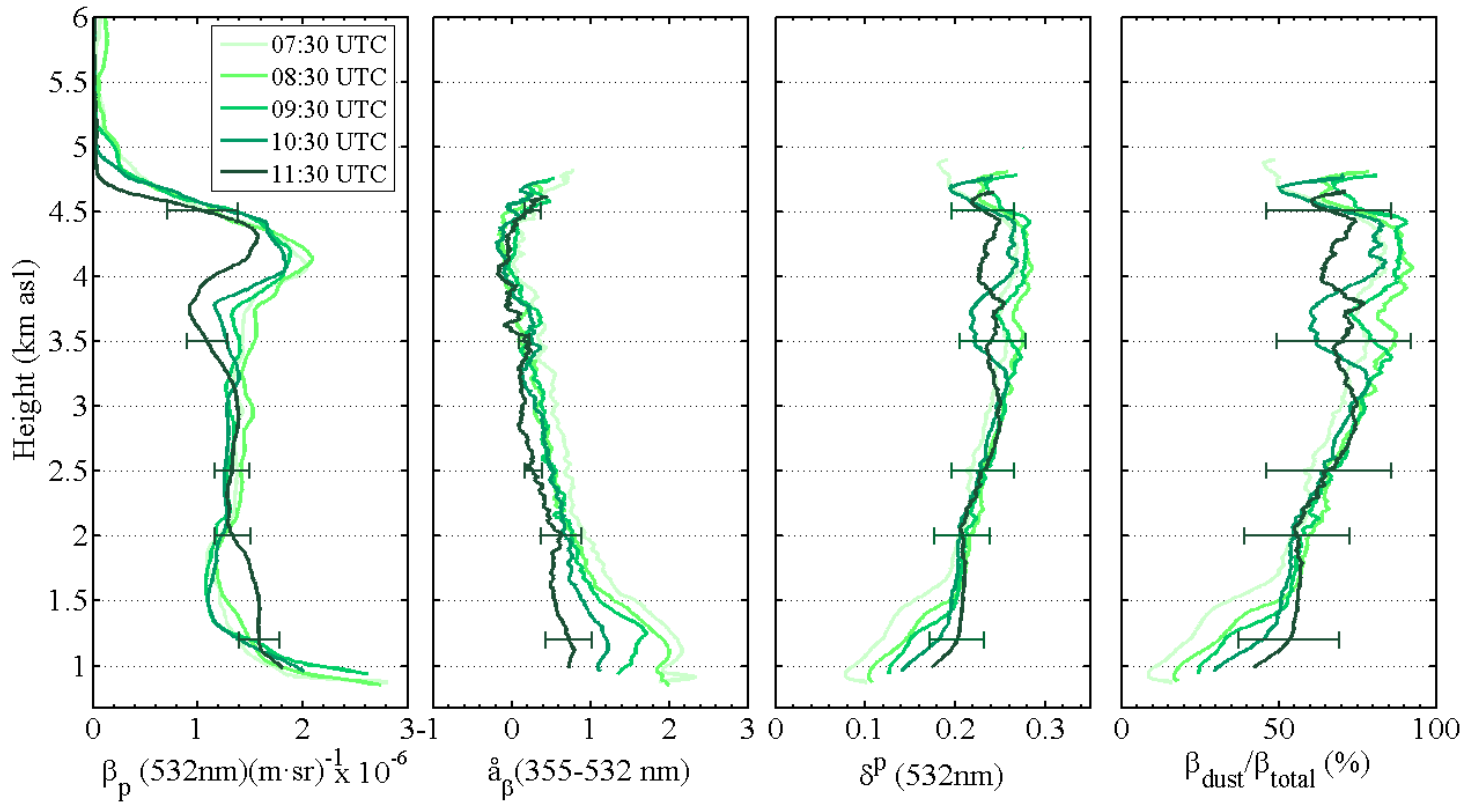
**Figure 8-8: β(532 nm), å$_β$ (355-532 nm), δ$^p$(532 nm) and β$_d$/β(532 nm) profiles at different hours following the label on 27 June 2011.**
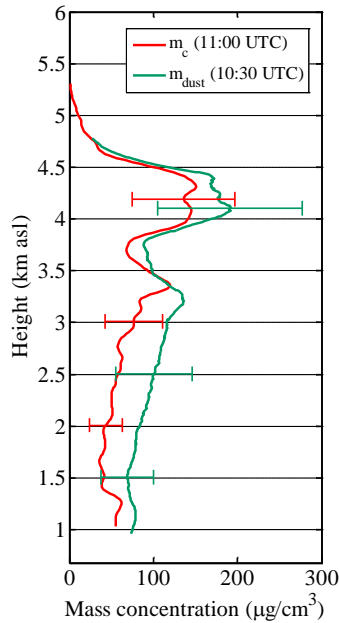
**Figure 8-9: Dust mass concentration ($m_{dust}$) provided by the airborne measurement and coarse mode mass concentration ($m_c$) retrieved by POLIPHON on 27 June 2011.**

different assumptions. On the one hand, POLIPHON includes assumptions as the height-constant LR used to retrieve the particle backscatter coefficient profile derived under the assumption by which the whole coarse volume concentration is linked to the mineral dust. On the other hand, the airborne measurements may be biased due to the sampling efficiency of the inlet system and $m_c$ was retrieved assuming spherical particles (Mie's theory). Moreover, both methods were not sampling the same region of the atmosphere above. Thus, it can be concluded that the POLIPHON method is an acceptable approximation to retrieve the mass concentration of two different aerosol type of a mixture, despite of the assumptions.

Furthermore, the increase of mineral dust at the lowest level (~1 km asl) is evidenced by the $\beta_d/\beta$ increase from 12±10% at 07:30 UTC to 45±10% at 11:30 UTC (Figure 8-8). In order to discard that the increase of mineral dust could be related to local sources, a reference measurement on 14 June under

non-dust conditions was chosen. $\delta^p$ value measured on 27 June 2011 (~0.19) was almost twice than the measured on 14 June 2011 (~0.10) in the lowermost layer. The large difference of $\delta^p$ near the surface between 27 and 14 June shows that the presence of the mineral dust in the PBL on 27 June 2011 cannot be solely due to local sources. Moreover, as the backward trajectory at 500 m agl (Figure 8-6) shows that air masses came from Europe across the Mediterranean basin, the increase of presence of mineral dust at low altitudes along the day only can be related to interaction between the dust layer and the PBL. The strong convective processes appear as a cause which accelerates the downward dust entrainment.

The interaction between the FT and the dust layer was also detected by the combination of the lidar and sun-photometer data. Although AOD(532 nm) was rather stable with values around 0.28 along the day, the FT and PBL contributions to the AOD ($AOD_{FT}$ and $AOD_{PBL}$) changed along the morning (Figure 8-4). In this sense, the $AOD_{PBL}$(532 nm) increased from 15% up to 58% between 07:30 UTC and 12:00 UTC whereas $AOD_{FT}$(532 nm) decreased from 85% up to 42% in the same period. Thus, the variation of $AOD_{FT}$ and $AOD_{PBL}$ evidenced the mixing between the FT and the PBL by strong convective processes. These convective processes are highlighted by the great enhancement of the PBL height in this period (see Figure 8-4). Similar phenomena were detected on Cape Verde island by *Engelmann et al.* [2011] where a vertical mixing between air masses in the PBL and the FT was detected because air flow can be significantly disturbed mainly by surface convection.

The temporal evolution of $\sigma_{sca}$(550 nm), $\sigma_{abs}$(637 nm), $å_{sca}$(450-700 nm), $\omega$(637 nm), $PM_1$, $PM_{10}$, $PM_{10-1}$, AOD(532 nm) and $\eta$(500 nm) on 27 June 2011
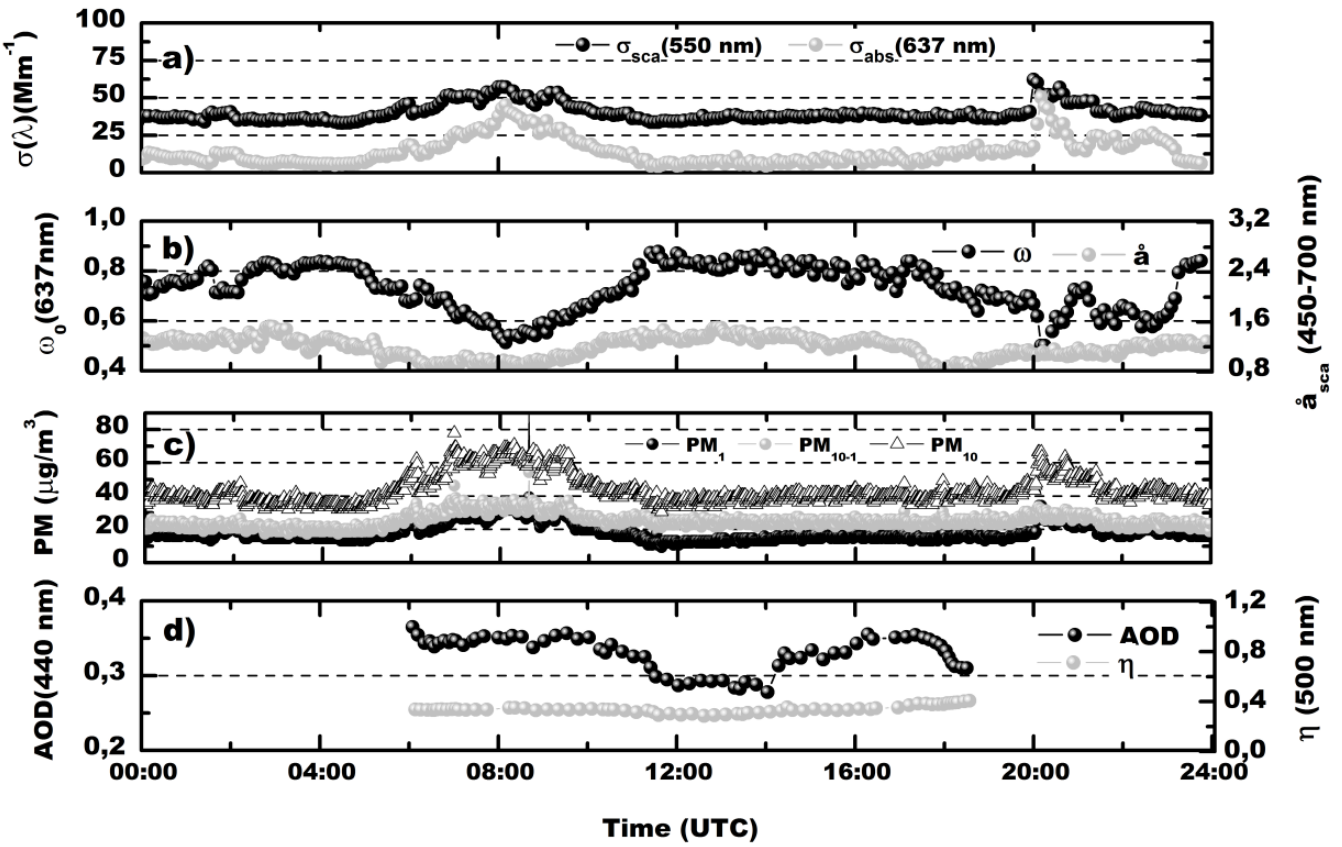
**Figure 8-10: Temporal evolution of $\sigma_{sca}$(550 nm), $\sigma_{abs}$(637 nm) (a), $\mathring{a}_{sca}$(450-700 nm), $\omega$(637 nm) (b), PM$_1$, PM$_{10}$ and PM$_{10-1}$ (c) ,AOD(532 nm), and F$_f$(500 nm) (d) on 27 of June 2011.**
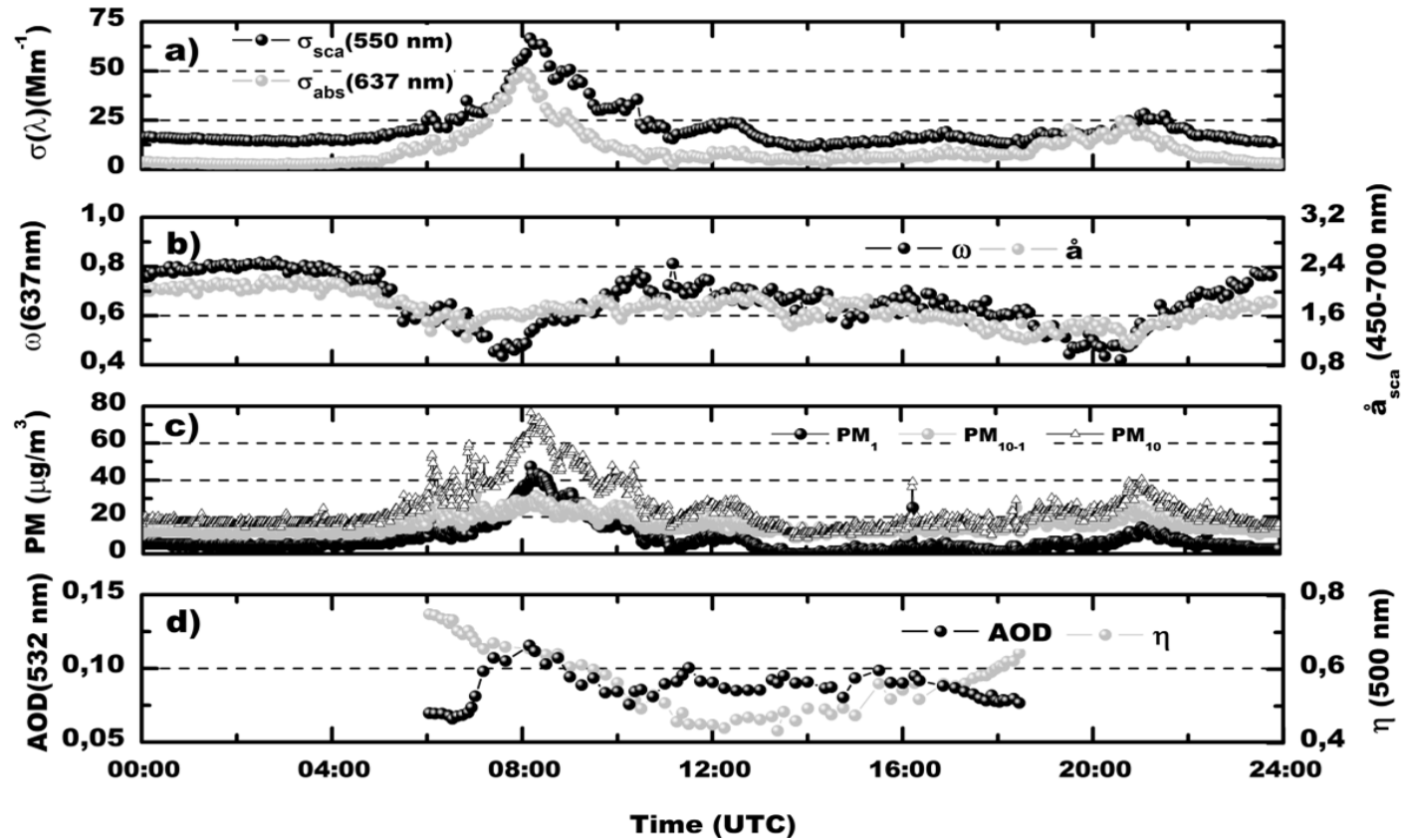
**Figure 8-11: Temporal evolution of $\sigma_{sca}$(550 nm), $\sigma_{abs}$(637 nm) (a), $\mathring{a}_{sca}$(450-700 nm), $\omega$(637 nm) (b), $PM_1$, $PM_{10}$ and $PM_{10\text{-}1}$ (c) ,AOD(532 nm), and $F_f$(500 nm) (d) on 14 of June 2011.**

(Figure 8-10) is used to highlight the increase of presence of mineral dust at the surface and study the influence of the mineral dust within the PBL. As reference, in-situ data on 14 June was used (Figure 8-11). On 14 June, AOD(532 nm) was very low (~0.1) with typical values of in-situ measurements compared with the statistical analysis performed by *Lyamani et al.* [2010] at the same station.

First, values of $\omega$(637 nm) and $\mathring{a}_{sca}$(450-700 nm) were markedly different in the afternoon on 14 and 27 June (Figure 8-10 and Figure 8-11). As can be seen in Table 8-2, $\omega$(637 nm) was larger on 27 than on 14 June as $\sigma_{sca}$(550 nm) was double on 27 June than on 14 June, whereas $\sigma_{abs}$ (637 nm) presented identical values in the afternoon of both days. In addition, $\mathring{a}_{sca}$(450-550 nm) was lower on 27 than on 14 June. These results indicate the predominance of coarse particles with high scattering contribution which is linked to a greater presence of mineral dust at the surface on 27 than on 14 June.

Table 8-2: Hourly mean of aerosol optical properties at 13:30 UTC on 14 and 27 June.

| Property (mean±SD) | 13:30 UTC 14 June | 13:30 UTC 27 June |
|---|---|---|
| $\sigma_{abs}$(637 nm) [Mm$^{-1}$] | 7±2 | 7±1 |
| $\sigma_{sca}$(550 nm) [Mm$^{-1}$] | 17±2 | 36±2 |
| $\omega$(637 nm) | 0.67±0.03 | 0.83±0.03 |
| $\mathring{a}_{sca}$(450-700 nm) | 1.8±0.2 | 0.91±0.05 |

Second, maxima of $\sigma_{sca}$(550 nm) and $\sigma_{abs}$(637 nm) during traffic-rush on 27 June were coincident in time although, on 14 June, the maxima of $\sigma_{abs}$(637 nm) and $\sigma_{sca}$(550 nm) were reached at 08:00 and 09:00 UTC, respectively. The temporal displacement found on 14 June was previously detected by [*Lyamani et al.*, 2010] and it is explained in terms of the time required for secondary particle formation in the atmosphere. Some hypothesis could be suggested to explain that the maxima of $\sigma_{sca}$(550 nm) and $\sigma_{abs}$(637 nm) were coincident in time during 27 June. The majority of scattering

aerosol particles emitted by anthropogenic activities are secondary aerosols formed by gas-to-particle conversion processes, like sulphates and nitrates [*Seinfeld and Pandis*, 1998]. However, if a high amount of particles are present in the atmosphere, gaseous deposition on particles can occur suppressing the gas-to-particle conversion processes and thus, the maxima of $\sigma_{sca}$(550 nm) and $\sigma_{abs}$(637 nm) would be coincident in time. In order to check this hypothesis, we can also analyse the evolution of the $PM_1$ and $PM_{10-1}$ as the gas-to-particle conversion causes an increase of $PM_1$ whereas the gaseous deposition on particles causes an increase of both $PM_1$ and $PM_{10-1}$. In this sense, on 14 June, the $PM_1$ and $PM_{10-1}$ presented a mean ($\pm$SD) of $41\pm2$ μg/m$^3$ and $28\pm2$ μg/m$^3$, respectively, around the maxima of $\sigma_{sca}$(550 nm) and $\sigma_{abs}$(637 nm) (08:10-08:30 UTC) (Figure 8-10 and Figure 8-11), whereas $PM_1$ and $PM_{10-1}$ were $31\pm2$ μg/m$^3$ and $34\pm2$ μg/m$^3$, respectively, during the same period on 27 June (Figure 8-11). Supporting this hypothesis, chemical composition measurements of Saharan dust aerosol, performed on Tenerife, Canary Islands, showed that internal aerosol mixing may occur (dust coated by sulphate in the coarse mode) during Saharan dust intrusions [*Rodriguez et al.*, 2011]. This is consistent with the reaction of different nitrate and sulphate species on dust surfaces [*Prospero et al.*, 1995; *Maring et al.*, 2000]. Finally, it is worthy to mention the study about the new particle formation given by *Sorribas et al.* [2014] performed at El Arenosillo station (Spain). This study shows a negative correlation between the growth rate in the range 14-30 nm and the $PM_{10}$ with land breeze and points that the particles within the coarse mode look like to inhibit the growth process. Therefore, the assessment of these results indicates that the entrainment of dust into the PBL can influence the internal mixing processes occurring within the PBL as the inhibition of the gas-to-particle conversion.
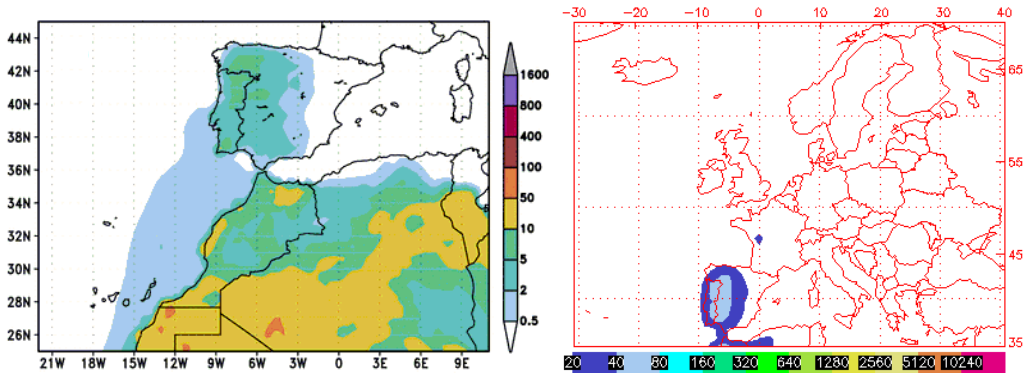
**Figure 8-12: Dry dust deposition [mg·m$^{-2}$] predicted by BSC-DREAM8b (left) and dust surface concentration [µg·m$^{-3}$] predicted by NAAPS (right) at 12:00 UTC 27 June 2011.**

As was aforementioned, NAAPS and BSC-DREAM8b forecast models successfully predicted the Saharan outbreak on 27 June 2011 in the atmospheric column over the Southern Iberian Peninsula as it was corroborated by lidar and sun-photometer measurements. However, NAAPS predicted absence of Saharan dust at surface on 27 June 2011 at 12:00 UTC whereas BSC-DREAM8b predicted downward entrainment of Saharan dust (Figure 8-12). As it has been previously indicated, the presence of Saharan dust was confirmed by in-situ instrumentation. Therefore, only BSC-DREAM8b predicted successfully the presence of Saharan dust on surface. The discrepancy with NAAPS could be related to the lack of a modelling of the interaction between FT and PBL due to strong convective processes.

## 8.4   Concluding remarks

Summarizing, the combination of measurements allowed the study of the interaction between the dust layer located in the FT and the PBL due to the enhancement of the convective processes. For this purpose, two different approaches were used. First, the temporal evolution of å$_\beta$ and δ$^p$ and $\beta_{dust}/\beta$ evidences an increase of the presence of mineral dust at lower levels along the

176

morning. Second, the temporal evolution of the FT and the PBL contributions to the total AOD shows an increase of the PBL contribution to the total AOD whereas the FT contribution decreases. Thus, the convective processes enhance the PBL which 'catches' the dust layer accelerating the downward dust entrainment. The study on the convection processes effect on the entrainment of aerosol load into the PBL could help to improve the models of aerosol transport and thus, further studies are needed.

The entrainment of the dust layer into the PBL caused significant variations on the aerosol optical properties. In this sense, the gas-to-particle conversion may be less important due to the gas deposition on particles surface when the mineral dust is present at surface level.

Regarding the role of lidar depolarization technique, the study of the temporal evolution of the particle linear depolarization ratio together with the backscatter-related Angström exponent leads to a better understanding of the mixing processes in the PBL. Furthermore, the depolarization measurements were used to split $\beta$ into the anthropogenic and mineral dust aerosol contributions using the POLIPHON method. Hence, this chapter showed the importance and potential of this technique in the atmospheric aerosol research.

# 9 Conclusions and outlook

The results of this thesis can be considered in two main topics: the improvements on the lidar depolarization technique and its applications to the atmospheric aerosol field. First, this thesis has contributed to the research field through the implementation and development of new depolarization calibration procedures and the detailed study of the lidar polarizing sensitivity. Second, the lidar depolarization technique was applied for determining the planetary boundary layer height and, for studying the interaction mechanisms between lofted aerosol layers and the PBL and its influence on the aerosol properties at surface.

Following, the achievements of this thesis are summarised in detail.

## 9.1 Methodological aspects

The Δ90°-calibration method with a rotator in front of the polarizing beam splitter (PBS) was successfully implemented in both MULHACEN and VELETA lidar systems. In addition, the Δ90°-calibration method with polarizer in front of the receiving optics was installed in MULHACEN. The combination of the two modes of the Δ90°-calibration method installed in MULHACEN allowed the development of a new procedure to determine the effective diattenuation of the receiving optics. Particularly, the effective diattenuation of the receiving optics for MULHACEN was evaluated in 0.35±0.03. The correction of this effective diattenuation of the receiving optics implied an increase of the particle linear depolarization ratio about 50% in those experimental cases with high depolarization-capability scatters (e.g., mineral dust). Additionally, a new procedure to determine the misalignment angle of the laser polarizing plane with respect to the incident plane of the polarizing beam

splitter was developed and applied to MULHACEN. The misalignment angle of the laser polarizing plane was estimated at 7°±1°.

The lidar polarizing sensitivity has been studied in detail by means of the Stokes-Müller formulism applied to lidar. To this end, a graphic user interface, called *Lidar Polarizing Sensitivity Simulator* (LPSS), has been developed. LPSS simulates the volume linear depolarization ratio, $\delta'$, uncertainty due to the uncertainties in lidar properties which can influence the polarization state of the laser or the receiving signal. In order to assess the total uncertainty due to the lidar polarizing sensitivity, a synthetic lidar was simulated using the uncertainties of lidar properties derived or assumed from different technical specifications of commercial optical devices. In some cases, the uncertainty ranges are very large due to the lack of information. From the analysis, the total uncertainty has been estimated in the range [–0.082, 0.243]. As typical $\delta'$ values ranges between 0.05 and 0.3, it can be concluded that the polarization sensitivity of lidar systems can affect the depolarization measurements to the point that the relative error of $\delta'$ would be larger than 100%. The most critical properties are the depolarization of the emitted laser light and the effective diattenuation of the receiving optics ($D_o$) with a contribution to the uncertainty is larger than 0.05. The emitting and receiving optics phase shifts and the rotational misalignment, between the polarizing plane of the laser and the incident plane of the PBS, are also relevant. These lidar properties contribute with 0.03 to the depolarization uncertainty. It is worthy to note that the uncertainty range is asymmetric, being greater the positive deviation, and thus, it can be concluded that the lidar polarizing sensitivity usually overestimates $\delta'$. In the case of MULHACEN and VELETA lidar systems, total uncertainty of $\delta'$ was estimated in the ranges [–0.03, 0.047] and [–0.08, 0.18], respectively.

## 9.2   Applications

The lidar depolarization technique has been applied to two topics of the atmospheric aerosol research: the determination of the planetary boundary layer height, $z_{PBL}$, and the study of the interaction mechanisms between Saharan dust layers and the planetary boundary layer (PBL).

The determination of the $z_{PBL}$ was performed through a new method developed in this thesis, called POLARIS (Pbl height estimatiOn based on Lidar depolARISation), using the wavelet covariance transform applied to the range corrected signal and the non-calibrated perpendicular-to-parallel signal ratio, both at 532 nm. By means of these profiles, different candidates for the $z_{PBL}$ are chosen and the attribution is performed through POLARIS. Finally, median filter was applied to obtain an appropriated temporal evolution of the $z_{PBL}$. POLARIS was applied, in an unsupervised way, to 72-hours lidar measurement performed in the ChArMEx 2012 where microwave radiometer measurements and radiosondes were available. Microwave radiometer measurements and radiosondes were used to obtain independent measurements of the $z_{PBL}$. The assessment of the obtained results demonstrate that the method presented by *Granados‑Muñoz et al.* [2012] and POLARIS show similar behaviour except in those cases when lofted aerosol layers are coupled to the planetary boundary layer (PBL). In these cases, the use of the depolarization profiles allows to distinguish between the PBL and the lofted aerosol layers. Therefore, the lidar depolarization technique allowed the improvement detection of the $z_{PBL}$ which is especially important in regions affected by desert dust outbreaks. To our knowledge, this is the first time that the lidar depolarization has been used to determine the $z_{PBL}$. Therefore, the extended application of POLARIS to lidars in networks such as EARLINET (European

Aerosol Research Lidar Network, [*Bösenberg*, 2001]), LALINET (Latin American Lidar Network, [*Robock and Antuña*, 2001]), MPLNET (Micro-Pulsed Lidar NETwork, [*Welton et al.*, 2001]) or ADNET (Asian Dust NETwork, [*Murayama et al.*, 2001]) could improve the automatic global-scale $z_{PBL}$ observations.

The lidar depolarization technique was also used in a case study combining co-located in-situ, passive and active remote sensing instrumentation and airborne in-situ measurements under a Saharan mineral dust scenario occurring on 27 June 2011. This case study was focused on the interaction mechanisms between the Saharan dust layer and the PBL, and the influence of mineral dust on the aerosol properties at the surface. It was demonstrated that the convective processes enhance the PBL which 'catches' the dust layer accelerating the downward dust entrainment. This result was based on: first, the temporal evolution of $å_\beta$, $\delta^p$ and $\beta_{dust}/\beta$, which demonstrate an increase of mineral dust at lower levels along the morning; second, the temporal evolution of the free troposphere and the PBL contributions to the total aerosol optical depth (AOD), showing an increase of the PBL contribution to the total AOD whereas the free troposphere contribution decreases. Additionally, it was shown that entrainment of the dust layer into the PBL causes significant variations on the aerosol optical properties changing the typical hourly evolution of working days. In this sense, under mineral dust present at surface level, the gas-to-particle conversion may be less important due to the gas deposition on particle surfaces.

## 9.3 Outlook

The analysis of the lidar polarizing sensitivity and the combination of different depolarization calibration methods has shown the relevance of the systematic error caused by an insufficient characterization of the lidar polarizing response to obtain trustable depolarization measurements. Therefore, the research of this field has to continue in different ways. First, deeper analysis of the lidar polarizing sensitivity is needed. For example, there are indications that the polarizing effect of Cassegrain telescopes is negligible but it could be important for reflector telescopes. Also, it was recently discovered that the laser light can be elliptically polarized[18] resulting in an overestimation of the depolarization products. Second, it is necessary to improve the depolarization calibration methods or develop a combination of procedures which allows the whole characterization of the lidar polarizing sensitivity and hence, the retrieval of depolarization products with lower uncertainties.

Concerning the automatic detection of the $z_{PBL}$ using depolarization products, as the sensitivity of the aerosol structure detection increases with wavelength, the new proposed method could improve the detection using depolarization at infrared wavelengths. This fact would support the implementation of depolarization in the new generation of ceilometers.

Furthermore, the lidar depolarization technique seems to be very useful in the study of mixing processes. However, internal and external mixture still being indistinguishable by means of lidar technique and thus, the use on

---

[18] As result of the ACTRIS Trans-national Access project titled *Error estimation in calibrated depolarization lidar measurements*. Project PI: Professor L. Alados-Arboledas. PI for RADO (Rumanian Atmospheric 3D Observatory): Dr. Doina Nicolae. Researchers: J. A. Bravo-Aranda, L. Belegante and V. Freudenthaler (October 2013, Bucharest, Romania).

ancillary information (e. g., in-situ measurements) is crucial. Therefore, further investigation is also required.

As both lidar systems, MULHACEN and VELETA, have been characterized in this thesis, depolarization products at 355 and 532 nm are available and thus, its spectral dependence may be used to study the aerosol typing. Additionally, depolarization products at 355 and 532 nm may be used to decrease the range of possible solutions of the microphysical retrieval, based on spheres and spheroids, being developed by the Atmospheric Physics Research Group.

# Conclusiones y perspectivas

Los resultados más relevantes de esta tesis pueden dividirse en dos temáticas bien diferenciadas: la mejora de la técnica de despolarización y sus aplicaciones en el campo de investigación del aerosol atmosférico. En primer lugar, esta tesis contribuye a través de la implementación y desarrollo de nuevos procedimientos de calibración de la despolarización y el estudio detallado de la sensibilidad polarizadora de los sistemas lídar. En segundo lugar, la técnica de despolarización lídar se ha aplicado satisfactoriamente al ámbito del aerosol atmosférico. Para ello se ha desarrollado un método de determinación automática de la altura de la capa límite planetaria ($z_{PBL}$) y se han estudiado los mecanismos de interacción entre capas de aerosol elevadas y la capa límite planetaria (PBL).

A continuación, se exponen detalladamente los logros de esta tesis.

## 9.1 Aspectos metodológicos

Se ha implementado con éxito, tanto en el sistema MULHACEN como en VELETA, el método de calibración de Δ90° basado en rotaciones ante el divisor de haz polarizante. Además, se instaló el método de calibración de Δ90° basado en rotaciones de un polarizador lineal ante la óptica receptora en MULHACEN. La combinación de ambos modos de calibración en MULHACEN permitió el desarrollo de un nuevo procedimiento para determinar la diatenuación efectiva de la óptica receptora. Concretamente, se ha determinado experimentalmente una diatenuación efectiva de 0.35±0.03 para MULHACEN. La corrección de esta diatenuación efectiva ha producido un aumento de la razón de la despolarización de partículas de entorno el 50 % en aquellos casos de estudio cuyas partículas presentaban una alta capacidad despolarizadora (por ejemplo, polvo mineral). Además, se ha desarrollado un

nuevo procedimiento experimental para determinar el ángulo de desalineamiento del plano de polarización del láser respecto del plano de incidencia del divisor de haz polarizante, estimándose un valor de 7°±1° para el sistema lídar MULHACEN.

Haciendo uso del formulismo de Stokes-Müller, se estudió detalladamente la sensibilidad polarizadora de los sistemas lídar. Con este fin, se desarrolló una interfaz gráfica, llamada *Lidar Polarizing Sensitivity Simulator (LPSS)*. Esta interfaz simula la incertidumbre de la razón de despolarización volúmica debido a las incertidumbres en las propiedades del lídar que pueden afectar al estado de polarización tanto del láser como de la señal recibida. Con el fin de evaluar la incertidumbre total debida a la respuesta polarizadora de los lídares, se diseñó un lídar sintético usando datos derivados de diferentes especificaciones técnicas de dispositivos ópticos comerciales. En algunos casos, el rango de incertidumbre usado fue muy grande debido a la falta de información. El análisis realizado estima que la incertidumbre total es de [−0.082, 0.243]. Como los valores típicos de la razón de despolarización volúmica varían entre 0.05 y 0.3, se concluye que la respuesta polarizadora de los sistemas lídar puede afectar a las medidas de despolarización hasta tal punto que el error relativo de la razón de despolarización volúmica sería mayor del 100 %. Las propiedades más influyente son la pureza de la polarización del láser y la diatenuación efectiva de la óptica receptora, cuya contribución a la incertidumbre es mayor del 0.05. Le siguen en orden de importancia el desfase de las ópticas emisoras y receptoras y el ángulo de desalineamiento entre el plano de polarización del láser y el plano de incidencia del divisor de haz polarizante, con una contribución del 0.03 a la incertidumbre total. Merece la pena poner de manifiesto que el rango de incertidumbre es asimétrico, siendo mucho mayor la desviación positiva. Por lo tanto, puede concluirse que,

190

generalmente, la respuesta polarizadora sobrestima la razón de despolarización volúmica. En el caso de MULHACEN y VELETA, la incertidumbre total de la razón de despolarización volúmica se estima en los rangos [−0.03, 0.047] y [−0.08, 0.18], respectivamente.

## 9.2 Aplicaciones

La técnica de despolarización lídar ha sido aplicada a dos ámbitos de la investigación sobre aerosol atmosférico: la determinación automática de la $z_{PBL}$ y el estudio de los mecanismos de interacción entre capas de polvo mineral sahariano y la PBL.

La determinación automática de la $z_{PBL}$ se ha realizado a través de un nuevo método desarrollado en esta tesis, llamado POLARIS (*PBL height estimatiOn based on Lidar depolARISation*), basado en la aplicación de la transformada *wavelet* a la señal corregida de rango y a la razón de las señales perpendicular y paralela, ambas en 532 nm. De estos perfiles se eligen tres candidatos a $z_{PBL}$, escogiéndose uno de ellos a partir mediante POLARIS. Finalmente, se usa un filtro de mediana para obtener una apropiada evolución temporal de la $z_{PBL}$. POLARIS se ha aplicado automáticamente a una medida continua de 72 horas realizada en el marco de ChArMEx[19] 2012, donde se midió simultáneamente con un radiómetro de microondas y se lanzaron tres radiosondeos. Los datos del radiómetro de microondas y de los radiosondeos se usaron para determinar independientemente la $z_{PBL}$. La evaluación de los resultados obtenidos demuestran que POLARIS y el método presentado por *Granados‑Muñoz et al.* [2012] muestran un comportamiento similar, excepto

---

[19] *Chemistry-Aerosol Mediterranean Experiment, http://charmex.lsce.ipsl.fr*

ante la presencia de capas de aerosol acopladas a la PBL. En estos casos el uso de perfiles de despolarización permite distinguir entre la capa de aerosol elevada y la PBL. Por lo tanto, la técnica de despolarización lídar ha permitido la mejora de la detección automática de la $z_{PBL}$, lo cual es especialmente relevante en aquellas regiones afectadas frecuentemente por intrusiones de polvo mineral desértico. Según nuestro conocimiento, esta es la primera vez que se usa la técnica de despolarización lídar para determinar la estratificación atmosférica. Por lo tanto, el uso extendido de POLARIS en redes de sistemas lídar como EARLINET (European Aerosol Research Lidar Network, [*Bösenberg*, 2001]), MPLNET (Micro-Pulsed Lidar NETwork, [*Welton et al.*, 2001]) o ADNET (Asian Dust NETwork, [*Murayama et al.*, 2001]) podría mejorar la observación automática de la $z_{PBL}$ a escala global.

La técnica de despolarización lídar también se utilizado para un caso de estudio bajo condiciones de intrusión de polvo mineral sahariano ocurrido el 27 de junio de 2011. En este estudio se ha utilizado instrumentación activa, pasiva e in situ, así como instrumentación in situ a bordo de un avión bajo una. Las medidas realizadas con esta instrumentación se usaron para el estudio de los mecanismos de interacción entre una capa de polvo mineral sahariano y la PBL y la influencia de la presencia de polvo mineral en las propiedades del aerosol a nivel superficial. En primer lugar, se demostró que los procesos convectivos que se desarrollan en la PBL «atrapan» la capa de polvo mineral acelerando su arrastre hacia la superficie. Este resultado se obtiene como consecuencia de la evolución temporal de $å_{\beta}$, $\delta^{p}$ y $\beta_{dust}/\beta$. Estos parámetros muestran un aumento de la presencia de polvo mineral a niveles bajos a lo largo de la mañana. Por otra parte, también se analizó la evolución temporal de la contribución de la troposfera libre y la PBL a la profundidad óptica del aerosol total. En este

sentido, se observó un aumento de la contribución de la PBL al AOD total y una disminución de la contribución de la troposfera libre a pesar de que el AOD permaneció casi constante a lo largo del día. Además, se puso de manifiesto que la entrada de polvo mineral en la PBL produce cambios significativos en las propiedades ópticas del aerosol modificando, por ejemplo, la típica evolución horaria de los días laborables. En este sentido, bajo la presencia de polvo mineral cerca de superficie, la conversión gas-partícula podría ser menos importante debido a la deposición de las moléculas gaseosas en la superficie de las partículas.

## 9.3 Cuestiones científicas abiertas

El análisis de la sensibilidad polarizadora de los sistemas lídar y la combinación de diferentes procedimientos de calibración de la despolarización han mostrado la importancia de los errores sistemáticos producidos por una insuficiente caracterización de la respuesta polarizadora. Por lo tanto, la investigación en este campo debe continuar teniendo en cuenta diferentes objetivos. En primer lugar, es necesario un análisis más profundo de la sensibilidad polarizadora. Por ejemplo, ya hay indicativos de que los efectos de los telescopios de tipo Cassegrain son despreciables, pero podrían ser importantes para los telescopios de tipo reflector. También, recientes experimentos han mostrado que la luz láser podría estar elípticamente polarizada, lo que implicaría una sobrestimación de los productos derivados de las medidas de despolarización[20]. En segundo lugar,

---

[20] Como resultado del proyecto ACTRIS de Acceso Trasnacional titulado *Error estimation in calibrated depolarization lidar measurements*. IP del proyecto: Dr. L. Alados-Arboledas. IP de la estación RADO (*Rumanian Atmospheric 3D Observatory*): Dra. Doina Nicolae. Investigadores: J. A. Bravo-Aranda, L. Belegante y V. Freudenthaler (October 2013, Bucarest, Rumania).

es necesario mejorar los métodos de calibración o desarrollar un conjunto de procedimientos para caracterizar la respuesta polarizadora de los lídares y así determinar los productos de la despolarización con menor incertidumbre.

En relación a la determinación automática de la altura de la capa límite planetaria usando POLARIS, sería muy interesante usar la despolarización con longitudes de onda mayores (por ejemplo, 1064 nm), ya que la sensibilidad de la detección de estructuras aumenta con la longitud de onda. Este hecho apoyaría la implementación de la despolarización en la nueva generación de ceilómetros.

Por otra parte, la técnica de despolarización lídar parece ser muy útil para el estudio de los procesos de mezcla. Sin embargo, los procesos de mezcla interno y externo son indistinguibles usando la despolarización lídar, por lo que es crucial el uso de información complementaria extraída, por ejemplo, de instrumentación in situ. Por lo tanto, es necesaria una mayor investigación en este sentido.

Dado que en esta tesis se han caracterizado MULHACEN y VELETA, es posible obtener razones de despolarización a dos longitudes de onda, 355 y 532 nm, por lo que el uso de la dependencia espectral de la despolarización es uno de los siguientes pasos. Esta dependencia espectral podría usarse tanto para mejorar la caracterización del aerosol atmosférico como en inversiones microfísicas. Concretamente, la razón de despolarización de partículas a 355 y 532 nm podría utilizarse para reducir el rango de soluciones posibles en los código de inversiones de propiedades microfísicas, tanto si se utiliza la aproximación de partículas esféricas como esferoides. Actualmente, en el Grupo de Física de la Atmósfera estamos trabajando en el desarrollo de este tipo de códigos de inversión.

194

# Appendix A: Software

## INDRA (Interface for Depolarization and Raman Analysis)

This section has the aim to be a manual for initial users to facilitate the use of INDRA. Knowledge about lidar is required to use this software.

INDRA is a graphical user interface (GUI) developed in MATLAB with more than 10 000 lines of code, 50 new functions and 7 sub-interfaces. The main INDRA interface is shown in the next page. The last version of this software, INDRA 4.1.8, includes the following tools:

- Elastic retrieval
- Inelastic retrieval
- Depolarization retrieval
- Overlap function retrieval
- Error bars retrieval
- Output in EARLINET format

INDRA works with MULHACEN and VELETA data and allows the simultaneous analysis of both lidar data.

Following, INDRA is explained providing the necessary information for its appropriate use.

### MULHACEN/VELETA data folders

Raw data are uploaded through the modules 1.1 and 1.2 for MULHACEN and VELETA respectively, shown below. *Input Data*, *DC Data* and *Output Data* buttons allow the selection of the folders that contain the measured data, the dark current measurement and the folder where the results are saved. Both

**Figure A-1: Main INDRA interface.**

MULHACEN and VELETA can be individually or jointly analysed saving the results in the same folder defined by *Output Data*.



**Figure A-2: Modules 1.1 and 1.2 used to upload the raw data.**

### Pre-processing

Once the data folders are selected, the pre-processing options are defined following the module:



**Figure A-3: The pre-processing module applied to raw data: background and dark current subtraction, trigger delay and overlap correction.**

*BG range*: Height range (in km asl) used to compute the background signal. This value is calculated and subtracted for each signal profile.

- *Top height*: Maximum height (in km asl) of the profiles used by INDRA.

- *Bin configuration*: Trigger delay values are included using this button. There are two options:

  o *Standard*: Trigger delay values determined in the Section 4.1.1.3.

  o *By user*: Trigger delay values defined by user can be introduced by the sub-interface shown below (MULHACEN and VELETA panels).

**Figure A-4: Popup interface to introduce the bin-zero values for MULHACEN (top) and for VELETA (bottom).**

- o *Overlap correction*: When checked, overlap function can be uploaded to perform the overlap correction.

- o *Dark Current*: When checked, dark current measurements selected in *DC Data* are used to perform the dark current subtraction (only for analog channels).

- o *Accept!*: the pre-processing is performed. Additional pop-up windows could appears to load necessary files (e.g., overlap function file). This step could take one minute or less depending on the number of files to average, dark current subtraction and the PC characteristics. In this step, error window may indicate possible mistakes in the procedure. For example, Figure A-5 indicates that the selected raw data folder is empty.



**Figure A-5: Error window *Fatal error*.**

**Optical retrieval**

This module allows the elastic, inelastic and depolarization retrieval and thus is the main part of INDRA.

- *3.1.- Atmosphere*: this pop-up menu allows the selection of the source of the atmospheric temperature and pressure profiles:
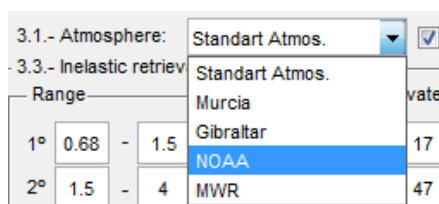


  o *Standard Atmos.:* atmospheric meteorological profiles are retrieved through the Standard Atmosphere 1976 scaled to the surface temperature and pressure taken from data of a co-located meteorological station.

  o *Murcia/Gibraltar:* INDRA obtains the radiosonde of Murcia or Gibraltar nearest in time when internet connection is available. These two locations are the closest stations with radiosonde launches. A warning window appears when data are not available.

    o *NOAA:* user can select radiosonde files from the NOAA (National Oceanic and Atmospheric Administration) website. The temperature and pressure profiles provided by NOAA website are an interpolation among the closest launched radiosondes.

  o *MWR:* combination of temperature profile provided by the microwave radiometer and the pressure from the Standard Atmosphere 1976 scaled to the pressure at surface.

  The check box allows the user to know if this step was successfully performed.

- *3.2.- Wavelength*: This button allows user to select the wavelength to perform the retrievals. Information shown in the panels 3.3 to 3.6 is related to this selected wavelength. Information of the panels 3.3 to 3.6 are always saved for each wavelength. INDRA allows the retrieval of the optical properties of each wavelength choosing the analog (AN), photon counting (PC) or glued (GL) signal if available.
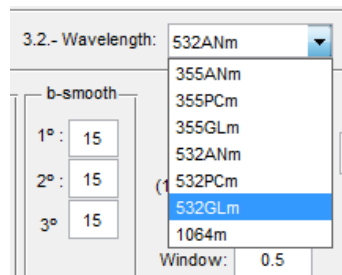


  o *Gluing sub-interface*: gluing of AN and PC signal is performed by means of the sub-interface (Figure A-6). The gluing procedure requires a range where the AN and PC signals present a linear behaviour. According to *Navas Guzmán* [2011], the optimal range for gluing is defined by AN and PC signal intensities. The lowest height of the optimal range is delimited by the PC signal intensity which has to be lower than 20 MHz (see graphic PC signal, orange arrow). The highest height of the optimal range is delimited by the AN signal which has to be larger than the 10% of the background signal (see graphic AN signal, yellow arrow).

    – *Min. gluing* and *Max. gluing* are the minimum and maximum of the gluing range (in km asl) selected by user.

    – *Try it!*: the linear fit can be evaluated by user using this button and the axes with the *Correlation Coeff.* in the title (purple arrow).

- *Get current values*: selects the last range checked by user and plot the results in the horizontal axes (red arrows). The green line is the glued signal.
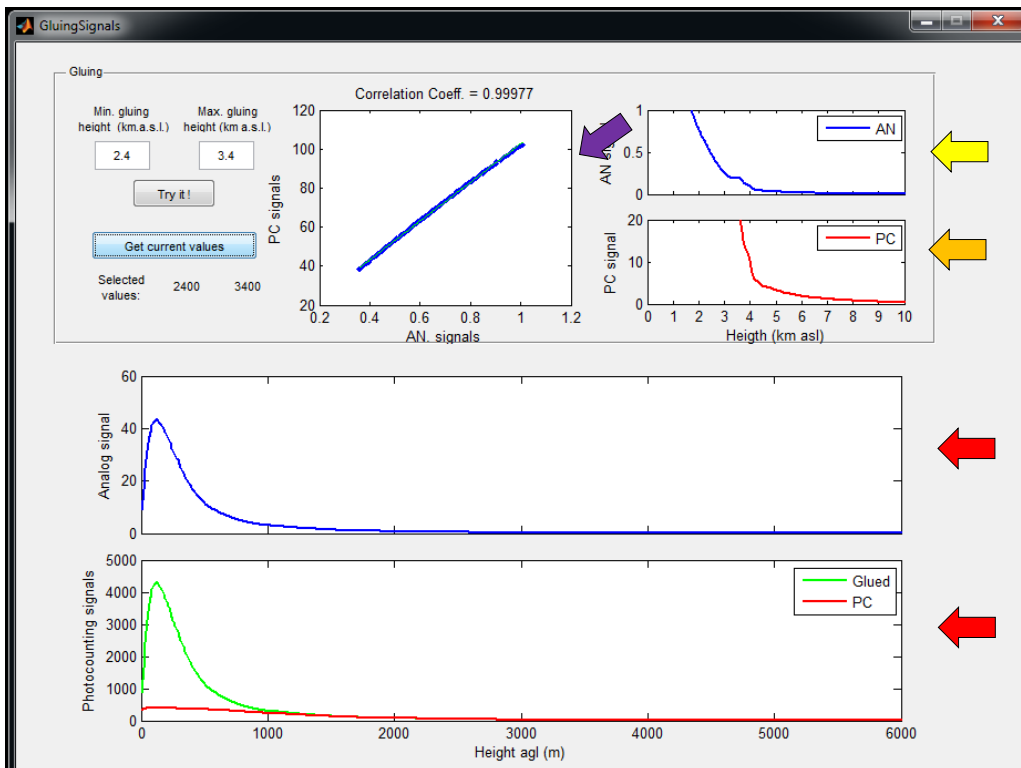


**Figure A-6: Popup interface to perform the gluing signals.**

- *3.3.- Raman retrieval*: this module, which is active only when Raman channels are available, includes all the required variables for the inelastic retrieval of the particle extinction and the backscatter coefficients as it is shown below:

- o *Range*: lidar raw profile is divided in three different height ranges to perform the optimal smooth and derivate for each range.
- o *e-smooth*: number of bins for the moving average smoothing perform to the Raman signal before the retrieval.
- o *Derivate:* number of bins for the linear fit. The slope of the linear fit provides the derivate of the Raman signals, which is used to retrieve the particle extinction coefficient profile.
- o *Spec.*: it is the assumed potential of the wavelength dependence of the aerosol extinction in the inelastic retrieval. More information in Section 4.1.3.
- o *BCR:* acronym of particle backscatter coefficient reference. Typically, an aerosol-free region is assumed as height reference and thus, $\beta$ is assumed zero. However, this text box allows the selection of a non-zero value.
- o *Z ref*: reference height needed to perform the inelastic retrieval.
- o *Window*: height range around *Z ref* to perform the average of the lidar signal.

   Both *Z ref* and *Window* can be evaluated using the Rayleigh fit plot. An example is shown in Figure A-7.
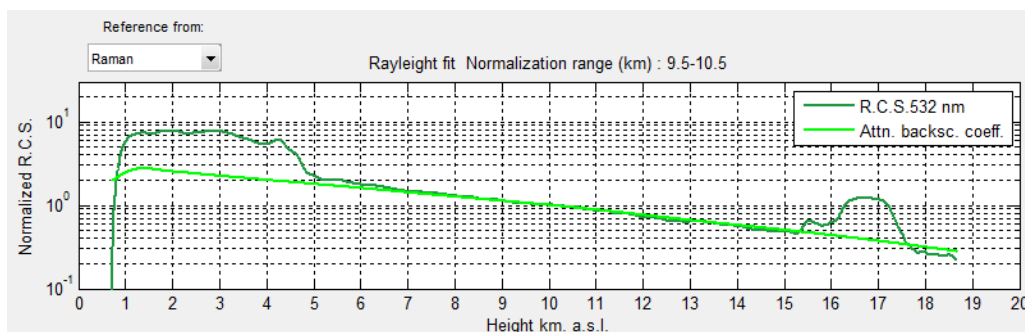
**Figure A-7: Rayleigh fit shown in the main INDRA interface. Upper left button is used to plot the Rayleigh fit using two different reference heights.**

- o *Extinction available range*: the inelastic retrieval allows the retrieval of the particle backscatter coefficient using the previously calculated particle extinction coefficient profile. Using these text boxes, the user can select the suitable range of this profile.

- *Retrieve*: perform the inelastic retrieval for the wavelength selected in the *wavelength* pop-up menu. The inelastic retrieval procedure can be performed iteratively in order to optimize the results. Only the parameters and results of the last retrieval are saved. The check box indicates whether the calculus was successfully performed.

- *3.4.- Elastic retrieval*: this module includes all the required variables for the elastic retrieval of the particle backscatter coefficient. Three different types of elastic retrieval are presented in INDRA included in the pop-menu within the module *Calibration method* (see Figure below).
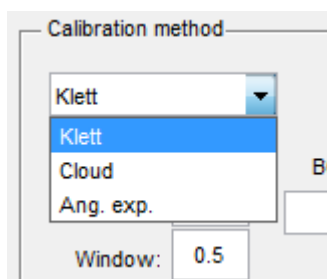
o *Klett:* This is the classical elastic retrieval which uses the parameters: *LR*, *Z ref.*, *Window* and *BCR*. These parameters are explained below.
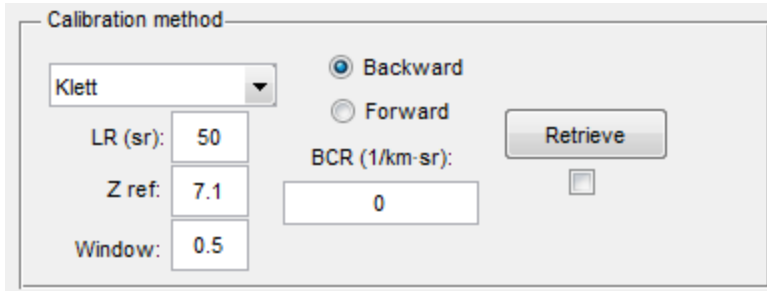


o *Cloud*: this procedure was included for the infrared channel calibration. The idea is calibrating with a channel (355 or 532 nm) with a large SNR in the far height range (above the cirrus cloud), where the aerosol component is negligible, and to retrieve the particle backscatter profile at this wavelength. After that, the value of the particle backscatter coefficient at cloud base is used as BCR of the infrared channel as $\beta_{par}$ is essentially independent of wavelength in cirrus clouds. For further details see [*Navas Guzmán*, 2011].
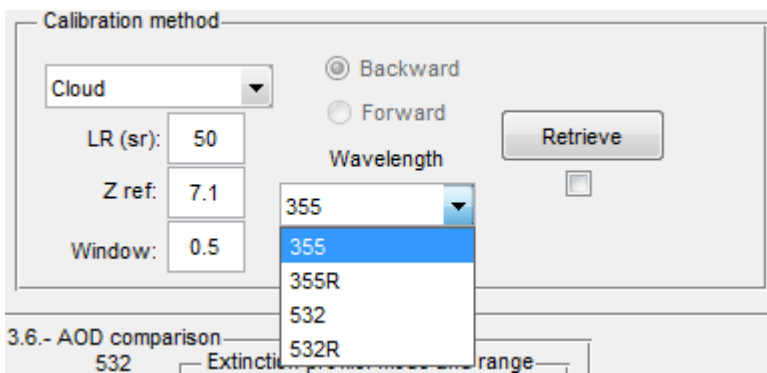


o *Angs. Exp.*: This module implements an alternative calibration developed for calibrating the infrared channel as the presence of cirrus clouds does not always occur. In this case, non-zero BCR at near-

height range is not assumed by the user but determined using the backscatter-related Angström exponent retrieved with the other two wavelengths (e.g., 355 and 532 nm). Further details were given by *Navas Guzmán* [2011]. In the next figure, it can be seen a pop-up menu named *Ang. exp. Ref.* with different options to retrieve the backscatter-related Angström exponent of 355 and 532 nm. Numbers without letters indicates elastic retrieval using MULHACEN data, R means inelastic retrieval and V indicates the use of VELETA data.
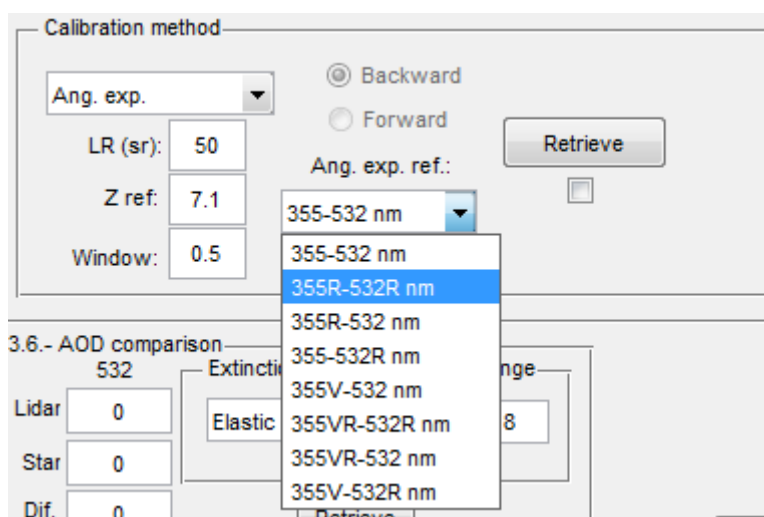


- o *LR (sr)*: the assumed LR has to be introduced here by the user.
- o *Z ref*: reference height needed to perform the elastic retrieval.
- o *Window*: the range around *Z ref* to perform the average of the lidar signal.

Both *Z ref* and *Window* can be evaluated using the Rayleigh fit plot. An example is shown below.
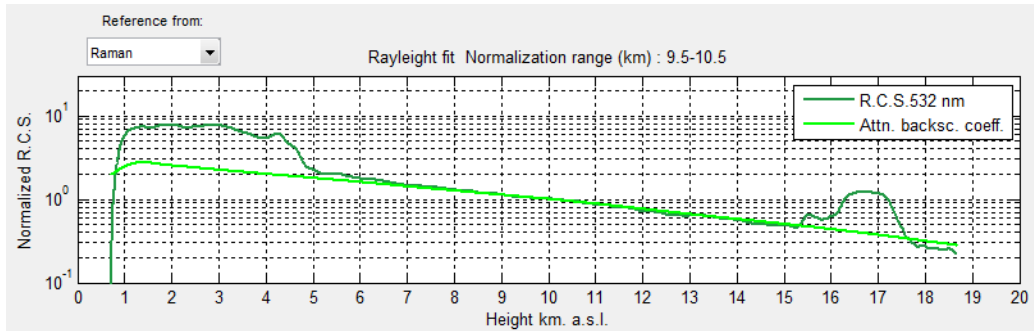
o *Backward/forward*: buttons allowing the retrieval of the backward and forward solution for the particle backscatter coefficient. The forward solution used to be instable and thus, it is not commonly used.

o *BCR ($km^{-1} \cdot sr^{-1}$):* acronym of particle backscatter coefficient reference. Typically aerosol-free region is assumed as height reference and thus, $\beta$ is assumed zero. However, this text box allows the selection of a non-zero value.

o Retrieve: perform the elastic retrieval for the wavelength selected in the *wavelength* pop-up menu. The elastic retrieval procedure can be performed iteratively in order to optimize the results. Only the parameters and results of the last retrieval are saved. The check box indicates whether the calculus was successfully performed.

o Smooth: this module allows the smoothing of the particle backscatter coefficient profile.

o *Zmin./Zmax.*: heights introduced in these text boxes split the profile in three regions: 0-*Zmin*; *Zmin-Zmax* and *Zmax-Top height*. Then, the number of bins of the moving average applied to each region is defined by *S1*, *S2* and *S3*.

o *S1/S2/S3:* number of bins of the moving average applied to each region defined by *Zmin./Zmax.*

o *Smooth it:* perform the smooth to the elastic $\beta_{par}$ for the wavelength selected in the *wavelength* pop-up menu. Check box indicates whether the calculus was successfully performed.



- *AOD comparison*: it allows the comparison of the AOD derived from sun or star photometer (external information provided by user) with the lidar AOD retrieved as the integral of the particle extinction coefficient (provided by INDRA).



o *Extinction profile: mode and range*: the particle extinction coefficient profile from elastic or inelastic retrieval as well as the integral range is selected using this module. Other option, called *Combined*, allows the calculus of the integral using the gluing between the inelastic extinction coefficient profile and the inelastic backscatter coefficient multiplied by the lowermost LR value.
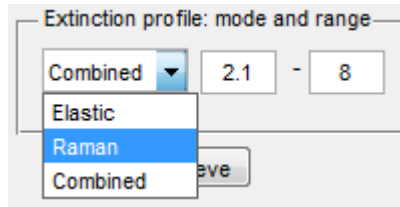
- o *Lidar*: AOD retrieved using the extinction coefficient profile determined with lidar data.

- o *Star*: AOD measured by means of sun- or star-photometer. This information has to be introduced by user.

- o *Dif*: Difference between both *Lidar* and *Star* values. It is a very useful tool to determine the best LR value for the elastic retrieval.

- o *Retrieve*: perform the AOD calculus and generate figures with information about the contribution to AOD of the overlap and profile height ranges as it is shown in the example of the figure below.
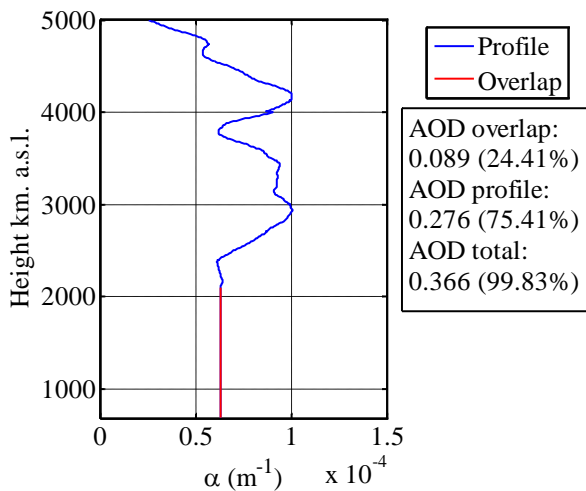


- • 3.5.- *Depolarization retrieval*: Volume and particle linear depolarization ratio profiles are retrieved using the check boxes VLDR and PLDR, respectively.

- o *Alpha*: rotational misalignment of the polarizing plane of the laser light respect to the incident plane of the PBS can be introduced by user. Default value is 7° according to Section 5.4.
- o *Ref. range*: $\delta'$ background value in the range defined by *Min.* and *Max.* can be subtracted to the whole profile as it is assumed to be due to depolarization of the laser.
- o *Min.*/Max: Region where the $\delta'$ background value is calculated.
- o *Rmin*: As the particle linear depolarization ratio becomes instable for low values of backscattering ratio (R), this text box allows the removal of these regions of $\delta^p$ with R<*Rmin*.
- *PAINT ALL*: depicts the new retrieved optical properties profiles in the vertical axes shown in Figure A-8. From left to right, axes presents the particle extinction coefficient profiles derived with inelastic retrieval (x-label: $\alpha_p(m^{-1})$), particle backscatter coefficient profiles derived with elastic and inelastic retrieval (x-label: $\beta_p(m^{-1} \cdot sr^{-1})$), particle lidar ratio profiles derived with inelastic retrieval (x-label: $LR_p(sr)$), extinction- and backscatter-related Angström exponent derived with different pairs of wavelengths (x-label: Angstrom Exponent) and finally, molecular, volume and particle linear depolarization ratio (x-label: δ).
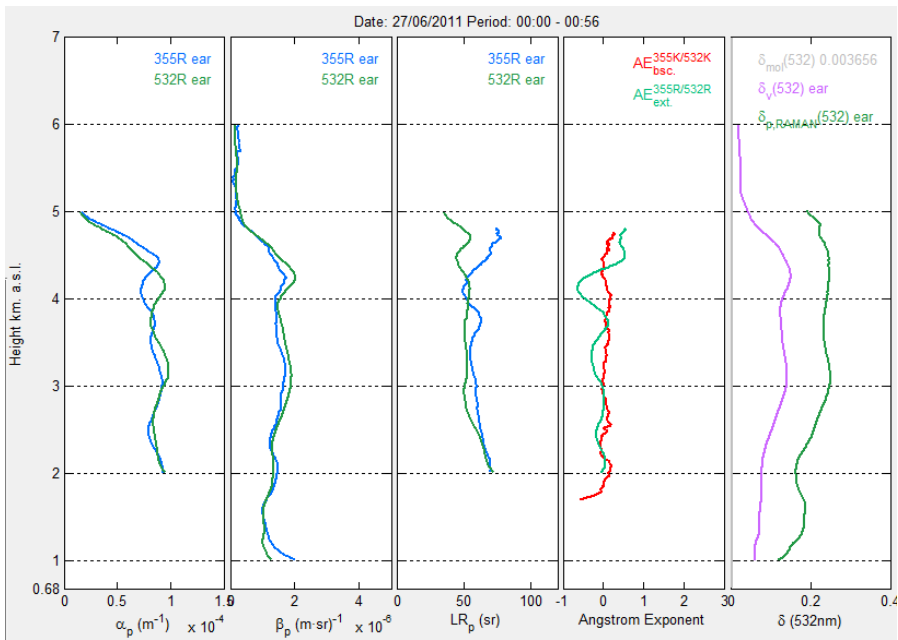
**Figure A-8: Rayleigh fit shown in the main INDRA interface. Upper left button is used to plot the Rayleigh fit using two different reference heights.**

- *to paint*: this button provides access to a sub-interface (Figure A-9) allowing the user to select the lidar products which will be shown in the vertical axes of the INDRA interface. *Backscatter ratio thresholds* can be used by user to paint the regions of the profiles with a certain level of aerosol load defined by the backscattering ratio, R. *Select Profiles* button saves the preferences and returns to INDRA.
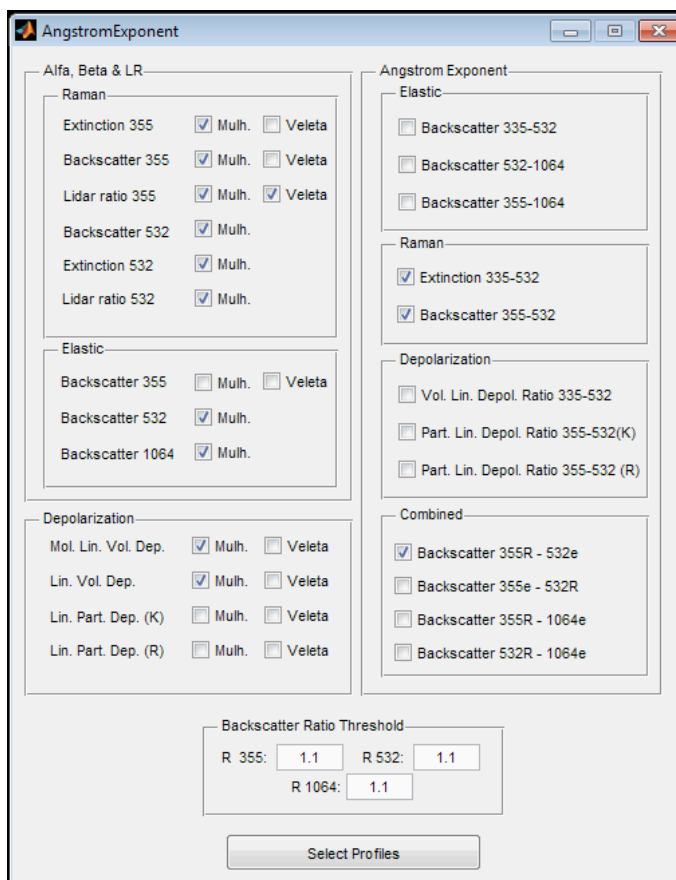
**Figure A-9: Interface *AngstromExponent*.**

## Overlap retrieval

This button provides access to another GUI which allows the retrieval of the overlap function of the 355 and 532 nm channels.
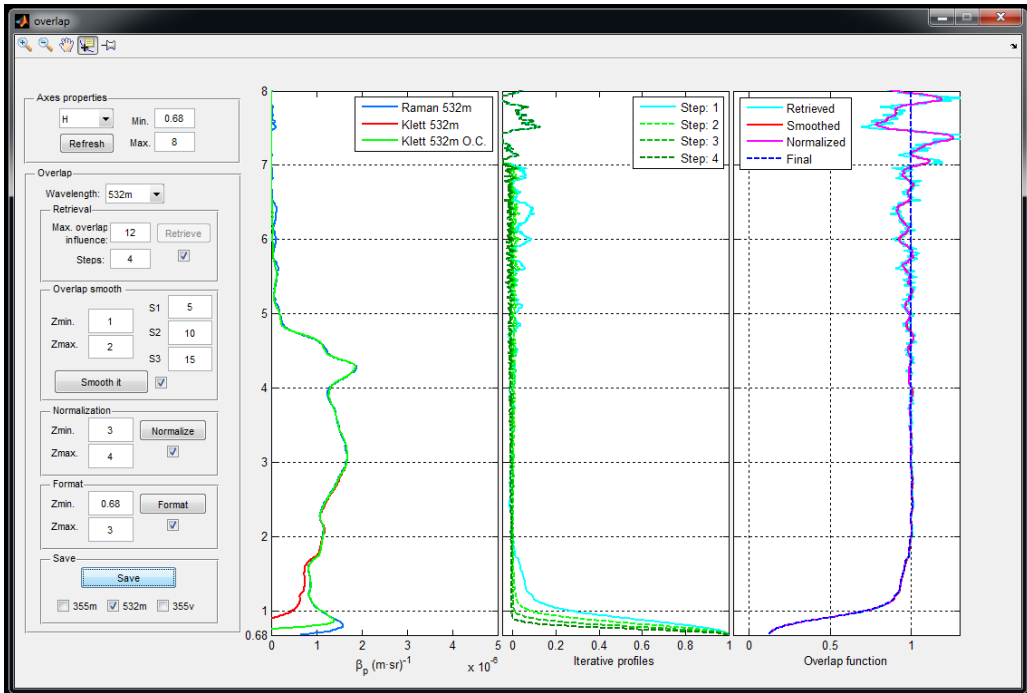
o   *Axes properties*: the pop-up menu allows the selection of the x-label or y-label for the three vertical axes included in the interface. Limits are selected using the *Min.* and *Max.* text boxes. Then, *refresh* updates the axes.
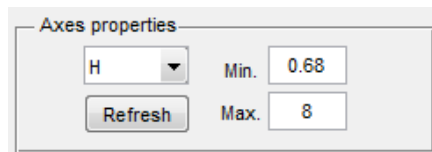


o   *Wavelength*: Wavelength of the lidar overlap function.
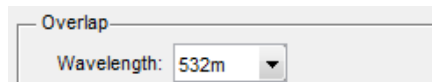


o   *Retrieval*: the iterative method proposed by *Wandinger and Ansmann* [2002] is used to determine the lidar overlap function. The method is based on the simultaneous measurement of pure molecular and elastic

backscattered signal using a Raman lidar system. The iterative approach is based on the fact that the elastic backscattered signal, after corrections for range and overlap dependency, is proportional to the aerosol backscatter coefficient.



- − *Max. overlap influence:* it is the height where user estimates full overlap.
- − *Steps*: number of iterations.
- − *Retrieve*: runs the procedure, depicts the different iterations in the first two vertical axes and the final retrieved overlap function in the third axes (see next figure). Check box indicates whether the calculus was successfully performed.
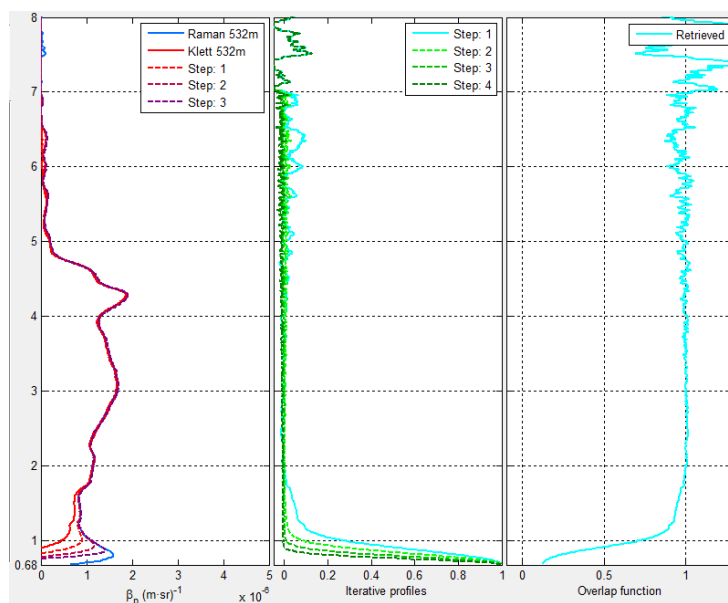


**Figure A-10: Outputs depicted by the module *Retrieval*.**

o *Overlap smooth*: this module allows the smoothing of the overlap function profile.
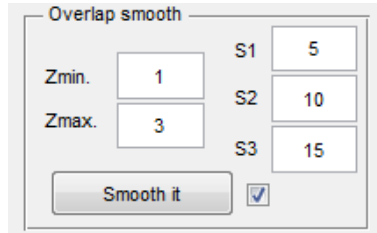


‒ *Zmin./Zmax.*: heights introduced in these text boxes split the profile in three regions: 0-*Zmin*; *Zmin-Zmax* and *Zmax- Max. overlap influence*. Then, the number of bins of the moving average applied to each region is defined by *S1*, *S2* and *S3*.

‒ *S1/S2/S3:* number of bins of the moving average applied to each region defined by *Zmin./Zmax.*

‒ *Smooth it:* performs a smoothing to the overlap function for the wavelength selected in the *wavelength* pop-up menu and depicts the smoothed overlap function as it is shown in the next figure. Check box indicates whether the calculus was successfully performed.
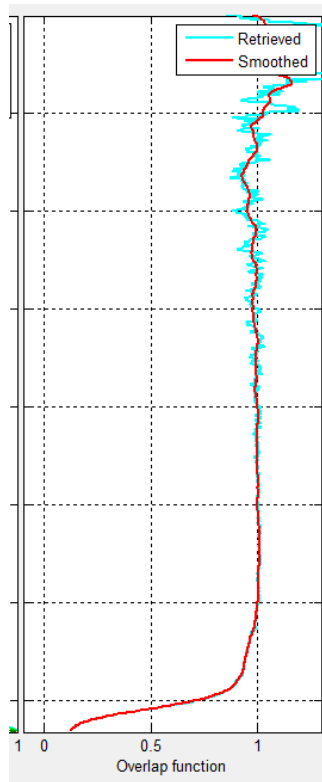
**Figure A-11: Output depicted by the module *Overlap smooth*.**

o  *Normalization*: Overlap function is scaled up to one in the far range defined by *Zmin.* and *Zmax.* text boxes.



&ndash;  *Zmin.* and *Zmax.*: height range of the normalization.

&ndash;  *Normalize*: performs the normalization to the overlap function for the wavelength selected in the *wavelength* pop-up menu and depicts the normalized overlap function as it is shown in the next figure. Check box indicates whether the calculus was successfully performed.

217
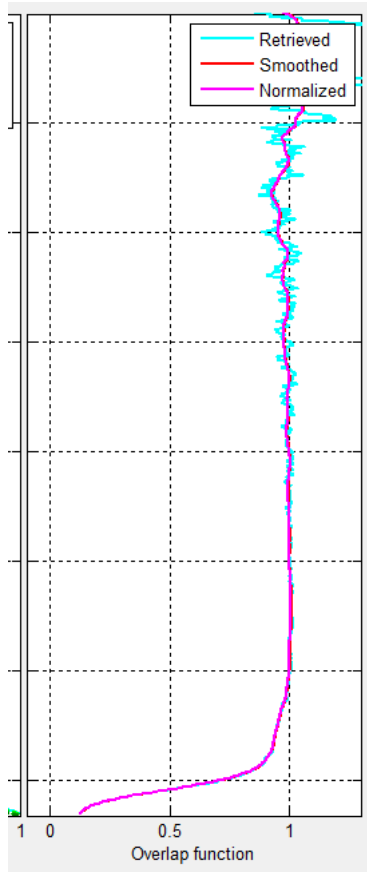
**Figure A-12: Output depicted by the module *Normalize*.**

o *Format*: the range of the correct overlap function profile, defined by *Zmin.* and *Zmax.* text boxes (in km asl), is selected. Below *Zmin.* height, overlap function value is NaN (Not a Number). Above *Zmax.* height, overlap function value is one.



o *Zmin.* and *Zmax.*: range of the correct overlap function profile.

o  *Format*: sets the NaN below *Zmin.* and ones above *Zmax.* for the overlap function of the wavelength selected in the *wavelength* pop-up menu. Check box indicates whether the calculus was successfully performed.
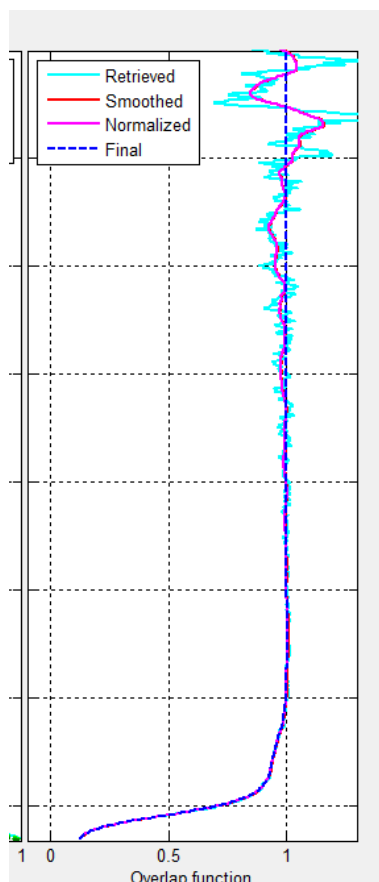


**Figure A-13: Output depicted by the module *Format*.**

o  *Save:* final overlap function is saved in ASCII file in the folder defined by user through *Output Data*. Corrected (green) and non-corrected (red) elastic and inelastic (blue) particle backscatter coefficient profiles and the final overlap function profile (dashed blue line) are depicted in the first and third vertical axes, respectively. Check box indicates

219

whether the file was successfully saved for the corresponding wavelength.
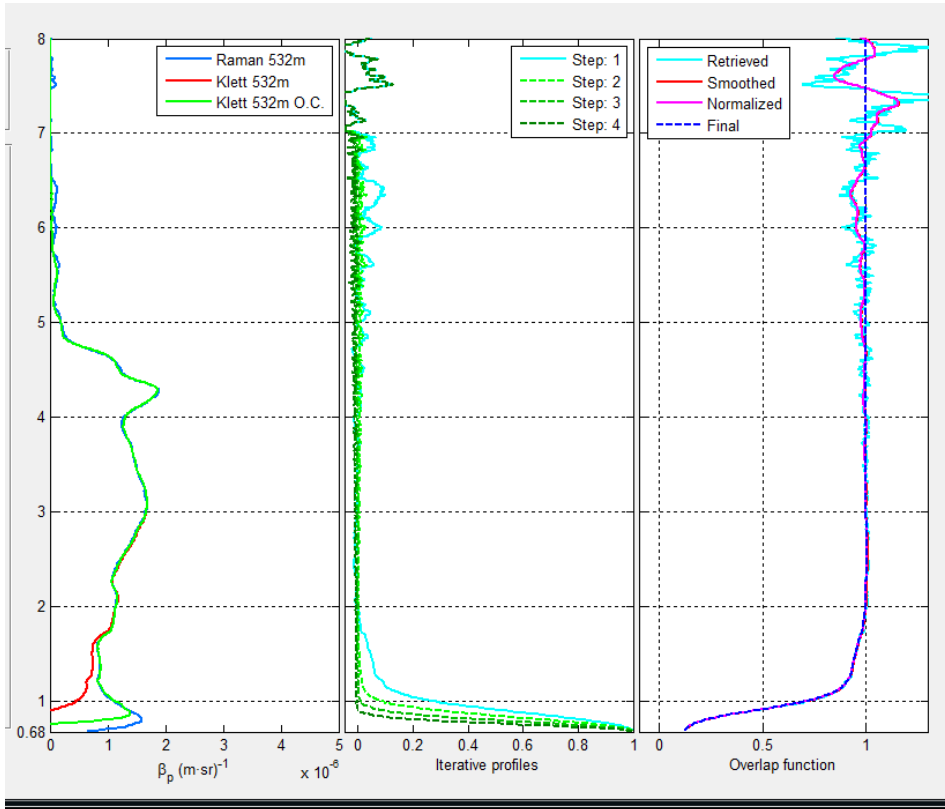


**Figure A-14: Final outputs depicted by the module *Save*. Corrected (green) and non-corrected (red) elastic and inelastic (blue) particle backscatter coefficient profiles and the final overlap function profile (dashed blue line) are depicted in the first and third vertical axes.**

### Earlinet format

Once the lidar product profiles are obtained, the valid range of each product is selected using this module.
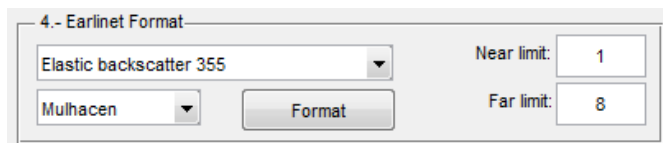
The pop-up menus allow the selection of the optical property profile derived with the data of the lidar system (e.g., the combination shown below select the *Elastic backscatter 355* of *Mulhacen*).
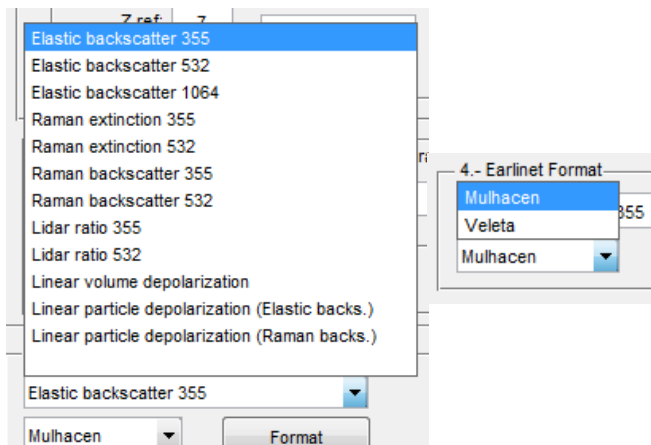
- *Near limit* and *Far limit* are the text boxes which define the height range valid for the profile selected.

- *Format*: sets the NaN below *Near limit* and above *Far limit* and updates the corresponding plotted vertical profile with the valid profile.
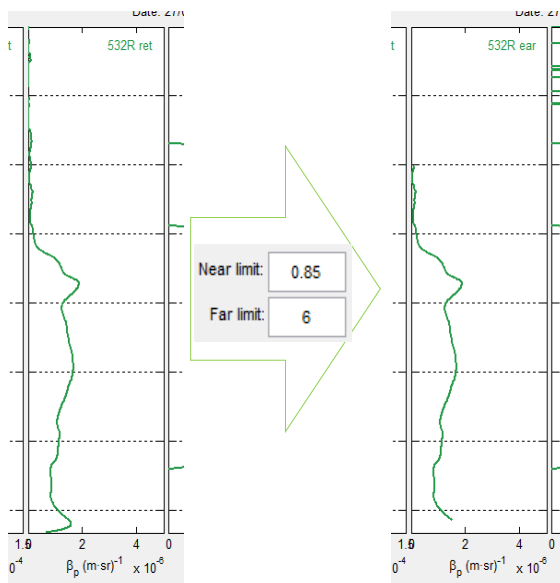
**Save profiles**

Once the valid ranges of the lidar products profiles are obtained, the user can save the results through this module.

- *graphic:* it allows the exportation of the five vertical axes in an image with *.png format as it is shown below.

Date: 27/06/2011 Period: 00:00 - 00:56
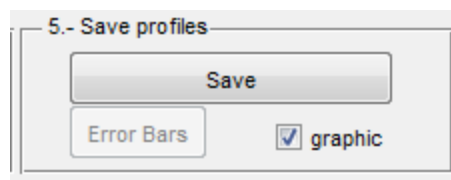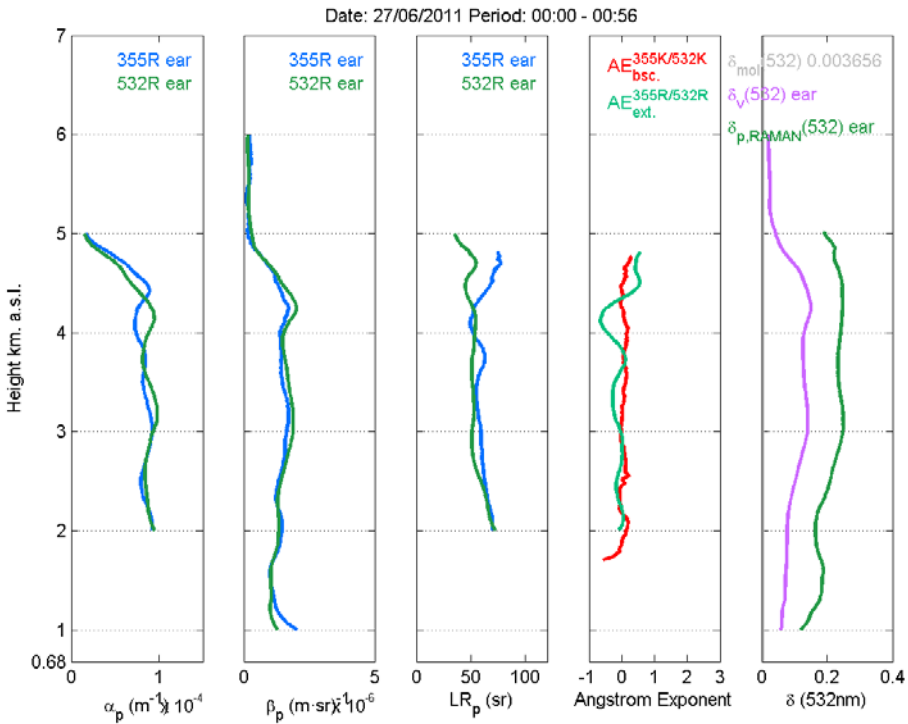
- *save:* it opens a sub-interface allows the user to select the profiles which have to be save. Step *4.- Earlinet Format* is a required step to save the profiles. Press *Select to save* to continue.
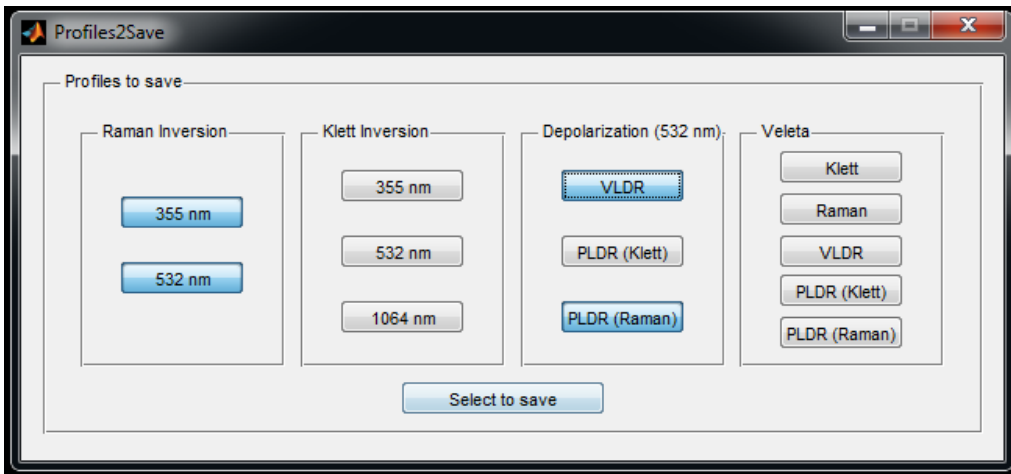
A window message request information about the maximum height of the profiles. *Earlinet* option cuts at 8 km asl, user chooses the height otherwise.
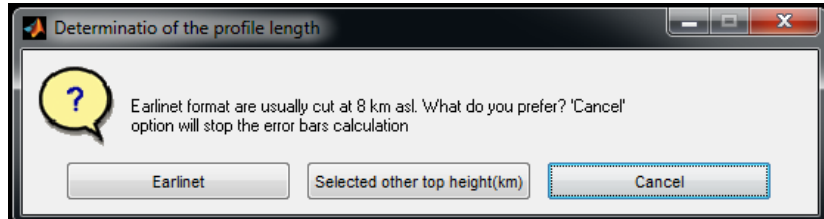


A window message reports that the profiles where successfully saved.
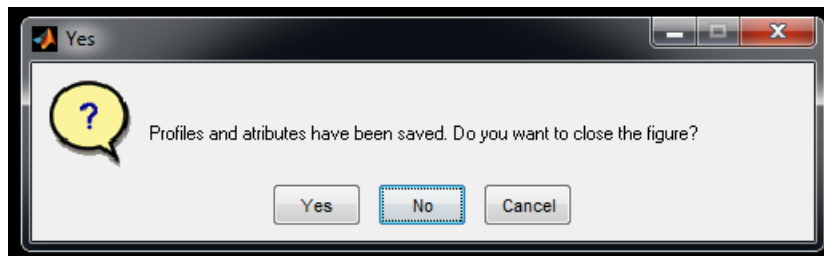


Only when the profiles are saved, the *Error Bars* button is active and allows the calculus of the error bars using the Monte Carlo technique.

## LPSS (Lidar Polarizing Sensitivity Simulator)

The simulator Lidar polarizing sensitivity simulator (LPSS) is a complex user GUI and thus, only an overview of the software is provided. The software has three main parts: modules, simulation and axes (Figure A-16). Properties are dimensionless except angles which are in degrees.

### Modules

Modules represent the modelled functional blocks of lidar systems: laser, laser emitting optics, receiving optics, polarizing beam splitter, photomultipliers and calibrator. Additionally, a module provides the information about the atmosphere (Figure A-15).



**Figure A-15: Modules included in LPSS.**

225
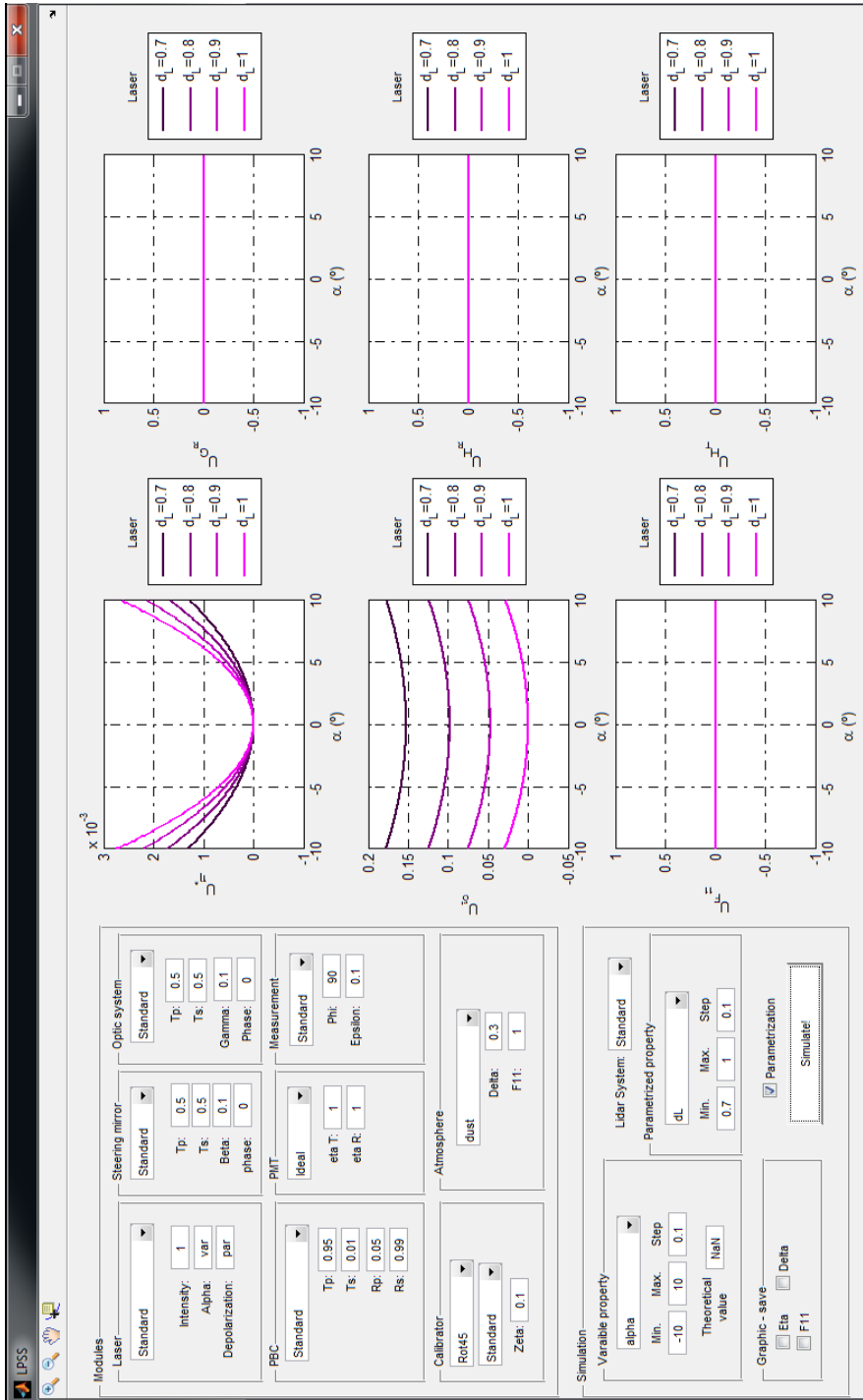
**Figure A-16: Main LPSS interface.**

Properties of each functional block are defined according to different lidar systems as shown in Figure A-17.



**Figure A-17: Pop-up menu showing different lidar systems. Functional block properties are taken from the selected lidar system.**

- *Laser*: properties defining the laser are intensity, rotational misalignment and depolarization.

- *Steering mirror* and *optic system*: both modules present the parameters which define an optic system. The first is the emitting laser optics ($M_E$) and the second is the receiving optics ($M_o$). Both systems are defined by the parallel and perpendicular transmittance ($T_p$ and $T_s$), the rotational misalignment (*Beta* and *Gamma*) and the phase shift (*phase*).

- *PBC*: Polarizing beam splitter. $T_p$ and Ts are the parallel and perpendicular transmittance and $R_p$ and Rs are the parallel and perpendicular reflectance.

- *PMT*: it defines by the gain factor of the reflected and the transmitted signal. As these values are always presented as ratio, their values are fixed at one.

- *Measurement*: this is defined by the axial rotation (*phi*) and its rotational misalignment (*epsilon*).

- *Calibrator*: first pop-up menu allows the selection of the calibration method: rotation in front of the PBS (*rot45*) and polarizer in front of the receiving optics (*Pol45)*.

- *Atmosphere:* characteristics of the atmospheric aerosol are defined by its depolarization capability represented by the parameter a (*Delta)* and the term $F_{11}$ which is related to the aerosol backscatter coefficient.

## Simulation

This module allows the selection of the two parameters of the hardware to analyse its effect on the volume linear depolarization ratio.
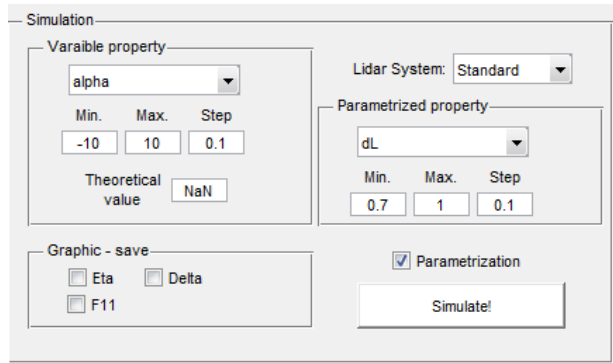


- *Variable property*: it defines the properties to vary between the minimum and maximum values, *Min.* and *Max.*, respectively, with a resolution set in *Step*.

- *Theoretical value*: it will be removed in the next version.

- *Lidar System*: sets the reference lidar system.

- *Parameterized property*: second variable used to understand possible compensation effect between two parameters.

- *Parameterization*: it allows the suppression of the parameterization option.

- *Simulate!*: Run the software and depict the results in the axes (see figure below). Different axes allow the study of the influence of each parameter in different steps of the process. Orange arrow indicates the $\delta'$ uncertainty.
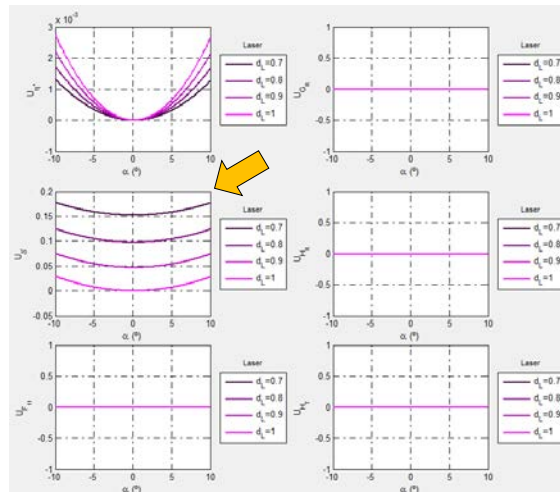


**Figure A-18: each axis shows the influence of the selected properties on steps of the process. The orange arrow indicates the systematic error of $\delta'$.**

# Appendix B: Müller matrices

**Intensity vector**

$$\boldsymbol{I}_L(\alpha, a_L) = I_L \begin{pmatrix} 1 \\ a_L c_{2\alpha} \\ a_L s_{2\alpha} \\ 0 \end{pmatrix}$$

**Laser emitting optics**

$$\boldsymbol{M}_E = \begin{pmatrix} 1 & D_E c_{2\beta} & D_E s_{2\beta} & 0 \\ D_E c_{2\beta} & (1 - s_{2\beta}^2 W_E) & W_E s_{2\beta} c_{2\beta} & -Z_E s_E s_{2\beta} \\ D_E s_{2\beta} & W_E s_{2\beta} c_{2\beta} & (1 - c_{2\beta}^2 W_E) & Z_E s_E c_{2\beta} \\ 0 & Z_E s_E s_{2\beta} & -Z_E s_E c_{2\beta} & Z_E c_E \end{pmatrix}$$

**Atmosphere**

$$\boldsymbol{F} = \begin{pmatrix} 1 & 0 & 0 & 0 \\ 0 & a & 0 & 0 \\ 0 & 0 & -a & 0 \\ 0 & 0 & 0 & 1-2a \end{pmatrix}$$

**Receiving optics**

$$\boldsymbol{M}_o = \begin{pmatrix} 1 & D_o c_{2\gamma} & D_o s_{2\gamma} & 0 \\ D_o c_{2\gamma} & (1 - s_{2\gamma}^2 W_o) & W_o s_{2\gamma} c_{2\gamma} & -Z_o s_o s_{2\gamma} \\ D_o s_{2\gamma} & W_o s_{2\gamma} c_{2\gamma} & (1 - c_{2\gamma}^2 W_o) & Z_o s_o c_{2\gamma} \\ 0 & Z_o s_o s_{2\gamma} & -Z_o s_o c_{2\gamma} & Z_o c_o \end{pmatrix}$$

**Ideal polarizing beam splitter**

$$T_S = \frac{T_S^p + T_S^s}{2}$$

$$\boldsymbol{M}_S^\# = T_S^\# \begin{pmatrix} 1 & D_S^\# & 0 & 0 \\ D_S^\# & 1 & 0 & 0 \\ 0 & 0 & 0 & 0 \\ 0 & 0 & 0 & 0 \end{pmatrix}$$

where S=[R,T], $T_R^\# = T_T^\# = 0.5$, $D_T^\# = 1$ and $D_R^\# = -1$.

$$\boldsymbol{I}_S(y, \varepsilon) = \eta_S \boldsymbol{M}_S^\# \boldsymbol{R}_y(y) \boldsymbol{C}(x45° + \varepsilon) \boldsymbol{F} \begin{pmatrix} 1 \\ 0 \\ 0 \\ 0 \end{pmatrix}$$

$$\eta_S M_S^{\#} R_y(y) \begin{pmatrix} 1 \\ 0 \\ 0 \\ 0 \end{pmatrix}$$

## General formula of $H_S$ and $G_S$

$H_S$: Simplifying according to $yD_S$

$$H_S = D_L D_o c_{2(\beta+\gamma)} + a_L D_o \left( c_{2(\gamma+\alpha)} - W_L s_{2(\beta-\alpha)} s_{2(\gamma+\beta)} \right)$$

$$+yD_S \begin{pmatrix} D_L c_{2(\beta-\varepsilon)} + a_L c_{2(\alpha-\varepsilon)} - W_o s_{2(\gamma+\varepsilon)} \left( D_L s_{2(\gamma+\beta)} + d_L s_{2(\gamma+\alpha)} \right) \\ + d_L \left( W_L s_{2(\beta-\alpha)} \left( s_{2(\beta-\varepsilon)} - W_o c_{2(\gamma+\beta)} s_{2(\gamma+\varepsilon)} \right) + 2Z_o s_o Z_L s_L s_{2(\beta-\alpha)} s_{2(\gamma+\varepsilon)} \right) \end{pmatrix}$$

$H_S$: Simplifying according to $D_L$ and $a_L$

$$H_S = D_L \left( D_o c_{2(\beta+\gamma)} + yD_S \left( c_{2(\beta-\varepsilon)} - W_o s_{2(\gamma+\beta)} s_{2(\gamma+\varepsilon)} \right) \right)$$

$$+a_L \begin{pmatrix} D_o c_{2(\gamma+\alpha)} + yD_S c_{2(\alpha-\varepsilon)} - W_L s_{2(\beta-\alpha)} \left( D_o s_{2(\gamma+\beta)} - yD_S \left( s_{2(\beta-\varepsilon)} - W_o c_{2(\gamma+\beta)} s_{2(\gamma+\varepsilon)} \right) \right) \\ - yD_S W_o s_{2(\gamma+\alpha)} s_{2(\gamma+\varepsilon)} + yD_S 2Z_o s_o Z_L s_L s_{2(\beta-\alpha)} s_{2(\gamma+\varepsilon)} \end{pmatrix}$$

$G_S$: Simplifying according to $yD_S$

$$G_S = \left( 1 + a_L D_L c_{2(\beta-\alpha)} \right) \left( 1 + yD_S D_o c_{2(\gamma+\varepsilon)} \right) - yD_S Z_o s_o a_L Z_L s_L s_{2(\beta-\alpha)} s_{2(\gamma+\varepsilon)}$$

## General formula of the Δ90°-calibration method using a rotator in front of the polarizing beam splitter

### Input vector, $I_{in}$

In this case, $I_{in}$ is defined as

$$I_{in} = FM_L I_L$$

of which explicit formula is

$$I_{in} = F_{11} T_L I_L (i \quad q \quad u \quad v)^T$$

with

$i = 1 + a_L D_L c_{2(\beta-\alpha)}$

$q = c_{2\beta} a D_L + a a_L \left[ c_{2\alpha} - s_{2\beta} W_L s_{2(\beta-\alpha)} \right]$

$u = -s_{2\beta} a D_L - a a_L \left[ s_{2\alpha} + c_{2\beta} W_L s_{2(\beta-\alpha)} \right]$

$v = (1 - 2a) a_L Z_L s_L s_{2(\beta-\alpha)}$

**Resulting matrix, $A_s$**

In this case, $A_S$ is defined as

$$A_S = M_S R_y R(\varepsilon) M_o$$

As only the first row is needed

$$\langle A_S| = T_S \langle 1 \quad y D_S c_{2\varepsilon} \quad -y D_S s_{2\varepsilon} \quad 0|$$

**Measured calibration factor, $\eta^*$**

According to the definition of $\eta^*$, its explicit formula is

$$\eta^*(y, x45^\circ + \varepsilon)$$

$$= \eta \frac{\left(1 + D_o a a_L c_{2(\gamma+\alpha)}\right) - x y D_R \left(D_o s_{2(\varepsilon-\gamma)} + a a_L \left(s_{2(\varepsilon-\gamma)} - W_o s_{2(\gamma+\alpha)} c_{2(\varepsilon+\gamma)}\right)\right)}{\left(1 + D_o a a_L c_{2(\gamma+\alpha)}\right) - x y D_T \left(D_o s_{2(\varepsilon-\gamma)} + a a_L \left(s_{2(\varepsilon-\gamma)} - W_o s_{2(\gamma+\alpha)} c_{2(\varepsilon+\gamma)}\right)\right)}$$

**General formula of the Δ90°-calibration method using a polarizer in front of the receiving optics**

**Input vector, $I_{in}$**

In this case, $I_{in}$ is defined as

$$I_{in} = M_o F M_L I_L$$

of which explicit formula is

$$I_{in} = T_o F_{11} T_L I_L (i \quad q \quad u \quad v)^T$$

with

$i = 1 + a_L D_L c_{2(\beta-\alpha)} + a D_L D_o c_{2(\beta+\gamma)} + D_o a a_L \left(c_{2(\gamma+\alpha)} - W_L s_{2(\beta-\alpha)} s_{2(\gamma+\beta)}\right)$

$q = D_o c_{2\gamma}\left(1 + a_L D_L c_{2(\beta-\alpha)}\right) + a D_L \left(c_{2\beta} - W_o s_{2\gamma} s_{2(\gamma+\beta)}\right)$
$\qquad\qquad + a a_L \left[c_{2\alpha} - W_o s_{2\gamma} s_{2(\gamma+\alpha)} + W_L s_{2(\beta-\alpha)}\left(-s_{2\beta} - W_o s_{2\gamma} c_{2(\gamma+\beta)}\right)\right]$
$\qquad\qquad - Z_o s_o s_{2\gamma}(1 - 2d) a_L Z_L s_L s_{2(\beta-\alpha)}$

$u = D_o s_{2\gamma}\left(1 + a_L D_L c_{2(\beta-\alpha)}\right) - a D_L \left(s_{2\beta} - W_o c_{2\gamma} s_{2(\gamma+\beta)}\right)$
$\qquad\qquad - a a_L \left[s_{2\alpha} - W_o c_{2\gamma} s_{2(\gamma+\alpha)} + W_L s_{2(\beta-\alpha)}\left(c_{2\beta} - W_o c_{2\gamma} c_{2(\gamma+\beta)}\right)\right]$
$\qquad\qquad + Z_o s_o c_{2\gamma}(1 - 2a) a_L Z_L s_L s_{2(\beta-\alpha)}$

$v = Z_o s_o \left(a D_L s_{2(\gamma+\beta)} + a a_L \left[s_{2(\gamma+\alpha)} + W_L s_{2(\beta-\alpha)} c_{2(\gamma+\beta)}\right]\right) + Z_o c_o (1 - 2a) a_L Z_L s_L s_{2(\beta-\alpha)}$

## Resulting matrix, $A_S$

In this case, $A_S$ is defined as

$$A_S = M_S R_y M_o M_P (x45^\circ + \varepsilon)$$

As only the first row is needed

$$\langle A_S| = T_S T_o T_P \left( 1 + y D_o D_S c_{2\gamma} - x \left( D_o s_{2(\varepsilon-\gamma)} + y D_S \left( s_{2\varepsilon} - W_o s_{2\gamma} c_{2(\varepsilon_P - \gamma)} \right) \right) \right) \begin{vmatrix} 1 \\ -x s_{2\varepsilon} \\ x c_{2\varepsilon} \\ 0 \end{vmatrix}$$

## Measured calibration factor, $\eta^*$

According to the definition of $\eta^*$, its explicit formula is

$$\eta^*(y, x45^\circ + \varepsilon)$$

$$= \eta^\# \frac{(1 - y D_o c_{2\gamma})i + y s_{2\gamma} Z_o s_o v + x \left( D_o \left( q s_{2\gamma} - u c_{2\gamma} \right) - y \left( W_o s_{2\gamma} \left( q c_{2\gamma} - u s_{2\gamma} \right) - u \right) \right)}{(1 + y D_o c_{2\gamma})i - y s_{2\gamma} Z_o s_o v + x \left( D_o \left( q s_{2\gamma} - u c_{2\gamma} \right) + y \left( W_o s_{2\gamma} \left( q c_{2\gamma} - u s_{2\gamma} \right) - u \right) \right)}$$

# Quick finder

## List of Abbreviations

| Abbreviation | Meaning |
| --- | --- |
| A/D | Analog-to-digital converter |
| aci | Aerosol-cloud interaction |
| ACTRIS | Aerosol Cloud and Trace gases Research InfraStructure network |
| AERONET | Aerosol robotic network |
| agl | Above ground level |
| AN | Analog |
| AOD | Aerosol Optical Depth |
| APD | Avalanche photodiode |
| ari | Aerosol-radiation interaction |
| asl | Above sea level |
| BSC-DREAM | Barcelona Supercomputing Center - Dust Regional Atmospheric Modeling |
| CAPS | Cloud, Aerosol, and Precipitation Spectrometer |
| ChArMEx | Chemistry-Aerosol Mediterranean Experiment |
| EARLINET | European Aerosol Research Lidar Network |
| ERFaci | ERF due to aci |
| ERFari | ERF due to ari |
| ERF | Effective Radiative Forcing |
| FWHM | Full Width at Half Maximum |
| GL | Gluing |
| HYSPLIT | Hybrid Single Particle Lagrangian Integrated Trajectory model |
| IPCC | Intergovernmental Panel on Climate Change |
| NAAPS | Navy Aerosol Analysis and Prediction System |
| MPLNET | MicroPulse Lidar Network |
| MWR | MicroWave Radiometer |
| PBL | Planetary Boundary Layer |
| PC | Photocounting |
| PCASP | Passive Cavity Aerosol Spectrometer Probe |
| $PM_1$ | Particle matter which particle diameters is less than 1 μm |

237

| Abbreviation | Meaning |
|:---:|:---|
| $PM_{10}$ | Particle matter which particle diameters is less than 10 μm |
| $PM_{10-1}$ | $PM_{10}$ - $PM_1$ |
| PMT | Photomultiplier |
| POLARIS | Pbl height estimatiOn based on Lidar depolARISation |
| POLIPHON | Polarizing Lidar Photometer Networking |
| RCS | Range corrected signal |
| RD | Rainfall days |
| SD | Sunny days |
| SH | Number of hour with sunlight |
| SNR | Signal-to-noise ratio |
| TOA | Top Of Atmosphere |

## List of Greek symbols

| Symbol | Name and specifications |
|:---:|:---|
| $\alpha$ | Particle extinction coefficient. Rotational misalignment of the polarizing plane of the laser in Chapter 5 and 6. |
| $\alpha_{aer}$ | Aerosol extinction coefficient |
| $\alpha_{mol}$ | Molecular extinction coefficient |
| $\beta$ | Particle backscatter coefficient. Rotational misalignment of laser emitting optics in Chapter 6. |
| $\beta_{aer}$ | Aerosol backscatter coefficient |
| $\beta_{att}$ | Attenuated backscatter coefficient |
| $\beta_{mol}$ | Molecular backscatter coefficient |
| $\beta_{Raman}$ | $\beta_{mol}$ at Raman-shifted wavelength |
| $\beta_s$ | Strong $\beta$ derived using POLIPHON |
| $\beta_w$ | Weak $\beta$ derived using POLIPHON |
| $\gamma$ | Rotational misalignment of receiving optics |
| $\delta$ | Perpendicular-to-parallel ratio |
| $\bar{\delta}_{C_{RCS}}$ | $\delta$ average around $C_{RCS}$ |
| $\bar{\delta}_g$ | $\delta$ average in the range 1-1.1 km asl |
| $\delta'$ | Volume linear depolarization ratio |

| Symbol | Name and specifications |
|---|---|
| $\delta^*$ | Reflected-to-transmitted received signal corrected by $\eta$ (Eq. 4-16) |
| $\delta_m$ | Molecular $\delta'$ |
| $\delta^p$ | Particle linear depolarization ratio |
| $\delta_{ant}^p$ | $\delta^p$ of anthropogenic aerosol |
| $\delta_s^p$ | Strong $\delta^p$ used in POLIPHON |
| $\delta_w^p$ | Weak $\delta^p$ used in POLIPHON |
| $\Delta_E$ | Phase shift of the laser emitting optics |
| $\Delta_o$ | Phase shift of the receiving optics |
| $\varepsilon$ | Rotational misalignment of the calibrator |
| $\varepsilon_r$ | Rotational misalignment of the rotator |
| $\varepsilon_p$ | Rotational misalignment of the polarizer |
| $\eta$ | Depolarization calibration factor. Fine fraction in Chapter 8 |
| $\eta_S$ | Gain factor of the reflected or transmitted PMT. |
| $\eta^{\#}$ | Depolarization calibration factor considering cleaned PBS |
| $\eta^*$ | Measured depolarization calibration factor |
| $\eta_{\sqrt{\pm}}^*$ | Geometric average of $\eta^*$ retrieved at $\pm45°$ |
| $\langle\eta_{\sqrt{\pm}}^*\rangle$ | Height average of $\eta_{\sqrt{\pm}}^*$ |
| $\langle\eta_{\sqrt{\pm}}^*\rangle^{pol}$ | $\langle\eta_{\sqrt{\pm}}^*\rangle$ retrieved using the $\Delta90°$-calibration method with polarizer in front of receiving optics |
| $\langle\eta_{\sqrt{\pm}}^*\rangle^{rot}$ | $\langle\eta_{\sqrt{\pm}}^*\rangle$ retrieved using the $\Delta90°$-calibration method with rotator in front of PBS |
| $\eta_{max}$ | Threshold used to find $C_{max}$ by means of the wavelet covariance transform applied to $\delta$ |
| $\eta_{min}$ | Threshold used to find $C_{min}$ by means of the wavelet covariance transform applied to $\delta$ |
| $\eta_{RCS}$ | Threshold used to find $C_{RCS}$ by means of the wavelet covariance transform applied to RCS |
| $\eta_{RCS}^{min}$ | Threshold used to find the local minimum of the wavelet covariance transform applied to RCS in the range $C_{min}\pm50m$ |
| $\rho$ | Particle density |
| $\sigma_a^{aer}$ | Aerosol absorption coefficient |

| Symbol | Name and specifications |
|---|---|
| $\sigma_a^{mol}$ | Molecular absorption coefficient |
| $\sigma_a$ | Particle absorption coefficient |
| $\sigma_s^{aer}$ | Aerosol scattering coefficient |
| $\sigma_s^{mol}$ | Molecular scattering coefficient |
| $\sigma_s$ | Particle scattering coefficient |
| $\lambda$ | Wavelength |
| $\lambda_L$ | Wavelength emitted by lidar |
| $\lambda_R$ | Raman wavelength |
| $\xi$ | Integral variable of height |
| $\Sigma_{max}$ | Sum of WCT($\delta$) at $C_{max}$ and the local maxima of the WCT(RCS) 100 m around $C_{max}$ |
| $\Sigma_{min}$ | Sum of WCT($\delta$) at $C_{min}$ and the local maxima of the WCT(RCS) 100 m around $C_{min}$ |
| $\tau_D$ | Detection time |
| $\tau_i$ | Interaction time |
| $\tau_L$ | Pulse duration |
| $\omega$ | Single scattering albedo |

## List of Latin symbols

| Symbol | Name and specifications |
|---|---|
| $a$ | Parameter a |
| $a_L$ | Laser parameter a |
| $\mathring{a}_{AOD}$ | AOD-related Angström exponent |
| $\mathring{a}_{sca}$ | Scattering-related Angström exponent |
| $\mathring{a}_{\alpha,\beta}$ | Extinction- and backscattering-related Angström exponent |
| $A$ | Telescope area |
| $AOD_s$ | Coarse mode AOD |
| $c$ | Light speed |
| Cs | Volume concentration |
| $C_{min}$ | PBL candidate determined using the minimum of WCT($\delta$) |
| $C_{max}$ | PBL candidate determined using the maximum of WCT($\delta$) |

| Symbol | Name and specifications |
|---|---|
| $C_{RCS}$ | PBL candidate determined using the maximum of WCT(RCS) |
| $D_E$ | Effective diattenuation of the laser emitting optics |
| $D_o$ | Effective diattenuation of the receiving optics |
| $D_o^{exp}$ | Effective diattenuation of the receiving optics determined experimentally |
| **E** | Electric field |
| $E_\delta$ | δ´ uncertainty |
| **F** | Atmosphere Müller matrix |
| $G_S$ | Correction factor. See Eq. 4-15 |
| $H_S$ | Correction factor. See Eq. 4-15 |
| I | Element of the Stokes Vector |
| $I_L$ | Stokes Vector of the laser signal |
| $\boldsymbol{I_S}$ | Stokes Vector of the received signal (reflected or transmitted) |
| $LR$ | Lidar ratio |
| M | Particle mass |
| $m(r)$ | Mass size distribution |
| $m_s$ | Mass concentration of the strong depolarizing capability aerosol |
| $m_{dust}$ | Dust mass concentration derived with POLIPHON |
| $m_c$ | Coarse mass concentration derived with airborne measurements |
| $\boldsymbol{M_E}$ | Laser emitting optics Müller matrix |
| $\boldsymbol{M_o}$ | Receiving optics Müller matrix |
| $\boldsymbol{M_S}$ | PBS Müller matrix (reflected or transmitted) |
| r | Particle radius |
| R | Backscattering ratio |
| **R** | Rotator Müller matrix |
| RCS | Range corrected signal |
| $R_{p,s}$ | Parallel (p) or perpendicular (s) reflectance |
| S | Subscript which indicates R (reflected or T (transmitted). |
| T | Transmittance |
| $T_{p,s}$ | Parallel (p) or perpendicular (s) transmittance |
| $T(z,\lambda)$ | Atmospheric transmittance (Eq. 2-1) |
| U | Element of Stokes Vector |

| Symbol | Name and specifications |
|:---:|:---|
| V | Element of Stokes Vector. Particle volume in Section 2.2.3. |
| $V_S$ | Voltage of the reflected or transmitted PMT |
| $v(r)$ | Volume size distribution |
| $x$ | Size parameter |
| z | Height |
| $z_{PBL}$ | Planetary boundary layer height |
| $z_{PBL}^{POL}$ | $z_{PBL}$ determined by POLARIS |
| $z_{PBL}^{MWR}$ | $z_{PBL}$ determined by the parcel method using the temperature profile obtained by means of the microwave radiometer |
| $z_{PBL}^{RS}$ | $z_{PBL}$ determined by the potential temperature using the temperature profile obtained by means of the radiosonde |
| Z | $\sqrt{1 - D^2}$ |

## List of figures

## List of tables

# References

Ackermann, J. (1998), The extinction-to-backscatter ratio of tropospheric aerosol: A numerical study, *J Atmos Ocean Tech*, *15*(4), 1043-1050.

Adriani, A., P. Massoli, G. Di Donfrancesco, F. Cairo, M. L. Moriconi, and M. Snels (2004), Climatology of polar stratospheric clouds based on lidar observations from 1993 to 2001 over McMurdo Station, Antarctica, *J Geophys Res-Atmos*, *109*(D24).

Alados-Arboledas, L., and F. J. Olmo (1997), Evolution of solar radiative effects of Mount Pinatubo at ground level, *Tellus B*, *49*(2), 190-198.

Álvarez, J. M., M. A. Vaughan, C. A. Hostetler, W. H. Hunt, and D. M. Winker (2006), Calibration technique for Polarization-Sensitive Lidars, *J Atmos Ocean Tech*, *23*, 683-699.

Anderson, T. L., and J. A. Ogren (1998), Determining aerosol radiative properties using the TSI 3563 integrating nephelometer, *Aerosol Science and Technology*, *29*(1), 57-69.

Anderson, T. L., et al. (2005), An "A-Train" strategy for quantifying direct climate forcing by anthropogenic aerosols, *B Am Meteorol Soc*, *86*(12), 1795-.

Andrey, J., E. Cuevas, M. C. Parrondo, S. Alonso-Pérez, A. Redondas, and M. Gil-Ojeda (2014), Quantification of ozone reductions within the Saharan air layer through a 13-year climatologic analysis of ozone profiles, *Atmospheric Environment*, *84*(0), 28-34.

Angelini, F., F. Barnaba, T. C. Landi, L. Caporaso, and G. P. Gobbi (2009), Study of Atmospheric Aerosols and Mixing Layer by Lidar, *Radiat Prot Dosim*, *137*(3-4), 275-279.

Ansmann, A., M. Riebesell, and C. Weitkamp (1990), Measurement of Atmospheric Aerosol Extinction Profiles with a Raman Lidar, *Opt Lett*, *15*(13), 746-748.

Ansmann, A., U. Wandinger, M. Riebesell, C. Weitkamp, and W. Michaelis (1992), Independent Measurement of Extinction and Backscatter Profiles in Cirrus Clouds by Using a Combined Raman Elastic-Backscatter Lidar, *Appl Optics*, *31*(33), 7113-7131.

Ansmann, A., M. Tesche, P. Seifert, D. Althausen, R. Engelmann, J. Fruntke, U. Wandinger, I. Mattis, and D. Muller (2009), Evolution of the ice phase in tropical altocumulus: SAMUM lidar observations over Cape Verde, *J Geophys Res-Atmos*, *114*.

Ansmann, A., et al. (2011), Ash and fine-mode particle mass profiles from EARLINET-AERONET observations over central Europe after the eruptions of the Eyjafjallajokull volcano in 2010, *J Geophys Res-Atmos*, *116*.

# References

Ansmann, A., et al. (2003), Long-range transport of Saharan dust to northern Europe: The 11-16 October 2001 outbreak observed with EARLINET, *J Geophys Res-Atmos*, *108*(D24).

Baars, H., A. Ansmann, R. Engelmann, and D. Althausen (2008), Continuous monitoring of the boundary-layer top with lidar, *Atmos Chem Phys*, *8*(23), 7281-7296.

Baran, A. J., P. Yang, and S. Havemann (2001), Calculation of the single-scattering properties of randomly oriented hexagonal ice columns: a comparison of the T-matrix and the finite-difference time-domain methods, *Appl Optics*, *40*(24), 4376-4386.

Barry, R. G., and R. J. Chorley (1987), *Atmosphere, Weather, and Climate*, Methuen.

Baumgardner, D., G. B. Raga, J. C. Jimenez, and K. Bower (2005), Aerosol particles in the Mexican East Pacific - Part I: processing and vertical redistribution by clouds, *Atmos Chem Phys*, *5*, 3081-3091.

Bohren, C. F., and D. R. Huffman (1983), *Absorption and scattering of light by small particles*, Wiley.

Bösenberg, J., et al. (Ed.) (2001), *EARLINET: A European aerosol research lidar network, laser remote sensing of the atmosphere*, Ed. Ecole Polytech., Palaiseau, France.

 ed., pp. 155–158 pp.

Boucher, O., et al. (2013), Clouds and Aerosols, in *Climate Change 2013: The Physical Science Basis*, edited by T. F. Stocker and D. Qin, pp. 571-657, CAMBRIDGE UNIVERSITY PRESS, Cambridge, New York, Melbourne, Madrid, Cape Town, Singapore, São Paolo, Delhi, Mexico City.

Bravo-Aranda, J. A., F. Navas-Guzmán, J. L. Guerrero-Rascado, D. Pérez-Ramírez, M. J. Granados-Muñoz, and L. Alados-Arboledas (2013), Analysis of lidar depolarization calibration procedure and application to the atmospheric aerosol characterization, *International Journal of Remote Sensing*, *34*(9-10), 3543-3560.

Cairo, F., G. Di Donfrancesco, A. Adriani, L. Pulvirenti, and F. Fierli (1999), Comparison of various linear depolarization parameters measured by lidar, *Appl Optics*, *38*, 4425-4432.

Comerón, A., M. Sicard, and F. Rocadenbosch (2013), Wavelet Correlation Transform Method and Gradient Method to Determine Aerosol Layering from Lidar Returns: Some Comments, *J Atmos Ocean Tech*, *30*(6), 1189-1193.

256

Cooney, J., J. Orr, and Tomasett.C (1969), Measurements Separating Gaseous and Aerosol Components of Laser Atmospheric Backscatter, *Nature*, *224*(5224), 1098-&.

Córdoba-Jabonero, C., J. L. Guerrero-Rascado, D. Toledo, M. Parrondo, M. Yela, M. Gil, and H. A. Ochoa (2013), Depolarization ratio of polar stratospheric clouds in coastal Antarctica: comparison analysis between ground-based Micro Pulse Lidar and space-borne CALIOP observations, *Atmos Meas Tech*, *6*(3), 703-717.

Córdoba-Jabonero, C., et al. (2011), Synergetic monitoring of Saharan dust plumes and potential impact on surface: a case study of dust transport from Canary Islands to Iberian Peninsula, *Atmos Chem Phys*, *11*(7), 3067-3091.

Chen, G., et al. (2011), Observations of Saharan dust microphysical and optical properties from the Eastern Atlantic during NAMMA airborne field campaign, *Atmos Chem Phys*, *11*(2), 723-740.

Cho, H. M., P. Yang, G. W. Kattawar, S. L. Nasiri, Y. X. Hu, P. Minnis, C. Trepte, and D. Winker (2008), Depolarization ratio and attenuated backscatter for nine cloud types: Analyses based on collocated CALIPSO lidar and MODIS measurements, *Opt Express*, *16*(6), 3931-3948.

D'Almeida, G. A., P. Koepke, and E. P. Shettle (1991), *Atmospheric aerosols: global climatology and radiative characteristics*, A. Deepak Pub.

Denman, K. L., and G. Brasseur (2007), Couplings Between Changes in the Climate System and Biogeochemistry, *Climate Change 2007: The Physical Science Basis*, 499-587.

Draxler, R. R., and G. D. Rolph (2003), HYSPLIT (HYbrid Single-Particle Lagrangian Integrated Trajectory) *Model access via NOAA ARL READY Website <http://wwww.arl.noaa.gov/ready/hysplit4.html>. NOAA Air Resources Laboratory, Silver Spring, MD.*

Dubovik, O., and M. D. King (2000), A flexible inversion algorithm for retrieval of aerosol optical properties from Sun and sky radiance measurements, *J Geophys Res-Atmos*, *105*(D16), 20673-20696.

Dubovik, O., B. Holben, T. F. Eck, A. Smirnov, Y. J. Kaufman, M. D. King, D. Tanre, and I. Slutsker (2002), Variability of absorption and optical properties of key aerosol types observed in worldwide locations, *J Atmos Sci*, *59*(3), 590-608.

Dubovik, O., et al. (2006), Application of spheroid models to account for aerosol particle nonsphericity in remote sensing of desert dust, *J Geophys Res-Atmos*, *111*(D11).

Eck, T. F., B. N. Holben, J. S. Reid, O. Dubovik, A. Smirnov, N. T. O'Neill, I. Slutsker, and S. Kinne (1999), Wavelength dependence of the optical

depth of biomass burning, urban, and desert dust aerosols, *J Geophys Res-Atmos*, *104*(D24), 31333-31349.

Engelmann, R., et al. (2011), Doppler lidar studies of heat island effects on vertical mixing of aerosols during SAMUM-2, *Tellus B*, *63*(4), 448-458.

Feingold, B., A. Girnita, P. Olesnevich, A. Zeevi, E. S. Quivers, S. A. Miller, and S. A. Webber (2006), Survival in allosensitized children after listing for heart transplantation, *J Heart Lung Transpl*, *25*(2), S50-S50.

Fernald, F. G. (1984), Analysis of atmospheric lidar observations: some comments, *Appl Optics*, *23*, 652-653.

Fernald, F. G., M. B. Herman, and J. A. Reagan (1972), Determination of aerosol height distributions by liddar, *J Appl Meteorol*, *11*, 482-489.

Ferrare, R. A., S. H. Melfi, D. N. Whiteman, and K. D. Evans (1992), Raman Lidar Measurements of Pinatubo Aerosols over Southeastern Kansas during November December 1991, *Geophys Res Lett*, *19*(15), 1599-1602.

Ferrare, R. A., S. H. Melfi, D. N. Whiteman, K. D. Evans, and R. Leifer (1998a), Raman lidar measurements of aerosol extinction and backscattering - 1. Methods and comparisons, *J Geophys Res-Atmos*, *103*(D16), 19663-19672.

Ferrare, R. A., S. H. Melfi, D. N. Whiteman, K. D. Evans, M. Poellot, and Y. J. Kaufman (1998b), Raman lidar measurements of aerosol extinction and backscattering - 2. Derivation of aerosol real refractive index, single-scattering albedo, and humidification factor using Raman lidar and aircraft size distribution measurements, *J Geophys Res-Atmos*, *103*(D16), 19673-19689.

Flynn, C. J., A. Mendoza, Y. H. Zheng, and S. Mathur (2007), Novel polarization-sensitive micropulse lidar measurement technique, *Opt Express*, *15*(6), 2785-2790.

Formenti, P., L. Schutz, Y. Balkanski, K. Desboeufs, M. Ebert, K. Kandler, A. Petzold, D. Scheuvens, S. Weinbruch, and D. Zhang (2011), Recent progress in understanding physical and chemical properties of African and Asian mineral dust, *Atmos Chem Phys*, *11*(16), 8231-8256.

Forster, P., et al. (2007), *Changes in Atmospheric Constituents and in Radiative Forcing. In: Climate Change 2007: The Physical Science Basis. Contribution of Working Group I to the Fourth Assessment Report of the Intergovernmental Panel on Climate Change [Solomon, S., D. Qin, M. Manning, Z. Chen, M. Marquis, K.B. Averyt, M.Tignor and H.L. Miller (eds.)]*, Cambridge University Press, Cambridge, United Kingdom and New York, NY, USA.

Franke, P. M., and R. L. Collins (2003), Evidence of gravity wave breaking in lidar data from the mesopause region, *Geophys Res Lett*, *30*(4).

Freudenthaler, V. (2014), Implementation of calibration concepts for quantitative particle depolarization ratio measurements [methodology], *Atmopheric Measurements and Techniques* (Earlinet Specia Issue).

Freudenthaler, V., et al. (2009), Depolarization ratio profiling at several wavelengths in pure Saharan dust during SAMUM 2006, *Tellus B*, *61*(1), 165-179.

Gimmestad, G. (2008), Reexamination of depolarization in lidar measurements, *Appl Optics*, *47*, 3795-3802.

Grabe, M. (2005), *Measurement Uncertainties in Science and Technology*, Springer.

Granados-Muñoz, M. J., F. Navas-Guzmán, J. A. Bravo-Aranda, J. L. Guerrero-Rascado, H. Lyamani, J. Fernández-Galvéz, and L. Alados-Arboledas (2012), Automatic determination of the planetary boundary layer height using lidar: One-year analysis over southeastern Spain, *J Geophys Res-Atmos*, *117*.

Granados-Muñoz, M. J., et al. (2014), Retrieving aerosol microphysical properties by LIdar-Radiometer Inversion Code (LIRIC) for different aerosol types, *Journal of Geophysical Research D: Atmospheres*.

Gross, S., M. Tesche, V. Freudenthaler, C. Toledano, M. Wiegner, A. Ansmann, D. Althausen, and M. Seefeldner (2011a), Characterization of Saharan dust, marine aerosols and mixtures of biomass-burning aerosols and dust by means of multi-wavelength depolarization and Raman lidar measurements during SAMUM 2, *Tellus B*, *63*(4), 706-724.

Gross, S., et al. (2011b), Characterization of the planetary boundary layer during SAMUM-2 by means of lidar measurements, *Tellus B*, *63*(4), 695-705.

Guerrero-Rascado, J. L., B. Ruiz, and L. Alados-Arboledas (2008a), Multi-spectral lidar characterization of the vertical strcture of Saharan dust aerosol over southern Spain, *Atmospheric Environment*, *42*, 2668-2681.

Guerrero-Rascado, J. L., B. Ruiz, G. Chourdakis, G. Georgoussis, and L. Alados-Arboledas (2008b), One year of water vapour Raman Lidar measurements at the Andalusian Centre for Environmental Studies (CEAMA), *International Journal of Remote Sensing*, *29*(17-18), 5437-5453.

Guerrero-Rascado, J. L., F. Navas-Guzmán, J. A. Díaz, J. A. Bravo-Aranda, and L. Alados-Arboledas (2011), Quality assurance at the EARLINET Granada station: Characterization of the optical subsystem for a multichannel Raman lidar, *Control de calidad en la estación de EARLINET en Granada: caracterización del subsistema óptico de un lidar Raman multicanal*, *44*(1), 19-23.

Guerrero-Rascado, J. L., F. J. Olmo, I. Avilés-Rodriguéz, F. Navas-Guzmán, D. Pérez-Ramírez, H. Lyamani, and L. A. Arboledas (2009), Extreme Saharan dust event over the southern Iberian Peninsula in september 2007: active and passive remote sensing from surface and satellite, *Atmos Chem Phys*, *9*(21), 8453-8469.

Guerrero Rascado, J. L. (2008), Técnica lidar para la caracterización atmosférica mediante dispersión elática y Raman, Granada, Granada, Spain.

Harrison, R. M., and R. Grieken (1998), *Atmospheric particles*, J. Wiley.

Hayman, M., and J. P. Thayer (2009), Explicit description of polarization coupling in lidar applications, *Opt Lett*, *34*(5), 611-613.

Hayman, M., and J. P. Thayer (2012), General description of polarization in lidar using Stokes vectors and polar decomposition of Mueller matrices, *J Opt Soc Am A*, *29*(4), 400-409.

Haywood, J. M., et al. (2008), Overview of the Dust and Biomass-burning Experiment and African Monsoon Multidisciplinary Analysis Special Observing Period-0, *J Geophys Res-Atmos*, *113*.

Heintzenberg, J. (2009), The SAMUM-1 experiment over Southern Morocco: overview and introduction, *Tellus B*, *61*(1), 2-11.

Heintzenberg, J., et al. (2006), Intercomparisons and Aerosol Calibrations of 12 Commercial Integrating Nephelometers of Three Manufacturers, *J Atmos Ocean Tech*, *23*(7), 902-914.

Holben, B. N., et al. (1998), AERONET - A federated instrument network and data archive for aerosol characterization, *Remote Sens Environ*, *66*(1), 1-16.

Holzworth, G. C. (1964), Estimate of mean maximum mixing depths in the contiguous United States, *Mon Weather Rev*, *92*(5), 235-242.

Houghton, J. T., G. J. Jenkins, and J. J. Ephraums (1990), *Scientific assessment of climate change: report*, Intergovernmental Panel on Climate Change.

Hu, Y. X., et al. (2009), CALIPSO/CALIOP Cloud Phase Discrimination Algorithm, *J Atmos Ocean Tech*, *26*(11), 2293-2309.

Huebert, B. J., T. Bates, P. B. Russell, G. Y. Shi, Y. J. Kim, K. Kawamura, G. Carmichael, and T. Nakajima (2003), An overview of ACE-Asia: Strategies for quantifying the relationships between Asian aerosols and their climatic impacts, *J Geophys Res-Atmos*, *108*(D23).

Iqbal, M. (1983), *An introduction to solar radiation*, Academic Press.

Jaegle, L., P. K. Quinn, T. S. Bates, B. Alexander, and J. T. Lin (2011), Global distribution of sea salt aerosols: new constraints from in situ and remote sensing observations, *Atmos Chem Phys*, *11*(7), 3137-3157.

Kahnert, F. M. (2003), Numerical methods in electromagnetic scattering theory, *J Quant Spectrosc Ra*, *79*, 775-824.

Klett, J. D. (1981), Stable analytical inversion solution for precessing lidar returns, *Appl Optics*, *20*, 211-220.

Klett, J. D. (1985), Lidar inversion with variable backsactter/extinction ratios, *Appl Optics*, *24*, 1638-1643.

Kondratyev, K. Y., L. S. Ivlev, V. F. Krapivin, and C. A. Varostos (2006), *Atmospheric Aerosol Properties: Formation, Processes and Impacts*, Springer, published.

Kwon, H. J., S. H. Cho, Y. Chun, F. Lagarde, and G. Pershagen (2002), Effects of the Asian dust events on daily mortality in Seoul, Korea, *Environ Res*, *90*(1), 1-5.

Landulfo, E., A. Papayannis, P. Artaxo, A. D. A. Castanho, A. Z. de Freitas, R. F. Souza, N. D. Vieira, M. Jorge, O. R. Sanchez-Ccoyllo, and D. S. Moreira (2003), Synergetic measurements of aerosols over Sao Paulo, Brazil using LIDAR, sunphotometer and satellite data during the dry season, *Atmos Chem Phys*, *3*, 1523-1539.

Liou, K. N. (2002), *An introduction to atmospheric radiation*, ACADEMIC PressINC.

Lyamani, H., F. J. Olmo, and L. Alados-Arboledas (2010), Physical and optical properties of aerosols over an urban location in Spain: seasonal and diurnal variability, *Atmos Chem Phys*, *10*(1), 239-254.

Macke, A., M. I. Mishchenko, K. Muinonen, and B. E. Carlson (1995), Scattering of Light by Large Nonspherical Particles - Approximation Versus T-Matrix Method, *Opt Lett*, *20*(19), 1934-1936.

Maring, H., D. L. Savoie, M. A. Izaguirre, C. McCormick, R. Arimoto, J. M. Prospero, and C. Pilinis (2000), Aerosol physical and optical properties and their relationship to aerosol composition in the free troposphere at Izana, Tenerife, Canary Islands, during July 1995, *J Geophys Res-Atmos*, *105*(D11), 14677-14700.

Mattis, I., M. Tesche, M. Grein, V. Freudenthaler, and D. Muller (2009), Systematic error of lidar profiles caused by a polarization-dependent receiver transmission: quantification and error correction scheme, *Appl Optics*, *48*(14), 2742-2751.

Melfi, S. H. (1972), Remote Measurements of Atmosphere Using Raman Scattering, *Appl Optics*, *11*(7), 1605-&.

Mie, G. (1908), Articles on the optical characteristics of turbid tubes, especially colloidal metal solutions., *Ann Phys-Berlin*, *25*(3), 377-445.

Miller, R. L., I. Tegen, and J. Perlwitz (2004), Surface radiative forcing by soil dust aerosols and the hydrologic cycle, *J Geophys Res-Atmos*, *109*(D4).

Mishchenko, M. I., L. D. Travis, and D. W. Mackowski (1996), T-matrix computations of light scattering by nonspherical particles: A review, *J Quant Spectrosc Ra*, *55*(5), 535-575.

Mishchenko, M. I., L. D. Travis, R. A. Kahn, and R. A. West (1997), Modeling phase functions for dustlike tropospheric aerosols using a shape mixture of randomly oriented polydisperse spheroids, *J Geophys Res-Atmos*, *102*(D14), 16831-16847.

Mona, L., A. Amodeo, M. Pandolfi, and G. Pappalardo (2004), Three years of Saharan dust observations over potenza in the framework of earlinet, *Esa Spec Publ*, *561*, 849-852.

Mona, L., A. Amodeo, M. Pandolfi, and G. Pappalardo (2006), Saharan dust intrusions in the Mediterranean area: Three years of Raman lidar measurements, *J Geophys Res-Atmos*, *111*(D16).

Moran, J. M., M. D. Morgan, and P. M. Pauley (1997), *Meteorology: the atmosphere and the science of weather*, Prentice Hall.

Morille, Y., M. Haeffelin, P. Drobinski, and J. Pelon (2007), STRAT: An automated algorithm to retrieve the vertical structure of the atmosphere from single-channel lidar data, *J Atmos Ocean Tech*, *24*(5), 761-775.

Morrison, H., and W. W. Grabowski (2011), Cloud-system resolving model simulations of aerosol indirect effects on tropical deep convection and its thermodynamic environment, *Atmos Chem Phys*, *11*(20), 10503-10523.

Müller, D., I. Mattis, U. Wandinger, A. Ansmann, D. Althausen, O. Dubovik, S. Eckhardt, and A. Stohl (2003), Saharan dust over a central European EARLINET-AERONET site: Combined observations with Raman lidar and Sun photometer, *J Geophys Res-Atmos*, *108*(D12).

Müller, D., et al. (2009), EARLINET observations of the 14-22-May long-range dust transport event during SAMUM 2006: validation of results from dust transport modelling, *Tellus B*, *61*(1), 325-339.

Murayama, T., D. Müller, K. Wada, A. Shimizu, M. Sekiguchi, and T. Tsukamoto (2004), Characterization of Asian dust and Siberian smoke with multiwavelength Raman lidar over Tokyo, Japan in spring 2003, *Geophys Res Lett*, *31*(23).

Murayama, T., et al. (2001), Ground-based network observation of Asian dust events of April 1998 in east Asia, *Journal of Geophysical Research: Atmospheres*, *106*(D16), 18345-18359.

Navas-Guzman, F., J. L. Guerrero-Rascado, J. A. Bravo-Aranda, and L. Alados-Arboledas (2011), Calibration of 1064nm-backscatter profiles with a multiwavelength Raman lidar, *Rom J Phys*, *56*(3-4), 460-466.

Navas-Guzmán, F., D. Muller, J. A. Bravo-Aranda, J. L. Guerrero-Rascado, M. J. Granados-Muñoz, D. Pérez-Ramírez, F. J. Olmo, and L. Alados-

Arboledas (2013), Eruption of the Eyjafjallajokull Volcano in spring 2010: Multiwavelength Raman lidar measurements of sulphate particles in the lower troposphere, *J Geophys Res-Atmos*, *118*(4), 1804-1813.

Navas Guzmán, F. (2011), Atmospheric vertical profiling by Raman lidar, Granada, Granada, Spain.

Navas Guzmán, F., J. L. Guerrero Rascado, and L. Alados Arboledas (2011), Retrieval ofthe lidar overlap function using Raman signals, *Óptica Pura y Aplicada*, *44*(1), 71-75.

Noel, V., E. Chepfer, M. Haeffelin, and Y. Morille (2006), Classification of ice crystal shapes in midlatitude ice clouds from three years of lidar observations over the SIRTA observatory, *J Atmos Sci*, *63*(11), 2978-2991.

Noel, V., H. Chepfer, G. Ledanois, A. Delaval, and P. H. Flamant (2002), Classification of particle effective shape ratios in cirrus clouds based on the lidar depolarization ratio, *Appl Optics*, *41*(21), 4245-4257.

O'Neill, N. T., O. Dubovik, and T. F. Eck (2001a), Modified Angström exponent for the characterization of submicrometer aerosols, *Appl Optics*, *40*(15), 2368-2375.

O'Neill, N. T., T. F. Eck, B. N. Holben, A. Smirnov, O. Dubovik, and A. Royer (2001b), Bimodal size distribution influences on the variation of Angstrom derivatives in spectral and optical depth space, *J Geophys Res-Atmos*, *106*(D9), 9787-9806.

Olmo, F. J., A. Quirantes, A. Alcántara, H. Lyamani, and L. Alados-Arboledas (2006), Preliminary results of a non-spherical aerosol method for the retrieval of the atmospheric aerosol optical properties, *J Quant Spectrosc Ra*, *100*(1-3), 305-314.

Olmo, F. J., A. Quirantes, V. Lara, H. Lyamani, and L. Alados-Arboledas (2008), Aerosol optical properties assessed by an inversion method using the solar principal plane for non-spherical particles, *J Quant Spectrosc Ra*, *109*(8), 1504-1516.

Osborne, S. R., B. T. Johnson, J. M. Haywood, A. J. Baran, M. A. J. Harrison, and C. L. McConnell (2008), Physical and optical properties of mineral dust aerosol during the Dust and Biomass-burning Experiment, *J Geophys Res-Atmos*, *113*.

Pal, S., A. Behrendt, and V. Wulfmeyer (2010), Elastic-backscatter-lidar-based characterization of the convective boundary layer and investigation of related statistics, *Ann Geophys-Germany*, *28*(3), 825-847.

Pal, S. R., and A. I. Carswell (1973), Polarization properties of lidar backscattering from clouds, *Appl Optics*, *12*(7), 1530-1535.

Pappalardo, G., A. Amodeo, L. Mona, M. Pandolfi, N. Pergola, and V. Cuomo (2004), Raman lidar observations of aerosol emitted during the 2002 Etna eruption, *Geophys Res Lett*, *31*(5).

Pérez, C., S. Nickovic, J. M. Baldasano, M. Sicard, F. Rocadenbosch, and V. E. Cachorro (2006), A long Saharan dust event over the western Mediterranean: Lidar, Sun photometer observations, and regional dust modeling, *J Geophys Res-Atmos*, *111*(D15).

Pérez, L., A. Tobías, X. Querol, N. Kunzli, J. Pey, A. Alastuey, M. Viana, N. Valero, M. González-Cabre, and J. Sunyer (2008), Coarse Particles From Saharan Dust and Daily Mortality, *Epidemiology*, *19*(6), 800-807.

Petzold, A., and M. Schonlinner (2004), Multi-angle absorption photometry - a new method for the measurement of aerosol light absorption and atmospheric black carbon, *J Aerosol Sci*, *35*(4), 421-441.

Petzold, A., H. Schloesser, P. J. Sheridan, W. P. Arnott, J. A. Ogren, and A. Virkkula (2005), Evaluation of multiangle absorption photometry for measuring aerosol light absorption, *Aerosol Science and Technology*, *39*(1), 40-51.

Philbrick, C. R. (2002), Overview of Raman lidar techniques for air pollution measurements, *Lidar Remote Sensing for Industry and Environment Monitoring Ii*, *4484*, 136-150.

Pincus, R., and M. B. Baker (1994), Effect of Precipitation on the Albedo Susceptibility of Clouds in the Marine Boundary-Layer, *Nature*, *372*(6503), 250-252.

Preissler, J. (2012), Vertically resolved monitoring of atmospheric aerosols over Portugal with a multi-wavelength Raman lidar, University of Évora.

Preissler, J., F. Wagner, J. L. Guerrero-Rascado, and A. M. Silva (2013), Two years of free-tropospheric aerosol layers observed over Portugal by lidar, *J Geophys Res-Atmos*, *118*(9), 3676-3686.

Prospero, J. M. (1999), Long-term measurements of the transport of African mineral dust to the southeastern United States: Implications for regional air quality, *J Geophys Res-Atmos*, *104*(D13), 15917-15927.

Prospero, J. M., R. Schmitt, E. Cuevas, D. L. Savoie, W. C. Graustein, K. K. Turekian, A. Volzthomas, A. Díaz, S. J. Oltmans, and H. Levy (1995), Temporal Variability of Summer-Time Ozone and Aerosols in the Free Troposphere over the Eastern North-Atlantic, *Geophys Res Lett*, *22*(21), 2925-2928.

Quirantes, A., F. J. Olmo, H. Lyamani, A. Valenzuela, and L. Alados-Arboledas (2012), Investigation of fine and coarse aerosol contributions to the total aerosol light scattering: Shape effects and concentration profiling by Raman lidar measurements, *J Quant Spectrosc Ra*, *113*(18), 323-330.

Raes, F., R. Van Dingenen, E. Vignati, J. Wilson, J. P. Putaud, J. H. Seinfeld, and P. Adams (2000), Formation and cycling of aerosols in the global troposphere, *Atmospheric Environment*, *34*(25), 4215-4240.

Rayleigh, J. W. (1871), On the Light from the Sky, its Polarization and Colour, *Philosophical Magazine*, *41*(4), 107-120; 274-279.

Redelsperger, J. L., C. D. Thorncroft, A. Diedhiou, T. Lebel, D. J. Parker, and J. Polcher (2006), African monsoon multidisciplinary analysis - An international research project and field campaign, *B Am Meteorol Soc*, *87*(12), 1739-+.

Reichardt, J., R. Baumgart, and T. J. McGee (2003), Three-signal methods for accurate measurements of depolarization ratio with lidar, *Appl Optics*, *42*, 4909-4913.

Reid, J. S., et al. (2003), Analysis of measurements of Saharan dust by airborne and ground-based remote sensing methods during the Puerto Rico Dust Experiment (PRIDE), *J Geophys Res-Atmos*, *108*(D19).

Robock, A., and J. C. Antuña (2001), Support for a tropical lidar in Latin America, *Eos, Transactions American Geophysical Union*, *82*(26), 285-289.

Rodríguez, S., A. Alastuey, S. Alonso-Pérez, X. Querol, E. Cuevas, J. Abreu-Afonso, M. Viana, N. Perez, M. Pandolfi, and J. de la Rosa (2011), Transport of desert dust mixed with North African industrial pollutants in the subtropical Saharan Air Layer, *Atmos Chem Phys*, *11*(13), 6663-6685.

Rogelj, N., J. L. Guerrero-Rascado, F. Navas-Guzmán, J. A. Bravo-Aranda, M. J. Granados-Muñoz, and L. Alados-Arboledas (2014), Experimental determination of UV- and VIS- lidar overlap function *Óptica Pura y Aplicada (under review)*.

Rose, T., S. Crewell, U. Lohnert, and C. Simmer (2005), A network suitable microwave radiometer for operational monitoring of the cloudy atmosphere, *Atmos Res*, *75*(3), 183-200.

Roy, G., X. Cao, and R. Bernier (2011), On linear and circular depolarization LIDAR signatures in remote sensing of bioaerosols: experimental validation of the Mueller matrix for randomly oriented particles, *OPTICE*, *50*(12), 126001-126001-126010.

Sassen, K. (1991), The polarization lidar technique for cloud research: A review and current assessment, *Bulletin American Meteorological Society*, *72*, 1848-1866.

Sassen, K., and B. S. Cho (1992), Subvisual Thin Cirrus Lidar Dataset for Satellite Verification and Climatological Research, *J Appl Meteorol*, *31*(11), 1275-1285.

Sassen, K., R. P. Benson, and J. D. Spinhirne (2000), Tropical cirrus cloud properties derived from TOGA/COARE airborne polarization lidar, *Geophys Res Lett*, *27*(5), 673-676.

Satheesh, S. K., K. K. Moorthy, S. S. Babu, V. Vinoj, and C. B. S. Dutt (2008), Climate implications of large warming by elevated aerosol over India, *Geophys Res Lett*, *35*(19).

Scarchilli, C., et al. (2005), Determination of polar stratospheric cloud particle refractive indices by use of in situ optical measurements and T-matrix calculations, *Appl Optics*, *44*(16), 3302-3311.

Schotland, R. M., K. Sassen, and R. Stone (1971), Observations by lidar of linear depolarization ratios for hydrometeors, *J Appl Meteorol*, 1011-1017.

Schryer, D. R. (1982), *Heterogeneous Atmospheric Chemistry*, Wiley.

Schuster, G. L., O. Dubovik, and B. N. Holben (2006), Angstrom exponent and bimodal aerosol size distributions, *J Geophys Res-Atmos*, *111*(D7).

Seibert, P., F. Beyrich, S. E. Gryning, S. Joffre, A. Rasmussen, and P. Tercier (2000), Review and intercomparison of operational methods for the determination of the mixing height, *Atmospheric Environment*, *34*(7), 1001-1027.

Seinfeld, J. H., and S. N. Pandis (1998), *Atmospheric chemistry and physics*, Wiley-Interscience.

Shao, Y. P., K. H. Wyrwoll, A. Chappell, J. P. Huang, Z. H. Lin, G. H. McTainsh, M. Mikami, T. Y. Tanaka, X. L. Wang, and S. Yoon (2011), Dust cycle: An emerging core theme in Earth system science, *Aeolian Res*, *2*(4), 181-204.

Shimizu, A., N. Sugimoto, I. Matsui, K. Arao, I. Uno, T. Murayama, N. Kagawa, K. Aoki, A. Uchiyama, and A. Yamazaki (2004), Continuous observations of Asian dust and other aerosols by polarization lidars in China and Japan during ACE-Asia, *J Geophys Res-Atmos*, *109*(D19).

Snels, M., F. Cairo, F. Colao, and G. Di Donfrancesco (2009), Calibration method for depolarization lidar measurements, *International Journal of Remote Sensing*, *30*(21), 5725-5736.

Sorribas, M., J. A. Adame, F. J. Olmo, J. M. Vilaplana, M. Gil, and L. Alados-Arboledas (2014), Long-term study of new particle formation in a coastal environment: meteorology, gas phase and solar radiation implications, *Science of the Total Environment*, *(submitted)*.

Stelitano, D., P. Di Girolamo, and D. Summa (2013), Characterization of Particle Hygroscopicity by Raman Lidar: Selected Case Studies from the Convective and Orographically-Induced Precipitation Study, *Radiation Processes in the Atmosphere and Ocean (Irs2012)*, *1531*, 204-207.

Stevens, B., and J. L. Brenguier (2009), Cloud-controlling Factors Low Clouds, *Clouds in the Perturbed Climate System: Their Relationship to Energy Balance, Atmospheric Dynamics, and Precipitation*, 173-196.

Stull, R. B. (1988), *An Introduction to Boundary Layer Meteorology*, Kluwer Academic Publishers.

Stull, R. B. (2000), *Meteorology: For Scientists and Engineers*, Thomson Learning.

Stunder, B. J. B. (1996), An assessment of the quality of forecast trajectories, *J Appl Meteorol*, *35*(8), 1319-1331.

Summa, D., P. Di Girolamo, and D. Stelitano (2013), Characterization of PBL Height and Structure by Raman Lidar: Selected Case Studies from the Convective and Orographically-induced Precipitation Study, *Radiation Processes in the Atmosphere and Ocean (Irs2012)*, *1531*, 208-211.

Tafuro, A. M., F. Barnaba, F. De Tomasi, M. R. Perrone, and G. P. Gobbi (2006), Saharan dust particle properties over the central Mediterranean, *Atmos Res*, *81*(1), 67-93.

Tanre, D., J. Haywood, J. Pelon, J. F. Leon, B. Chatenet, P. Formenti, P. Francis, P. Goloub, E. J. Highwood, and G. Myhre (2003), Measurement and modeling of the Saharan dust radiative impact: Overview of the Saharan Dust Experiment (SHADE), *J Geophys Res-Atmos*, *108*(D18).

Tegen, I., and I. Fung (1995), Contribution to the Atmospheric Mineral Aerosol Load from Land-Surface Modification, *J Geophys Res-Atmos*, *100*(D9), 18707-18726.

Tegen, R., and H. G. Miller (2004), Magnetic moment of a massive neutrino due to its pion cloud, *Phys Rev D*, *70*(3).

Tesche, M., A. Ansmann, D. Muller, D. Althausen, R. Engelmann, V. Freudenthaler, and S. Gross (2009a), Vertically resolved separation of dust and smoke over Cape Verde using multiwavelength Raman and polarization lidars during Saharan Mineral Dust Experiment 2008, *J Geophys Res-Atmos*, *114*.

Tesche, M., S. Gross, A. Ansmann, D. Muller, D. Althausen, V. Freudenthaler, and M. Esselborn (2011), Profiling of Saharan dust and biomass-burning smoke with multiwavelength polarization Raman lidar at Cape Verde, *Tellus B*, *63*(4), 649-676.

Tesche, M., et al. (2009b), Vertical profiling of Saharan dust with Raman lidars and airborne HSRL in southern Morocco during SAMUM, *Tellus B*, *61*(1), 144-164.

Titos, G., I. Foyo-Moreno, H. Lyamani, X. Querol, A. Alastuey, and L. Alados-Arboledas (2012), Optical properties and chemical composition of aerosol particles at an urban location: An estimation of the aerosol mass scattering

and absorption efficiencies, *Journal of Geophysical Research D: Atmospheres*, *117*(4).

Twomey, D. (1977), Health-Care Institutions under National-Labor-Relations-Act, *Am Bus Law J*, *15*(2), 225-241.

Valenzuela, A., F. J. Olmo, H. Lyamani, M. Antón, A. Quirantes, and L. Alados-Arboledas (2012), Analysis of the columnar radiative properties retrieved during African desert dust events over Granada (2005-2010) using principal plane sky radiances and spheroids retrieval procedure, *Atmos Res*, *104*, 292-301.

Wandinger, U., and A. Ansmann (2002), Experimental determination of the lidar overlap profile with Raman lidar, *Appl Optics*, *41*(3), 511-514.

Wang, Z., X. Cao, L. Zhang, J. Notholt, B. Zhou, R. Liu, and B. Zhang (2012), Lidar measurement of planetary boundary layer height and comparison with microwave profiling radiometer observation, *Atmos Meas Tech*, *5*(8), 1965-1972.

Waterman, P. C. (1971), Symmetry, Unitarity, and Geometry in Electromagnetic Scattering, *Phys Rev D*, *3*(4), 825-&.

Weitkamp, C. (2005), *Lidar: Range-Resolved Optical Remote Sensing of the Atmosphere*, Springer.

Welton, E. J., J. R. Campbell, J. D. Spinhirne, and V. S. Scott Iii (2001), Global monitoring of clouds and aerosols using a network of micropulse lidar systems.

Whitby, K. T., D. B. Kittelson, B. K. Cantrell, N. J. Barsic, D. F. Dolan, L. D. Tarvestad, D. J. Nieken, J. L. Wolf, and J. R. Wood (1976), Aerosol Size Distributions and Concentrations Measured during Gm Proving Ground Sulfate Study, *Abstr Pap Am Chem S*, *172*(Sep3), 32-32.

Whiteman, D. N., S. H. Melfi, and R. A. Ferrare (1992), Raman Lidar System for the Measurement of Water-Vapor and Aerosols in the Earths Atmosphere, *Appl Optics*, *31*(16), 3068-3082.

Winker, D. M., and M. T. Osborn (1992), Airborne Lidar Observations of the Pinatubo Volcanic Plume, *Geophys Res Lett*, *19*(2), 167-170.

Woodward, R., R. L. Collins, and R. S. Disselkamp (1998), paper presented at 19th International Laser Radar conference, Annapolis, MD, USA.

The information extracted from the webpages included in this thesis have been checked for the last time of 19 March 2014.

# List of scientific contributions

## Articles in peer-review journals

2014    **Assessment of lidar depolarization uncertainties by means of lidar polarizing sensitivity simulator**
*Atmospheric Measurements and Techniques (to be submitted)*
**J. A. Bravo-Aranda**, L. Belegante, V. Freudenthaler, L. Alados-Arboledas, D. Nicolae, A. Amodeo, R. Engelmann, P. Kokkalis, A. Papayannis and U. Wandinger

2014    **Experimental assessment of the lidar polarizing sensitivity**
*Atmospheric Measurements and Techniques (to be submitted)*
L. Belegante, **J. A. Bravo-Aranda**, V. Freudenthaler, L. Alados-Arboledas, D. Nicolae, A. Amodeo, R. Engelmann, P. Kokkalis, A. Papayannis and U. Wandinger

2014    **Active and passive remote sensing for monitoring the planetary boundary layer height**
*Óptica Pura y Aplicada (under review)*
J.L. Corredor-Ardoy, **J.A. Bravo-Aranda**, M.J Granados-Muñoz, J.L. Guerrero-Rascado, J. Fernández-Gálvez, A. Cazorla and L. Alados-Arboledas

2014    **Experimental determination of UV- and VIS- lidar overlap function**
*Óptica Pura y Aplicada (under review)*
N. Rogelj, J. L. Guerrero-Rascado, F. Navas-Guzmán, **J. A. Bravo-Aranda**, M. J. Granados-Muñoz and L. Alados-Arboledas

2014    **Characterization of atmospheric aerosols for a long range transport of biomass burning particles from Canadian forest fires over the southern Iberian Peninsula in July 2013**
*Óptica Pura y Aplicada (under review)*
P. Ortiz-Amezcua, J. L. Guerrero-Rascado, M. J. Granados-Muñoz, **J. A. Bravo-Aranda** and L. Alados-Arboledas

2014 **Retrieving aerosol microphysical properties by LIdar-Radiometer Inversion Code (LIRIC) for different aerosol types**
Journal of Geophysical Research (*accepted*)
M. J. Granados- Muñoz, J. L. Guerrero-Rascado, **J. A. Bravo-Aranda**, F. Navas-Guzmán, A. Valenzuela, H. Lyamani, A. Chaikovsky, U. Wandinger, A. Ansmann, O. Dubovik and L. Alados-Arboledas

2013 **Tropospheric water vapour and relative humidity profiles from lidar and microwave radiometry**
*Atmospheric Measurement Techniques Discussions, 6, 10481-10510*
F. Navas-Guzmán, J. Fernández-Gálvez, M. J. Granados-Muñoz, J. L. Guerrero-Rascado, **J. A. Bravo-Aranda** and L. Alados-Arboledas

2013 **Statistical analysis of aerosol optical properties retrieved by Raman lidar over Southeastern Spain**
*Tellus B, 65, 21234*
F. Navas-Guzmán, **J. A. Bravo-Aranda**, J.L. Guerrero-Rascado, M.J. Granados-Muñoz and L. Alados-Arboledas

2013 **Four-dimensional distribution of the 2010 Eyjafjallajökull volcanic cloud over Europe observed by EARLINET**
*Atmospheric Chemistry and Physics, 13, 4429-4450*
G. Pappalardo, L. Mona, G. D'Amico, U. Wandinger, M. Adam, A. Amodeo, A. Ansmann, A. Apituley, L. Alados-Arboledas, D. Balis, A. Boselli, **J. A. Bravo-Aranda**, A. Chaikovsky, A. Comerón, J. Cuesta, F. De Tomasi, V. Freudenthaler, M. Gausa, E. Giannakaki, H. Giehl, A. Giunta, I. Grigorov, S. Groß, M. Haeffelin, A. Hiebsch, M. Iarlori, D. Lange, H. Linné, F. Madonna, I. Mattis, R. E. Mamouri, M. A.P. McAuliffe, V. Mitev, F. Molero, F. Navas-Guzman, D. Nicolae, A. Papayannis, M. R. Perrone, C. Pietras, A. Pietruczuk, G. Pisani, J. Preißler, M. Pujadas, V. Rizi, A. A. Ruth, J. Schmidt, F. Schnell1, P. Seifert, I. Serikov, M. Sicard, V. Simeonov, N. Spinell, K. Stebel, M. Tesche, T. Trickl, X. Wang, F. Wagner, M. Wiegner, and K. M. Wilson

2013 **Aerosol size distribution from inversion of solar radiances and measured at ground-level during SPALI10 campaign**
*Atmospheric Research, 127, 130-140*
J. Fernández-Gálvez, J. L. Guerrero-Rascado, F. Molero, H. Lyamani, M. A. Revuelta, F. Navas-Guzmán, M. Sastre, **J. A. Bravo-Aranda**, A. J. Fernández, M. J. Granados-Muñoz, F. J. Gómez-Moreno, F. J. Olmo, M. Pujadas, and L. Alados-Arboledas

2013 **Analysis of lidar depolarization calibration procedure and application to the atmospheric aerosol characterization**
*International Journal of Remote Sensing, 34 (9-10), 3543-3560*
**J. A. Bravo-Aranda**, F. Navas-Guzmán, J. L. Guerrero-Rascado, D. Pérez-Ramírez, M. J. Granados-Muñoz, and L. Alados-Arboledas

2013 **Eruption of the Eyjafjallajökull Volcano in spring 2010: Multiwavelength Raman Lidar Measurements of Sulfate Particles in the Lower Troposphere**
*Journal of Geophysical Research, 118 (4) 1804-1813*
F. Navas-Guzmán, D. Müller, **J. A. Bravo-Aranda**, J. L. Guerrero-Rascado, M. J. Granados-Muñoz, D. Pérez-Ramírez, F. Olmo-Reyes and L. Alados-Arboledas

2012 **Monitoring of the Eyjafjallajökull volcanic aerosol plume over the Iberian Peninsula by means of four EARLINET lidar stations**
*Atmospheric Chemistry and Physics, 12, 3115-3130*
M. Sicard, J.L. Guerrero-Rascado, F. Navas-Guzmán, J. Preißler, F. Molero, S. Tomás, **J.A. Bravo-Aranda**, A. Comerón, F. Rocadenbosch, F. Wagner, M. Pujadas, L. Alados-Arboledas

2012 **Four-dimensional distribution of the 2010 Eyjafjallajökull volcanic cloud over Europe observed by EARLINET**
*Atmospheric Chemistry and Physics Discussion, 12, 30203-30257*
G. Pappalardo, L. Mona, G. D'Amico, U. Wandinger, M. Adam, A. Amodeo, A. Ansmann, A. Apituley, L. Alados-Arboledas, D. Balis, A. Boselli, **J. A. Bravo-Aranda**, A. Chaikovsky, A. Comerón, J. Cuesta, F. De Tomasi, V. Freudenthaler, M. Gausa, E. Giannakaki, H. Giehl, A. Giunta, I. Grigorov, S. Groß, M. Haeffelin, A. Hiebsch, M. Iarlori, D. Lange, H. Linné, F. Madonna, I. Mattis, R. E. Mamouri, M. A.P. McAuliffe, V. Mitev, F. Molero, F. Navas-Guzman, D. Nicolae, A. Papayannis, M. R. Perrone, C. Pietras, A. Pietruczuk, G. Pisani, J. Preißler, M. Pujadas, V. Rizi, A. A. Ruth, J. Schmidt, F. Schnell1, P. Seifert, I. Serikov, M. Sicard, V. Simeonov, N. Spinell, K. Stebel, M. Tesche, T. Trickl, X. Wang, F. Wagner, M. Wiegner, and K. M. Wilson

2012 **Study on aerosol properties over Madrid (Spain) by multiple instrumentation during SPALI10 lidar campaign**
*Óptica Pura y Aplicada, 45 (4), 405-413*
F. Molero, M. Sicard, F. Navas-Guzmán, J. Preißler, A. Amodeo, V. Freudenthaler, A. J. Fernández, S. Tomás, M. J. Granados-Muñoz, F. Wagner, A. Giunta, I. Mattis, M. Pujadas, A. Comerón, L. Alados-Arboledas, J. L. Guerrero-Rascado, G. D'Amico, D. Lange, **J. A. Bravo-Aranda**, D. Kumar, G. Pappalardo, J. Giner, C. Muñoz, and F. Rocadenbosch

271

2012 **Automatic determination of the boundary layer height using lidar: one-year analysis over southeastern Spain**
*Journal of Geophysical Research, 117, D18208*
M. J. Granados-Muñoz, F. J. Navas-Guzmán, **J. A. Bravo-Aranda**, J. L. Guerrero-Rascado, H. Lyamani, J. Fernández-Gálvez, L. Alados-Arboledas

2011 **Study on aerosol properties over Madrid (Spain) by multiple instrumentation during SPALI10 lidar campaign**
*Revista Boliviana de Física, 20, 16-18*
F. Molero, A. j. Fernández, M. Pujadas, M. Sicard, S. Tomás, A. Comerón, D. Lange, D. Kumar, J. Giner, C. Muñoz, F. Rocadenbosch, F. Navas-Guzmán, M. J. Granados-Muñoz, L. Alados-Arboledas, **J. A. Bravo-Aranda**, J. Preißler, F. Wagner, and J. L. Guerrero-Rascado

2011 **Calibration of 1064nm-backscatter profiles with a multiwavelength Raman lidar**
*Romanian Journal of Physics, 56 (3-4) 460-466*
F. J. Navas-Guzmán, J. L. Guerrero-Rascado, **J.A. Bravo-Aranda**, and L. Alados-Arboledas

2011 **Monitoring of the Eyjafjallajökull volcanic aerosol plume over the Iberian Peninsula by means of four EARLINET lidar stations**
*Atmospheric Chemistry and Physics Discussion, 11, 29681-59721*
M. Sicard, J.L. Guerrero-Rascado, F. Navas-Guzmán, J. Preißler, F. Molero, S. Tomás,, **J.A. Bravo-Aranda**, A. Comerón, F. Rocadenbosch, F. Wagner, M. Pujadas, L. Alados-Arboledas

2011 **On the use cirrus clouds for elastic lidar calibration**
*Óptica Pura y Aplicada, 44 (1) 49-53*
F. Navas-Guzmán, J.L. Guerrero-Rascado, **J.A. Bravo-Aranda** and L. Alados-Arboledas

2011 **Quality assurance at the EARLINET Granada station: characterization of the optical subsystem for a multichannel Raman lidar**
*Óptica Pura y Aplicada, 44 (1) 19-23*
J.L. Guerrero-Rascado, F. Navas-Guzmán, J.A. Díaz, **J.A. Bravo-Aranda** and L. Alados-Arboledas

## Book chapters

**2013** **Monitoring daily evolution of the atmospheric aerosol in an urban environment by means of remote sensing and in-situ methodologies**
*Juan Antonio Morente Chiquero: in memoriam, 75-80, ISBN: 978-84-338-5540-4*
L. Alados-Arboledas, I. Foyo, H. Lyamani, J. L. Guerrero-Rascado, F. Navas-Guzmán, **J. A. Bravo-Aranda**, A. Cazorla, J. Fernández-Gálvez, G. Titos, M. J. Granados-Muñoz, I. Alados, A. Valenzuela and F. J. Olmo

**2011** **Aerosol size distribution from inversion of solar radiances and measured at ground-level during SPALI10 campaign**
*Proceedings of the Global Conference on Global Warming 2011, ISBN: 978-989-95091-3-9*
J. Fernández-Gálvez, J. L. Guerrero-Rascado, F. Molero, H. Lyamani, M. A. Revuelta, F. Navas-Guzmán, M. Sastre, **J. A. Bravo-Aranda**, A. J. Fernández, M. J. Granados-Muñoz, F. J. Gómez-Moreno, F. J. Olmo, M. Pujadas, and L. Alados-Arboledas

**2011** **Study on aerosol properties over Madrid (Spain) by multiple instrumentation during EARLINET lidar intercomparison campaign: SPALI10**
*Book of extended abstracts of V Reunión Española de Ciencia y Tecnología de Aerosoles, ISBN: 978-84-7834-662-2*
F. Molero, A. Amodeo, M. Sicard, J. Preißler, F. Navas-Guzmán, V. Freudenthaler, A. J. Fernández, A. Giunta, S. Tomás, F. Wagner, M. J. Granados-Muñoz, I. Mattis, M. Pujadas, G. D'Amico, A. Comeron, J. L. Guerrero-Rascado, L. Alados-Arboledas, D. Lange, **J. A. Bravo-Aranda**, D. Kumar, G. Pappalardo, J. Giner, C. Muñoz, and F. Rocadenbosch

**2011** **Multi-instrumental detection of the mixing layer height over Granada**
*Book of extended abstracts of V Reunión Española de Ciencia y Tecnología de Aerosoles, ISBN: 978-84-7834-662-2*
M. J. Granados-Muñoz, F. Navas-Guzmán, **J. A. Bravo-Aranda**, J. L. Guerrero-Rascado, J. Fernández-Gálvez, and L. Alados-Arboledas

**2011** **Atmospheric aerosol characterization by dual lidar depolarization**
*Book of extended abstracts of V Reunión Española de Ciencia y Tecnología de Aerosoles, ISBN: 978-84-7834-662-2*
**J. A. Bravo Aranda**, F. J. Navas-Guzmán, M. J. Granados-Muñoz, J. L. Guerrero-Rascado, and L. Alados-Arboledas

2011 **Study of ground-based vertical profiles of tropospheric aerosol in coincidence with CALIPSO overpasses at Granada, Spain**
*Book of extended abstracts of V Reunión Española de Ciencia y Tecnología de Aerosoles, ISBN: 978-84-7834-662-2*
F. Navas-Guzmán, **J. A. Bravo-Aranda**, J. L. Guerrero-Rascado, M. J. Granados-Muñoz, and L. Alados-Arboledas

2010 **Study on the planetary boundary layer top with Raman lidar**
*Book of extended abstracts of IV Reunión Española de Ciencia y Tecnología de Aerosoles, ISBN: 978-84-693-4839-0*
F. Navas-Guzmán, **J. A. Bravo-Aranda**, M. J. Granados-Muñoz, J. L. Guerrero-Rascado, and L. Alados-Arboledas

2010 **Long-term air quality trends over Granada, Spain**
*Book of extended abstracts of IV Reunión Española de Ciencia y Tecnología de Aerosoles, ISBN: 978-84-693-4839-0*
**J.A. Bravo-Aranda**, H. Lyamani, F. J. Olmo, J. Vera and L. Alados-Arboledas

2010 **Evaluation of two correction schemes of particle soot absorption photometer data**
*Book of extended abstracts of IV Reunión Española de Ciencia y Tecnología de Aerosoles, ISBN: 978-84-693-4839-0*
H. Lyamani, I. Foyo-Moreno, **J. A. Bravo-Aranda**, F. J. Olmo and L. Alados-Arboledas

2010 **Monitoring of the Eyjafjallajökull ash plume at four lidar stations over the Iberian Peninsula: 6 to 8 May 2010**
*Book of extended abstracts of IV Reunión Española de Ciencia y Tecnología de Aerosoles, ISBN: 978-84-693-4839-0*
J.L. Guerrero-Rascado, M. Sicard, F. Molero, F. Navas-Guzmán, J. Preissler, D. Kumar, **J. A. Bravo-Aranda**, S. Tomas, M. D. Reba, L. Alados-Arboledas, A. Comerón, M. Pujadas, F. Rocadenbosch, F. Wagner and A. M. Silva

2010 **On the synergetic use of passive and active remote sensing for atmospheric aerosol radiative effect computations**
*Book of extended abstracts of IV Reunión Española de Ciencia y Tecnología de Aerosoles, ISBN: 978-5-94458-109-9*
F. Navas-Guzmán, D. Pérez-Ramírez, F.J. Olmo, H. Lyamani, J.L. Guerrero-Rascado, **J. A. Bravo-Aranda** and L. Alados-Arboledas

2010 **Optical and microphysical properties of tropospheric aerosol from Raman lidar**
*Third recent advances in quantitative remote sensing, ISBN: 978-84-370-7952-3*
F. Navas-Guzmán, D. Pérez-Ramírez, J.L. Guerrero-Rascado, **J. A. Bravo-Aranda** and L. Alados-Arboledas

2010 **Monitoring of lofted aerosol layers of mineral desert dust with Raman Lidar and a set of photometers at different altitudes**
*Book of extended abstracts of IV Reunión Española de Ciencia y Tecnología de Aerosoles, ISBN: 978-84-693-4839-0*
F.J. Olmo, F. Navas-Guzmán, H. Lyamani, **J. A. Bravo-Aranda,** J.L. Guerrero-Rascado and L. Alados-Arboledas

2010 **Atmospheric aerosol characterization by lidar depolarization profiles**
*Third recent advances in quantitative remote sensing, ISBN: 978-84-370-7952-3*
**J. A. Bravo-Aranda,** F. Navas-Guzmán, M. J. Granados-Muñoz and L. Alados-Arboledas

2010 **Study on the assumption of using a range-independent lidar ratio in elastic lidar**
*Third recent advances in quantitative remote sensing, ISBN: 978-84-370-7952-3*
F. Navas-Guzmán, F. J. Olmo, J. L. Guerrero-Rascado, **J. A. Bravo-Aranda** and L. Alados-Arboledas

2009 **Airborne and ground based instrumentation comparison: closure study during CAPEX project**
*Proceedings of the 8 International Symposium on Tropospheric Profiling: Integration of Needs, Technologies and Applications, ISBN: 978-90-6960-233-2*
J. L. Guerrero-Rascado, H. Lyamani, A. M. Silva, F. Wagner, S. Pereira, F. Navas-Guzmán, **J. A. Bravo-Aranda** and L. Alados-Arboledas

2009 **Atmospheric aerosol properties in an urban atmosphere: ESTIO2005**
*Proceedings of the 8 International Symposium on Tropospheric Profiling: Integration of Needs, Technologies and Applications, ISBN: 978-90-6960-233-2*
L. Alados-Arboledas, H. Horvath, X. Querol, J. L. Guerrero-Rascado, H. Lyamani, F. Navas-Guzmán, **J. A. Bravo-Aranda**, S. Castillo and A. Alastuey

2009 **Optical properties of free tropospheric aerosol from multi-wavelength Raman lidars over the Southern Iberian Peninsula**
*Proceedings of the 8 International Symposium on Tropospheric Profiling: Integration of Needs, Technologies and Applications, ISBN: 978-90-6960-233-2*
J. Preissler, **J. A. Bravo-Aranda**, F. Wagner, M. J. Granados-Muñoz, F. Navas-Guzmán, J. L. Guerrero-Rascado, H. Lyamani and L. Alados-Arboledas

## International conference contributions

2013 **Characterization of atmospheric aerosols for a long range transport of biomass burning particles from Canadian forest fires over the southern Iberian Peninsula in July 2013**
*Poster. VII Workshop on Lidar Measurements in Latin America, Pucón, Chile*
P. Ortiz-Amezcua, J. L. Guerrero-Rascado, M. J. Granados-Muñoz, **J. A. Bravo-Aranda** and L. Alados-Arboledas

2013 **Improvements on planetary boundary layer height estimates using lidar depolarization during CHARMEX 2012 campaign**
*Poster. VII Workshop on Lidar Measurements in Latin America, Pucón, Chile*
**J. A. Bravo-Aranda**, M.J. Granados-Muñoz, F. Navas-Guzmán, J.L. Guerrero-Rascado, J. Fernández-Gálvez, F. J. Olmo and L. Alados-Arboledas

2013 **Active and passive remote sensing for monitoring the planetary boundary layer height**
*Poster. VII Workshop on Lidar Measurements in Latin America, Pucón, Chile*
J.L. Corredor-Ardoy, **J. A. Bravo-Aranda**, M.J. Granados-Muñoz, J.L. Guerrero-Rascado, J. Fernández-Gálvez, A. Cazorla and L. Alados-Arboledas

2013 **Experimental determination of UV- and VIS- lidar overlap function**
*Poster. VII Workshop on Lidar Measurements in Latin America, Pucón, Chile*
N. Rogelj, J. L. Guerrero-Rascado, F. Navas-Guzmán, **J. A. Bravo-Aranda**, M. J. Granados-Muñoz and L. Alados-Arboledas

2013 **Lidar depolarization evolution during the CHARMEX intensive field campaign**
*Poster. European Aerosol Conference 2013, Prague, Czech Republic*
**J. A. Bravo-Aranda**, M. J. Granados-Muñoz, F. Navas-Guzmán, J.L. Guerrero-Rascado, F. J. Olmo and L. Alados-Arboledas

**2013** **First retrievals of aerosol properties derived from measurements of the new airborne sunphotometer plasma during the campaigns shadows and CHArMEx**
*Poster. 7$^{th}$ International Workshop on Sand/Dust storms and Associated Dustfall, Frascati, Rome, Italy*
B. Torres, L. Blarel, P. Goloub, M. Mallet, T. Bourrianne, D. Tanré, F. Dulac, O. Dubovik, C. Verwaerde, T. Podvin, A. Mortier, Y. Derimian, J. L. Guerrero-Rascado, L. Alados-Arboledas, M. J. Granados-Muñoz, **J. A. Bravo-Aranda**, G. Roberts, G, Monboisse, P. Chazette, J. Totems, M. L. Boytard and D. Fuertes

**2013** **Analysis of aerosol hygroscopic properties by combination of lidar, microwave radiometer and radiosounding data**
*Poster. European Aerosol Conference 2013, Prague, Czech Republic*
M. J. Granados-Muñoz, F. Navas-Guzmán, **J. A. Bravo-Aranda**, J.L. Guerrero-Rascado, A. Valenzuela, J. Fernández-Gálvez and L. Alados-Arboledas

**2013** **72h-temporal evolution of lidar depolarization during CHARMEX**
*Poster. 1$^{st}$ Iberian Meeting on Aerosol Science and Technology (RICTA2013), Évora, Portugal*
**J. A. Bravo-Aranda**, M.J. Granados-Muñoz, F. Navas-Guzmán, J.L. Guerrero-Rascado, F. Olmo and L. Alados-Arboledas
**Awarded as the best poster in RICTA2013**

**2013** **Bimodal particle concentration profile retrieved from ground-based Lidar and CIMEL measurements**
*Poster. European Aerosol Conference 2013, Prague, Czech Republic*
A. Quirantes, F.J. Olmo, A. Valenzuela, M. J. Granados-Muñoz, J.L. Guerrero-Rascado, **J.A. Bravo-Aranda**, F. Navas-Guzmán and L. Alados-Arboledas

**2013** **Application of active and passive remote sensing to study aerosol hygroscopic growth**
*Oral. 1$^{st}$ Iberian Meeting on Aerosol Science and Technology (RICTA2013), Évora, Portugal*
F. Navas-Guzmán, **J. A. Bravo-Aranda**, J.L. Guerrero-Rascado, A. Valenzuela, J. Fernández-Gálvez and L. Alados-Arboledas

2013 **Layer-by-layer concentration retrieval of an airborne two-component particle mixture from ground-based lidar and Cimel measurements**
*Oral. 1$^{st}$ Iberian Meeting on Aerosol Science and Technology (RICTA2013), Évora, Portugal*
A. Quirantes, F. J. Olmo, A. Valenzuela, M. J. Granados-Muñoz, J. L. Guerrero-Rascado, **J. A. Bravo-Aranda**, F. Navas-Guzmán, and L. Alados-Arboledas

2012 **Combined observations with multi-wavelength Raman lidars and sun photometers on the southern Iberian Peninsula**
*Poster. Europena Aerosol Conference 2012, Granada, Spain*
J. Preißler, **J. A. Bravo-Aranda**, F. Wagner, M. J. Granados-Muñoz, F. J. Navas-Guzman, J. L. Guerrero-Rascado, H. Lyamani, L. Alados-Arboledas

2012 **Optical properties of free tropospheric aerosol from multi-wavelength Raman lidars over the Southern Iberian Peninsula**
*Poster. 9 International Symposium on Tropospheric Profiling (ISTP2012), L'Aquila, Italy*
J. Preißler, **J. A. Bravo-Aranda**, F. Wagner, M. J. Granados-Muñoz, F. Navas-Guzmán, J. L. Guerrero-Rascado, H. Lyamani and L. Alados-Arboledas

2012 **Retrieval of aerosol microphysical properties profiles by combination of Lidar and sun photometer measurements. Application to mineral dust and volcanic aerosols**
*Oral. Europena Aerosol Conference 2012, Granada, Spain*
M. J. Granados-Muñoz, **J. A. Bravo-Aranda**, F. Navas-Guzmán, J.L. Guerrero-Rascado, H. Lyamani, A.Chaikovsky, J. Wagner, U. Wandinger, F.J.Olmo and L. Alados-Arboledas

2012 **CLIMARENO-GRA 2011 campaign: Aerosol optical properties characterization from ground-based instrumentation**
*Oral. Europena Aerosol Conference 2012, Granada, Spain*
**J. A. Bravo-Aranda**, F. Navas-Guzmán, J. Andrey, M.J. Granados-Muñoz, J.L. Guerrerro-Rascado, M.Gil, H. Lyamani, A. Valenzuela, G. Titos, J. Fernández-Gálvez, F.J. Olmo and L. Alados-Arboledas

2012    **CLIMARENO-GRA 2011 campaign: retrieval of vertically-resolved aerosol microphysical properties by lidar at daytime**
*Oral. Europena Aerosol Conference 2012, Granada, Spain*
Guerrero-Rascado, M. J. Granados-Muñoz, F. Navas-Guzmán, **J. A. Bravo-Aranda**, F. J. Olmo, J. Andrey, M. Gil, A. Chaikovsky, U. Wandinger and L. Alados-Arboledas

2012    **Detection of the stratospheric volcanic aerosol plume from the Nabro eruption in summer 2011 in the framework of SPALINET**
*Poster. Europena Aerosol Conference 2012, Granada, Spain*
J.L. Guerrero-Rascado, **J.A. Bravo-Aranda**, F. Wagner, C. Córdoba-Jabonero, F. Molero, D. Lange, M. J. Granados-Muñoz, J. Preißler, D. Toledo, A.J. Fernández, M. Sicard, F. Navas-Guzmán, Y. Hernández, A.M. Silva, M. Pujadas, A. Comerón, S. Pereira, F. Rocadenbosch and L. Alados-Arboledas

2012    **An update on ChArMEx (the Chemistry-Aerosol Mediterranean Experiment) activities and plans for aerosol studies in the Mediterranean region**
*Poster. Europena Aerosol Conference 2012, Granada, Spain*
F. Dulac and an international ChArMEx Team: T. Agacayak, L. Alados Arboledas, A. Alastuey, Z. Ameur, G. Ancellet, E.-M. Assamoi, J.-L. Attié, S. Becagli, M. Beekmann, G. Bergametti, M. Bocquet, F. Bordier, T. Bourrianne, **J.A. Bravo-Aranda**, P. Chazette, I. Chiapello, P. Coddeville, A. Colomb, A. Comerón, G. D'Amico, B. D'Anna, K. Desboeufs, J. Descloitres, M. Diouri, C. Di Biagio, G. Di Sarra, P. Durand, L. El Amraoui, R. Ellul, L. Fleury, P. Formenti, E. Freney, E. Gerasopoulos, P. Goloub, M.J. Granados-Muñoz, J.L. Guerrero Rascado, C. Guieu, D. Hadjimitsis, E. Hamonou, H.C. Hansson, M. Iarlori, S. Ioannou, E. Jaumouillé, M. Jeannot, W. Junkermann, C. Keleshis, S. Kleanthous, P. Kokkalis, D. Lambert, B. Laurent, J.-F. Léon, C. Liousse, M. Lopez Bartolome, R. Losno, M. Mallet, R.-E. Mamouri, N. Marchand, L. Menut, N Mihalopoulos, R. Morales Baquero, P. Nabat, F. Navas-Guzmán, D. Nicolae, J. Nicolas, G. Notton, C. Paoli, A. Papayannis, G. Pappalardo, S. Pandis, J. Pelon, J. Pey, V. Pont, X. Querol, F. Ravetta, J.-B. Renard, V. Rizi, G. Roberts, K. Sartelet, J.-L. Savelli, J. Sciare, K. Sellegri, D.M. Sferlazzo, M. Sicard, A. Smyth, F. Solmon, D. Tanré, A. Tovar Sánchez, N. Verdier, F. Wagner, Y. Wang, J. Wenger, N. Yassaa, et al.

2012    **Towards a remote sensing tool for aerosol hygroscopicity studies combining lidar and passive microwave radiometry**
*Poster. Europena Aerosol Conference 2012, Granada, Spain*
F. Navas-Guzmán, **J. A. Bravo-Aranda**, M. J. Granados-Muñoz, J. L. Guerrero-Rascado, J. Fernández-Gálvez, A. J. Fernández and L. Alados-Arboledas

279

2012 **Optical and microphysical characterization of volcanic sulphate particles in the lower troposphere by Raman lidar**
*Poster. Europena Aerosol Conference 2012, Granada, Spain*
F. Navas-Guzmán, D. Müller, **J. A. Bravo-Aranda**, D. Pérez-Ramírez, F. J. Olmo, J. L. Guerrero-Rascado, U. Wandinger and L. Alados-Arboledas

2011 **Study on aerosol properties over Madrid (Spain) by multiple instrumentation during SPALI10 lidar campaign**
*Poster. VI Workshop on lidar measurements in latin America, La Paz, Bolivia*
F. Molero, A. J. Fernández, M. Pujadas, M. Sicard, S. Tomás, A. Comerón, D. Lange, D. Kumar, J. Giner, C. Muñoz, F. Rocadenbosch, F. Navas-Guzmán, M.J. Granados-Muñoz, L. Alados-Arboledas, **J. A. Bravo-Aranda**, J. Preißler, F. Wagner, and J.L. Guerrero-Rascado

2011 **Aerosol size distribution study by airborne and ground-level in-situ measurements and remote sensing during EARLINET lidar intercomparison campaign: SPALI10**
*Poster. European Aerosol Conference 2011, Manchester, England*
F. Molero, F. J. Andrey, J. Preißler, F. Navas-Guzmán, A. Giunta, M. Sicard, A. J. Fernández, M. C. Parrondo, F. Wagner, M.J. Granados-Muñoz, G. D'Amico, S. Tomás, M. Pujadas, C. Córdoba-Jabonero, J. L. Guerrero-Rascado, L. Alados-Arboledas, A. Amodeo, A. Comerón, **J. A. Bravo-Aranada**, G. Pappalardo, D. Kumar, I. Mattis, V. Freudenthaler, D. Lange, J. Giner, C. Muñoz, and F. Rocadenbosch

2011 **Multi-instrumental characterization of the mixing of Eyjafjallajökull volcanic aerosols and boundary layer aerosols at Granada, Spain**
*Poster. European Aerosol Conference 2011, Manchester, England*
L. Alados-Arboledas, F. Navas-Guzmán, **J. A. Bravo-Aranda**, H. Lyamani, D. Pérez-Ramírez, J. L. Guerrero-Rascado, I. Foyo, I. Alados, M. J. Granados-Muñoz, G. Titos, J. Fernández-Gálvez, A. Valenzuela, M. Antón, A. Quirantes, X. Querol, A. Alastuey, and F. J. Olmo

2011 **Three years of Raman lidar measurements in correspondence with CALIPSO overpasses over the South of the Iberian Peninsula**
*Poster. European Aerosol Conference 2011, Manchester, England*
F. Navas-Guzmán, **J. A. Bravo-Aranda**, J. L. Guerrero-Rascado, M. J. Granados-Muñoz, and L. Alados-Arboledas

2011 **Aerosol size distribution from inversion of solar radiances and measured at ground-level during SPALI10 campaign**
*Poster. Global Conference on Global Warming 2011, Lisbon, Portugal*
J. Fernández-Gálvez, J. L. Guerrero-Rascado, F. Molero, H. Lyamani, M. A. Revuelta, F. Navas-Guzmán, M. Sastre, **J. A. Bravo-Aranda**, A. J. Fernández, M. J. Granados-Muñoz, F. J. Gómez-Moreno, F. J. Olmo, M. Pujadas, and L. Alados-Arboledas

2011 **Study on aerosol properties over Madrid (Spain) by multiple instrumentation during EARLINET lidar intercomparison campaign: SPALI10**
*Poster. V Reunión Española de Ciencia y Tecnología de Aerosoles, Madrid, Spain*
F. Molero, A. Amodeo, M. Sicard, J. Preißler, F. Navas-Guzmán, V. Freudenthaler, A. J. Fernández, A. Giunta, S. Tomás, F. Wagner, M.J. Granados-Muñoz, I. Mattis, M. Pujadas, G. D'Amico, A. Comeron, J. L. Guerrero-Rascado, L. Alados-Arboledas, D. Lange, **J. A. Bravo-Aranda**, D. Kumar, G. Pappalardo, J. Giner, C. Muñoz, and F. Rocadenbosch

2011 **Multi-instrumental detection of the mixing layer height over Granada**
*Poster. V Reunión Española de Ciencia y Tecnología de Aerosoles, Madrid, Spain*
M. J. Granados-Muñoz, F. Navas-Guzmán, **J. A. Bravo-Aranda**, J. L. Guerrero-Rascado, J. Fernández-Gálvez, and L. Alados-Arboledas

2011 **Study of ground-based vertical profiles of tropospheric aerosol in coincidence with CALIPSO overpasses at Granada, Spain**
*Poster. V Reunión Española de Ciencia y Tecnología de Aerosoles, Madrid, Spain*
F. Navas-Guzmán, **J. A. Bravo-Aranda**, J. L. Guerrero-Rascado, M. J. Granados-Muñoz, and L. Alados-Arboledas

2011 **Atmospheric aerosol characterization by dual lidar depolarization**
*Poster. V Reunión Española de Ciencia y Tecnología de Aerosoles, Madrid, Spain*
J. A. Bravo Aranda, F. J. Navas-Guzmán, **M. J. Granados-Muñoz**, J. L. Guerrero-Rascado, and L. Alados-Arboledas

2011 **4D distribution of the 2010 Eyjafjallajökull ash plume over Europe observed by the European Lidar network EARLINET**
*Poster. EGU General Assembly 2011, Wien, Austria*
G. Pappalardo, L. Alados-Arboledas, F. Navas-Guzmán, **J. A. Bravo-Aranda**, et al.

2010 **Atmospheric Aerosol Characterization by lidar depolarization profiles**
*Poster. 3 International Symposium on Recent Advances in Quantitative Remote Sensing, Torrent, Spain*
**J. A. Bravo-Aranda**, F. Navas-Guzmán, M. J. Granados-Muñoz, and L. Alados-Arboledas

2010 **Optical and microphysical properties of tropospheric aerosol from Raman lidar**
*Poster. 3 International Symposium on Recent Advances in Quantitative Remote Sensing, Torrent, Spain*
F. Navas-Guzmán, D. Muller, D. Pérez-Ramírez, J. L. Guerrero-Rascado, **J. A. Bravo-Aranda** and L. Alados-Arboledas

2010 **Study on the assumption of using a range-independent lidar ratio in elastic lidar**
*Poster. 3 International Symposium on Recent Advances in Quantitative Remote Sensing, Torrent, Spain*
F. Navas-Guzmán, F. J. Olmo, J. L. Guerrero-Rascado, H. Lyamani, **J. A. Bravo-Aranda** and L. Alados-Arboledas

2010 **Study on the planetary boundary layer top with Raman lidar**
*Poster. IV Reunión Española de Ciencia y Tecnología de Aerosoles, Granada, Spain*
F. Navas-Guzmán, **J. A. Bravo-Aranda**, M. J. Granados-Muñoz, J. L. Guerrero-Rascado, and L. Alados-Arboledas

2010 **Evaluation of two correction schemes of particle soot absorption photometer data**
*Poster. IV Reunión Española de Ciencia y Tecnología de Aerosoles, Granada, Spain*
H. Lyamani, I. Foyo-Moreno, **J. A. Bravo-Aranda**, F. J. Olmo-Reyes and L. Alados-Arboledas

2010 **Long-term air quality trends over Granada, Spain**
*Poster. IV Reunión Española de Ciencia y Tecnología de Aerosoles, Granada, Spain*
**J. A. Bravo-Aranda**, H. Lyamani, F. J. Olmo-Reyes, J. Vera and L. Alados-Arboledas

2010 **Tracking the Eyjafjallajökull aged plume over Spain by instrumented aircraft**
*Poster. International Aerosol Conference, Helsinki, Finland*
J. Andrey, M. Gil, F. Molero, **J. A. Bravo-Aranda**, O. Serrano, M. Molina, J. Rus and B. Marqués

2010 **Monitoring of lofted aerosol layers of mineral desert dust with Raman lidar and a set of photometers at different altitudes**
*Poster. IV Reunión Española de Ciencia y Tecnología de Aerosoles, Granada, Spain*
F. J. Olmo, F. Navas-Guzmán, H. Lyamani, **J. A. Bravo-Aranda**, J. L. Guerrero-Rascado and L. Alados-Arboledas

2010 **Monitoring of the Eyjafjallajökull ash plume at four lidar stations over the Iberian Peninsula: 6 to 8 May 2010**
*Poster. IV Reunión Española de Ciencia y Tecnología de Aerosoles, Granada, Spain*
M. Sicard, J. L. Guerrero-Rascado, F. Molero, F. Navas-Guzman, J. Preissler, D. Kumar, **J. A. Bravo-Aranda**, S. Tomas, M. D. Reba, L. Alados-Arboledas, A. Comerón, M. Pujadas, F. Rocadenbosch, F. Wagner and A. M. Silva

2010 **Seguimiento de las cenizas del Eyjafjalla sobre la Península Ibérica por la red de lidares hispano-portuguesa Spalinet**
*Poster. X Congreso Nacional del Medio Ambiente, Madrid, Spain*
M. Sicard, A. Comerón, F. Molero, J. L. Guerrero-Rascado, F. Navas-Guzman, J. M. Bolarín, F. Rocadenbosch, S. Tomas, D. Kumar, M. Pujadas, J. Preissler, F. Wagner, **J. A. Bravo-Aranda**, L. Alados-Arboledas, A. Requena and A. M. Silva

2010 **Vertical structure of the atmospheric aerosol derived from Raman lidar and a set of photometers at different altitudes**
*Poster. International Aerosol Conference, Helsinki, Finland*
F. J. Olmo, F. Navas-Guzmán, H. Lyamani, **J. A. Bravo-Aranda**, J. L. Guerrero Rascado and L. Alados-Arboledas

2010 **Ground-based active and passive remote sensing of the Eyjafjallajökull volcanic aerosols at Granada, Spain**
*Poster. 25th International Laser Radar Conference, San Petersburg, Russia*
L. Alados-Arboledas, F. Navas-Guzmán, **J. A. Bravo-Aranda**, H. Lyamani, D. Pérez-Ramírez, J. L. Guerrero-Rascado, M. Antón-Martínez and F. J. Olmo

2010 **Monitoring of the Eyjafjallajökull volcanic ash plume at Granada, Spain, in the framework of earlinet and aeronet**
*Poster. International Aerosol Conference, Helsinki, Finland*
L. Alados-Arboledas, F. Navas-Guzmán, **J. A. Bravo-Aranda**, H. Lyamani, D. Pérez-Ramírez, J. L. Guerrero-Rascado and F. J. Olmo

**2010** **On the synergetic use of passive and active remote sensing for atmospheric aerosol radiative effect computations**
*Poster. 25$^{th}$ International Laser Radar Conference, San Petersburg, Russia*
F. Navas-Guzmán, D. Pérez-Ramírez, F. J. Olmo, H. Lyamani, J. L. Guerrero-Rascado, **J. A. Bravo-Aranda**, L. Alados-Arboledas

**2009** **Caracterización del aerosol atmosférico y gases contaminantes en el ambiente urbano de Granada**
*Poster. III Reunión Española de Ciencia y Tecnología de Aerosoles, Bilbao, Spain*
H. Lyamani, **J. A. Bravo-Aranda**, F. J. Olmo, J. Vida-Manzano and Alados-Arboledas

**2009** **Calibration of 1064nm-backscatter profiles with cirrus clouds for a multiwavelength Raman lidar**
*Poster. III Reunión Española de Ciencia y Tecnología de Aerosoles, Bilbao, Spain*
F. Navas-Guzmán, J. L. Guerrero-Rascado, **J. A. Bravo-Aranda**, H. Lyamani and L. Alados-Arboledas

**2009** **Airborne and ground based instrumentation comparison: closure study during CAPEX project**
*Poster. 8$^{th}$ International Symposium on Tropospheric Profiling: integration of needs, technologies and applications, Delft, Holland*
J. L. Guerrero-Rascado, H. Lyamani, A. M. Silva, F. Wagner, S. Pereira, F. Navas-Guzmán, **J. A. Bravo-Aranda** and L. Alados-Arboledas

**2009** **Atmospheric aerosol properties in an urban atmosphere: ESTIO2005**
*Poster. 8$^{th}$ International Symposium on Tropospheric Profiling: integration of needs, technologies and applications, Delft, Holland*
L. Alados-Arboledas, H. Horvath, X. Querol, F. J. Olmo, J. L. Guerrero-Rascado, H. Lyamani, F. Navas-Guzmán, **J. A. Bravo-Aranda**, M. Gangl and A. Alastuey

**2009** **Quality assurance at the earlinet Granada station: characterization of the optical subsystem for a multichannel Raman lidar**
*Poster. 5$^{th}$ Workshop Lidar Measurements in Latin America, Buenos Aires, Argentina*
J. L. Guerrero-Rascado, F. Navas-Guzmán, J. A. Díaz, J. A: Díaz-Navas, **J. A. Bravo-Aranda** and Alados-Arboledas